Studies of Venus using a comprehensive General Circulation Model

João M. Mendonça

Lincoln College

University of Oxford

A thesis submitted to the Faculty of Physical Sciences for the degree of

Doctor of Philosophy

Trinity 2013

Abstract

The profusion of observational data made available by the Venus Express and previous space missions, increases our need to develop numerical tools to interpret the data and improve our understanding of the Venus meteorology.

The main objective of this work is to develop an improved Venus general circulation model and to study the most likely mechanisms driving the atmosphere to the current observed circulation. Our new model is an extension of a simplified version and includes a new radiative transfer scheme and convection and an adapted boundary layer scheme and dynamical core that take into account the dependence of the heat capacity with temperature, at constant atmospheric pressure. The new radiative transfer formulation implemented is more suitable for Venus climate studies than previous works due to its easy adaptability to different atmospheric conditions. This flexibility of the model was very important in this work to explore the uncertainties on the lower atmospheric conditions such as the gas absorption and the possible presence of aerosols near the surface.

The new general circulation model obtains, after long periods of integration, a super-rotation phenomenon in the cloud region quantitatively similar to the one observed. However, this phenomenon is sensitive to some radiative parameters such as the amount of the solar radiative energy absorbed by the surface and the amount of clouds. The super-rotation in the model is formed due to the combined influence of the zonal mean circulation, thermal tides and transient waves, and the main mechanisms involved are identified and studied. In this process the momentum transported by the semidiurnal tide excited in the upper clouds has a key contribution. These migrating waves transport prograde momentum mainly from the upper atmosphere to the cloud region. In this work we also explored the model parameters to gain a better understanding of the effect of topography, the diurnal cycle and convective momentum mixing. In general the results showed that: the topography seemed capable of sustaining stronger global super-rotation; without diurnal cycle the strong winds in the cloud region are not produced; the convective momentum mixing experiment did not lead to significant changes. A simple experiment done advecting the UV absorber in the atmosphere, qualitatively showed several atmospheric phenomena that are important for the distribution of clouds. Among them is the presence of a region of low permeability isolating the polar vortex. This last experiment also showed that when increasing the amount of UV absorption in the upper cloud region the winds get stronger.

Following the interpretation of observational data using numerical models, we also used a simplified version of the general circulation model to assess the accuracy of zonal wind retrievals from measured temperatures using the cyclostrophic thermal wind equation in the Venus mesosphere. From this analysis we suggest a method which better estimates the lower boundary condition, and improves the consistency of the results at high latitudes when compared with cloud tracking measurements.

To my parents, brothers and dearest Sandra,
who always believed in me.

Acknowledgements

First of all I want to thank my supervisor Peter Read for his guidance and friendship. It was a privilege having had the opportunity to be one of his students. I also want to thank Colin Wilson, Roland Young, Luca Montabone and Yixiong Wang for enthusiastic scientific discussions during the last years which were important for the preparation of this work.

I acknowledge financial support from FCT - Fundação para a Ciência e a Tecnologia (Portugal) - Programme SFRH / BD / 43291 / 2008. Without their help this work would not have been possible. I also thank the Met Office for the use of the HadAM3 dynamical core in this work.

Contents

List of Figures

List of Tables

1

Introduction

1.1 Venus

Venus is the second closest planet to the Sun, has no moons, and it is the most Earth-like astronomical object in terms of size, mass and orbital properties in our solar system (see Table 1.1). Despite this similarity, Earth and Venus have very distinct atmospheres, which is a puzzling fact if we assume that at the time of their formation their composition was roughly the same, due to the bombardment by icy planetesimals and cometary nuclei (e.g., Ip & Fernandez 1988; Taylor 2011). The evolution of both planets must have been different, which can be associated to the different levels of solar irradiation that are more intense on Venus (Kasting 1988). However, the mechanisms by which Venus evolved still remains poorly understood.

Galileo Galilei observed Venus for the first time using a telescope in 1609, and later on, in 1631, Johannes Kepler mapped its orbit around the sun and observed the first transit of Venus. These were early discoveries about the planet that hid its rotation velocity in the dense layers of its atmosphere for more than 200 years. The first attempts to calculate the rotation velocity were made by Jean-Dominique Cassini between 1666 and 1667 and suggested a period of less than one Earth day from the observations of bright areas in the Venus atmosphere. Several scientists tried in the 18th and 19th century to obtain an accurate result for the Venus rotation period, but these measurements had difficulties such as finding points of reference on the planet. All the results indicated a rotation for Venus of around 24h, but the observations from 1877 to 1878 by Giovanni Virginio Schiaparelli did not show any signal of variation related to rotation. Based on his results, Schiaparelli

suggested that the rotation was synchronised with the movement around the sun, 224.7 Earth days. This idea was in contrast to a period of rotation of 24 Earth hours, a point of view that was shared by several scientists of his time. An accurate value was only found in the 20th century, using radar measurements that can penetrate the thick atmosphere and gain more precise measurements of the rotation of the planet. The observations in 1962 by the Jet Propulsion Laboratory (NASA, USA) obtained, surprisingly, a very slow rotation in the inverse direction, with a period of 240.0 Earth days (Goldstein 1964 and Carpenter 1964). Combining the period of rotation with the orbital period of 224.7 Earth days, one gets a Solar day on Venus of 116.7 Earth days, with the Sun rising in the west and setting in the east. The seasonal variability of the solar influx on Venus is minor than the Earth's case due to the lower spin inclination axis ($\sim 2.64^\circ$ in Venus; $\sim 23.26^\circ$ in Earth) and eccentricity orbit (~ 0.007 in Venus; ~ 0.017 in Earth).

Understanding the origin of the mysterious retrograde rotation, opposite to most of the other bodies in the Solar System, has been a challenging problem. The inclination of the rotation axes of the interior planets is a degree of freedom with irregular movement, due to the coupling between the rotation itself with perturbations due to the motion of other bodies in the solar system. In Neron de Surgy & Laskar (1997) and Yoder (1997), it is shown that a mechanism based on dissipative effects that includes both gravitational and thermal tides and the core-mantle friction, coupled with the gravitational perturbations from other planets could tilt the rotation axis to 180° for a large range of initial obliquities. In Correia & Laskar (2001) the mechanisms proposed by Neron de Surgy & Laskar (1997) and Yoder (1997) were confirmed. In this work it is also claimed that the current state of the retrograde rotation in Venus is the most probable state for almost any initial condition in their model, which can also be obtained when the obliquity goes towards zero (the rotation axis does not flip). These studies show that the Venus retrograde rotation is caused by its post-formation dynamical evolution and not of primordial origin (in the formation planet/solar system).

Despite being called Earth's "sister planet", because of their similar size, gravity, and bulk composition, Venus has the most massive atmosphere of the terrestrial Solar System planets, covered by an opaque layer of highly reflective clouds preventing its surface from being seen from space at visible wavelengths. The main gas of its atmosphere is CO_2. On Earth this gas can be efficiently removed from the atmosphere by dissolving into the oceans, but on Venus the surface is dry and this mechanism does not work given the present state of the planet. CO_2 is a "greenhouse" gas and is the major cause of the high temperature

Figure 1.1: Ultraviolet image of Venus clouds obtained by the Pioneer Venus Orbiter (Feb. 26, 1979).

in the Venus lower atmosphere and surface. The large amount of this gas component in the atmosphere (Venus contains a total of about 92 bars of CO_2) raises the surface temperature to about 735 K, three times higher than if this effect did not exist on Venus. The clouds are mainly composed of droplets of sulphuric acid and have a relatively small total mass but enough to contribute to the planet's visible appearance (see Fig. 1.1), atmospheric thermal structure and energy balance.

The circulation of the Venus atmosphere is well known to exhibit strong super-rotation and a variety of dynamically enigmatic features, which remain poorly understood. The super-rotation is characterised by a faster rotation of the atmosphere compared to the rotation rate of the solid body, and is most likely found in all slowly rotating "telluric bodies" (e.g., Titan, Table 1.1). This is a surprising phenomenon because it is counter intuitive if we think about the atmosphere-surface mechanical interaction as the main mechanism to drive the planet's atmosphere circulation. By having a better understanding of the main atmospheric processes for formation and maintenance of this phenomenon, we will be able to develop a more complete theory about the global atmospheric circulation of slowly rotating planets such as Venus.

1.1.1 Surface

The first observations of the Venus surface temperature were done in the 1950's, through the possibility of measuring the intensity of the microwave radiation coming from the planet

	Venus	Titan	Earth
Mean Radius (km)	6051.8	2575.0	6371.0
Surface gravity (equator m s^{-2})	8.87	1.35	9.78
Bond Albedo	0.75	0.2	0.306
Solar Irradiance (W s^{-2})	2623.9	14.90	1367.6
Black-body temperature (K)	231.7	84.5	254.3
Sidereal orbit period (days)	224.701	(15.95)	365.256
Tropical orbit period (days)	224.695	(15.95)	365.242
Orbit inclination (deg)	3.39	27 (relative to Saturn)	0.0
Orbit eccentricity	0.0067	0.029	0.0167
Sidereal rotation period (hrs)	(-)5832.5	382.68	23.9345
(Solar) Length of day (hrs)	2802.0	383.68	24.0
Solar day / Sidereal day	0.480411	(1.000)	1.000274
Obliquity of orbit (deg)	177.36		23.45
Surface Pressure (atm)	92	1.5	1
Mean molecular weight (kg/mole)	0.04345	28	28.97
Gas constant (J/K/kg)	188	290	287
Specific heat (J/K/kg)	900.0	1005	1005
κ=R/C_p	0.222	0.277	0.286
Atmospheric composition	0.95 CO_2	0.9-0.97 N_2	0.78 N_2
	0.035 N_2		0.201 O_2
Global Super-rotation	10	6-10	0.015
Local super-rotation (maximum)	60		3-8
Sidereal day (Earth days)	243	1.025	1
Solar Days (Earth days)	116.95	1.027	1.000274
Surface Temperature (approx K)	735	94	285

Table 1.1: Table from Lee (2006) with the bulk, orbital and atmospheric parameters for Venus (Williams, 2003b), Earth (Williams, 2003a) and Titan (Coustenis & Taylor (1999) and Allison & Travis (1985)).

using radio telescopes. These measurements estimated a hot surface, which was confirmed later by the probe Mariner 2 (Sonett 1963). In the 1970's the Venera landers measured a surface temperature of roughly 741±7 K (Marov *et al.* 1973), showing a sterile, mainly basaltic, surface like a scorched desert dominated by a rock-strewn landscape.

The satellite Magellan mapped the planet's surface concluding that Venus is 70% covered by smooth (rolling) plains, 20% of lowlands and 10% of highland regions (Basilevsky & McGill 2007; Taylor 2006), see Fig. 1.2. Apparently the movement of tectonic plates does not exist due to the lack of observed large-scale linear tectonic features or linear patterns in the distribution of volcanic features. The formation of highlands, which appear as massive local mountains, is suggested to be caused by a deep process within the crust, like a vigorous convection in a large "hot spot" or mantle plumes (Smrekar *et al.* 2007). Analysing of near-inferred data from the Visible and Infrared Thermal Imaging Spectrometer (VIRTIS) instrument on Venus Express, Smrekar *et al.* (2007) revealed hints of recent or ongoing vulcanic activity. The results obtained show higher levels of emissivity in the "hot spot" regions which can be interpreted as the presence of a very young surface (because surface weathering would reduce emissivity) and that Venus is actively resurfacing. Much of the Venus surface appears to have been shaped by volcanic activity, which may indicate that the geological surface is relatively young (Basilevsky & McGill 2007). The several hundred craters in the surface are uniformly distributed and in a well-preserved condition suggesting that the "young" plain surfaces were formed over a geologically short-time (Schaber *et al.* 1992). The size of the craters in the Venus surface is determined by the filtering done by the huge atmosphere that covers the entire planet, which makes the formation of relatively small meteoric craters unlikely.

1.1.2 Atmospheric composition and clouds

Venus has a dense atmosphere mainly composed of carbon dioxide (∼96.5%) and a small amount of nitrogen (∼3.5%), Table 1.2. Sometimes minor constituents are observed in the atmosphere, such as sulphur dioxide, carbon monoxide and water, exhibiting local concentrations with temporal and spatial variations, which are linked with atmospheric circulation and meteorology, and/or possibly with some localised sources in the surface like volcanism. The images in the UV (see Fig. 1.1), show a dominant pattern in the atmosphere with the shape of the letter "Y" (laid sideways) or the inverse "C". This feature is visualised by some

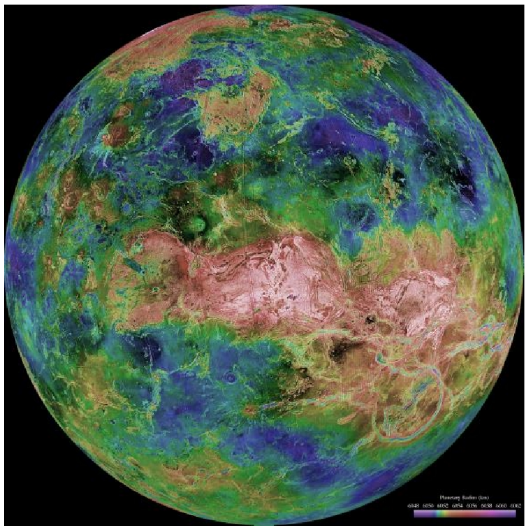

Figure 1.2: Radar map of the surface of Venus measured by Magellan probe (1990's). The red colour represents the highest levels and blue the depressions. The north pole is at the centre of the image.

unidentified UV absorber substances that are redistributed spatially by the dynamics in the atmosphere (Markiewicz *et al.* 2007; Titov *et al.* 2008).

The main cloud deck is composed mostly of a mixture of sulphuric acid and water droplets and it extends from about 45 to 65 km above the surface, with haze layers above and below (Knollenberg & Hunten 1980). At the UV, visible and most of the infrared wavelength range, the clouds are very optically thick, with a high single scattering albedo that hide the surface of the planet. In addition to these optical properties, there are some visible and near-IR spectral windows that have been observed in the Venus atmosphere (Allen & Crawford 1984). From the near-IR mapping spectrometer aboard the Galileo spacecraft (see Fig. 1.3), it is possible to observe variability in the horizontal and vertical structure of the lower clouds (Carlson *et al.* 1991), which is a consequence of the dynamical transport and the production and destruction of particles in the atmosphere. The clouds have particles of three different modal populations (e.g., Crisp (1986)) whose proportions are different in the different layers, with sizes ranging from less than 1 to over 30 μm in diameter. The smallest particles (aerosol haze), termed 'mode 1' droplets, are distributed throughout the cloud region and their composition is still unknown. The droplets of the 'mode 2' are mainly H_2SO_4 and H_2O, and the 'mode 3' are probably composed of "bigger droplets" of H_2SO_4 and are located at the lower and middle cloud layers.

Total mass of atmosphere	4.8×10^{20} kg
Mean molecular weight	0.04345 kg/mol
Scale height	15.9 km
Atmospheric composition (near surface)	
Major	Carbon dioxide (CO_2) 96.5%
	Nitrogen (N_2) 3.5%
Minor (ppm)	Sulphur dioxide (SO_2) 150
	Argon (Ar) 70
	Water (H_2O) 20
	Carbon monoxide (CO) 17
	Helium (He) 12
	Neon (Ne) 7

Table 1.2: Venus atmospheric composition (von Zahn *et al.* 1983; Taylor 2006)

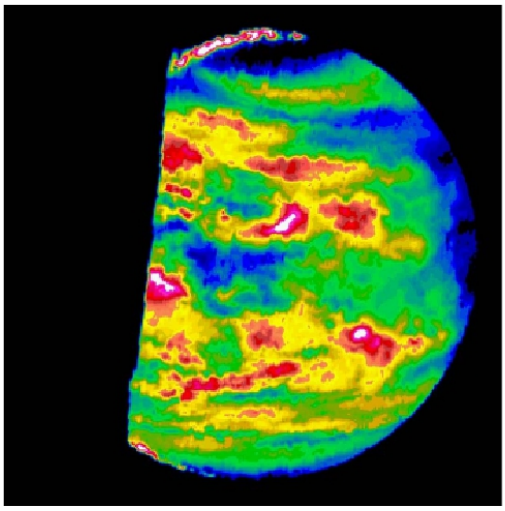

Figure 1.3: This false colour image is from the night side of Venus in the near-infrared window at 2.3 μm (26 to 45 km altitude, Taylor *et al.* 1997), and was obtained by the NIMS aboard the Galileo spacecraft during its flyby in February 1990 (Carlson *et al.*, 1991). The variations in brightness (more than one order of magnitude) show the change in thickness of the lower clouds from white and red (thin cloud regions) to black and blue (thick clouds).

1.1.3 Thermal structure and energy balance

In the case of planets without an internal heat source, the Sun is the main source of energy. If Venus was an airless planet with an albedo of 0.76 and with the same astronomical parameters, the expected value for the surface temperature would be around 230 K, which is very different from the value observed. The discrepancy in the values is associated with the composition of the massive atmosphere in Venus that creates a significant "greenhouse" effect (e.g., Sagan 1961). This feature is responsible for the high temperatures at the surface. The lower atmosphere (troposphere), due to the large opacity of the overlying layers, does not radiate enough energy to space at the long wavelengths. It re-emits part of the energy received back to the surface, raising its expected temperature to around 735 K.

The clouds have a very important influence on the thermal structure of the atmosphere since they absorb and reflect a major part of the solar insolation and have an important impact on the determination of the surface temperature. Due to the highly reflective properties of the clouds, the planet receives less total solar energy than the Earth, despite being closer to the Sun.

Height and density profiles were retrieved from the accelerometer measurements of the Pioneer Venus entry probe. These data were used later to compute temperature profiles for different locations using the hydrostatic equation and the equation of state Seiff *et al.* (1980). In Fig. 1.4, taken from Lee (2006), four vertical profiles of temperature are shown plus one that was used in the thermal forcing parameterisation of the OPUS-Vs (explained in the next section). For the range of altitudes shown, we see that the difference in temperature between the bottom and top of the atmosphere is much larger on Venus ($\sim$ 500 K) than on the values observed for the Earth atmosphere ($\sim$ 90 K). The vertical variation of the atmospheric static stability gives us a first hint of how the atmospheric circulation must be organised. The static stability (γ) is defined as:

$$\gamma = \frac{dT}{dz} - \Gamma, \tag{1.1}$$

where Γ_d is the dry adiabatic lapse rate which can be calculated, treating the atmosphere as an ideal gas, as $\frac{g}{c_p}$ (where g is the planetary acceleration due to gravity and c_p is the specific heat capacity at constant pressure). Coupling the buoyancy forces with gravitational forces and using the first law of thermodynamics, it is easy to verify that for $\frac{dT}{dz} < -\Gamma_d$ the atmosphere is unstable with respect to vertical motions and stable when $\frac{dT}{dz} > -\Gamma_d$.

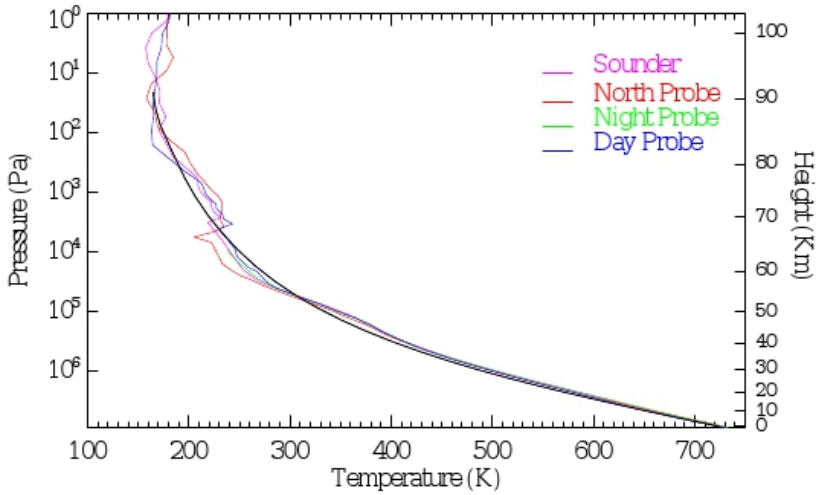

Figure 1.4: The black line is the temperature profile used in the thermal forcing parameterisation of the OPUS-Vs (Lee 2006). The figure was obtained from Lee (2006) which used the data from the Pioneer Venus descent probe (Seiff *et al.*, 1980). The night probe measured the temperatures up to 65 km only. The four probes obtained the data from different latitudes and local times: Sounder - 4.4° N, 7:38 am; Day - 32.1° S, 6:46 am; Night - 28.7° S, 0:07 am; North - 59.3° N, 3:35 am.

The observational temperature profiles indicate regions of different static stability, being nearly adiabatic in the deep atmosphere and within the cloud region (50-60 km) and stably stratified above the clouds ($z > 60$ km). Nearly adiabatic conditions are associated with regions more favourable to the occurrence of unstable upward convection, where the variation of the temperature with height becomes roughly equal to the dry adiabatic lapse rate.

The above equation 1.1 is obtained assuming that the gas in the atmosphere has the characteristics of a perfect gas, and follows the well-known equation of state:

$$pV = nRT \tag{1.2}$$

where p is the pressure, V is the volume, T is the temperature, R is the gas constant and n is related to the amount of gas. The accuracy of this equation depends on pressure and temperature. Some effects such as the molecular volume and the molecular attractive forces are the main factors responsible for the incorporation of imperfections in the "perfect" gas behaviour. At very low pressure the intermolecular distance is large enough so that neither repulsive nor attractive forces have an important contribution, which makes the perfect gas a

good approximation. Upon increasing the pressure, the molecular attraction effect becomes important favouring compression, however, at even higher pressures repulsive forces become dominant because the molecules resist being pressed together. These effects depend on the gas composition. In the Venus deep atmosphere the pressure reaches values larger than 92×10^3 hPa, which raises concerns about the validity of the perfect gas relation in that region. A simple estimation of the weight of these inaccuracies in the prefect gas can be done following (e.g., Atkins 1982):

- The Volume V is replaced by $V - nb$, which takes into account the volume occupied by the molecules (nb).
- The pressure is reduced by an^2/V^2, which estimates the effect of attractive forces.

In these equations the parameters a and b are called the Van Der Waals constants. In the case of CO_2 a is equal to 3.639×10^{-3}m^6 hPa mol^{-2} and b is equal to 0.427 m^3 mol^{-1} (Atkins 1982). Using these two corrections in the equation of state, it is possible to estimate the error when computing the pressure at the deep Venus atmosphere, which was estimated here to be about 2%. This result indicates that the perfect gas approximation is still a good approximation in the deep Venus atmosphere, which is mainly due to the high temperatures that reduce the effect of the repulsive forces by the molecular compression.

1.1.4 Atmospheric dynamics

The circulation of the atmosphere on Venus (see Fig. 1.5) is mainly found in one of two regimes: the retrograde zonal super-rotation in the troposphere and mesosphere (Gierasch *et al.*, 1997), and a solar-antisolar circulation across the terminator in the thermosphere (Bougher *et al.*, 1997) ($z > 100$ km). Several observations made by descent probes, the Vega balloons (e.g., Preston *et al.* 1986) or using cloud tracking in the UV (e.g., Moissl *et al.* 2009), show the winds reaching a maximum of 100 m s^{-1} at the cloud tops and decreasing to roughly zero at 10 km altitude (Fig. 1.6). In average, the main cloud deck rotates around the planet in a period of 4-5 days, being roughly 50-60 times faster than the rotation of the solid planet, which has a maximum of 2 m s^{-1} at the equator relative to the background stars.

The observations in the infrared (IR) made by Venus Express show a bright south pole surrounded by a cold "collar" (Piccioni *et al.*, 2007a), that is very similar to what was observed in previous missions to the north pole (Taylor *et al.*, 1979) (see Fig. 1.7). These

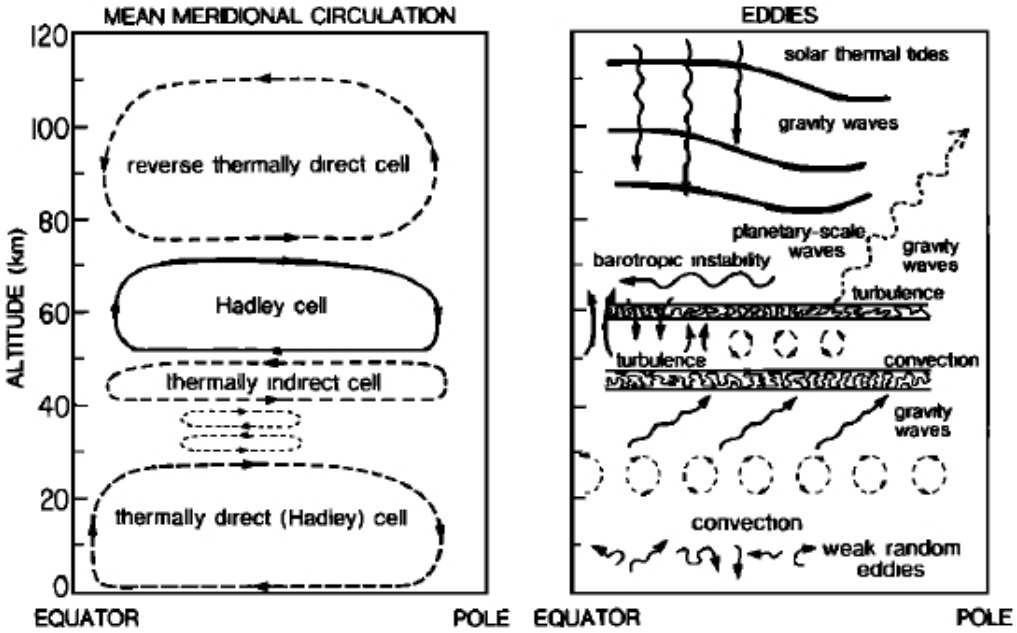

Figure 1.5: The Figure summarises schematically the main features of the atmospheric circulation on Venus from Schubert *et al.* (1980).

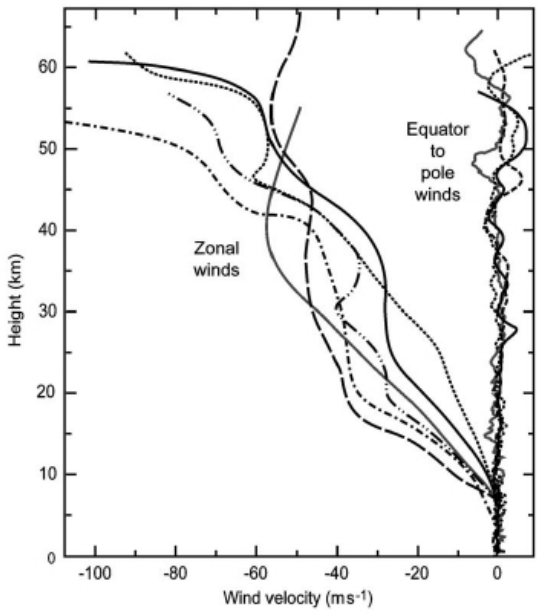

Figure 1.6: Venus wind profiles (height-wind velocity) measured for different locations by the Pioneer Probes (Counselman *et al.*, 1980).

huge cyclonic structures change their central morphology continually, resembling a single, double or tri-vortex structure that rotates around the pole. There are two phases that characterise the polar vortex: at about 50 km altitude, a cold "collar" circulating around a higher temperature polar cap, and at about 90 km, a warm pole, where the temperature of the polar region is higher than at lower latitudes. The nature and mechanisms of the polar temperature structures and the polar vortices are still not clear. A possible mechanism for the formation of the inverted polar temperature structure could be a result of the compressional adiabatic warming from the descending branch of the meridional cell circulation, and/or variations in the solar heating, due to variations in the haze densities at 80 km. The dynamics of the polar vortices on Venus seems to be related to the possibility of barotropic instabilities in the circumpolar flow (Limaye *et al.*, 2009).

Global wave activity in the Venus atmosphere is likely to play an important role in the transport of momentum and energy in the atmosphere. The planetary-scale cloud patterns observed in the UV measurements, in the shape of a large horizontal "Y", can be explained by the presence of atmospheric waves travelling slowly with respect to the cloud-top winds. The combination of mid-latitude waves travelling slower than the winds, interfering with faster equatorial waves coupled with some non-linear effects, seem sufficient to explain the pattern observed (Covey & Schubert 1983). The real nature of the waves in the atmosphere of Venus is difficult to explain, however, due to the lack of observational data. del Genio & Rossow (1990) explored UV images to study the characteristics of waves in the atmosphere of Venus, and correlated the contrasts of an unknown UV absorber with winds and temperature fields. The waves observed at 65-70 km altitude were of two types: equatorially trapped waves moving in the same direction as the wind but faster, extending from its equator to roughly 20° latitude and with a period of 4 days, identified as a Kelvin wave; mid-latitude waves moving in the same direction as the winds but slower, with two different periods of 4 and 5.2 days, which were intrepreted as Mixed-Rossby-Gravity waves (MRG waves).

1.1.4.1 Atmospheric super-rotation

As was pointed out above, the dynamics of the atmosphere in Venus below 100 km is characterised by a global atmospheric super-rotation. This phenomenon is related to the much larger total angular momentum of the atmosphere in comparison with the case of an atmosphere at rest. From Read (1986) this global phenomenon is quantified using the

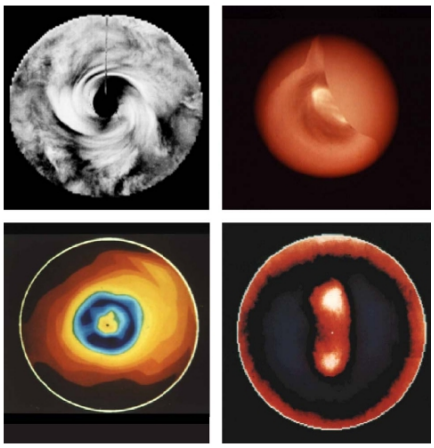

Figure 1.7: The figure shows four images of the North polar vortex (Taylor, 2006). The one in the top left is a composite UV image from Mariner 10. The top right image was taken at 11.5 μm by Pioneer Venus and shows an S structure surrounded by a cold "collar". The two bottom images are both averaged over 72 days. The one on the left used coordinates that were fixed with respect to the solid planet, which emphasises the cold "collar". The lower right image is an average in coordinates that were fixed with respect to the axis of the double vortex, and shows the double wave structure surrounded by a cold "collar" again. The darker/bluer regions are associated with cooler regions (Taylor *et al.* 1980).

following equation,

$$S = \frac{M_t}{M_0} - 1, \tag{1.3}$$

where S is defined as the global super-rotation index, M_t is the total angular momentum of the atmosphere and M_0 is the total angular momentum of the atmosphere with zero zonal wind velocities relative to its underlying planet. The total angular momentum of the atmosphere (M_t) is defined by:

$$M_t = \int\int\int \frac{ma^2 \cos\phi}{g} d\phi d\lambda dp \tag{1.4}$$

where a is taken to be the radius of the planet, ϕ is latitude, λ is longitude, p is pressure, g is planetary gravity acceleration and m is the angular momentum per unit mass ($m = a\cos\phi(\Omega a\cos\phi + u)$, Ω is the rotation rate of the planet and u is the zonal component of the wind velocity). Using these equations (1.3 and 1.4) and the observational vertical profiles of zonal winds and their uncertainties from Kerzhanovich & Limaye (1985), we can estimate $S = 7.66^{+4.15}_{-3.56}$. The vertical profiles from Kerzhanovich & Limaye (1985) are associated with low latitudes. Three different profiles corresponding to the lowest, mean and highest wind

values observed at each altitude, were used to build three global wind fields to compute three different values of S (the mean value and its uncertainties). The three global wind fields were defined using the observational vertical wind profiles at the equator and were extrapolated to the pole region assuming that the atmospheric circulation follows a solid body rotation profile at each altitude. These three dimensional wind fields are axisymmetric. In general, the solid body rotation assumption slightly underestimates the values of the zonal winds at high latitudes, but is a very good approximation for the altitudes where the winds have the largest contribution to angular momentum density (at 20 km, Schubert 1983).

The global atmospheric circulation below 100 km on Venus is however, still poorly understood. In general, the dynamics of the atmosphere on Venus is driven by a differential insolation in latitude, which might be expected to induce atmospheric circulation in the form of cells with rising atmospheric flow at low latitudes and descending at high latitudes, represented in Fig. 1.5 (for a thermally direct Hadley circulation). The presence of middle or high latitude local super-rotation is well explained as a consequence of the existence of these cells that transport angular momentum from low toward high latitudes. The presence of a large equator-to-pole Hadley circulation in each hemisphere (e.g., Schubert *et al.* 1980) is due to the slow planetary rotation, which weakens the coriolis acceleration, increasing the efficiency of the latitudinal heat transport of the atmosphere. More difficult to explain is the presence of the observed equatorial super-rotation. The strong winds at the equatorial region are not produced or maintained by the influence of zonal mean mechanisms (Hide 1969). Such a phenomenon requires the presence of nonaxisymmetric eddy motions, unless super-rotation was its initial condition.

Using the equations of motion we can learn more about the possible atmospheric mechanisms for the strong winds in the equatorial region (Gierasch *et al.* (1997)):

$$\underbrace{\frac{\partial}{\partial t}(\rho m)}_{[A]} + \underbrace{\vec{\nabla}\cdot(\rho \mathbf{v} m)}_{[B]} + \underbrace{\frac{\partial p}{\partial \lambda}}_{[C]} = \underbrace{\vec{\nabla}\cdot(\tau\cdot\hat{\mathbf{z}}\times\mathbf{r})}_{[D]} \tag{1.5}$$

where $\hat{\mathbf{z}}$ is the unit vector in the direction of the planetary angular velocity (Ω) and τ is the viscous stress tensor. m in this equation is the angular momentum per unit mass as mentioned previously. Zonally averaging this equation and assuming the friction is negligible, the terms [C] and [D] drop out. This simplification makes it easier to interpret the conservation of angular momentum in a circulating atmospheric cell. Unless there is convergence of the angular momentum flux, $\mathbf{F}_m = \rho \mathbf{v} m$, towards a location of maximum

angular momentum per unit of mass, it is not possible to produce, for example, the observed strong prograde winds at low latitudes in the Venus atmosphere. It was demonstrated in Hide (1969) that global or local super-rotation cannot be obtained in a purely inviscid, axisymmetric system that evolved from rest. This result is frequently called "Hides's first theorem" (Read 1986), and implies that the excess of angular momentum, $S > 0$, can only be obtained from non-axisymmetric motions. This non-axisymmetric phenomenon can be represented by the known Reynolds' stress terms (zonal pressure torques) that are defined by:

$$\overline{F}_m = \rho a \cos\phi(\overline{u'v'}, \overline{u'w'}) \tag{1.6}$$

where ρ is the atmospheric density, a is the planet radius, the bar over the variables denotes a zonal average, v is the meridional component of the wind velocity and w is the wind speed in the vertical direction. The primes on each variable mean that they are disturbances in relation to their respective zonal average. The first and second terms are the meridional and vertical components of the eddy fluxes. From Equation (1.6), the weight of each component of the Reynold's stress (horizontal and vertical) is in general related to different possible mechanisms that contribute to the formation and/or maintenance of the super-rotation. To be able to complete the puzzle on the real nature of the general super-rotation, there is a need to identify the atmospheric processes involved in these two terms and quantify their contribution to the phenomenon.

Different mechanisms may be at work in different regions of the atmosphere to explain the equatorial super-rotation due to the diverse atmospheric conditions in the mesosphere ($z \approx 55 - 100$ km) and deep atmosphere ($z < 55$ km):

- In the mesosphere, the atmospheric circulation is largely influenced by the solar thermal tides, due to the relatively small radiative time constant of a few days in comparison with the total solar day length (Crisp 1989). This time constant represents the radiative response of the atmosphere to a change in temperature and is quantified as the time that the atmospheric temperature takes to exponentially decay to a fraction e^{-1} of its initial value. A mechanism proposed by Fels & Lindzen (1974) suggests that the acceleration of the atmosphere in the cloud top region is due to the existence of thermally excited gravity waves of unspecified scale. These disturbances propagate vertically and carry momentum away from their excitation region (in the vertical eddy term, $\overline{u'w'}$) accelerating the atmosphere in the opposite direction to the transmitted

wave. In the cloud top region the significant solar heating forcing drives various harmonics of the thermal tides that propagate upward and downward. In Pechmann & Ingersoll (1984), and more recently in Zasova *et al.* (2007), it was shown that the amplitude and phase structure of the semi-diurnal tidal component agreed well with observational data. The atmospheric circulation, coupled with the vertical propagation of these waves, creates a phase shift (tilted convective cells) ideal for inducing positive Reynolds stress acceleration in the prograde direction within the excitation region. The thermal tide is stationary with respect to the sub-solar point, and moves against the mean flow. These waves thus accelerate the region where they are excited and decelerate the region where they are absorbed by radiative damping. The downward component is weaker in the Venus mesosphere due to the large thermal inertia of the lower atmosphere inducing a smaller acceleration effect. Another mechanism that may be important in this region is the formation of eddies by barotropic instability of a high-latitude jet produced by the Hadley cell in a stratified atmosphere (GRW mechanism, Gierasch 1975 and Rossow & Williams 1979). The formation of such synoptic planetary waves at high latitudes has the property of pumping momentum horizontally towards lower latitudes, weakening the jet strength (horizontal component of the Reynolds stress, $\overline{u'v'}$) and accelerating the winds at lower latitudes.

From observable data it is still unknown which mechanism is more important in driving the strong winds, or if there is a mechanism that has not been suggested by theoretical studies yet. However, results from the latest Venus **G**eneral **C**irculation **M**odels (including e.g., the GCM results from Lebonnois *et al.* 2010a and this work) indicate that the main mechanism for the formation of strong equatorial winds in the cloud top region is due mainly to the vertical component of the Reynold stress forcing, induced by the atmospheric semi-diurnal tide.

- In the deep atmosphere the large atmospheric thermal inertia makes the radiative time scale much larger than the length of a Venusian solar day. For this reason the solar thermal tides do not significantly influence the atmospheric circulation. A mechanism based on the atmospheric absorption in critical layers of small-scale gravity waves with prograde phase speed was proposed in Hou & Farrell (1987). These waves propagate upwards, transporting momentum vertically via ($\overline{u'w'}$), and are excited near the surface by penetrative atmospheric convection. Other possible causes for

the formation and maintenance of the strong equatorial wind in this region may be associated once again with synoptic planetary waves and transient or topographically forced waves (Yamamoto & Takahashi 2009).

The scarce available observational data from the deep atmosphere makes it difficult to analyse and study its meteorology and also to constrain the physical parameterisations needed for GCMs. The atmospheric circulation in this region has a large weight in the quantification of super-rotation, however, due to fast prograde winds being associated with a very large atmospheric density.

1.2 Simplified atmospheric numerical models

General Circulation Models (GCM) applied to the planet Venus have become important tools to understand its atmospheric dynamics and climate. These models solve the complex physical and dynamical equations that incorporate fundamental principles of atmospheric fluid dynamics and use various approximations and parameterisations for radiative transfer, convection and the lower boundary conditions. They have been very important in investigating the climate and weather forecasting on Earth. The implementation of new methods in the GCM's dynamical core and improvements in computer technology have brought many advances in these computationally expensive models. In this work, the term "simplified GCMs", will refer to models which do not try to use complete physics-based representations of all physical processes, but include simplified representations of heating, cooling and friction processes.

Adapting GCMs for Venus's atmospheric conditions require solutions for some technical difficulties associated with computational accuracy and execution time. The minimum spatial resolution required to simulate the Venus atmosphere is still not known, because it is still not clear what are the main mechanisms driving the atmosphere towards the actual observable atmospheric state that need to be resolved. The atmospheric simulations for Venus take much longer time of integration to reach a statistically steady state (indicated e.g., by a roughly constant kinetic energy) than for other planets with thinner atmospheres (e.g., Earth and Mars). These timescales are partly due to the slow thermal adjustment of the mean deep atmospheric structure. In the upper atmosphere, these time scales are shorter, with the atmospheric tides involving time scales of less than a Venus solar day.

Venus GCMs began to be developed more than three decades ago. They have typically used simple physical parameterisations or restrictions to less than three dimensions due to the difficulties highlighted above, but their success has been gradually increasing over the years. As part of this evolution, we find works such as those of Kalnay de Rivas (1975), based on a simple quasi-three-dimensional spectral model and which produced a weak super-rotation, with a maximum westward wind speed of 20 m s^{-1}. It was pointed out later by Mayr & Harris (1983) that this previous work had an inappropriate parameterisation of the thermal conductivity. In Young & Pollack (1977), a simplified GCM for Venus was developed which produced an equatorial super-rotation similar to the observations. However to drive the winds to produce such a particular atmospheric circulation, the model used unrealistic momentum sources included in an eddy diffusion parameterisation.

In the 1980s, several models tried to simulate the observed super-rotation (Rossow 1983, Covey *et al.* 1986 and del Genio & Suozzo 1987), but with no clear success. These models, which did not include a diurnal cycle, were not capable of reproducing the strong equatorial super-rotation, despite the GRW mechanism using barotropic eddies to transport momentum towards the equator being active in the simulations. Later in Williams (1988a) and Williams (1988b), the influence of diurnal forcing in the atmosphere using a dry Earth GCM at slow rate was tested for the first time. The results obtained showed that the thermal tides could play an important role and produce a stronger equatorial super-rotation (but still smaller than the observations), increasing the generation of the momentum-transferring planetary waves.

The simplified dry Earth GCM from del Genio & Suozzo (1987) was unable to reproduce strong equatorial super-rotation as cited above, but later del Genio *et al.* (1993) explored this problem again in an atmospheric parametric study. In this work, the amount of clouds was changed, which consequently affected the solar heating profile (the model did not contain a diurnal or seasonal cycle). Upon removing the clouds in the GCM, it was found that the static stability in the atmosphere decreased, which consequently increased the 'friction' (i.e. down-gradient mixing of angular momentum) due to vertical convective mixing, preventing the formation of strong equatorial super-rotation. Increasing the amount of clouds, the heating profiles were modified so that this 'friction' is reduced, and following the GRW mechanism, it was then possible to produce both equatorial and mid-latitude super-rotation. del Genio & Zhou (1996), showed, using their GCM, that in general the super-rotation index mentioned in the previous section increases with the decrease of the planetary rotation rate.

Stronger high latitude jets are obtained when the rotation rate is reduced because the Hadley cell strengthens and expands poleward, which favours the GRW mechanism. It was also noted that the equatorial super-rotating atmospheric state is commonly expected on planets with statically stable radiative equilibrium structures and does not depend on the initial state.

Nowadays, simplified Venus GCMs are being developed at several institutions around the world. The OPUS-Vs is among the leading simplified models (Lee *et al.* 2007), and it has led to some success in producing qualitatively realistic Venus-like global circulations, with a significant super-rotation (within a factor of 2, see next section). Some of these more recent simplified models are shown and compared in section 1.2.2.

1.2.1 OPUS-Vs

This section briefly reviews the simplified OPUS-V (i.e., the simplified **O**xford **P**lanetary **U**nified (Model) **S**ystem for **V**enus - OPUS-Vs), which obtains a dynamically self-consistent representation of the Venus atmospheric circulation (Lee *et al.* 2005; Lee 2006; Lee *et al.* 2007).

The model uses physical and dynamical parameters corresponding to Venus (Colin 1983; Williams 2003b), and simplified parameterisations for radiative forcing and boundary layer dissipation. It is based on the dynamical core of the version 4.5 of the UK Hadley Centre Unified Model (Cullen *et al.*, 1992) and is configured on an Arakawa B grid (Arakawa & Lamb, 1981), using horizontal resolution of 5°x5°, covering the entire global domain with 32 σ-pressure vertical levels (with a maximum vertical grid spacing of ∼3.5 km). The atmosphere modelled extends from the surface to an altitude of around 90 km (∼0.5hPa). Chapter 4 describes in more detail the dynamical core of this model which, for the latest version (not the simplified one), also takes into account the variation of the specific heat capacity of the atmosphere with temperature at constant pressure.

The thermal forcing scheme used in OPUS-Vs is not based on a full radiative transfer model, but on a simplified formulation using a linear temperature relaxation scheme towards a prescribed temperature field, which is a function of latitude and height (pressure) only. The latter is derived from the superposition of a global-averaged reference temperature profile, obtained from Pioneer Venus probe data (Seiff *et al.*, 1980), plus a perturbation which is a function of latitude and pressure that determines the equator-to-pole thermal contrast at each altitude. This structure is chosen to produce a peak in solar heating within the

altitude range of the observed cloud deck (Tomasko *et al.* 1985; Lee 2006; Lee *et al.* 2007). This parameterisation forces the temperature towards a radiative equilibrium atmosphere at each point (λ-longitude, ϕ-latitude, p-pressure, t-time) using temperature increments of the form

$$\delta T_{rad}(\lambda, \phi, p, t) = -\frac{T(\lambda, \phi, p, t) - T_0(\phi, p)}{\tau}\delta t \tag{1.7}$$

where $T_0(\phi, p)$ is the reference temperature pattern and τ is the time constant. The form of $T_0(\phi$,p) is,

$$T_0(\phi, p) = T_{ref}(p) + T_1(p)(cos(\phi) - C), \tag{1.8}$$

designed to represent an approximation to a radiative equilibrium state. In this equation T_{ref}(p) is taken as the reference temperature profile obtained from Seiff *et al.* (1980) and Seiff (1983), T_1(p) is a perturbation term that shapes the equator-to-pole difference, and finally the constant C is the result of forcing the integral of cos(ϕ) - C to be zero over the domain (i.e. C = $\frac{\pi}{4}$). The values for the time constant used are smaller than the values appropriate for the atmosphere of Venus in order to save computational time. The value for τ used is 25 Earth days, decreasing slightly in the uppermost levels.

The mechanical interaction of the atmosphere with the surface was modelled by a simple boundary layer drag scheme with a linearised Rayleigh friction parameterisation. This simple formulation was determined using,

$$\frac{d\vec{u}}{dt} = -\frac{\vec{u}}{\tau_d}, \tag{1.9}$$

where τ_d is the relaxation time scale and $\vec{u}$ is the horizontal velocity vector at the lowest layer only. The planet's surface is assumed to be flat, so the value for τ_d is the same at all the surface points, 32 Earth days, which was obtained using a relation between the relaxation period and the bulk transfer coefficients for approximately the typical values for the Earth (Lee, 2006).

In the three uppermost layers a sponge layer is included, with Rayleigh friction acting to damp horizontal *eddy* winds to zero (though it does not act on the zonal mean flow; Lee 2006; Lee *et al.* 2007).

Using this model for Venus, it was possible to reproduce a substantially super-rotating atmosphere via the well-known GRW mechanism (Gierasch 1975; Rossow & Williams 1979) without any arbitrary non-physical forcing, and also without diurnal or seasonal cycles.

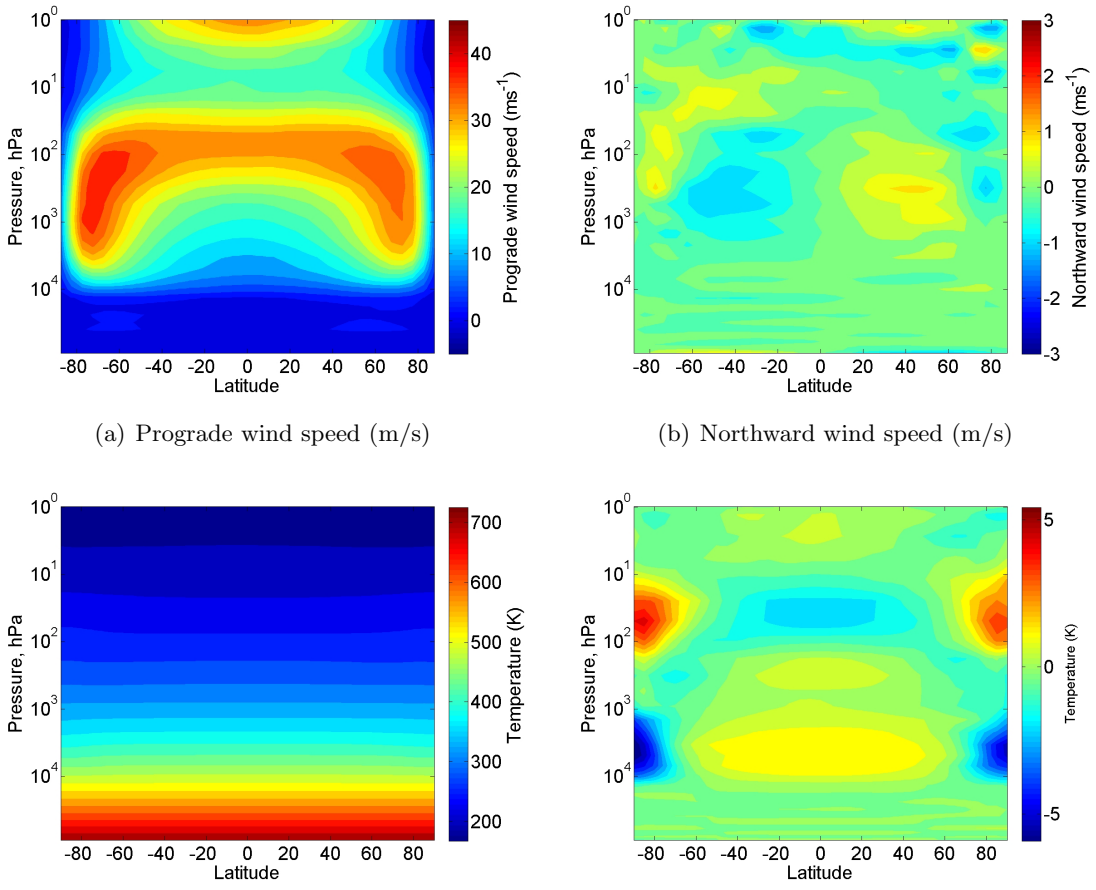

(a) Prograde wind speed (m/s)

(b) Northward wind speed (m/s)

(c) Temperature (K)

(d) Temperature (K)

Figure 1.8: Results obtained after 500 Earth days of zonal average from the OPUS-Vs without the diurnal forcing, and after 30000 Earth days of integration from a rest atmosphere. **(a)** Prograde wind speed (m/s). **(b)** Northward wind speed (m/s). **(c)** Temperature (K). **(d)** Temperature (K) after the latitude mean has been removed. Note that the term "prograde" refers to winds in the direction of the planet's rotation, i.e. westward.

The zonal wind map in Fig. 1.8(a) shows this global atmospheric phenomenon clearly. The horizontal equatorward eddy transport of momentum at 40-80 km is largely responsible for maintaining this equatorial super-rotation. The model also produces equatorial Kelvin and Mixed-Rossby-Gravity (MRG) waves spontaneously. Lee (2006) found that the MRG waves contribute to equatorward momentum transport and help maintain the equatorial super-rotation. The model also simulates, amongst other phenomena, a "cold collar" in the middle atmosphere and a warm pole in the upper atmosphere as is shown in Fig. 1.8(d), although with weaker amplitudes than observed. Further details can be found in Lee (2006) and Lee *et al.* (2007).

In the next chapter, the OPUS-Vs is used to develop an improved method to retrieve the zonal thermal winds. This is a good example of how the combination of simplified models and data can help to guide the analysis of observational data.

1.2.2 Inter-comparison of simplified Venus GCMs

In Lebonnois *et al.* (2013), results of different simplified GCMs applied to the Venus atmosphere were compared. This work was similar to the previous inter-comparison exercise carried out by Lee & Richardson (2010), but in Lebonnois *et al.* (2013) a wider variety of atmospheric models which were developed around the world were included. These include the OPUS-Vs presented in the previous section, the CCSR/NIES GCM (e.g., Yamamoto & Takahashi 2003; which is a spectral model), the LMD GCM (as used by Lebonnois *et al.* 2010a, but with a simplified radiative forcing scheme; which is a finite difference model), the Open University spectral GCM (Lebonnois *et al.* 2013; which is a spectral model), the UCLA/LLNL Aerospace CAM GCM (Parish *et al.* 2011; which is a finite volume model) and the GFDL FMS GCM (Lee & Richardson 2010; which has the option of implementing three diferent dynamical cores: a spectral, a finite differences and a finite volume model). These models all used a common configuration based on the physical schemes of Lee *et al.* (2007) and also similar horizontal spatial resolution (roughly $5^o \times 5^o$). The aim was to compare the atmospheric circulation produced by the different models and to study how the different dynamical cores affect the simulated atmospheric circulation, and how sensitive is each model to changes in topography, upper boundary conditions, the lower boundary layer scheme, horizontal/vertical resolution and different initial states.

Using the standard physical schemes and parameters, the models produced qualitatively similar but quantitatively quite different steady state atmospheric circulations, except the

UCLA/LLNL Aerospace CAM GCM. In the work by Parish *et al.* (2011), large scale oscillations (with a ten Earth year's period) in the zonal wind distribution were obtained, predominantly in the deep atmosphere, affecting the total angular momentum budget which clearly registered this trend. In Fig. 1.9, the zonally and time averaged zonal wind fields (averaged over 5 Venus days) are shown for the baseline simulation by each model. A super-rotating atmosphere is reproduced in all models but with quite different shapes and intensities. The various maxima of the wind speeds, 15 to 50 ms^{-1}, are located in the cloud region with jets at latitudes higher than 50^o and usually deeper in the atmosphere than the equatorial maxima. The super-rotation obtained by these simplified GCMs is consistently weaker than the super-rotation inferred from observational data, e.g., Sánchez-Lavega *et al.* (2008).

In this study, it was found that the results are less sensitive to changes in the upper boundary conditions, the topography or the vertical grid, which contrasted with the significant changes in the atmospheric circulation obtained when the horizontal spatial resolution is changed. The CCSR/NIES and Paris LMD GCMs experimented starting the simulation with an atmosphere already in super-rotation. These simulations were found to keep a realistic atmospheric super-rotation, but which did not converge to the same state as obtained with an atmosphere starting from rest. This result indicates that this type of model may support multiple equilibrium states for the same parameters. However, a similar experiment after the publication of this work was done, using the OPUS-Vs. In that case the multiple-equilibrium states were not verified, so the physical existence of such multistable equilibria may not be robust.

The differences between the standard results for different GCMs raises questions about the specific methods used by each model's dynamical core to conserve the atmospheric angular momentum and approximations taken to solve the primitive equations, despite the different convection and horizontal dissipation schemes. The intrinsic numerical error combined with the Venus physical conditions (a massive atmosphere), may add difficulties to the accurate representation of the Venus global atmospheric circulation by these models. More work needs to be done to understand the nature of the diversity of results produced by different models and their sensitivity to some important parameters.

1.2.3 Overview

Simplified GCMs use idealised parameterisations, fast and easy to tune and adapt, to represent atmospheric physical processes, such as: radiative transfer, boundary layer turbulence

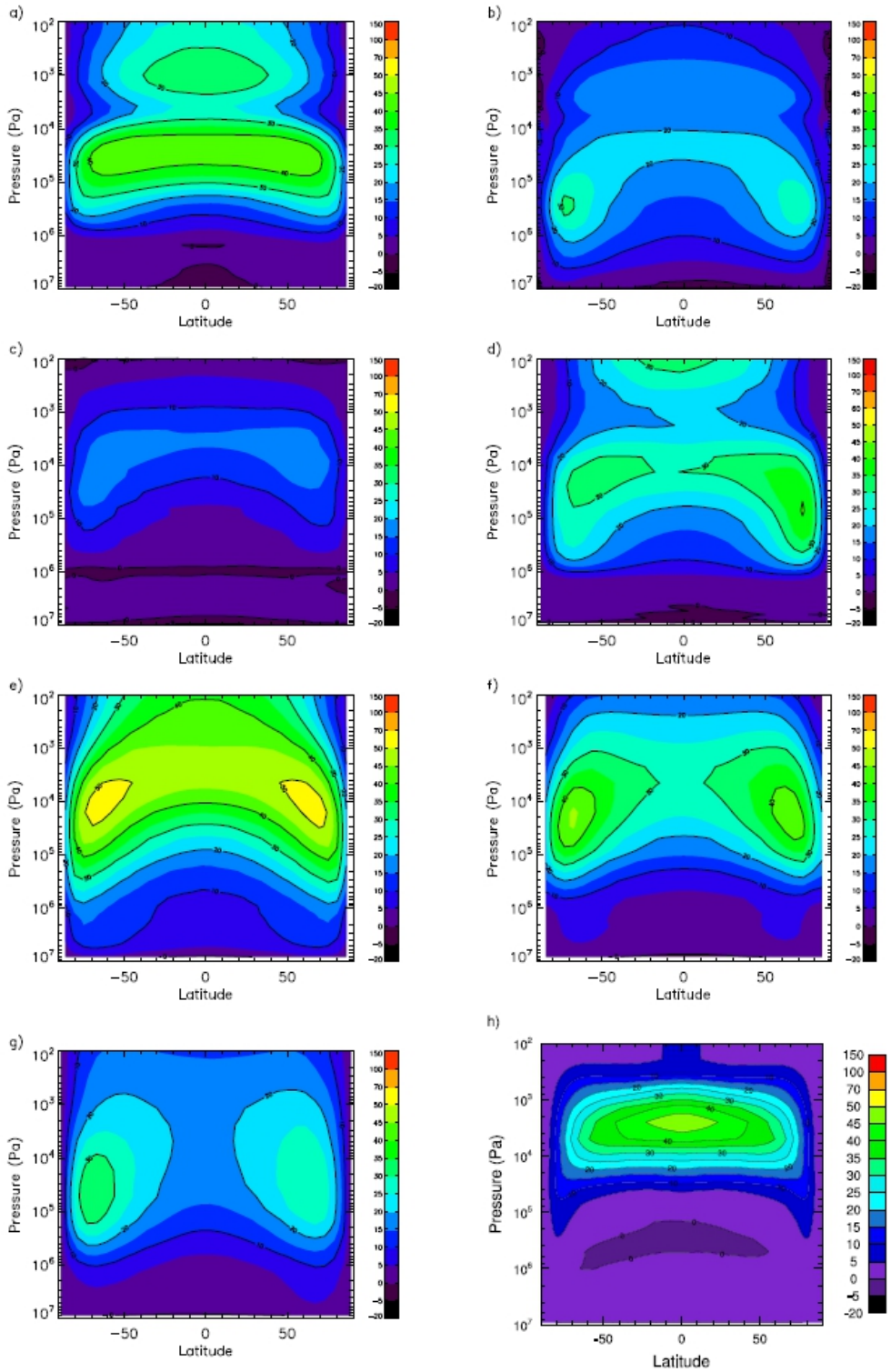

Figure 1.9: Zonally and temporally averaged zonal wind fields from the control run for each model in the inter-comparison project (Lebonnois *et al.* 2011): **(a)** CCSR, **(b)** LMD, **(c)** OU, **(d)** OPUS-Vs, **(e)** LR10-s, **(f)** LR10-fd, **(g)** LR10-fv and **(h)** UCLA.

and convection. Most of the recent models applied to Venus and reviewed in section 1.2.2 use a zonally averaged thermal forcing (with no seasonal or diurnal cycles), which produces a moderately super-rotating state that extends throughout most of the atmosphere. The strong winds in the equatorial region when using this particular forcing are due to the synoptic planetary waves at mid-high latitudes from the barotropic unstable jets, which transport momentum equatorwards. These models showed that it is possible to represent a strong super-rotation in a sufficient statically stable atmosphere without diurnal or seasonal cycles or surface topography. However, the magnitude of the super-rotation produced in these simulations is smaller than the one observed (Sánchez-Lavega *et al.* 2008). In Yamamoto & Takahashi (2009), the authors employed a stronger thermal forcing in the deep atmosphere than a physically realistic case, using the simplified radiative forcing, to produces zonal wind speeds peaking around 100 ms^{-1} (Hollingsworth *et al.* 2007).

The inter-comparison analysis shows how diverse the atmospheric circulation can be when using apparently similar physical parameterisations but different dynamical cores. In all the simulations investigated the atmospheric circulation was in a super-rotation regime, but the zonal wind fields were clearly different in terms of their amplitudes and shape. A good agreement between different models is important if one is to have confidence in the consistency and robustness of the results. For example, the numerical formulation of a GCM can introduce some intrinsic error in the simulations when applied to Venus conditions, which can be easier to detect if other models repeat the same processes. The inter-comparison study discussed here (Lebonnois *et al.* 2011) needs to be studied in more detail to understand the reasons for such diversity of simulated atmospheric states using similar physical forcing.

OPUS-Vs has been used in the study presented in this thesis as the basis for the model presented in chapter 4, which includes more physically-based representations of radiative cooling and heating, and boundary layer processes. This GCM in its simplified form captures some aspects of the Venus meteorology such as the cold collar phenomenon and the global super-rotation, despite the magnitude of the phenomena simulated being weaker than the ones observed. The plausible cyclostrophic atmospheric regime represented by this model motivated the work presented in the next chapter, where a improved method to retrieve the mesospheric zonal thermal winds from Venus Express observations is suggested.

1.3 Advanced Venus GCMs

Venus models are now at the stage of evolving from simplified GCMs, as presented above, towards more complete and physically-based codes. The process is complex and challenging due to difficulties in reproducing the physical and dynamical conditions of the global atmosphere of Venus in a realistic numerical approach.

The results presented by Lebonnois *et al.* (2010a) are the only ones published in the peer reviewed literature so far describing a Venus GCM that has successfully implemented a consistent thermal radiative transfer representation. To simulate the solar radiation, this work uses prescribed fluxes from Crisp (1986). Other new characteristics of this model in relation to the simplified versions presented in the previous section include the dependence of the specific heat capacity of the atmophere on temperature that was taken into consideration. Fig. 1.10 shows the mean winds and stream function obtained by Lebonnois *et al.* (2010a) that also included the Venus topography. The results presented show a super-rotation in the upper cloud region that is similar to observations but still slightly weaker. Below the clouds, the results are not so promising since the observed variation with height of the super-rotating zonal winds is not obtained, at least when starting the model from an initial condition of a resting atmosphere. Upon comparing the results for experiments with and without diurnal cycle, the effect of the atmospheric thermal tides is clear in the production and maintenance of the strong zonal winds. This phenomenon was identified as the main mechanism to cause a low latitude momentum accumulation in the region of strong zonal winds. The thermal tides induced by the diurnal cycle transport significant zonal momentum downwards in the equatorial region, similar to the mechanism suggested, e.g., by Pechmann & Ingersoll (1984) and Newman & Leovy (1992).

Despite improvements over the results on Venus's mesospheric dynamics in relation to the simplified GCMs to represent the data observed, some important aspects of the general atmospheric circulation remain poorly represented and simulated in the Lebonnois *et al.* (2010a) model such as: the formation of high latitude jets, the presence of stronger zonal winds in the upper cloud region and the development of strong winds in the deep atmosphere. These are some atmospheric features that may be important for the complete characterisation of the atmospheric circulation in Venus that have been suggested by several observational data studies but continue to be only poorly represented in Venus GCMs (e.g., Schubert (1983); Moissl *et al.* (2009); Piccialli *et al.* (2008); Mendonça *et al.* (2012)).

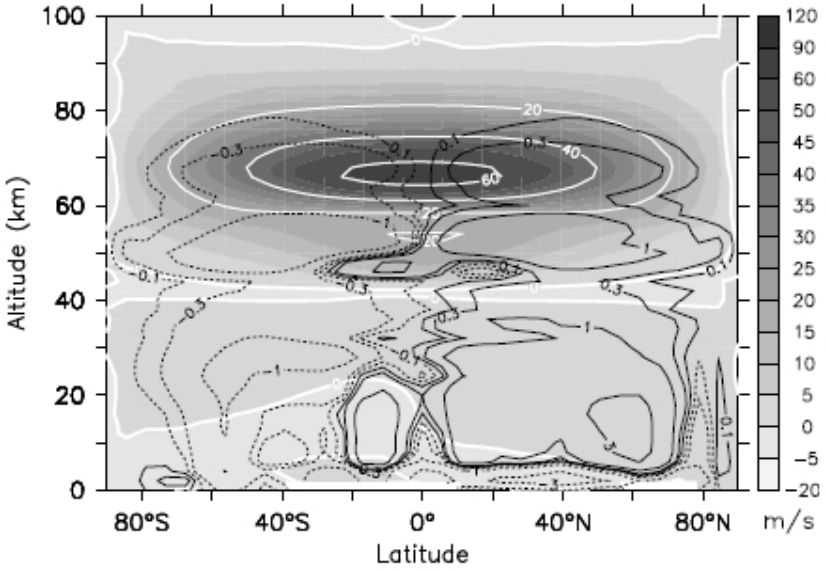

Figure 1.10: Zonally and temporally averaged mass stream function (10^9 Kg/s) and zonal winds (m/s) from the reference simulation in Lebonnois *et al.* (2010a).

1.4 Thesis Outline

The main challenge in this work is to simulate and gain a better understanding of the atmospheric circulation of the Venus lower and middle atmosphere (0-100 km), and in particular the general phenomenon of super-rotation. The simplified GCMs (e.g., OPUS-Vs) can characterize qualitatively some aspects of the Venus meteorology, and one good example of the advantages of using the results of these models to improve the interpretation of observational data is shown in the next chapter. However, the inaccurate and incomplete representation of the energy budget associated with radiative processes makes it difficult to obtain realistic numerical simulations of the atmospheric winds and compare them to the observations. It is to try to overcome this problem that a GCM with a more physically based representation of the radiative transfer has been developed here to study the atmospheric circulation. This new model is capable of exploring easily the uncertainties in the Venus atmospheric conditions, which is an advantage against the LMD Venus model (Lebonnois *et al.* 2010a), and an important tool to do a more detailed study of the global atmospheric circulation.

There are a number of key scientific questions that need to be answered to understand more about the real mechanisms that drive a slowly rotating planet like Venus to have a

strongly super-rotating atmosphere. We explore and develop a new Venus GCM to help unveil several questions such as:

- Is the super-rotation an inevitable state of slowly rotating planets?
- To which atmospheric parameters is the atmosphere sensitive to in its transition to super-rotation?
- Are phenomena such as the polar vortex or the large-scale wave patterns observed in the atmosphere of Venus an inevitable result of the super-rotating atmosphere?
- Which types of waves are most important for sustaining super-rotation?
- What is the role of topography and surface interactions in generating and sustaining super-rotation?
- What determines the distribution and properties of clouds across the planet?

In this thesis I explain how we developed a new Venus General Circulation Model called **O**xford **P**lanetary **U**nified (Model) **S**ystem for **V**enus that includes a new **r**adiation scheme (OPUS-Vr), and used it to simulate the Venus atmospheric circulation. This work is also important for present/future exploration and interpretation of the observational data from previous and future observational missions.

Thus, in chapter 2, the results from the OPUS-Vs are explored to help interpreting observational data. This study suggests a new method which improves the results of the zonal thermal wind retrievals at high latitudes. In chapter 3, I present the new radiation transfer formulation and convection scheme to be implemented in OPUS-Vr. The new formulation of the OPUS-Vr is presented in chapter 4. The results of the new model are explored and compared with observational results in chapters 5 (baseline simulation), 6 (sensitivity simulations) and 7 (cloud distribution experiments).

In the last chapter, I present the general concluding remarks of this work and suggest possible applications to be implemented in the OPUS-Vr in the near future.

2

Zonal thermal winds retrieval

2.1 Summary

In this chapter, we learn how the analysis of observational data can benefit from the numerical simulations. The material in this chapter was published in Mendonça *et al.* (2012), and is a good example of a direct application of GCM results in the development and validation of an improved method to be applied to observational data.

Recent retrievals of zonal thermal winds obtained in a cyclostrophic regime on Venus are generally consistent with cloud tracking measurements at mid-latitudes, but become unphysical in polar regions where the values obtained above the clouds are often less than or close to zero. Using OPUS-Vs, we show that the main source of errors that appear in the polar regions when retrieving the zonal thermal winds, is most likely due to uncertainties in the zonal wind intensity introduced when choosing the lower boundary condition.

In the next sections of this chapter, we suggest an improved and robust method to better estimate the lower boundary condition for high latitudes, thereby improving the retrieved zonal thermal winds throughout the high latitude middle atmosphere. This improved method is applied to temperature fields derived from the Visible and Infrared Thermal Imaging Spectrometer (VIRTIS) data on board the Venus Express spacecraft. We obtain a zonal thermal wind field that is in better agreement with other, more direct methods based on either retrieving the zonal winds from cloud tracking or from direct measurements of the meridional slope of pressure surfaces.

2.2 Prior work

The retrieval of the zonal thermal winds from temperature measurements in Venus' atmosphere has been shown to be a very powerful tool to study the dynamics of the atmosphere in the absence of direct wind measurements (Chub & Iakovlev 1980; Seiff 1983; Newman *et al.* 1984; Limaye 1985; Roos-Serote *et al.* 1995; Zasova *et al.* 2007; Piccialli *et al.* 2008; Piccialli *et al.* 2012). These methods are based on a particular dynamical balance that characterises quite well the nature of the circulation in the Venus mesosphere (between 55 and 100 km altitude). The Earth is a relatively rapidly rotating planet (with small zonal Rossby number), where the geostrophic approximation is often assumed for large-scale atmospheric motions. In this case, the pressure gradient term is approximately balanced by the Coriolis acceleration. In the mesosphere of Venus, this approximation fails because in those layers of the atmosphere we have strong winds overlying a slowly rotating planet. In this case, the cyclostrophic approximation, in which the centrifugal acceleration balances the geopotential gradient term, may be used (Leovy 1973). From the meridional component of the equation of motion in a planetary atmosphere, we can obtain the cyclostrophic thermal wind equation from the balance of these two terms,

$$\frac{u^2 \tan\phi}{a} = -\frac{1}{a}\frac{\partial \Phi}{\partial \phi}, \tag{2.1}$$

where ϕ is latitude, u is the zonal wind velocity, a is the radius of the planet and Φ is the geopotential. Differentiating in altitude each side of the equation and assuming a hydrostatic equilibrium balance, this can be simply written in pressure coordinates, following Newman *et al.* (1984) and Piccialli *et al.* (2008), as:

$$2u\frac{\partial u}{\partial \zeta} = -\frac{R}{\tan\phi}\frac{\partial T}{\partial \phi}|_{p=const}, \tag{2.2}$$

where R is the gas constant and T is the temperature. The variable ζ is defined as $-log(\frac{p}{p_o})$, where p is the pressure at each altitude level and p_o is a reference pressure. This last form of the equation is usually called the thermal wind equation, where the zonal winds can be retrieved from the atmospheric temperature maps.

Recent determinations of the zonal thermal winds obtained in a cyclostrophic regime are typically consistent with the cloud tracking results at mid-latitudes, but inconsistent

or unphysical in the polar region, where the values obtained are less than or close to zero (e.g., Newman *et al.* 1984 for the north polar vortex and Piccialli *et al.* 2008 for the south polar vortex). Note that in this thesis we use the term "prograde" to refer to winds in the direction of the planet's rotation, i.e., westward. On the other hand, observations such as in Schofield & Diner (1983), Piccioni *et al.* (2007a), Moissl *et al.* (2009) and Sánchez-Lavega *et al.* (2008), show clear evidence for the rotation of the polar vortex in the same direction as the global mean zonal wind, which contradicts the low or negative zonal velocities apparently retrieved from thermal winds.

In this chapter, we investigated the likely cause of these unphysical and inaccurate thermal wind retrievals in the polar regions, using fully self-consistent simulations of Venus atmospheric circulation with the OPUS-Vs (Lee *et al.* 2005; Lee 2006; Lee *et al.* 2007). Likely causes are either due to a breakdown of cyclostrophic balance or the amplifications of observational errors in the assumed lower boundary condition of the cyclostrophic retrieval.

In the next section I briefly describe the simulation from the OPUS-Vs, which produced the velocity and temperature fields needed for the work in this chapter. We study the full zonally averaged meridional component of the equation of motion in section 2.4, where we analyse the contributions of all the different terms from the OPUS-Vs's results. The aim is to clarify the dynamical nature of the circulation and, in particular, to assess the applicability of cyclostrophic balance at high latitudes.

In section 2.5, we study the impact of uncertainties in the lower boundary condition for the upward integration of the thermal wind equation. The high sensitivity of the "traditional" zonal thermal wind retrieval method to the lower boundary condition motivated the development of a simple method capable of recovering the zonal thermal winds mainly at high latitudes. In this region, it is often difficult to define a reliable and accurate lower boundary condition from cloud tracking results due to the uncertainties associated with the altitudes of the clouds and the strength of the zonal winds. In this section we also explore the robustness of this new method for different conditions and obtain improved maps of the zonal thermal winds, retrieved from a simulated temperature field to test its accuracy.

In section 2.6, we apply the corrected retrieval method to temperature fields obtained from the VIRTIS data on board the Venus Express spacecraft, to obtain a new zonal wind field which we compare with other recent observational results.

Finally, concluding remarks on the work developed in this chapter is presented in section 2.7.

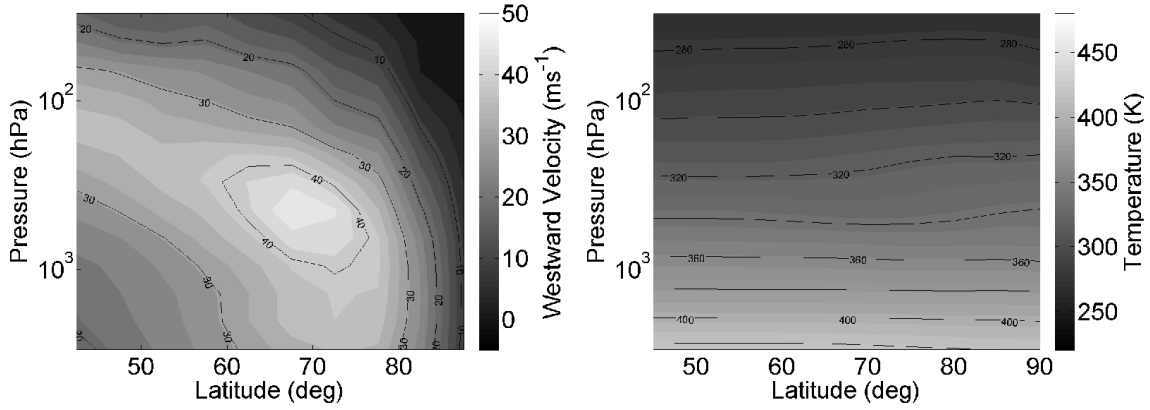

(a) Prograde velocity (m/s)

(b) Temperatures (K)

Figure 2.1: Zonally and time (one hour) averaged maps calculated by the OPUS-Vs, at the end of the model's integration in the North Hemisphere: (**a**) zonal winds; (**b**) temperature map.

2.3 Base run

In this chapter we use the results from OPUS-Vs described previously. A reference simulation used for the work in this chapter was integrated for 4.1×10^4 (Earth) days with a time-step of 10 minutes, and did not include a diurnal cycle or surface topography. The numerical model integration started with the atmosphere at rest with respect to the underlying planet, a surface pressure of 92.0 bar and a vertical temperature profile very close to the VIRA (Venus International Reference Atmosphere) model for each grid point. Fig. 2.1 shows meridional cross-sections of the zonal winds and a temperature map that were zonally and time averaged in the last hour of the simulation. The atmospheric circulation is close to being statistically steady, although it does exhibit a slight increasing tendency in the kinetic energy of the global atmosphere even after more than 100 Earth years of spin-up.

The zonal winds produced by the model are illustrated in Fig. 2.1(a) for the Northern hemisphere (the pattern is similar for the Southern hemisphere). A jet structure is seen to form at roughly 450 hPa and 67.5° N latitude with a maximum of around 47.5 $\mathrm{m\,s^{-1}}$ (about a half of the wind strength observed by, e.g., Schubert 1983). The zonal wind speed in the equatorial mesosphere region is slower than in the mid-latitudes but it is still prograde and super-rotating with respect to the solid planet.

The temperature map in Fig. 2.1(b) shows two regions with very different gradients of temperature towards the pole. Near the bottom of the jet there is a negative gradient

(poleward decreasing) while near the top a positive gradient (poleward increasing) is formed. From the temperature map it is possible to observe in the polar regions of the atmosphere (around 75° N latitude), between 200 hPa and 650 hPa, colder temperatures than in the poles or the equator, which is a feature known as the "cold collar". The warm pole and the polar "cold collar" temperature structures are also observed in the Venus atmosphere (Taylor *et al.* 1979), although with higher magnitude than produced in the model.

2.4 Zonally averaged meridional equation of motion

The full zonally averaged meridional component of the equation of motion on a spherical planet of radius, a, and angular velocity, Ω, is used in this work as a basis for studying the respective contribution of each term and to examine the qualitative validity of the cyclostrophic approximation. The equation is defined using an Eulerian-mean (denoted by $\bar{u}$ for variable u), at fixed latitude ϕ, time t and pressure level p,

$$\underbrace{\bar{u}^2 a^{-1}\tan\phi}_{[\mathrm{A}]} - \underbrace{\bar{u}f}_{[\mathrm{B}]} + \underbrace{a^{-1}\bar{\Phi}_\phi}_{[\mathrm{C}]} = -\underbrace{(a\cos\phi)^{-1}(\overline{v'^2}\cos\phi)_\phi}_{[\mathrm{D}]} - \underbrace{\overline{u'^2}a^{-1}\tan\phi}_{[\mathrm{E}]} + \mathscr{R} \tag{2.3}$$

where the subscript denotes a partial derivative, [A] represents the centrifugal acceleration, [B] the Coriolis acceleration, [C] the geopotential gradient, [D] and [E] the quadratic terms in disturbance variables which are written on the right hand side and represent the "rectified eddy-forcing" terms (e.g., Andrews *et al.* 1987), and $\mathscr{R}$ the residual. The eddy terms govern the interaction of the zonal mean flow with superimposed disturbances, which could have a very important effect on the zonal mean circulation in regions of strong eddy activity. The residual term $\mathscr{R}$ quantifies the remaining terms neglected in this approximation and represents residual time dependence and other effects (such as frictional processes) not included explicitly in Equation (2.3).

The magnitude of each of the terms in Equation (2.3), averaged over an hour in the model run, are plotted in Fig. 2.2. It can be seen that the equation is dominated mainly by two terms: the centrifugal acceleration [A] and the geopotential gradient [C], indicating that the cyclostrophic balance is accurate to better than 20% for latitudes lower than 80°. However, the residual $\mathscr{R}$ is not negligible in the polar region and becomes more significant for higher altitudes above the jet. It includes all the terms that we are neglecting and seems to be more relevant in the "turbulent" regions where eddy activity is strong. An

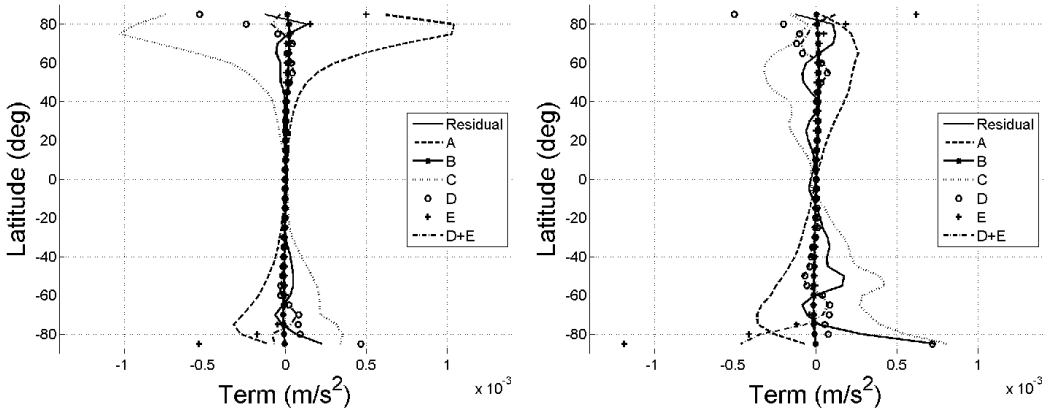

(a) Evaluation at 951 hPa.

(b) Evaluation at 100 hPa.

Figure 2.2: The different lines represent each term of the meridional component of the equation of motion. They were obtained after 4.1×10^5 earth days in the OPUS-Vs integration without diurnal forcing. Each term was averaged over longitude and time (1 hour). Note: $A = \frac{u^2 \tan\phi}{a}$, $B = u2\Omega\sin\phi$, $D = \frac{1}{a}\frac{\partial\Phi}{\partial\phi}$, $C = (a\cos\phi)^{-1}(\overline{v'^2}\cos\phi)_\phi$ and $D = \overline{u'^2}a^{-1}\tan\phi$; where ϕ is the latitude and Ω is the rotation rate of the planet.

important contribution to the residual is almost certainly due to the term $\frac{\partial v}{\partial t}$ related to the flow variability, especially in the polar regions. The two eddy terms [D] and [E], do not have negligible magnitude in the polar region and seem to be related to the "turbulent" zone near the jets as well. A latitude-pressure map of the two main eddy terms [D] and [E] for this case are shown in Fig. 2.3. Both terms have important contributions at high latitudes, stronger in the jet region (around 300 hPa), and apparently leading to a partial breakdown of the cyclostrophic balance. In Fig. 2.2, we can see that the eddy terms can have a larger magnitude than the zonal mean cyclostrophic terms for latitudes higher than 80°.

Upon averaging each term of Equation 2.3 for a longer time (60 Earth days), we reduce the contribution of the "turbulent" term $\frac{\partial v}{\partial t}$. Fig. 2.4 shows the results obtained. A smoother residual profile for the two altitudes is sampled here (100 hPa and 952 hPa), which is now nearly zero almost everywhere but with a slight increase towards the pole. A pure cyclostrophic balance is, in general therefore, a good approximation to describe the time- and zonal-mean atmospheric circulation, however, for latitudes higher than 80° the significant total contribution of the eddy (dashed-dot line) terms can lead to a partial breakdown of the cyclostrophic approximation, as mentioned before. The benefit of neglecting the two eddy terms is that it simplifies the method to retrieve the zonal thermal winds. A more

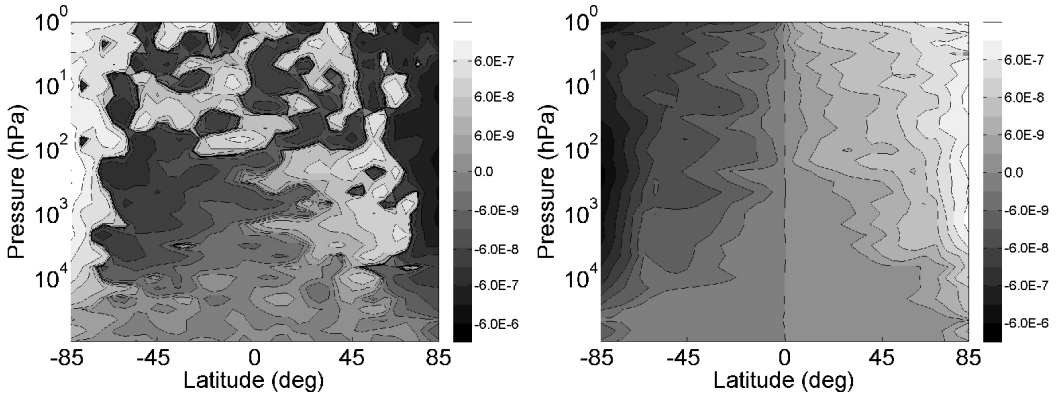

(a) Eddy forcing term: $(a\cos\phi)^{-1}(\overline{v'^2}\cos\phi)_\phi$ (b) Eddy forcing term: $\overline{u'^2}a^{-1}\tan\phi$

Figure 2.3: Eddy terms obtained from Equation (2.3) and time averaged for 1 hour. The derivation of these terms are explained in Andrews *et al.* (1987).

complete retrieval method would need to be based on a combination of the cyclostrophic balance terms and an eddy diffusion parameterisation (e.g., Luz *et al.* 2003). However, we show below that this is not the main source of error present in cyclostrophic wind retrievals, and that an alternative approach based on applying a simple dynamical constraint to pure cyclostrophic balance, can still yield good estimates of zonal winds at high latitudes.

2.5 Retrieving the zonal thermal winds in Venus model simulations

The zonal thermal wind equation applied to the Venus mesosphere, Equation (2.2), can be used to obtain the zonal velocity u given the temperature field, provided that the cyclostrophic balance condition is valid. Here, it is assumed that the solutions for u are always positive (prograde). One of the main difficulties in this method is related to finding an appropriate lower boundary condition to be used in the upward integration. Cloud tracking techniques have typically been used to estimate the winds at the lower boundary, but this method is often not very accurate at high latitudes because of a lack of clearly defined features in cloud images and uncertainties in defining the cloud top altitude.

In this chapter we suggest, therefore, an improved method to better estimate the lower boundary condition in the polar region. This method complements previous work on zonal

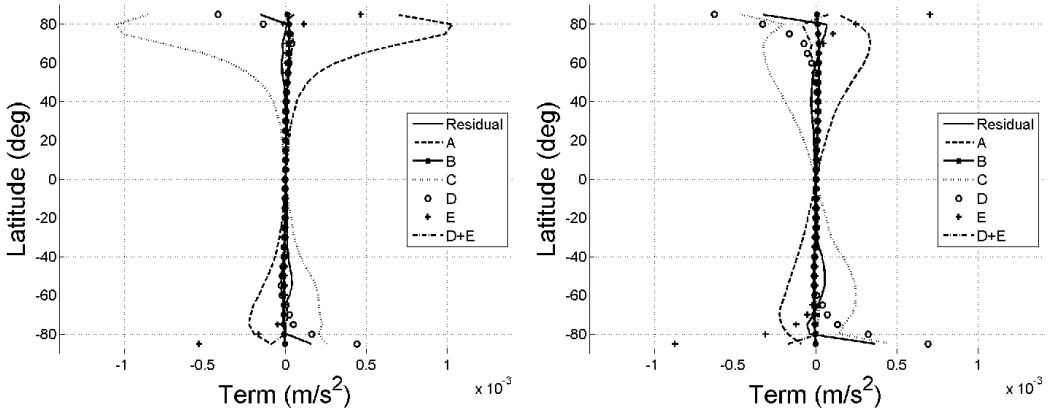

(a) Evaluation at 951 hPa.

(b) Evaluation at 100 hPa.

Figure 2.4: Similar to Figure 2.2, but time averaging each term for 60 Earth days.

thermal wind retrievals and it comprises additional iterations. The new method to retrieve the zonal winds has the following structure:

1. Integrate the thermal wind equation upwards using Equation (2.2), starting from a first initial guess for the lower boundary.

2. Correct the circumpolar winds at the top of the model domain (p_{top}) to be consistent with a solid body rotation profile (with the form $\frac{u_0(p_{top},\phi_0)}{\cos\phi_0}\cos\phi$) in the latitude region starting from the position of the jet core (ϕ_0), up to the pole. The position of the jet core is defined here to be 5 degrees lower in latitude than the position of the zonal thermal wind maximum (equivalent to the latitudinal resolution of the OPUS-Vs).

3. Integrate Equation (2.2) *downwards* with the new upper boundary condition. Here we are effectively estimating a new lower boundary condition, which fits better with the conditions of Venus' mesosphere circulation.

The imposition of a mean atmospheric vortex in the Venus mesosphere approximating to a solid body rotation close to the pole, is plausible for several reasons. The zonal flow is approximately angular momentum conserving at low latitudes but this cannot hold up to the pole, otherwise the zonal winds would be unrealisticaly large, increasing with the inverse of *cos* ϕ. The circumpolar jet is typically barotropically unstable, and barotropic eddies associated with the jet in the Venus atmosphere tend to mix towards a state of approximately

uniform vorticity ξ (Schubert *et al.* 1999). In cylindrical polar coordinates centred on the rotation axis, uniform axial vorticity corresponds exactly to solid body rotation at angular velocity $w = \frac{\xi}{2}$. This equivalence is not exact in spherical polar coordinates, but is a close approximation near the pole, broadly similar to the approximate Rankine vortex inferred from observations on Venus (Limaye 2007). A near-solid body rotation is also in line with the pattern of zonal winds most commonly obtained by the OPUS-Vs in the polar region for altitudes above the jet.

Results in Fig. 2.5 were obtained from the upward integration of Equation (2.2) using an ensemble of different lower boundary conditions prescribed to have the following form:

$$U_o = (a \times \mathrm{sech}(\frac{|\phi| - b}{c}) + d) \times cos(\phi). \tag{2.4}$$

where a, b, c and d are free parameters and ϕ is the latitude. This equation was first used by Newman *et al.* (1984), to fit measured winds at about 42 km from Pioneer Venus differential long-baseline interferometry (DLBI) experiments (Counselman *et al.* 1980). The different parameters determine different characteristics of a zonal wind profile, where a, b and c are the magnitude, latitude position and width of the jet, and d is the zonal wind flow at low latitudes. The lower boundary is applied at a pressure level around 3×10^3 hPa. In these experiments the parameter a was varied randomly over the interval $[0 - 300]$ $\mathrm{m\,s^{-1}}$, b on $[82.5° - 87.5°]$, c on $[8 - 12]$ and d on $[10 - 40]$ $\mathrm{m\,s^{-1}}$ with uniform probability. For the results in Fig. 2.5, a temperature field that was zonally and time averaged (over 60 Earth days) from the OPUS-Vs was used, and the top of the model domain was fixed at 30 hPa. The dashed line represents the standard deviation of the zonal winds profile obtained at the top of the domain over the standard deviation of the initial profiles for the lower boundary condition (the denominator is represented in Fig. 2.6(e)). From this line it is possible to conclude the high sensitivity (values higher than one) of the upward integration to the values chosen for the lower boundary. The solid line corresponds to the standard deviation of the profile which is corrected to have the form of a solid body rotation at the top of the domain as explained in the step (2) of the improved method, over the standard deviation of the initial profiles for lower boundary condition. The variability of this profile is weaker than the one represented by the dashed line. The important conclusion from Fig. 2.5 is that the results from the upward integration are very sensitive to changes in the lower boundary condition in the polar region. The use of an inappropriate lower boundary condition is

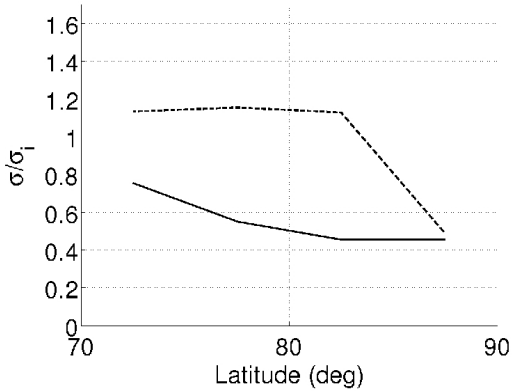

Figure 2.5: The dashed line represents the ratio of the standard deviation of the zonal thermal winds at the top of the domain over the standard deviation of the initial guesses. The solid line is the ratio of the standard deviation of the "corrected" top profiles (solid body rotation shape) over the standard deviation of the initial guesses.

therefore clearly likely to produce inaccurate results, even with a well constrained thermal field. This problem can be improved with the new method proposed above.

In order to study the reliability and robustness of the new method as a means of better estimating the winds at the lower boundary in the polar region, the results were studied using an ensemble of initial lower boundary profiles. The large number of initial guesses for the lower boundary condition was obtained using the same method and parameters used for Fig. 2.5.

In Fig. 2.6 the top and the bottom of the temperature field studied were set again at 30 hPa and 3×10^3 hPa respectively. This experiment shows the effect of different time averaging periods on the final result of the estimation of the lower boundary in the polar region. As expected, the longer time averaging of the temperature field gives better results, because we are closer to the conditions of a pure cyclostrophic regime. The zonal winds near the jet region are being underestimated for shorter time periods. The dashed line in the figure represents the zonally- and time-averaged zonal winds obtained by the OPUS-Vs at the pressure level where the lower boundary condition is defined. Note that the retrieved results from the initial latitude position of the jet up to the pole occupy a small range of values that are always close to the "true" values (indicated by the dashed line). The small values of the ratio of the final result's standard deviation to the standard deviation of the initial guesses (solid line), suggest that the final best estimate is well constrained and is not significantly affected by different initial guess profiles.

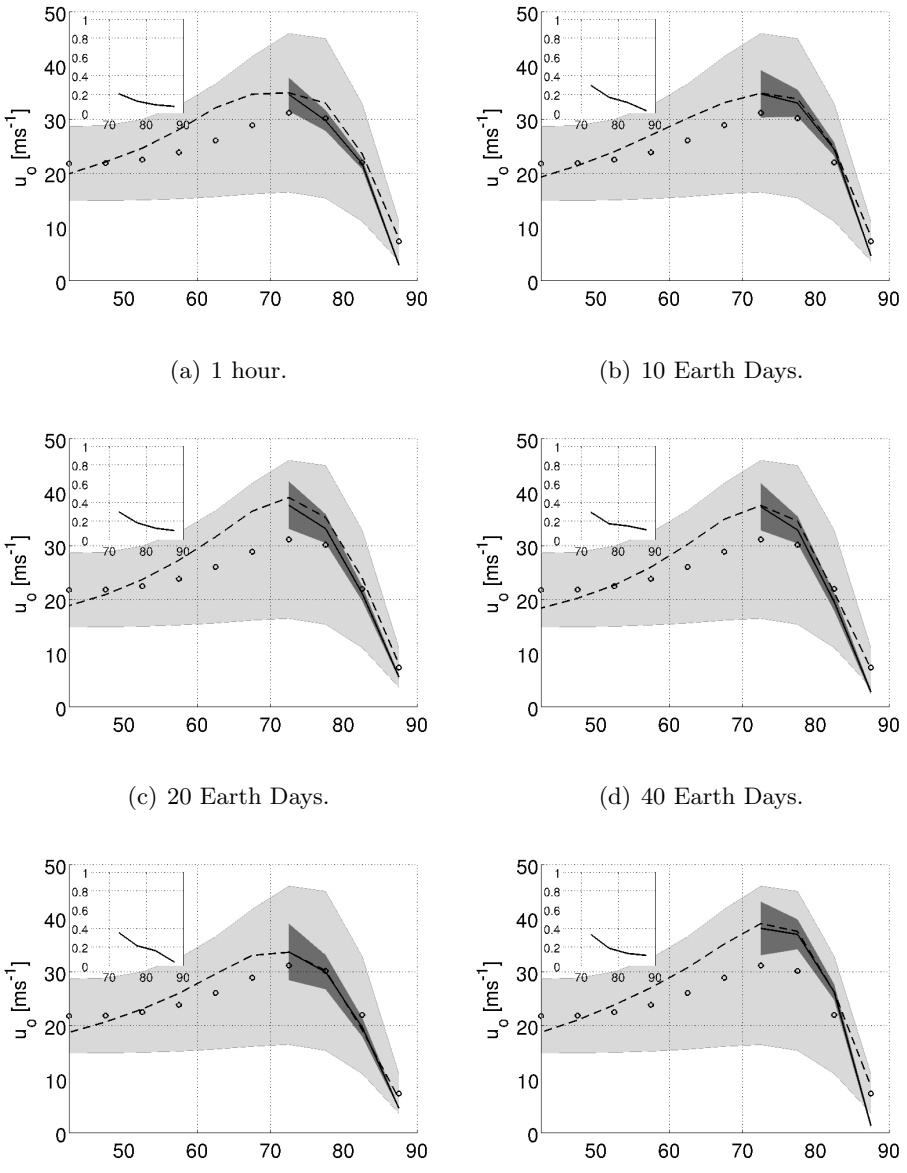

(a) 1 hour.

(b) 10 Earth Days.

(c) 20 Earth Days.

(d) 40 Earth Days.

(e) 60 Earth Days.

(f) 80 Earth Days.

Figure 2.6: An ensemble of initial lower boundary profiles is used for six different time averaging periods of the temperature field, applied to the improved method to estimate the lower boundary. **(a)** 1 hour, **(b)** 10 Earth days, **(c)** 20 Earth days, **(d)** 40 Earth days, **(e)** 60 Earth days and **(f)** 80 Earth days. The unfilled circles represent the mean of the initial profiles; the dashed line is the actual zonal winds from the OPUS-Vs at an altitude where the lower boundary condition is defined, and the solid line is the mean final result. The darker shaded region represents the standard deviation of the final results and the other for the initial guesses. The small plot represents the ratio of the standard deviation of the solid line over the standard deviation of the initial guesses.

For the experiments shown in Fig. 2.7, the top pressure level where the suggested method is applied, was changed. Six different top pressures were tested: 2.1 hPa, 4.6 hPa, 9.8 hPa, 21 hPa, 45 hPa and 100 hPa. The time period for averaging the zonally averaged temperature field from the OPUS-Vs was 60 Earth days. The accuracy of the results depends to some extent on where the top is defined. For atmospheric pressures below 21 hPa the values of the zonal winds at the lower boundary tend to be overestimated near the jet region. The zonal winds in the OPUS-Vs at this region appear to decrease faster with latitude than for solid body rotation between 65° and 80°. Defining the top for pressure levels deeper than 21 hPa, leads to an underestimate of the value of the lower boundary obtained, because we are then forcing the zonal winds near the latitude position of the jet core to decrease more rapidly with latitude than observed in the original OPUS-Vs results (Fig. 2.8(a)). The pressure layer at 21 hPa is where the zonal winds better approximate solid body rotation, due to the very weak meridional motions in the atmosphere. Above 21 hPa there is a poleward circulation which becomes equatorward below 21 hPa, and this weakens the solid body rotation assumption.

In addition, the values of zonal wind speeds at the lower boundary estimated for latitudes higher than 80°, are usually underestimated due to the presence of a non-negligible residual term and the two eddy terms, as shown in Fig. 2.4. The standard deviation of the final results is larger in the latitudes farthest from the pole, due to the high sensitivity of u_o, that is used to reconstruct the profiles $\frac{u_0(p_{top},\phi_0)}{\cos\phi_0}\cos\phi$ (solid body rotation's profile) at the top of the model domain. This implies that, for better results when retrieving the zonal thermal winds, one needs to constrain the flows to low latitudes.

In general, the improved method used to estimate the lower boundary condition for latitudes higher than the centre of the jet, produces results very close to the expected profile. The duration of time averaging affects the results, with longer periods leading to better results due to the improved accuracy of the assumed cyclostrophic balance in characterising the large scale flow for these cases. The suggested method is easy to apply and reduces the difficulties due to inaccurate initial conditions for the upward integration of the thermal wind equation.

On further exploring Equation (2.2), the accuracy of this method to retrieve the entire zonal thermal wind map is studied from a zonally and time averaged temperature field obtained at the end of the OPUS-Vs simulation (averaged for 60 Earth days). Fig. 2.8 shows the zonal thermal wind maps retrieved using three different lower boundary conditions:

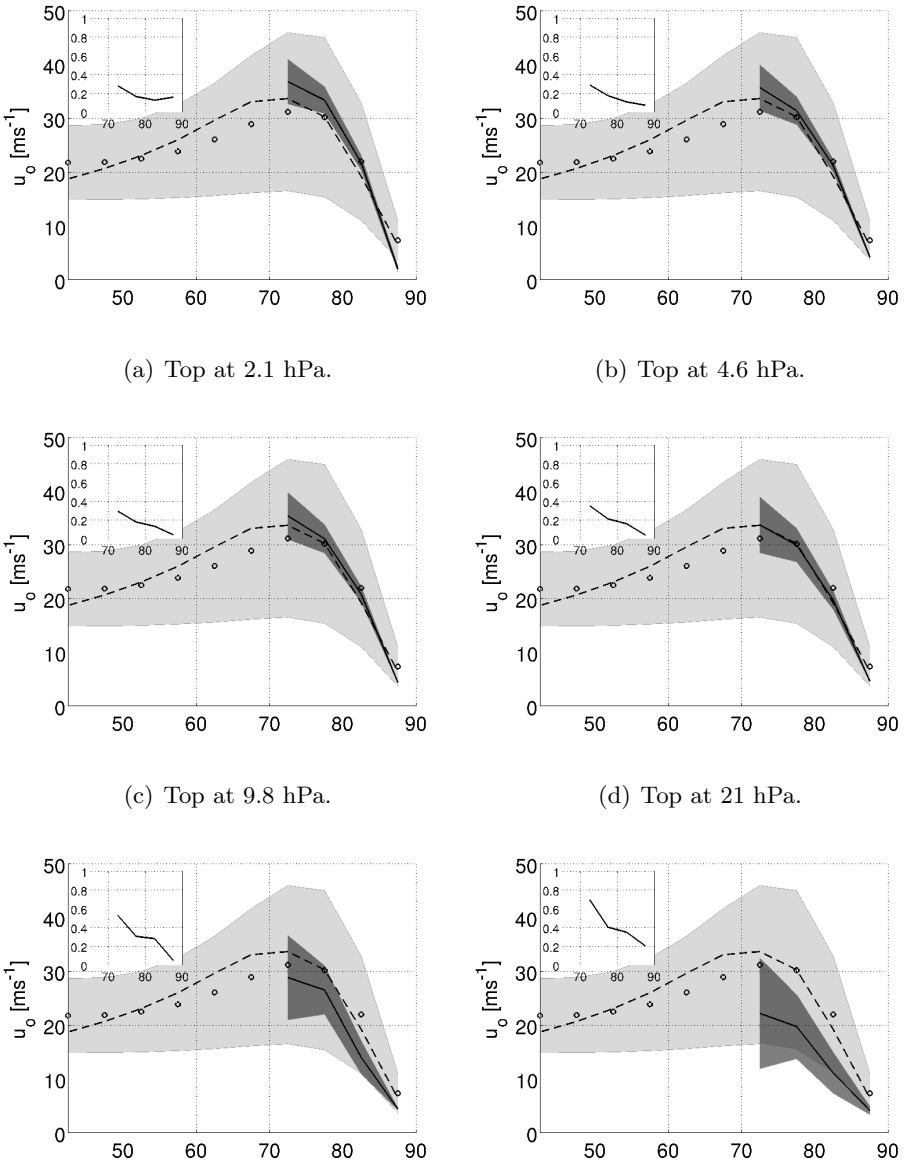

(a) Top at 2.1 hPa.

(b) Top at 4.6 hPa.

(c) Top at 9.8 hPa.

(d) Top at 21 hPa.

(e) Top at 45 hPa.

(f) Top at 100 hPa.

Figure 2.7: Similar to Fig. 2.6. Here we explored the influence of different pressure tops. Six altitudes were chosen to test the method to estimate the lower boundary, applied to: **(a)** 2.1 hPa, **(b)** 4.6 hPa, **(c)** 9.8 hPa, **(d)** 21 hPa, **(e)** 45 hPa and **(f)** 100 hPa. The temperature fields were averaged to 60 Earth days.

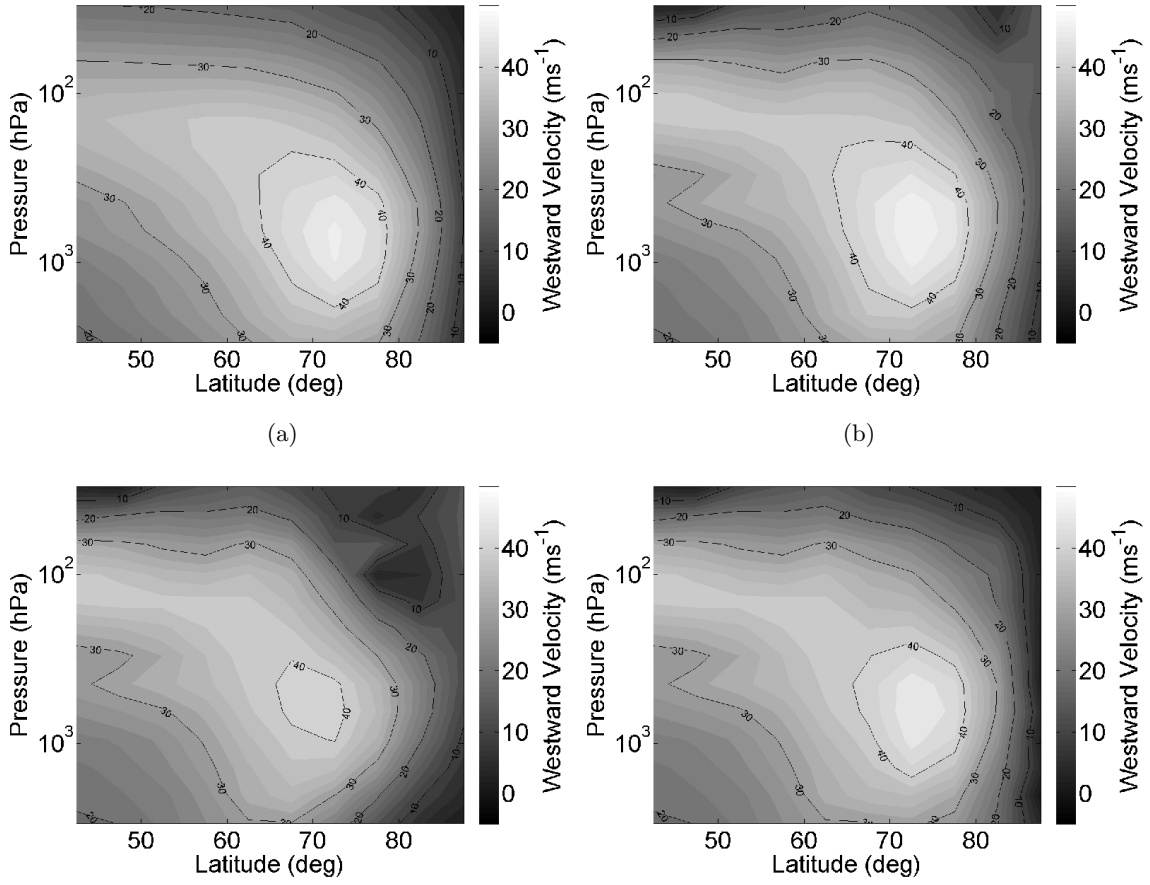

Figure 2.8: **(a)** Zonally and time (60 Earth days) averaged zonal winds obtained by the OPUS-Vs. **(b)**, **(c)** and **(d)** are zonal thermal winds maps retrieved from the zonally and time averaged (60 Earth days) temperature field obtained by the OPUS-Vs. For **(b)**, a zonally and time averaged zonal wind profile obtained by the OPUS-Vs was used as lower boundary condition and for **(c)** the Equation (2.4) was used instead, with $a = 50\ \mathrm{m\,s^{-1}}$, $b = 70°$, $c = 10$ and $d = 20\ \mathrm{m\,s^{-1}}$. In **(d)** the zonal thermal winds were obtained applying the method that better estimates the lower boundary condition on case **(c)**.

1. A zonally and time averaged zonal wind profile obtained by the OPUS-Vs.

2. One with the typical shape assumed before but which deliberately underestimates the zonal wind velocities in the polar regions (Equation (2.4) with $a = 50$ m s^{-1}, $b = 70°$, $c = 10$ and $d = 20$ m s^{-1})

3. Using the method suggested previously to better estimate the lower boundary in the polar region applied to the above condition (2).

Fig. 2.8(b) shows the zonal thermal winds obtained using the best answer for the lower boundary, case (1), which obtains in general, zonal wind magnitudes close to the ones expected from the OPUS-Vs results (Fig. 2.8(a)). As expected, the use of an inappropriate lower boundary condition for case (2) underestimates the values in the polar region and produces incorrect results at all heights. The magnitude of the zonal thermal winds from Fig. 2.8(c) are in general smaller than the zonal winds produced by the OPUS-Vs (Fig. 2.8(a)). The application of the improved method to estimate the lower boundary condition reconstructs the zonal wind field in the region from 65° latitude up to the pole for all altitudes (Fig. 2.8(d)), converging to the ones represented in Fig. 2.8(b) that uses the best lower boundary estimation. The maximum of the recovered wind velocity at the jet core is 46.0 m s^{-1} at 72.5° latitude, which is almost identical to the one produced by the OPUS-Vs, $\bar{u} = 46.5$ m s^{-1} at 72.5°. The final zonal thermal wind field is in better agreement with the zonal winds from the OPUS-Vs than the case (2), despite using a general, and not very accurate, first guess for the lower boundary profile.

2.6 A map of zonal thermal winds obtained from VIRTIS data

In this section the zonal thermal winds are obtained from the latitude-pressure mesosphere temperature map for a particular local time, retrieved by the mapping IR channels of the Visual and Infrared Thermal Imaging Spectrometer (VIRTIS-M) on board the Venus Express spacecraft (Drossart *et al.* 2007; Piccioni *et al.* 2007b).

The latitude-pressure temperature map used is part of the compilation of temperature retrievals from Grassi *et al.* (2010), which are roughly equivalent to the previous long time averaged results using the OPUS-Vs temperature fields. The time averaging process decreases the magnitude of the residual term, making the conditions closer to the regime of

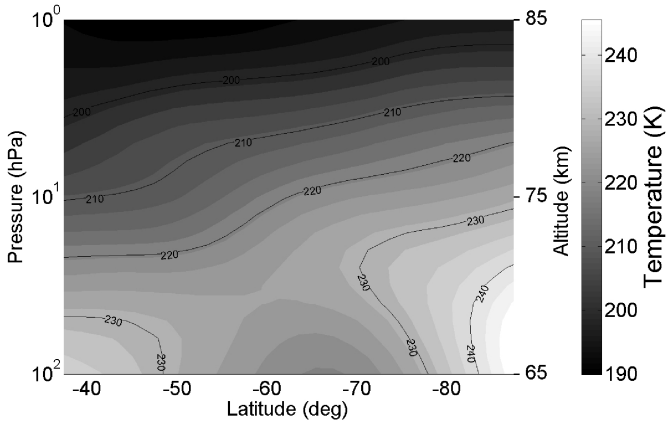

Figure 2.9: Temperature map for 2400 LT derived from VIRTIS temperature retrievals (Grassi *et al.* 2010).

pure cyclostrophic balance. The different local times correspond to different thermal structures that drive changes in the atmospheric circulation, such as the position of the jet (Held & Hou 1980 and Newman & Leovy 1992). The map covers the domain 1-100 hPa from 45° latitude up to the pole in the Southern hemisphere for 2400LT (local time). The overall uncertainty in the retrieved temperature in this region does not exceed 4 K and is better than 1 K between 7 and 70 hPa. The map of temperatures is shown in Fig. 2.9, where it is possible to observe the "cold collar" at 65°S and the temperatures increasing monotonically towards the pole for altitudes above the pressure level 12.6 hPa.

The zonal thermal winds shown in Fig. 2.10 are obtained from the temperature map using Equation (2.2). Fig. 2.10(a) was obtained just from a single upward-integration of the Equation (2.2) from a lower boundary condition that was prescribed to have the form given in Equation (2.4) with $a = 52$ m s^{-1}, $b = 56°$, $c = 9$ and $d = 86$ m s^{-1}. This profile was constrained using the one presented in Piccialli *et al.* (2008) for a surface pressure altitude of 275 hPa. The values for a and d are larger by $\sim 15\%$ here, which were estimated from Piccialli *et al.* (2008) zonal thermal wind retrieval maps (for altitudes below the pressure level 100 hPa the zonal wind speed decreases with pressure). The lower boundary was not set at 275 hPa because we do not have temperature data available below the 100 hPa level. For each level the latitudinal profile of the temperature data was smoothed using a cubic spline method with a smoothing parameter of 0.01, to facilitate the evaluation of $[\partial T/\partial \phi]_{p=const}$. This procedure can affect the pattern of the zonal thermal winds, and we

may create artificially thermal structures not consistent with the real Venus meteorology. Fig. 2.10(a) shows the zonal thermal winds obtained from VIRTIS data, with a mid-latitude jet reaching a maximum of 108± 7 $\mathrm{m\,s^{-1}}$ at a latitude of −48± 5°. As observed in other studies (Newman *et al.* 1984; Piccialli *et al.* 2008), the zonal thermal winds in the polar region appear to be weaker than what would be expected from direct observation of the clouds in the polar vortex (Piccioni *et al.* 2007a). The clumpy dark region (latitudes higher than 65°) is related to integration problems since we cannot determine if the winds reverse direction.

In Fig. 2.10(b) the improved method described in section 2.5 is used to calculate zonal thermal winds from a VIRTIS data set. This method, which estimates the lower boundary condition, increases the zonal winds in the region where it is applied (for all altitudes from the latitude position of the jet core up to the pole). In this case the maximum velocity in the jet is still 108 ± 7 $\mathrm{m\,s^{-1}}$ at $-48 \pm 5°$ latitude.

A modified equation for the lower boundary was also tested, this profile increases the final zonal thermal winds mainly at mid-latitudes, replacing $d = 86$ $\mathrm{m\,s^{-1}}$ by $d = 105$ $\mathrm{m\,s^{-1}}$. Here we are assuming stronger winds in the low/mid-latitudes, which were constrained using the Sánchez-Lavega *et al.* (2008) results. Retrieving the zonal thermal winds using the method to estimate the lower boundary and the new first initial guess, we infer slightly stronger mid-latitude winds, although they are consistent within the errors (Fig. 2.10(c)). The maximum wind speed is now 116 ± 7 $\mathrm{m\,s^{-1}}$ at -48 ± 5°. The results derived here are in good agreement with the results obtained by Zasova *et al.* (2000), who obtained a jet centred at around 50°S with u ∼ 110 m $\mathrm{s^{-1}}$. Other works obtained roughly the same position but different maximum wind speeds, such as ∼ 160 $\mathrm{m\,s^{-1}}$ from Newman *et al.* (1984), ∼ 90 $\mathrm{m\,s^{-1}}$ from Piccialli *et al.* (2008) and more recently ∼ 140 $\mathrm{m\,s^{-1}}$ from Piccialli *et al.* (2012).

The retrieved zonal thermal winds start to converge for latitudes higher than 70° when the same technique to obtain the lower boundary but different initial guesses is used (e.g., the black solid line and solid circles in Fig. 2.12). It is also important to point out the large horizontal shear in these last results close to the pole. This is consistent with barotropic instability becoming important, influencing the dynamics of the polar vortices.

The uncertainties in the jet magnitude and position presented were estimated using a Monte-Carlo method, where the temperature for each point varied with uniform probability within ±4 K, before fitting the temperature profiles for each level (10^4 steps). The 4 K uncertainty is indicated in Grassi *et al.* (2010) and previously in this paper as the maximum

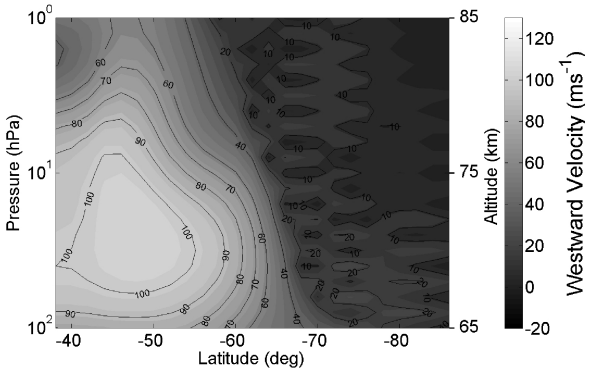

(a)

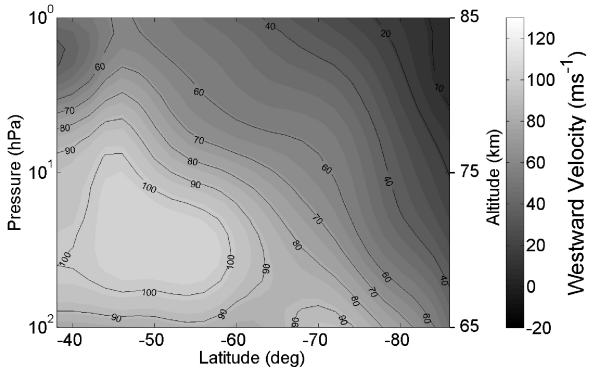

(b)

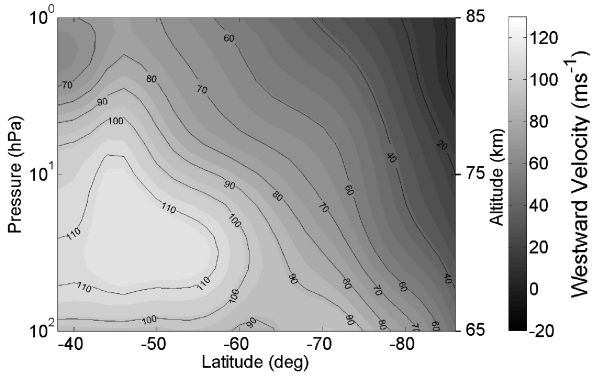

(c)

Figure 2.10: Prograde zonal thermal wind speed (m/s) derived from VIRTIS 2400 LT temperature field (Grassi *et al.*, 2010) assuming cyclostrophic balance. Figure **(a)** was obtained from the upward integration of the thermal wind equation using for lower boundary the Equation (2.4) with $a = 52\ \mathrm{m\,s^{-1}}$, $b = 56°$, $c = 9$ and $d = 86\ \mathrm{m\,s^{-1}}$. **(b)** and **(c)** use the improved method to estimate the lower boundary but different initial guesses. **(b)** uses the same first initial guess as **(a)** for the lower boundary but in **(c)** we use a modified equation with d =105 $\mathrm{m\,s^{-1}}$ instead of d =86 $\mathrm{m\,s^{-1}}$.

total error in the temperature retrievals throughout the entire range 100.0-1.0 hPa (65-85 km). The uncertainty is computed for each particular lower boundary condition, and is the root mean square of all standard deviations in each point, including implicitly the error of the fit. The error in latitude is the standard deviation of the position of the maximum magnitude in the wind map after running all the Monte-Carlo steps.

Limaye (1985), and more recently Piccialli *et al.* (2012), also used a second method that obtains the zonal winds using the cyclostrophic approximation directly via Equation (2.1) from the meridional slope of the pressure surfaces. This method has the advantage of not requiring a vertical integration, thereby avoiding problems with the choice of the lower boundary condition. However, this method requires measurement of the height of pressure surfaces, which is obtained by radio occultation, so profiles are few in number and widely separated in space and time. Nevertheless, the results obtained with this method show strong prograde zonal winds in the polar region in agreement with our method, as showed in Fig. 2.11 in the dashed-dotted line for an altitude of ~ 65 km (100 hPa). The solid line in Fig. 2.11 represents the zonal thermal wind obtained using our improved method with the previously indicated lower boundary condition with d = 105 $\mathrm{m\,s^{-1}}$. For latitudes lower than 70° the zonal winds obtained by Piccialli *et al.* (2012) are in general larger, reaching ~ 120 $\mathrm{m\,s^{-1}}$ at 50°, contrasting with our zonal thermal wind magnitude of 95 $\mathrm{m\,s^{-1}}$.

The comparison with cloud-tracked wind measurements, acquired also from Venus Express, allow us to obtain a first validation of our method based on cyclostrophic balance. The profiles used and presented in Fig. 2.11, are the VIRTIS near infrared cloud-tracked winds obtained by Sánchez-Lavega *et al.* (2008) at ~ 66 km (filled circles) and the VIRTIS UV paired method at ~ 70 km from Moissl *et al.* (2009) (unfilled circles). These two profiles are in general in good agreement, the main differences being: a more pronounced peak in the zonal winds in the Sánchez-Lavega *et al.* (2008) results, reaching ~ 110 $\mathrm{m\,s^{-1}}$, and the larger zonal wind around 35 $\mathrm{m\,s^{-1}}$ at -85° latitude derived from VIRTIS UV images. The differences between these results and the ones obtained using the improved method at high latitudes are clear, and could be related to difficulties in both methods. One important source of error in the cloud-tracked methods is the determination of the altitude of the cloud top map. In Ignatiev *et al.* (2009), simultaneous observations from VIRTIS and the Venus Monitoring Camera (VMC) onboard the Venus Express spacecraft mapped the mean cloud top altitude as a function of latitude and local time. The presence of a depression in the cloud top altitudes for latitudes higher than 50° (from $\sim$ 74 km to 63-69 km) is

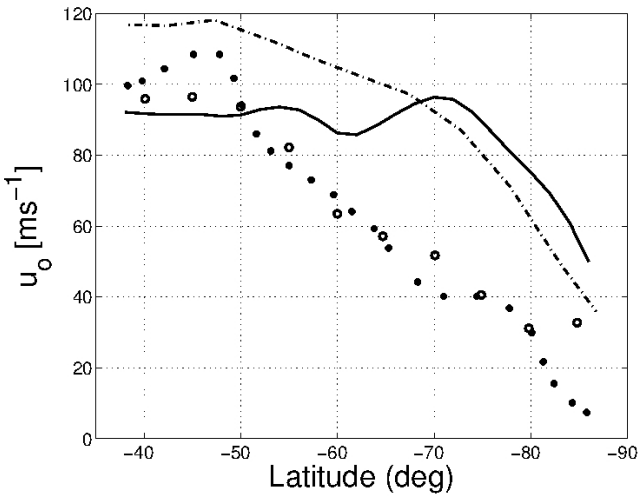

Figure 2.11: Comparison between the different latitudinal wind profiles: our improved method (solid line) using an initial lower boundary condition that was prescribed to have the form given in Equation (4) with $a = 52$ m s^{-1}, $b = 56°$, $c = 9$ and $d = 105$ m s^{-1}, the results from Piccialli *et al.* (2012) (dashed-dot line) at $\sim$ 65 km, and the cloud tracked winds from Sánchez-Lavega *et al.* (2008) at $\sim$ 66 km (black circles) and Moissl *et al.* (2009) at $\sim$ 70 km (unfilled circles).

clear from these results, which can imply that the zonal winds at high latitudes obtained by cloud-tracked methods correspond to altitudes deeper in the atmosphere. On the other hand, the new method is based on a cyclostrophic approximation that might be weakened by the presence of the eddy terms and the residual term presented before.

In Fig. 2.12, the method to estimate the lower boundary is explored to study its sensitivity to the initial guess (analogous to the work done using the OPUS-Vs data). The initial guesses again have the form of Equation (2.4). N = 2.5×10^5 different random profiles are explored where a varied over the range $[0-90]$m s^{-1}; b $[46°-66°]$; c $[0-18]$ and d $[50-120]$m s^{-1} with uniform probability distribution. The mean profile is represented by the dashed line in Fig. 2.12. The embedded plot in Fig. 2.12 represents the ratio of the standard deviation of the final results (shaded region) to the standard deviation of the initial guesses (as in the OPUS-Vs results section). The low numbers obtained indicate that the method to estimate the zonal thermal winds from the observed temperature fields for latitudes higher than the position of the jet is weakly sensitive to changes in the initial guesses under this approach.

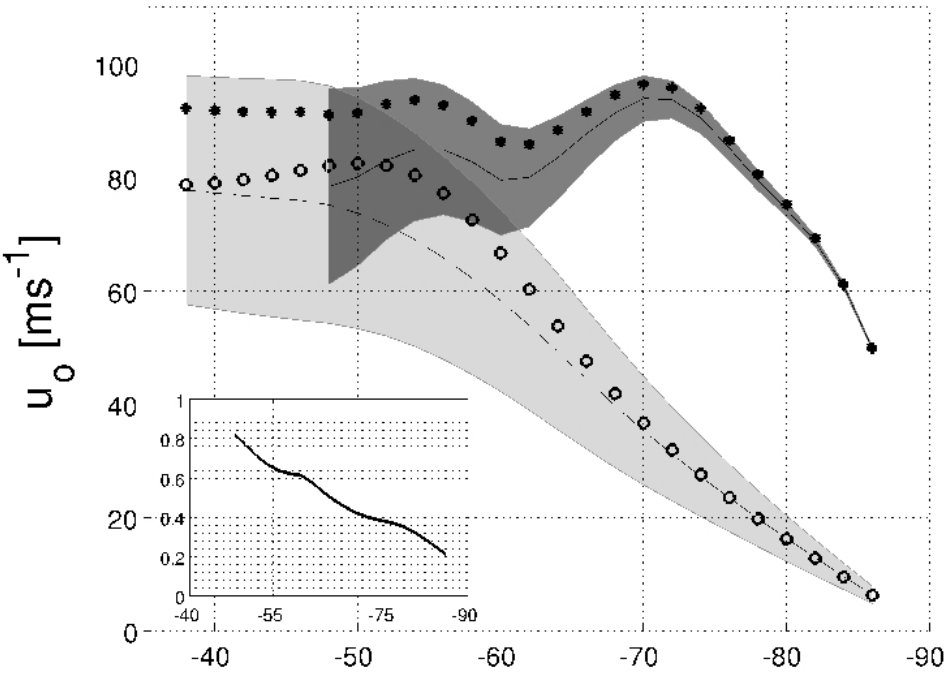

Figure 2.12: Similar to Figs. 2.6 and 2.7 but now using VIRTIS temperature retrievals (Grassi *et al.* 2010). The zonal winds are defined in the prograde direction and the lower boundary condition at 100 hPa. The dashed line represents the mean of the initial profiles and the solid line is the mean final result. The darker shaded region represents the standard deviation of the final results and the other for the initial guesses. The small plot represents the ratio of the standard deviation of the solid line over the standard deviation of the initial guesses. The initial lower boundary condition that was prescribed to have the form of Equation (2.4) with $a = 52$ m s^{-1}, $b = 56°$, $c = 9$ and $d = 86$ m s^{-1} is represented by unfilled circles. The calculated lower boundary condition starting with the Equation (2.4) where $a = 52$ m s^{-1}, $b = 56°$, $c = 9$ and $d = 105$ m s^{-1} is represented with filled circles.

2.7 Conclusions

Previous work on thermal wind retrievals failed to obtain the zonal winds in the polar regions (latitudes higher than 70°). In this chapter, we find that one of the main difficulties is the use of an inaccurate lower boundary condition in the upward integration of the cyclostrophic thermal wind equation, which produces inaccurate results that propagate and amplify with the upward integration. Another minor factor is that at latitudes higher than 60°, the presence of eddy fluxes and variance terms weaken the validity of the cyclostrophic approximation, although this source of systematic error seems to be fairly small. Following the work in this chapter, we propose an improved method to estimate the lower boundary from the latitude position of the jet up to the pole. The procedure was explored for different conditions, showing that it is robust to changes in the initial lower boundary guess provided the low-latitude flow is well constrained. We also learned that the method is more accurate when applied to temperature fields that are a product of long time averaging (closer to the regime of pure cyclostrophic balance). The choice of the top level of the retrieval domain can also affect the results, with the most problematic case happening when the top is defined near the jet region, leading to an underestimation of the final zonal thermal wind speed.

The improved method applied to observational data is found to increase the magnitude of the winds at high latitudes, improving previous results where the values for the lower boundary at high latitudes may have been underestimated or inaccurately specified. The magnitude of the winds at latitudes higher than 70° are now in good agreement with recent results from Piccialli *et al.* (2012), who use a method which computes directly the zonal winds from the evaluation of the meridional slope of the pressure surfaces (removing the need to define a lower boundary condition). The results also show significant zonal wind speeds in the polar region and strong horizontal shear at the poles, in contrast to previous works that obtained weaker winds. The well-known rotation of the double-vortex (Piccioni *et al.*, 2007a) implies significant zonal wind speed in the prograde direction as obtained in our work.

The new method developed can help to better characterise the atmospheric circulation in the Venus mesosphere using the several temperature retrievals available. It can also be applied in conjunction with results from cloud tracking in the high-latitude region, to study and characterise winds near the altitude of the cloud top.

3

A new radiative-convective scheme for OPUS-Vr

3.1 Summary

In this chapter I present a new radiation scheme developed for the OPUS-Vr (OPUS-V that includes a radiative transfer formulation), which works in the solar and thermal spectra. This new radiative parameterisation uses a different approach in the two main wavelength bands: solar radiation (0.1-5.5μm) and thermal radiation (1.7-260μm). The solar radiation calculation is based on the δ-Eddington approximation (two-stream-type) with an adding layer method. For the thermal radiation case, a code based on an absorptivity/emissivity formulation is used.

The code developed allows an easy inclusion of time dependent absorption and scattering in the atmosphere due e.g. to aerosols. The results of radiative heating/cooling rates and the global-mean radiative-convective equilibrium temperature profiles are presented and discussed for different atmospheric conditions. A new convection scheme was developed and used which includes the dependence with temperature of the atmosphere's heat capacity at constant pressure.

3.2 Introduction

Venus has a dense atmosphere mainly composed of carbon dioxide ($\sim$ 96.5%) and a small amount of nitrogen ($\sim$ 3.5%). Despite being closer to the sun than the Earth, the net absorption of solar radiation by the atmosphere is less than on the Earth due to the high

albedo of the cloud deck that covers the planet almost entirely. The main cloud deck is composed mostly of sulphur dioxide and sulphuric acid droplets. In the UV, visible and most of the infrared wavelength ranges, the clouds are very thick, hiding completely the surface of the planet.

There has been an important effort in the last 30 years, as mentioned in chapter 1, to simulate and understand the atmospheric dynamics and climate of this planet using simplified GCMs. These models are usually adaptions of Earth GCMs and use simplified physical parameterisations, including the radiation scheme. The Venus GCM from Lebonnois *et al.* (2010a), is the only work published in the peer reviewed literature so far that has implemented with relative success, a consistent radiative transfer calculation for the thermal radiation, based on the work from Eymet *et al.* (2009). However, their radiative parameterisation has significant limitations, such as the need to re-compute new exchange matrices for variations in the atmospheric composition or variations in surface pressure. They also typically maintain a cloud structure constant with latitude in the model, via the use of a pre-computed table of solar fluxes from Crisp (1986) to calculate the solar heating rates.

The radiation plays a very important role in the atmospheric dynamics and climate, and to simulate a realistic self consistent dynamical state in a GCM, it is important to use a radiative transfer model. It is with this purpose that a suitable and complete radiative transfer formulation for the OPUS-Vr was developed. The code was planned to enable us to take into account temporal variations of the atmospheric constituents, such as clouds in GCM simulations. A parameterisation of radiation-cloud variability interactions in a Venus GCM is important to study more accurately the cloud distribution and its influence on the atmospheric dynamics.

In sections 3.3 and 3.4, the methods used to prepare the input data and compute the heating/cooling rates of the solar and thermal radiation are described. In section 3.5 the new radiation code is implemented in a 1D radiative-convective model (1D R-CM). The convection scheme used was developed and adapted to take into account the dependence of the specific heat capacity of the atmosphere with temperature at constant pressure. The final equilibrium state profiles are obtained and discussed, and the conclusions are presented in section 3.7.

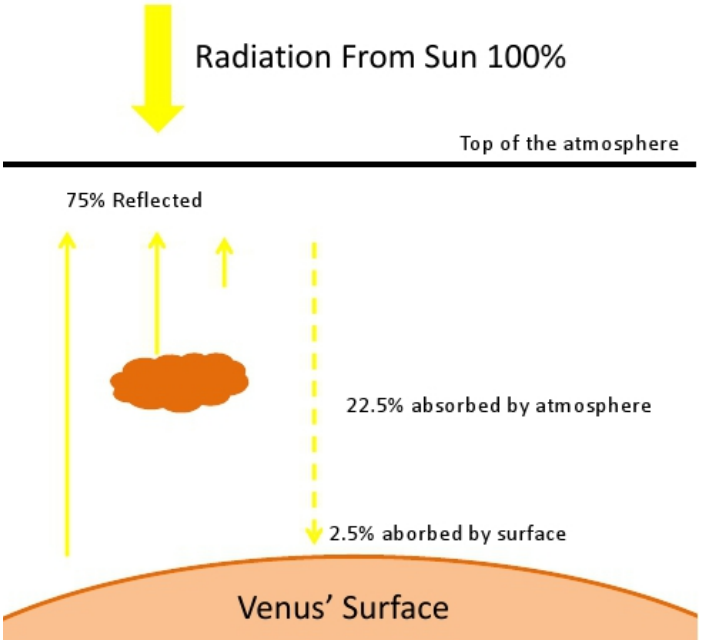

Figure 3.1: The different components of the radiative energy budgets in Venus.

3.3 Solar radiation

The portion of the atmosphere explored in the OPUS-Vr described in the next chapter, covers the region between the surface and 100 km altitude with 37 layers. The main solar radiative processes in the Venus atmosphere occur in the mesosphere (between 55 and 100 km altitude) which accounts for the important contribution of the cloud deck that reflects $\sim$ 75 % of the incident sunlight (Fig. 3.1). A large amount of solar energy is also absorbed within the cloud region where an unidentified substance is responsible for the absorption of the UV radiation in the upper clouds, causing remarkable features in the UV images of the atmosphere (e.g., del Genio & Rossow 1990, Titov *et al.* 2012). Above the cloud top the CO_2 absorption dominates. In the deepest atmosphere the absorption of the gases such as: CO_2, H_2O and SO_2 (the mass mixing ratio of H_2O and SO_2 increases), become important as well as the Rayleigh scattering, but producing very small heating rates in comparison with the rest of the atmosphere. The solar energy absorbed at the surface averaged over the planet is is estimated to be around 2.5% of the total incident solar energy (Tomasko *et al.*, 1980).

The differential absorption of the sunlight by the atmosphere has a key role driving the

circulation of the atmosphere and in maintaining the thermal structure. The thermal tides are thought to be an important mechanism to maintain the equatorial super-rotation of the atmosphere (Pechmann & Ingersoll 1984; Newman & Leovy 1992; Lebonnois *et al.* 2010a), which increases the importance of having a self-consistent parameterisation for the solar radiation in a Venus GCM.

The method developed here uses a combination of the δ-Eddington method and an adding-layer technique. The important active components that interact with the solar radiation were taken into account. The model uses the absorption and scattering of three different gases (CO_2, SO_2 and H_2O), four size categories of H_2SO_4/H_2O aerosols, an unidentified UV absorber and the Rayleigh scattering due to CO_2 and N_2 molecules.

3.3.1 Optical properties of the Venus atmosphere for solar radiation

3.3.1.1 Gases

The optical properties of the three main gases that interact with the solar radiation in the Venus atmosphere were computed: carbon dioxide (CO_2), water (H_2O) and sulfur dioxide (SO_2). Fig. 3.2 shows the volume mixing ratios for these three gases. The three profiles were taken from the VIRA model (**V**enus **I**nternational **R**eference **A**tmosphere, Kliore *et al.* 1985). The Venus atmosphere is composed mainly of CO_2 (assumed to be well mixed in the atmosphere at 0.96 vmr). The independent coefficients of absorption used in this section for CO_2, H_2O and SO_2, were compiled in Lee & Richardson (2011). These coefficients were computed using parameters from the HITRAN 2004 database (Rothman *et al.* 2005) and the HITEMP CO_2 (Rothman *et al.* 1995) and stored using a k-distribution method (Lacis & Oinas 1991). They were calculated on a 0.1 micron resolution grid between 0.1 and 5.5μm, for twenty reference pressures between 10^{-3} hPa and 14×10^4 hPa (equally spaced in a log scale), twenty reference temperatures from 150K to 1100K (equally separated intervals) and twenty Gaussian ordinates (spectral fractions).

Self-broadening was used when calculating the CO_2 opacity and due to the limited foreign broadening data available in HITRAN/HITEMP, air-broadened was assumed for H_2O and SO_2 (Lee & Richardson 2011). The absorption line shape of CO_2 was assumed to be a sub-Lorentzian as suggested in Meadows & Crisp (1996). The coefficient of absorption for each model layer was obtained by interpolating the k-table linearly (in log scale for pressure) for the required temperature and pressure. For more details see Lee & Richardson (2011).

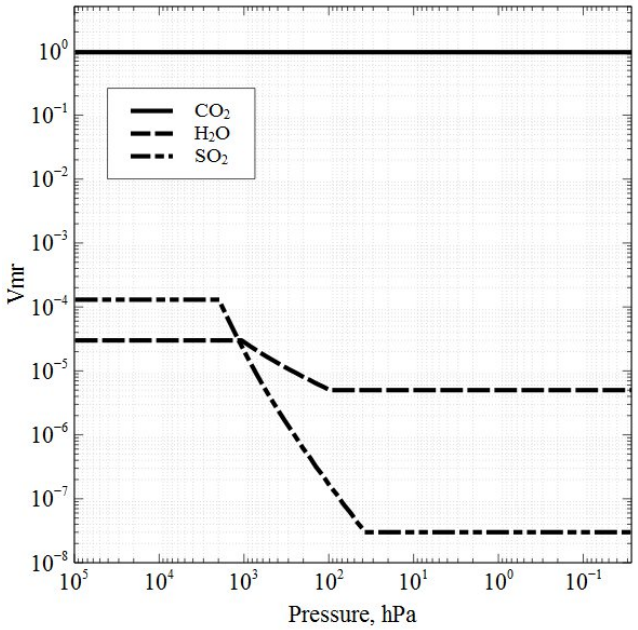

Figure 3.2: Volume mixing ratios of CO_2, H_2O and SO_2.The values were obtained from VIRA model (von Zahn & Moroz 1985).

3.3.1.2 Aerosols

As pointed out in chapter 1, Venus is covered by a cloud deck which hides completely the lower atmosphere and surface at the UV, visible and most of the infrared wavelength ranges, despite the observed existence of some near-IR spectral windows (e.g., Allen & Crawford 1984). Fig. 3.3 shows schematically how the clouds in Venus are distributed vertically. For simplicity, a latitudinal uniform cloud distribution was assumed in this work for the reference atmosphere. The clouds are composed of three different size distribution modes plus an extra unidentified UV absorber. The cloud model (composition, particle sizes and vertical distribution) used in this work is similar to the equatorial cloud model in Crisp (1986). The scattering and extinction efficiencies used in Crisp (1986) were interpolated to our spectral resolution, including also the values suggested in that work for an empirical UV absorber modification to mode 1 parameters. The UV absorber in the mesosphere is simulated assuming that the distribution of this "artificial" constituent is the same as the mode 1 particles between 56.5 km and 71 km, as suggested in, e.g., Tomasko *et al.* (1980), Pollack *et al.* (1980) and Crisp (1986). The empirical absorption between 0.3 and 0.7 μm is fine-tuned until the spectral dependence of the spherical albedo matches the values from the

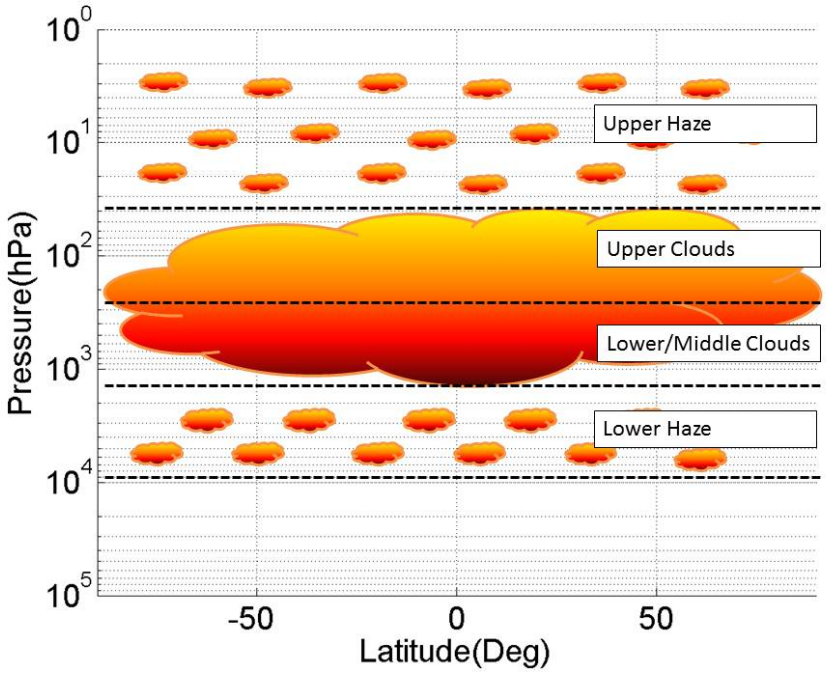

Figure 3.3: Schematic cloud distribution in Venus and adopted in this work.

solar flux radiometer aboard the Pioneer Venus probe (Tomasko *et al.* 1980; Crisp 1986). Outside this spectral region the absorption is set to zero. Following the work from Crisp (1986), the composition of the cloud droplets is assumed to be 75% sulphuric acid and 25% water. The values of $\tau_{ext}(0.63\mu\text{m})$ in Crisp (1986), were determined by the study of observational experiments onboard the Pioneer Venus satellite, and in Fig. 3.4 it is compared these values with the optical depth at 0.63 μm used in this work.

The computation of the optical depth for each particle mode was done using a rescaling method,

$$\tau_x(\lambda) = \frac{Q_x(\lambda)}{Q_{ext}(0.63\mu m)}\tau_{ext}(0.63\mu m), \tag{3.1}$$

where $\tau_{ext}(0.63\mu m)$ and $Q_{ext}(0.63\mu m)$ are the extinction optical depth and efficiency at 0.63 μm and the symbol x identifies the variable with extinction, absorption or scattering properties.

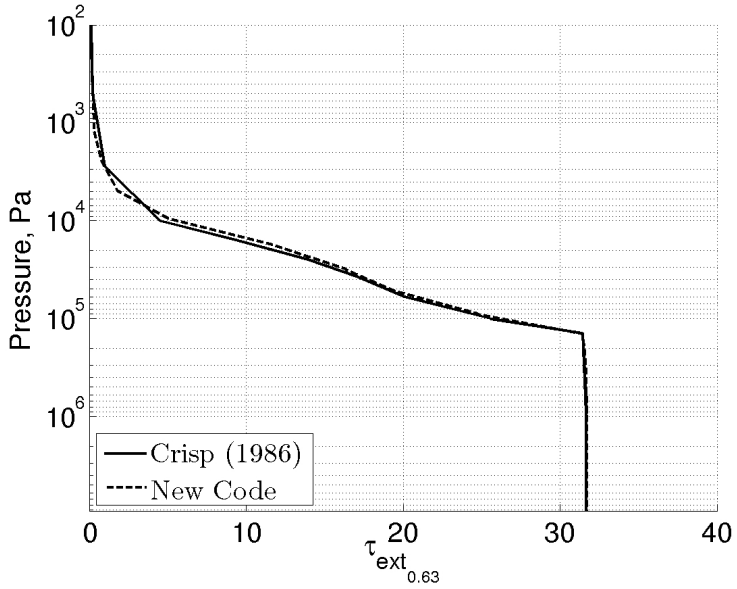

Figure 3.4: Comparison between the cloud optical depth at 0.63 μm used in this work and the one in Crisp (1986).

	Mode 1 and UV absorber	Mode 2	Mode 2'	Mode 3
Effective radius (μm)	0.49	1.18	1.40	3.65
Effective variance (μm)	0.22	0.07	1.23	1.30

Table 3.1: Microphysical properties of the aerosols (Crisp 1986). Mode 2 is divided into submodes 2‘ and 2, that corresponds to different regions in the clouds (lower/middle clouds and upper clouds respectively).

Constant	CO_2	N_2
ϵ	169.94 μm^{-2}	156.63 μm^{-2}
β	55939	69049
$\frac{1}{\alpha}$	273 K	269.1 K

Table 3.2: Empirically-determined constants form Washburn (1930).

3.3.1.3 Rayleigh scattering

The Rayleigh scattering effect due to the presence of CO_2 and N_2 molecules in the Venus atmosphere was included in the solar radiation code. This phenomenon is related to the elastic scattering of the radiation with much larger wavelengths than the particle sizes (in this case gas molecules). One well known phenomenon related to this type of scattering is the blue sky in the Earth atmosphere or "hotter" colours for larger optical paths.

The scattering coefficient per unit length for anisotropic gaseous molecules in random orientation is defined as,

$$k_{sca} = \frac{8\pi^3}{3} \frac{(n_g^2 - 1)^2}{\lambda^4 N} \frac{6 + 3\delta}{6 - 7\delta} \tag{3.2}$$

where δ is the anisotropy factor of the molecule, N is the number of molecules per unit volume and n_g is the refractive index. The values of n_g for CO_2 and N_2 were obtained for different pressures (P) and temperatures (T),

$$n_g = 1 + \frac{\beta \times 10^{-6}(P/P_0)}{(1 - \alpha T)(\epsilon - \lambda^{-2})} \tag{3.3}$$

where P_0 is a reference pressure (1.01325 bars), λ is the wavelength and β, ϵ and α are empirically constants from Washburn (1930) (Table 3.2). The values of δ are respectively 0.0305 for N_2 and 0.0805 for CO_2.

3.3.1.4 Additional absorption in the lower atmosphere and surface albedo

Below the cloud base, in the lower atmosphere, an additional absorption was included within the spectral range 0.4 - 1.0 μm. The need for this correction was first noticed by Tomasko *et al.* (1980). This fault in the model is thought to be related to the poor representation of the hot-bands of CO_2 in this spectral region. The correction was made by adding a

blue gas absorber with an empirically determined absorption coefficient increasing linearly with decreasing wavelength. The effect of the Rayleigh scattering in this spectral region was also increased to have a good match with the integrated upward and downward fluxes obtained in Crisp (1986), who calibrated his results against Pioneer Venus Sounder probe solar radiometer data. Another possible explanation could be the incapacity of the two-stream solutions in fully representing multiple-scattering in this atmospheric region.

The surface albedo (α) values used were obtained by fitting the wavelength dependent observational results presented by Pieters *et al.* (1986), for wavelengths shorter than 1 μm. Above this limit α was set to 0.15.

3.3.2 The solar radiative transfer model

The solar radiation code was written from scratch and is based on a two-stream solution that incorporates a delta-Eddington approximation and a layer-adding method, which were adapted from the Community Atmosphere Model (CAM) version 3 (Briegleb 1992). The two-stream solution simplifies the radiative transfer equation that becomes more complex to solve when scattering effects are included. This method divides the radiance into an upward and downward component. The atmosphere is divided into 37 horizontally and vertically homogeneous layers. The assumed homogeneity of the layers means that the physical properties in each layer are constant. An extra layer was included to avoid excessive heating in the model's top layer, when the top pressure is not sufficiently low (Briegleb 1992).

For each model's layer the monochromatic optical properties were defined taking into account the several absorbers' and/or scatterers' constituents,

$$\tau = \sum_i \tau_i, \tag{3.4}$$

$$w = \frac{\sum_i w_i \tau_i}{\tau}, \tag{3.5}$$

$$g = \frac{\sum_i g_i w_i \tau_i}{w\tau}, \tag{3.6}$$

$$f = \frac{\sum_i f_i w_i \tau_i}{w\tau}. \tag{3.7}$$

These equations define the extinction optical depth τ, the single-scattering albedo w, the asymmetry parameter g and the forward scattering fraction f for each homogeneous layer.

The simple two-stream method does not produce accurate results in the presence of scattering particles with highly asymmetric phase functions. A simple approach to avoid this

difficulty is to use a δ adjustment in the radiative parameters, the δ-Eddington approximation. The radiative parameters are scaled removing the fraction of scattered energy related to the forward peak. Using this approximation, in Wiscombe (1977) it was shown for the Earth's atmosphere, that flux errors are not larger than 15% for the more problematic cases: i.e., for very small single scattering conditions and for large zenith angles (larger than 80°). For the Venus mesospheric conditions, Crisp (1986) compares the results of his model, that uses a δ-Eddington approximation, with the work from Tomasko *et al.* (1985), who used a more accurate adding-doubling method, and the differences are not larger than 5%.

The δ-Eddington approximation incorporates a simple representation of the multiple scattering phenomena in the atmosphere. The scaled parameters are defined as,

$$\tau^\star = \tau(1 - wf), \tag{3.8}$$

$$w^\star = w(\frac{1-f}{1-wf}), \tag{3.9}$$

$$g^\star = \frac{g-f}{1-f}. \tag{3.10}$$

The radiation was divided into direct and diffuse components. The reflectivity and transmissivity were computed for each layer, using the following equations (for non-conservative solutions, for which $w < 1$, Briegleb 1992),

$$R(\mu_0) = (\alpha-\gamma)\bar{T}e^{-\frac{\tau^\star}{\mu_0}} + (\alpha+\gamma)\bar{R} - (\alpha-\gamma), \tag{3.11}$$

$$T(\mu_0) = (\alpha-\gamma)\bar{R}e^{-\frac{\tau^\star}{\mu_0}} + (\alpha+\gamma)\bar{T} - (\alpha+\gamma-1)e^{-\frac{\tau^\star}{\mu_0}} \tag{3.12}$$

$$\bar{R} = (u+1)(u-1)(e^{\lambda\tau^\star} - e^{-\lambda\tau^\star})N^{-1} \tag{3.13}$$

$$\bar{T} = 4uN^{-1} \tag{3.14}$$

where α, γ, λ, N and u are defined respectively as,

$$\alpha = \frac{3}{4}w^\star\mu_0\frac{1+g^\star(1-w^\star)}{1-\lambda^2\mu_o^2} \tag{3.15}$$

$$\gamma = \frac{1}{2}w^\star\frac{1+3g^\star(1-w^\star)\mu_0^2}{1-\lambda^2\mu_0^2} \tag{3.16}$$

$$N = (u+1)^2e^{\lambda\tau^\star} - (u-1)^2e^{-\lambda\tau^\star} \tag{3.17}$$

$$u = \frac{3}{2}\frac{1-w^\star g^\star}{\lambda} \tag{3.18}$$

$$\lambda = \sqrt{3(1-w^\star)(1-w^\star g^\star}} \tag{3.19}$$

The notation used here is the same as in Coakley *et al.* (1983) and Briegleb (1992). R and T are the reflectivity and transmissivity related to the direct radiation, and $\bar{R}$ and $\bar{T}$ to

the diffuse radiation. The variable μ_0 is the cosine zenith angle. As in Briegleb (1992), the diffuse reflectivity was set to zero for the cases where w is very small - noting that mathematically using this formulation $\bar{R}$ can be less than zero.

The transmissivity and reflectivity computed for each layer, that was explained previously, are now combined for two consecutive layers to determine the total transmission and reflection properties, taking into account the successive backward and forward reflections. The equations for the total reflection and transmission to direct and diffuse radiation between two layers (Liou 1992 and Briegleb 1992) are,

$$R_{12}(\mu_0) = R_1\mu_0 + \frac{\bar{T}_1((T_1(\mu 0) - e^{-\frac{\tau_1^\star}{\mu_0}})\bar{R}_2 + e^{-\frac{\tau_1^\star}{\mu_0}}R_2(\mu_0))}{1-\bar{R}_1\bar{R}_2} \tag{3.20}$$

$$T_{12}(\mu_0) = e^{-\frac{\tau_1^\star}{\mu_0}}T_2(\mu_0) + \frac{\bar{T}_2((T_1(\mu 0) - e^{-\frac{\tau_1^\star}{\mu_0}}) + e^{-\frac{\tau_1^\star}{\mu_0}}R_2(\mu_0)\bar{R}_1)}{1-\bar{R}_1\bar{R}_2} \tag{3.21}$$

$$\bar{R}_{12} = \bar{R}_1 + \frac{\bar{T}_1\bar{R}_2\bar{T}_1}{1-\bar{R}_1\bar{R}_2} \tag{3.22}$$

$$\bar{T}_{12} = \frac{\bar{T}_1\bar{T}_2}{1-\bar{R}_1\bar{R}_2}. \tag{3.23}$$

Fig. 3.5 shows a schematic plot of the combination between two layers (called 1 and 2). This formulation is named as "adding layer method" and transforms homogeneous problems (the solution for one layer) into an inhomogeneous system.

For the computation of the spectral upward and downward fluxes at every interface, the layers of the entire atmospheric column are combined in the upward and downward direction. The equations obtained are:

$$F_{up} = \frac{e^{-\frac{\tau^\star}{\mu_0}}R_{up}(\mu_0) + (T_{dn}(\mu_0) - e^{-\frac{\tau^\star}{\mu_0}})\bar{R}_{up}}{1-\bar{R}_{dn}\bar{R}_{up}} \tag{3.24}$$

$$F_{dn} = e^{-\frac{\tau^\star}{\mu_0}} + \frac{(T_{dn}(\mu_0) - e^{-\frac{\tau^\star}{\mu_0}}) + e^{-\frac{\tau^\star}{\mu_0}}R_{up}(\mu_0)\bar{R}_{dn}}{1-\bar{R}_{dn}\bar{R}_{up}}. \tag{3.25}$$

$\tau^\star$ is the total optical depth above the interface, $\bar{R}_{up}/\bar{R}_{dn}$ is the reflectivity below/above the interface due to the diffuse radiation from above/below, $T_{dn}(\mu_0)$ is the total transmission to downward direct solar radiation and $R_{up}(\mu_0)$ is the reflectivity to upward direct solar radiation. For more details about these equations see Briegleb (1992).

The solar spectrum was divided into fifty five bands from 0.1 to 5.5 μm, in consistency with the k-coefficients described previously. The solar fluxes at the top of the atmosphere

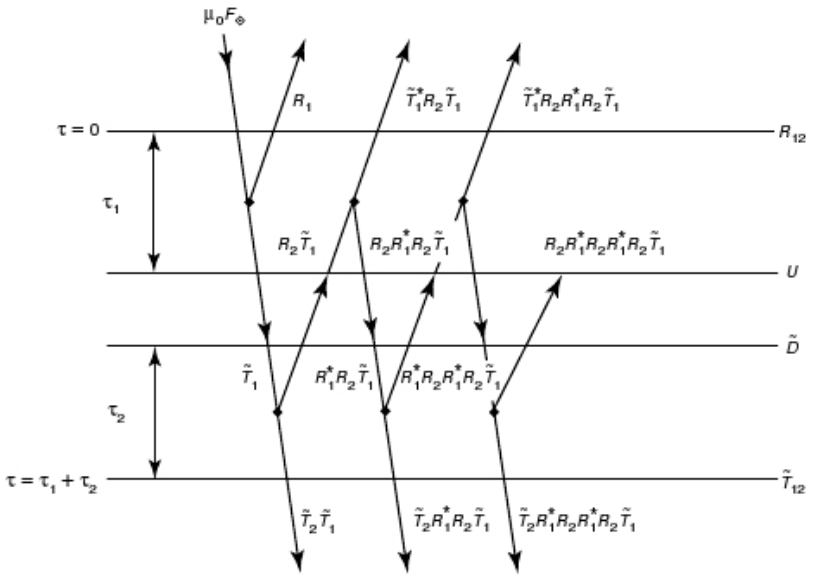

Figure 3.5: Illustration of the adding method configuration from Liou (1992) for two layers.

were based on the results presented in the MODTRAN 3.7 program (Liou 2002) for the Earth and converted for the Venus values using a mean distance Venus-Sun of 0.7 AU.

The computation of the solar heating rates in each layer is associated with the divergence of the spectral-integrated net radiative flux (F^{net}), the acceleration due to gravity and to the specific heat capacity at constant pressure (c_p),

$$\frac{dT}{dt} = \frac{1}{\rho c_p} \frac{dF^{net}}{dz}. \tag{3.26}$$

The observational results summarised in the Venus International Reference Atmosphere (VIRA, Seiff *et al.* 1980), indicate that the specific heat capacity at constant pressure (c_p) of the atmosphere varies from 1181 J kg^{-1}K^{-1} near the planet's surface to around half of this value for temperatures around the ones typically obtained near the top of our model domain (around 100 km). An analytic expression that evaluates efficiently the approximate dependence of c_p with temperature is suggested in Lebonnois *et al.* (2010a),

$$c_p = c_{p0} \times (\frac{T}{T_0})^{\nu} \tag{3.27}$$

where C_{p0} = 1000 J kg^{-1}K^{-1}, T_0 = 460 K and ν = 0.35.

3.3.2.1 Simple approximation in spectral bands for gas absorption

The k-distribution method keeps good accuracy and consists in applying to each predefined spectral band a reorganization in the ascending order of the absorption coefficients by their strength (Lacis & Oinas 1991). $k(\lambda)$ is mapped from spectral space to a space defined by the cumulative probability function $g(k)$. The k-distribution method was developed mainly to reduce the integration time of the transmission's calculations that use line-by-line methods.

Using the complete available k-tables for each gas, the code would need to compute solar fluxes for each spectral fraction, twenty times per spectral band, which is a time-consuming procedure. In conditions such as we have on Venus, massive CO_2 atmosphere with highly reflective clouds, a spectral averaging method reduces drastically the efficiency of the code in representing the scattering phenomena, mainly due to the presence of strong absorption CO_2 lines. This difficulty is relevant in the near-infrared spectra region where the gas absorption coefficients rapidly change with frequency. To overcome this difficulty and reduce the number of computations, the spectral bands were divided into a weak absorption part and a stronger absorption part, ensuring the total absorption in each band was conserved. The two parts have different relative weights and occupy different fractions of the spectrum, and are kept the same for all the bands in the three gases.

The weight and the spectral fraction of the two parts are calibrated and validated for different zenith angles with the non-spectral-averaged version code. In this approximation we assumed that the absorption spectral lines of the different gases are uncorrelated.

3.3.3 Reference Solar heating rates and fluxes

The absorbed spectral integrated and globally averaged solar flux obtained from the code developed and the atmospheric condition assumed is 163.6 W/m^2. This result corresponds to a bolometric albedo of 0.76, which agrees with the values observed (Taylor *et al.* 1980; Moroz 1983 and Moroz *et al.* 1985). Fig. 3.6 shows the albedo of the atmosphere at the sub-solar point as a function of wavelength. As seen in this figure, the H_2SO_4/H_2O droplets and the UV absorber, have a very important impact on the values obtained. A relative change of these two species can produce bright or dark regions in the UV/Infrared spectra that contribute to the contrasting features in the well-known images captured by the Pioneer Venus probe (e.g., del Genio & Rossow 1990). The absence of the UV absorber results in a significant increase in the albedo in the UV spectral region. In cases where the clouds are

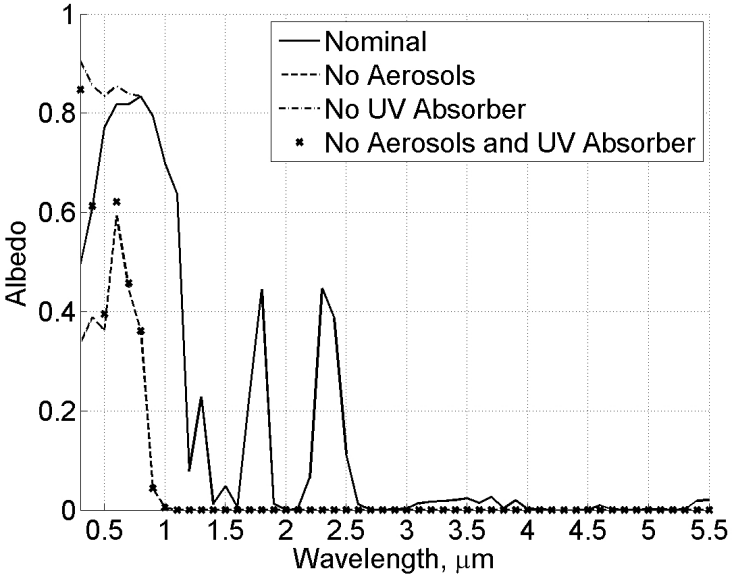

Figure 3.6: Albedo obtained at the sub-solar point for four different conditions: solid line is the reference case; dashed line for the case without H_2SO_4/H_2O clouds; dot-dashed line for the case without the UV absorber; crosses for the case without the clouds and the UV absorber.

removed the albedo decreases significantly, resulting in a larger absorption of solar energy by the atmosphere, where the scattering effects become less important. The spectrally integrated and globally-averaged downward and upward fluxes are shown in Fig. 3.7. In this result the sudden drop in the downward solar flux caused by the optical properties of cloud deck is clearly seen in region between 1.5×10^3 and 100 hPa. Fig. 3.8 represents the solar heating rates as a function of height for two solar zenith angles (0° and 75°). The solid line corresponds to the results obtained by the new code and the dashed line represents the results from Crisp (1986). Both methods obtain qualitatively similar results. This figure is also the validation that the method described previously (where the spectral band is divided into two parts - low and high absorbing parts) works well for large variations in the optical depth for the two zenith angles tested. The differences between the results of the new code and the ones in Crisp (1986) are thought, despite the different formulation of the code and input, to be due to slight differences in the assumed cloud distribution and different vertical discretisation (Crisp 1986 uses a better vertical resolution). Fig. 3.9 illustrates the effect of the presence of the UV absorber in the cloud region, where this absorber is responsible for a bump in the heating profile with a maximum at 100 hPa ($\sim$ 66 km, solid line). On

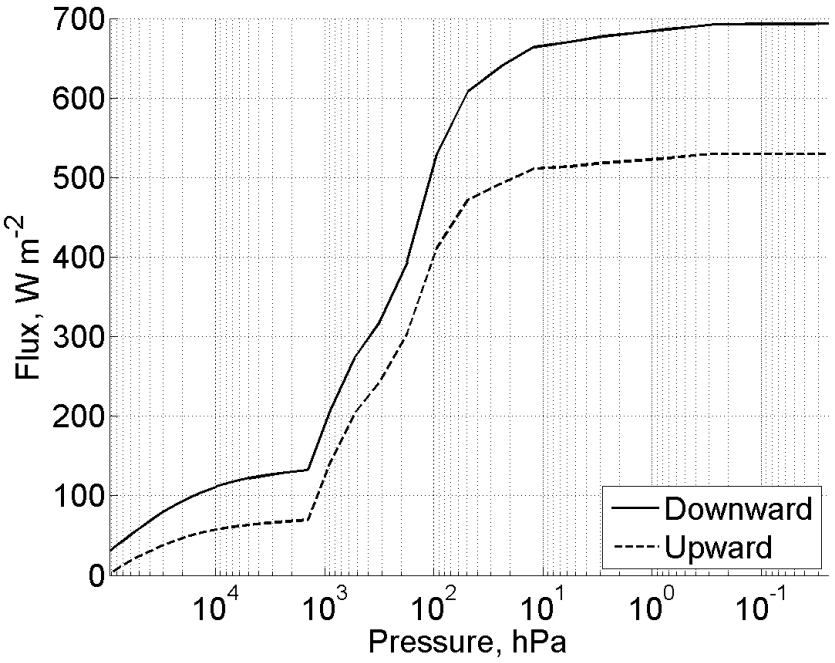

Figure 3.7: The global-mean spectral integrated downward and upward fluxes of the new solar radiation code.

reducing the amount of aerosols it has also an important impact in the solar heating profiles, which contributes to a large extinction of the solar radiation. Upon removing all the aerosols and UV absorber, the heating profile approximately follows a pure CO_2 atmosphere, with a smooth profile throughout the entire atmosphere. The aerosols here are referring to the three droplet modes described previously. The validation/comparison exercise between the results obtained and the observational data on the deep atmosphere was not explored due to the large uncertainties associated with the small amount of data available in that region.

3.4 Thermal radiation

Fast and accurate computations of the atmosphere's energy exchange via infrared (IR) radiation for long periods of integration has long been a challenging problem within the Venus GCM community. Here a new simple formulation capable of rapidly computing the exchanges of IR radiative energy between different layers of the atmosphere, surface and space in Venus is developed. The thermal radiation code was written from scratch following

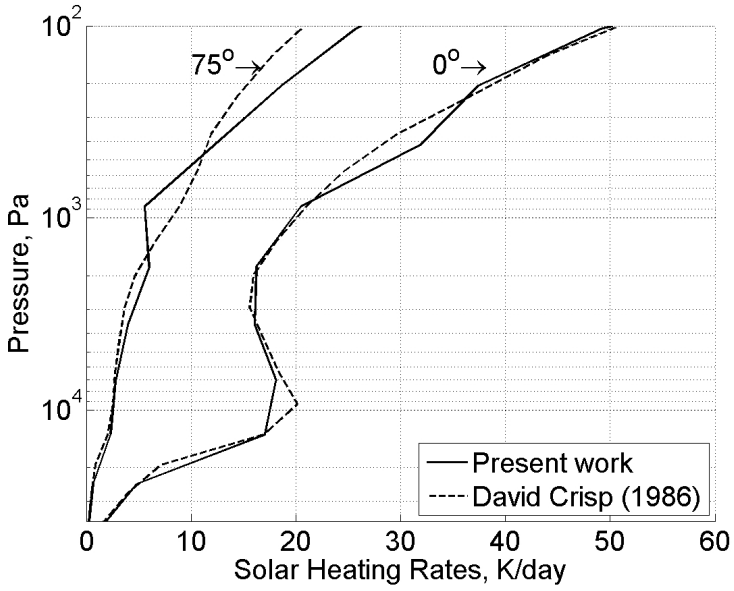

Figure 3.8: Compares the heating rates of the new solar radiation code (solid line) with the results from Crisp (1986)(dashed line) in the mesosphere. The results shown are for two different zenith angles (0° and 75°).

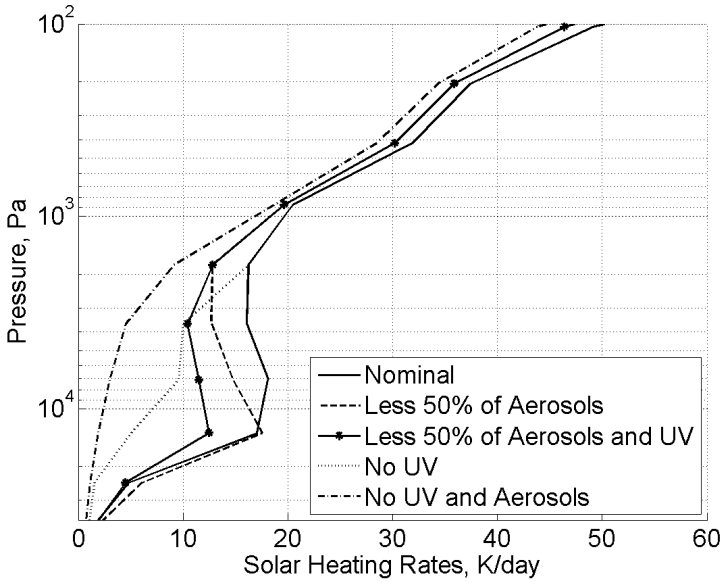

Figure 3.9: The solar heating rates for different atmospheric conditions at the sub-solar point: reference (solid line), less 50% of aerosols (dashed line), less 50% of aerosols and UV absorber (solid line with stars), no UV absorber (points), no aerosols or UV absorber (dashed-pointed line).

the ideas of Lacis & Oinas (1991) and Fu (1991).

The method is based on an absorptivity/emissivity formulation (neglecting scattering) and has a similar structure to what has been used for Earth GCM studies (e.g., appendix in Lacis & Oinas 1991). The results shown in Crisp & Titov (1997) suggest that the errors in the cooling rates are no larger than 10% for almost the entire atmosphere if we ignore the effects of multiple scattering by gases and aerosols at thermal infrared wavelengths in Venus. The largest errors occur at the near-infrared wavelengths, where the clouds act almost as pure scatterers.

The code permits an easy control of the opacity used in both solar and thermal radiation codes, which helps to keep consistency between them (the same gas and aerosol densities). The structure of the new parameterisation allows also an easy implementation of an interface to take into account changes in the opacity structure (e.g., changes in the cloud structure) with little computational time during the GCM integration.

3.4.1 Optical properties of the Venus atmosphere for thermal radiation

3.4.1.1 Gases

For the thermal spectral region studied here (1.7-260.75 μm) the main gaseous absorption lines are due to the molecular rotational transitions of carbon dioxide (CO_2), water (H_2O) and sulphur dioxide (SO_2). The coefficients of absorption for these three gases were obtained using the k-tables produced by Lee & Richardson (2011). These data have the same meaning as the ones described previously in the solar radiation (section 3.3), where the only differences are related to the spectral resolution and of course the spectral range. Here the spectral range is 1.7-260.0 μm and divided into two hundred and seventy three bands with variable spectral resolution, see Table 3.3. To reduce the time of integration to compute the cooling rates, reducing the number of integration steps, the coefficients of absorption were averaged within the spectral bands using the following simple equation,

$$\begin{aligned} k(\lambda, p, T, q_{H_2O}, q_{SO_2}) &= \sum_i (k_{CO_2}(\lambda, p, T) + \frac{q_{H_2O}}{q_{CO_2}} k_{H_2O}(\lambda, p, T) + \\ &\quad \frac{q_{SO_2}}{q_{CO_2}} k_{SO_2}(\lambda, p, T)) \Delta g_i \end{aligned} \tag{3.28}$$

where q_{H_2O} and q_{SO_2} are the mixing ratios for H_2O and SO_2, and q_{CO_2} is the mixing ratio of CO_2 which is assumed to be well mixed in the atmosphere. Δg_i are the spectral fractions

Spectral range (μm)	Spectral resolution (μm)
1.70 - 2.55	0.02
2.55 - 22.75	0.1
22.75 - 40.75	1.0
40.75 - 100.75	10.0
100.75 - 260.75	40.0

Table 3.3: Spectral range and resolution for each band defined in the k-tables for the thermal radiation scheme.

within each spectral band defined in the k-tables, where $g_i(k)$ is an accumulative probability function in the k space. This method assumes that the absorption lines of the three gases are uncorrelated as in the solar radiation section. The accuracy of using this formulation depends largely on the width of the spectral band and on the variability of the absorption lines within the spectral band itself, and it is higher for small widths and low variability. The method used is simple and more advanced methods are not explored in this work. Here, k is considered as the coefficient of absorption of a single-component gas where the optical depth can be calculated using

$$\tau(\lambda) \quad = \quad q_{CO_2} \int k(\lambda, p, T) \rho_a dz, \tag{3.29}$$

where ρ_a is the air density.

3.4.1.2 Aerosols

The cloud composition, spatial distribution and particle sizes adopted are based on the same ones as for the solar radiation (section 3.3). This option keeps the cloud structure consistent for GCM applications. The optical properties used were interpolated from Crisp (1989) for the same spectral resolution of the k-tables as described previously between 1.70 and 260.75 μm.

3.4.1.3 Continuum absorption

The atmospheric conditions found in Venus, high temperatures and pressures, induce a significant production of extra opacity due to the molecular collisions. This phenomenon results in extra absorption and emission of mainly infrared radiation from the momentary

deformation of the colliding molecules. This collision-induced absorption is generally associated with a smooth absorption profile (lacking line structure) with wavelength. In Venus the presence of this contribution to absorption is mostly due to CO_2-CO_2 collisions. We have also included in this work the effect of H_2O-H_2O collisions but its contribution is much smaller than the effect of CO_2-CO_2 collisions. Other types of collision effect are neglected.

The quantification of carbon dioxide continuum effects is still poorly explored for conditions in the deep Venus atmosphere. The parameterisation used in this work to simulate this effect is based on laboratory data from the 1970s by Moskalenko *et al.* (1979), which are still very commonly used for Venus climate studies (e.g., McGouldrick 2007 and Eymet *et al.* 2009). This part of the code was developed following, e.g., Bullock & Grinspoon (1996), Bullock (1997) and McGouldrick (2007).

We represent the carbon dioxide continuum optical depth in the following form,

$$\tau_{con,co_2} \quad = \quad k_{con,CO_2} \times p \times u_{CO_2} \tag{3.30}$$

where p is the atmospheric pressure, u_{co_2} is the column abundance of carbon dioxide in a layer and k_{con,CO_2} is the continuum absorption coefficient for constituent CO_2. The latter is based on the laboratory data referred to previously (Moskalenko *et al.* 1979), which were collected at a temperature of 293 K. For a more general purpose these data were also fitted by a temperature dependent equation with the following form,

$$k_{con,co_2} \quad = \quad a \times T^n \tag{3.31}$$

where a and n are two coefficients that themselves depend on the wavelength, and T is the atmospheric temperature. Near the spectral windows at 1.7 and 2.3 μm the continuum absorption was estimated using the parameters suggested in de Bergh *et al.* (1995) and Satoh *et al.* (2009).

The continuum representation due to the H_2O molecules is implemented on the sum of self-broadening and foreign broadening components. The empirical equation that defines the continuum absorption of the water vapor is given by

$$k_{con,h_2o} \quad = \quad \sigma_s(q_{h_2o}p + \frac{\sigma_n}{\sigma_s}(1 - q_{h_2o})p) \tag{3.32}$$

(McGouldrick 2007) where σ_s is the self-broadening and σ_n is the foreign broadening component, and q_{h_2o} is the number mixing ratio of the H_2O molecule. σ_s is defined as,

$$\sigma_s \quad = \quad e^{c(T_r/T)-1}(a + be^{-\frac{b}{\lambda}}). \tag{3.33}$$

Constant	H_2O
a	0.01 cm^2/g atm
b	120.0 cm^2/g atm
c	6.08
β	0.002
$\frac{\sigma_n}{\sigma_s}$	0.002

Table 3.4: Empirical constants for water vapor continuum from Roberts *et al.* (1976) and Liou (1992).

The empirical constants at a reference temperature (T_r) of 296 K (Roberts *et al.* 1976) and the value of σ_n/σ_s (Liou 1992) are displayed in Table 3.4. For more information about these two parameterisations see McGouldrick (2007).

3.4.2 Thermal emission from an isolated layer

Within each layer the thermal emission is defined using a simple differential equation,

$$dE(\mu) \quad = \quad B(\tau')exp[-\tau'/\mu]\frac{d\tau'}{\mu}, \tag{3.34}$$

where $\mu = cos(\theta)$ (θ is the emission angle relative to the normal of the layer basis), τ the optical depth (τ' is a point in the relative scale given by τ within the layer) and $B(\tau')$ is the spectrally integrated Planck function for one spectral band. Fu (1991) and Fu & Liou (1993) suggested an exponential form to model the function $B(\tau')$,

$$B(\tau') \quad = \quad B(0)exp[b\tau'/\tau_1] \tag{3.35}$$

where $b = \ln(B_{bot}/B_{top})$ with $B_{top} = \mathrm{B}(0)$ and $B_{bot} = \mathrm{B}(\tau_{bot})$ as Planck functions for temperature at the top and bottom of the atmospheric layer. The variable τ_1 is the total optical depth of the layer.

Integrating Equation (3.34) for the entire layer in a spectral band gives us the following explicitly analytic solution for the intensity of the thermal radiation emitted in the upward direction:

$$E(\mu) \quad = \quad \frac{(B_{bot} - B_{top}exp[-\tau_1/\mu])\tau_1}{\tau_1 - \mu\ ln(B_{top}/B_{bot})}. \tag{3.36}$$

For the downward direction the equation is,

$$E^{\star}(\mu) \quad = \quad \frac{(B_{top} - B_{bot}exp[-\tau_1/\mu])\tau_1}{\tau_1 - \mu\ ln(B_{bot}/B_{top})} \tag{3.37}$$

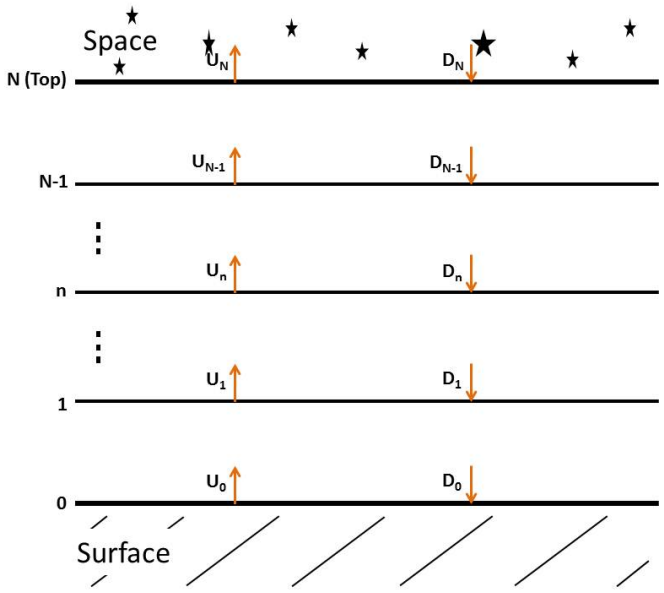

Figure 3.10: Illustration of the stacked layer atmosphere. The arrows represent the upward and downward directed intensities, which can be obtained using Equations. 3.38 and 3.39.

3.4.3 Upward and downward directed intensities

Using the thermal emission from an isolated layer described above, a simple formulation is used to obtain the upward and downward thermal intensities (U and D) at each layer interface. Fig. 3.10 illustrates the stacked layer atmosphere configuration used to compute the thermal intensities following the equations described in Lacis & Oinas 1991. The upward thermal intensity for each spectral band was obtained from

$$\begin{aligned} U_0(\mu_i) &= B(T_{gr}) \\ U_1(\mu_i) &= E_1(\mu_i) + U_0(\mu_i) exp[-\tau_1/\mu_i] \\ &\cdots \\ U_n(\mu_i) &= E_n(\mu_i) + U_{n-1}(\mu_i) exp[-\tau_n/\mu_i] \end{aligned} \tag{3.38}$$

where T_{gr} is the temperature of the ground. μ_i represents the possible different directions and the indices on U, E and τ indicate the level number (0 is the surface and N the top layer of the stack).

The equations for the downward direction are,

$$\begin{aligned} D_N(\mu_i) &= 0 \\ D_{N-1}(\mu_i) &= E^{\star}_N(\mu_i) + D_N(\mu_i) exp[-\tau_N/\mu_i] \\ &... \\ D_n(\mu_i) &= E^{\star}_{n+1}(\mu_i) + D_{n+1}(\mu_i) exp[-\tau_{n+1}\mu_i]. \end{aligned} \tag{3.39}$$

The downward long-wave intensity at the top of the model's atmosphere, $D_N(\mu_i)$, was assumed to be zero.

The upward and downward fluxes at each interface layer are the result of the angular integration of the upward and downward intensities described above. The thermal cooling rates can be obtained for each layer by computing the divergence of the fluxes that are summed for all spectral bands.

3.4.4 The diffusivity factor

The thermal intensities are evaluated for specific directions and the computation of the atmospheric cooling rates requires the integration over a hemisphere. The time spent by the integration of the radiation code can be greatly affected by the choice of the method used in the integration over the emission angle. The method adopted in this work was the diffusivity approximation in preference to other fast methods such as Gaussian quadrature (Lacis & Oinas 1991). The diffusivity approximation consists in the use of a diffusivity factor r to replace $1/\mu$ from the equations, given approximately an equivalent result to solving the angular integration. This approximation was first tested in Elsasser (1942), who suggested a value of $\sim$1.66 for r. In our work we use a diffusivity factor that depends on the optical depth of an atmospheric layer (Ramanathan *et al.* 1985). The best-fit function over the optical depth from Ramanathan *et al.* (1985) and coded in our long-wave scheme is

$$r = 1.5 + \frac{0.5}{1 + 4\tau + 10\tau^2}. \tag{3.40}$$

3.4.5 Extension to improve model stability and integration time

The vertical resolution used, in which 37 levels cover 100 km of the atmosphere (OPUS-Vr resolution), combined with Venus's deep atmospheric conditions (high pressure and temperature) causes some instabilities when integrating the radiation scheme in time as implemented

in a 1D radiative-convective model (1D R-CM). The problems were identified in the model's results as local spurious peaks in the temperature profile. The main cause of these sudden changes of temperature is related to the inability of the long-wave scheme to estimate accurately the thermal emission at the middle of the optical thick layers when computing the emission intensities. In order to improve this parameterisation, the layers are further divided into two equally optical thick parts within which the thermal emission intensities are computed separately.

The model also has the option to reduce the number of spectral bands automatically in the long-wave code. This process is done by binning the spectral bands defined in the k-tables. Later in this chapter we conduct a sensitivity study to investigate the impact of this option on the final steady state temperature profiles.

An explicit numerical integration of the Planck function is not suitable for GCM studies due to time constraints and it was therefore replaced by a linear numerical interpolation in temperature from a predefined table. The data stored contains the values of the integral for all spectral bands used and over a range of temperatures that covers the Venus atmospheric conditions. A large number of experiments we carried out using this interpolation showed that the implicit error of this procedure is very small, and does not compromise the accuracy of the long-wave scheme. When implemented in the GCM it improves significantly its integration time.

Thus, the thermal radiation code developed is fast and the trade-off between speed and accuracy can be adjusted, which makes it very suitable for climate studies.

3.4.6 Reference radiative fluxes

Some examples of the computed net upward thermal flux in the mesosphere is shown in Fig. 3.11. The three different lines here obtained are based on a radiative-convective equilibrium temperature profile but with different cloud distributions. The temperature profile was obtained using the 1D R-CM (radiative-convective model presented in the next section 3.5) for the reference case. The three cases represent the reference profile (solid line); 50% less clouds (dashed line) and finally no clouds (solid line with circles). Reducing the aerosol densities allows more thermal flux from the deep layers in the atmosphere to reach the upper parts, increasing the infrared flux emitted to space. Despite the atmosphere's higher loss rate of thermal energy, the reduced atmosphere actually increases its temperature, as it will be shown in the next section 3.5. This phenomenon is caused by the lower efficiency of

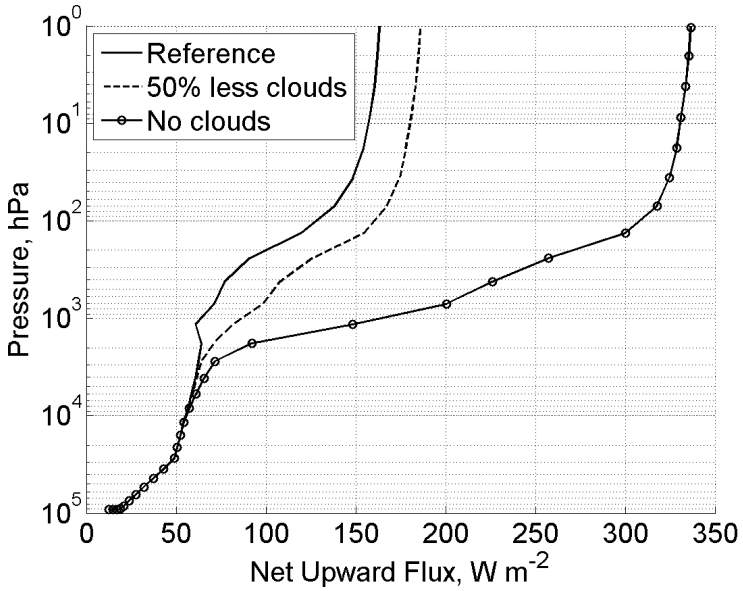

Figure 3.11: The net upward infrared fluxes for three atmospheric conditions: reference (solid line), less 50% of aerosols (dashed line) and no aerosols (solid line with circles)

the less dense clouds in reflecting incoming solar energy back to space, which is consequently absorbed radiation more strongly in the lower regions of the atmosphere plus the surface.

The solid line in Fig. 3.11 represents a radiative-convective equilibrium net upward flux profile. The $\sim$ 165 W/m^2 at the top model domain is close to the globally averaged solar radiation absorbed by the atmosphere ($\sim$ 163 W/m^2, calculated in section 3.3). The same happens at the surface where the small amount of net absorbed solar energy flux by the surface ($\sim$ 28 w/m^2) is balanced by the net upward infrared flux.

Data from observational missions (Revercomb *et al.* 1985) suggests a net upward infrared flux profile with smaller values in the lower atmosphere. The larger values in the thermal upward fluxes simulated is mainly due to the hotter lower atmosphere obtained by the 1D R-CM compared with the estimated values from the observational data. However, in this simulation, the surface temperature is 750.5 K, in good agreement with Lee & Richardson (2011).

The radiative cooling rate of the atmosphere is obtained from the differentiation of the frequency-integrated net radiative infrared flux with pressure, and has roughly the same magnitude as the heating due to insolation at the radiative-convective equilibrium state. The small decrease at $\sim 10^3$ hPa in the net upward flux profile is related to the position

of the clouds which block a large part of the upwelling thermal radiation that comes from the deep atmosphere. As a consequence of the positive net radiative heating, there is a tendency for the formation of convectively unstable cells in this region. A qualitatively good representation of the cloud distribution effect on the thermal structure of the atmosphere is important to understand the role of clouds in the atmospheric circulation.

A more complex version of the thermal radiation parameterisation taking into account the scattering effects in the atmosphere (though more expensive in terms of computational time), could be done using the same scheme from section 3.3.2 (δ-Eddington code) and adding a thermal source function in each layer (Bell *et al.* 1991). Despite this alternative parameterisation being more complete than the one presented here, we do not explore that method in this work.

3.5 1D radiative-convective model

We then implemented the new radiation code in a 1D radiative-convective model (1D R-CM), which calculates the radiative equilibrium temperature profile with convective adjustment where the lapse rate becomes super-adiabatic. The time step used was 1.5 hr, which is smaller than the radiative relaxation time in the Venus mesosphere and guarantees the stability of the model. In all the simulations to obtain the radiative-convective equilibrium temperatures, the radiative equilibrium temperature profile, obtained without convection, was used as input. Thermal equilibrium was reached when the temperature tendency in each model layer becomes small and the surface temperature does not change by more than 0.001% for a period of 10 Venus solar days.

The radiative solar forcing in the 1D R-CM is obtained by globally averaging the solar heating profiles obtained for each zenith angle from the solar radiation code. The equation used has the following form,

$$\frac{dT}{dt}(p) = \frac{1}{2}\int_0^{\frac{\pi}{2}} \frac{dT}{dt}(\theta_z, p) sin(\theta_z) d\theta_z, \tag{3.41}$$

where θ_z is the solar zenith angle. The integral was evaluated using a Gauss-Legendre quadrature method, 8 point rule.

3.5.1 Method of convective adjustment

As was mentioned before, in this work the values of the Venus atmospheric specific heat capacity at constant pressure (c_p) are calculated following Equation (3.27). Some fundamental thermodynamic variables need to be redefined from their typical format if the dependence of c_p with temperature is taken into account (for Earth studies, constant c_p is a good approximation). For example, in Lebonnois *et al.* (2010a) the potential temperature is derived using Equation (3.27), giving the following result

$$\theta^{\nu} = T^{\nu} + \nu T_0^{\nu} \ln(\frac{p_{ref}}{p})^{k_0} \tag{3.42}$$

where the constants ν, $k_0 = \frac{R}{C_{p0}}$ and T_0 are the same as in Equation (3.27). In this work, the variable $c_p(T)$ was taken into consideration for the development and improvement of the parameterisations in the OPUS-Vr (see next chapter).

One of the new parameterisations developed was in the application of convective adjustment, which is the same in both the 1D R-CM and OPUS-Vr. This scheme consists in adjusting the atmospheric lapse rate ($\partial T/\partial z$, T absolute temperature; z - altitude) to the dry adiabatic lapse rate (g/c_p, g - gravitational acceleration) whenever the value of the former exceeds the value of the latter during the model integration (natural upward convection). For conventional Earth-type convection schemes, a constant value of c_p is usually assumed. This is a good approximation for the Earth but is not appropriate for Venus conditions. The scheme developed here mixes the potential temperature of an unstable column ($\delta\theta/\delta p > 0$, taking in consideration Equation (3.42) in a dry atmosphere while also conserving the total specific entropy,

$$\bar{\theta} = \left(\frac{\int_{p_{bot}}^{p_{top}} \theta^{\nu} \Delta p}{\int_{p_{bot}}^{p_{top}} \Delta p} \right)^{1/\nu} \tag{3.43}$$

where ν is a parameter from Equation (3.42), and p_{top} and p_{bot} are the pressures at the top and bottom of the unstable column.

3.6 Global-mean radiative-convective equilibrium temperatures

The results of the global-mean radiative-convective equilibrium temperatures are divided in four parts. In the first part are presented the results of the reference simulation. The other

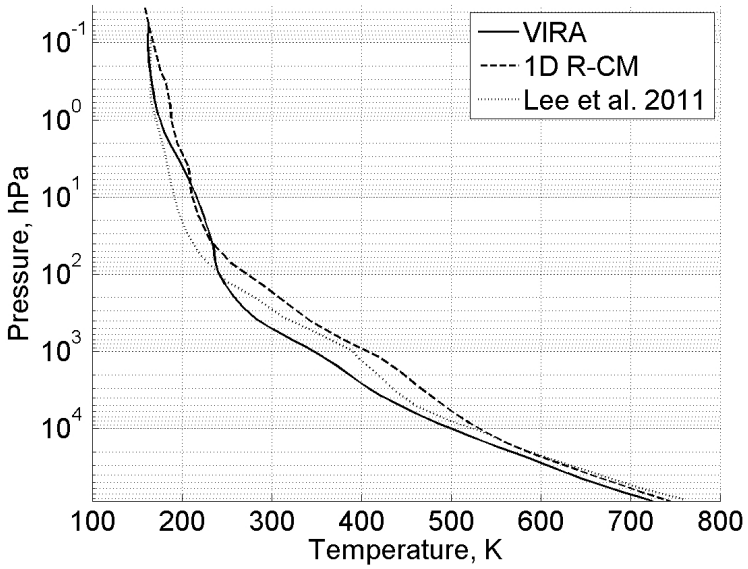

Figure 3.12: Comparison between the VIRA temperature profile, the results in Lee & Richardson (2011) and the result obtained by the 1D radiative-convective model using the reference atmospheric conditions.

three parts are three experiments to study the final temperature profile when cloud amount and atmospheric conditions near the surface (assumed to be made of basalt) are changed, and finally to explore the effect of the reduction of the number of spectral bands in the long-wave scheme.

3.6.1 Reference radiative-convective temperature profile

Fig. 3.12 shows two temperature profiles: VIRA temperature profile and the reference profile obtained by the 1D R-CM. The VIRA profile is an average of temperature profiles from observational retrievals at five latitudes above $\sim 5.8 \times 10^3$ hPa (0-30°, 45°, 60°, 75° and 85°) and just a single profile below this pressure level (Kliore *et al.* 1985). The uncertainties in the deep atmosphere are large and even some regions of the VIRA profile are superadiabatic. The differences between these two profiles are clear in the lower atmosphere, where the one obtained by the model is hotter than the one estimated in the VIRA profile. A pressure level of roughly 100 hPa, separates two regions: above with small temperature gradients (statically stable atmosphere) and large temperature gradients below this level (nearly adiabatic atmosphere).

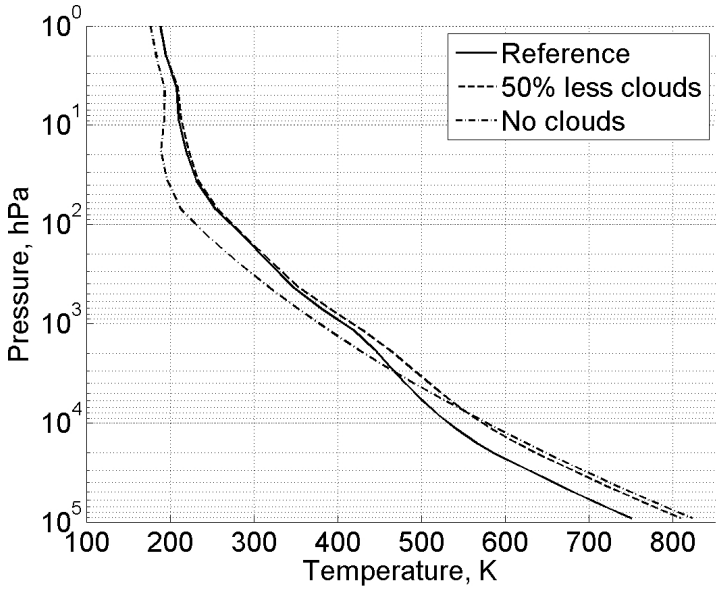

Figure 3.13: Comparison between the reference 1D radiative-convective temperature profile (solid line) and a simulation with less 50% of clouds (dashed line) and other with no clouds (dotted line).

This result is consistent with the work from Lee & Richardson (2011), who used a more complex radiative transfer code but the same gas k-tables. That code uses a two-stream flux solver (TWOSTR, Kylling *et al.* 1995) combined with a multiple-stream multiple scattering **DIS**crete **O**rdinate **R**adiative **T**ransfer model (DISORT, Stamnes *et al.* 2000). The integration explored in that work is too computationally expensive for use in a GCM, unless the spatial and spectral resolution of the model is much reduced. In Fig. 3.12 we show a temperature profile obtained in Lee & Richardson (2011) with the same vertical resolution used in this work. The results show temperature differences never larger than 5% for all altitudes and also similar surface temperatures - our code obtains 751 K and their model 757K.

3.6.2 Different cloud amounts

Fig. 3.13 shows three different profiles to study the influence of cloud amount (three aerosol modes and the UV absorber): solid line is the reference simulation, the dashed line has less 50% of clouds and the dotted line does not have any clouds.

Reducing the cloud amount clearly affects the temperature of the deep atmosphere,

where the temperatures obtained can be hotter than 800 K. The main factors affecting these results are related to the amount of solar radiation passing through the clouds and reaching the deepest regions of the atmosphere (a reduction of the UV absorber has a very important impact).

The clouds warm the Venus mesosphere and this effect is clearly visible if we compare the profiles which include clouds with the "clear-sky" profile (dotted profile). Upon reducing the cloud amount, the absolute lapse rate in the region between 10^4 and 10^3 hPa becomes steeper, which is due to the reduced efficiency of the cloud base in blocking the radiation from the deep atmosphere. Above this region, in the two cases with clouds, the static stability decreases again and is more likely to initiate upward convection. In the case with no clouds the lapse rate is roughly constant from near the surface until a pressure level of 100 hPa, which clearly defines an extended tropospheric region.

3.6.3 Different atmospheric conditions near the surface

The atmospheric conditions near the surface and surface optical properties are poorly constrained from observations. We therefore explore the sensitivity of the thermal structure to these factors in the 1D R-CM. Fig. 3.14 shows five different profiles obtained for five different surface albedos in the short-wave radiation scheme. Upon increasing the albedo, the surface reflects more solar energy and consequently less solar energy is absorbed by the surface. This change could be associated not just with different optical properties of the surface but also with different representations of atmospheric extinction processes near the surface. The use of a large albedo in this scheme is roughly equivalent to a correction in the radiation code for the poor representation either of the radiative extinction in the extreme deep atmospheric conditions, or of the possible existence of extra missing constituents of the atmosphere that interact with solar radiation, such as for example, a thin cloud deck near the surface.

The main difference in the profiles is near the surface where the profile with $\alpha = 0.95$ results in a cooler surface (736 K). Using this value the absorbed spectrally-integrated and globally-averaged solar flux is roughly 153.6 W/m^2. This corresponds to a bolometric albedo of 0.778, which is still close to the values estimated from observations: e.g. $0.76^{+0.02}_{-0.03}$ from Taylor *et al.* (1980), 0.75±0.03 from Moroz (1983) or 0.76±0.01 from Moroz *et al.* (1985).

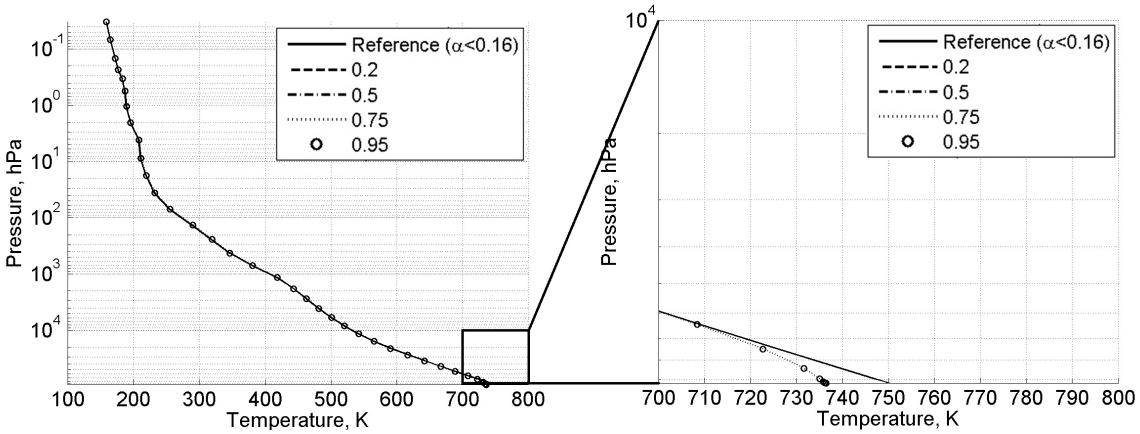

Figure 3.14: Comparison between the reference 1D radiative-convective temperature profile (solid line) and simulations with four different albedos for the short-wave code: 0.2 (dashed line), 0.5 (dash-dotted line), 0.75 (dotted line) and 0.95 (circles).

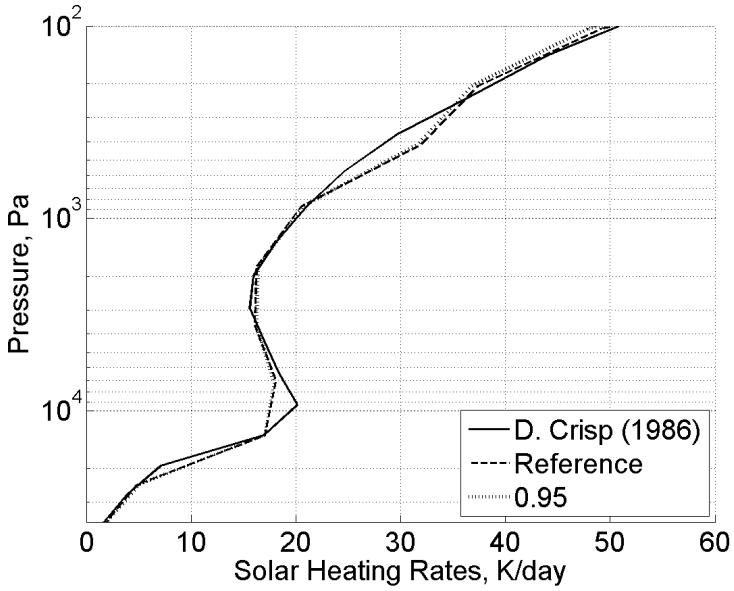

Figure 3.15: Comparison between the heating profile obtained in Crisp (1986) (solid line), the one from the reference simulation (dashed line) and using an high surface albedo of 0.95 (dotted line).

Fig. 3.15 shows that the heating rates in the Venus mesosphere do not change significantly when the surface albedo is increased, since the dashed line (reference simulation) and dotted line (using high albedo) are almost indistinguishable from each other.

The profile obtained with $\alpha = 0.95$ represents a more statically stable atmosphere in the deepest region, and the influence of this atmospheric condition will be explored later with the OPUS-Vr. The stability of the atmosphere near the surface will be important for the formation and maintenance of a realistic mesospheric super-rotation as will be shown in the next chapter.

3.6.4 Reducing the number of long-wave spectral bands

The long-wave radiation code allows the user to define the number of spectral bands used in the integration. Upon reducing the number of bands, the accuracy of thermal heating rate calculation is also reduced but the code becomes faster.

This option can be a great advantage for running the code in a GCM, which may require integrating the radiation code for thousands of different horizontal locations per timestep. In the development of a GCM the relative weight between accuracy and integration time needs to be considered. An optimal approximation must be taken which does not compromise both sides.

Fig. 3.16 shows four temperature profiles: the black solid line is the VIRA profile, the red line is the reference simulation, and the spectral resolution used to obtained the blue and green lines was degraded. A four band binning is represented by the blue line, while the green line indicates an eight band binning. Reducing the number of spectral bands mainly increases the opacity of the lower atmosphere (by increasing the gas absorption) and less thermal energy is transmitted upward from the deepest regions of the atmosphere and absorbed in the cloud region.

In the remaining chapters of the thesis the option chosen for the OPUS-Vr integrations was the four bands binning, which boosts by four the speed of the long-wave code. As has been pointed out in several parts of this chapter, the atmospheric conditions in the lower atmosphere are poorly constrained, and increasing artificially the gas absorption in the lower atmosphere seems to match the VIRA data and the results from Lee & Richardson (2011) more closely. Another point is that some radiation extinction (such as scattering processes) is neglected by the long-wave code, which can justify the technical slight increase of the optical depth.

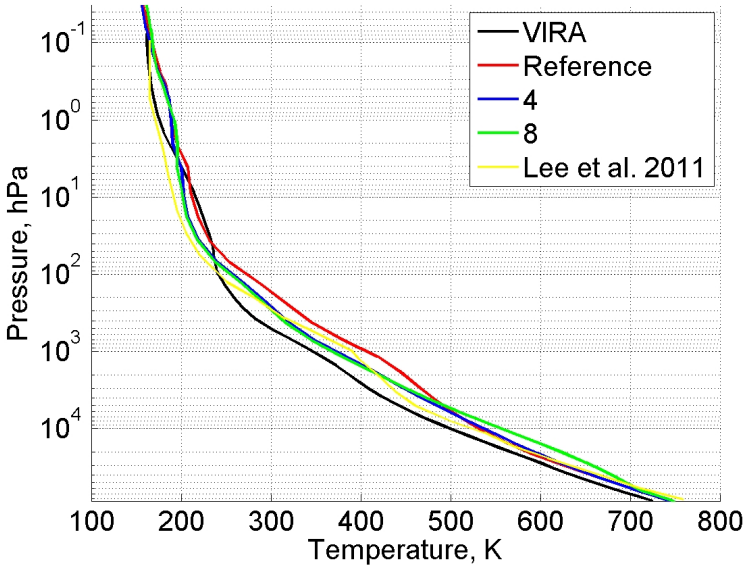

Figure 3.16: Comparison between the VIRA profile (solid line) and simulations with different number of long wave bands: reference simulation (original number of bands, dashed line), binning using four spectral bands (dash-dotted line) and binning using eight bands (dotted line).

3.7 Conclusions

In this chapter I presented a flexible and fast single-column radiative transfer model for the atmosphere of Venus that is suitable for GCM applications. The scheme developed simulates realistically the mean thermal structure of the extreme Venus climate for the region between 0-100 km. The greenhouse effect maintains the surface temperature very high (∼750 K), and is well represented in all the simulations. The observationally poorly constrained deep atmosphere is hotter in the simulations than in the results estimated from the VIRA profile. Despite these differences, the results in this region are consistent with the results obtained by Lee & Richardson (2011), who used a more complex radiative transfer model but based on the same k coefficients.

In the upper atmosphere (above the pressure level of 100 hPa) the temperature differences between the VIRA profile and the results obtained decreased, despite some uncertainties related to the atmospheric composition and structure in this region, such as the cloud distribution. It is important to simulate realistically the radiative properties in this region since it is associated with an active radiative-dynamical region where, for instance,

the thermal tides have an important role.

The code has a structure which allows one to easily change the atmospheric conditions or integration parameters, such as the number of spectral bands. The cloud amount is known to have an important role in controlling the surface temperature and the lapse rate in the atmosphere. Less cloud mainly causes an increase of the surface temperature and the absolute atmospheric lapse rate near/below the cloud base.

The atmospheric static stability near the surface is largely governed by the amount of solar radiation that is absorbed by the surface. The uncertainty in optical extinction components in the atmosphere, which is large in the deep atmosphere, makes a realistic quantification of the value of solar radiation absorbed unclear. For the cases studied, the changes in the surface albedo in the short-wave scheme resulted in almost identical final temperature profiles, because it corresponds to only a small change in the amount of solar radiation that is absorbed by the surface, $\sim 4\%$ of the incoming solar radiation using the reference input. However, if the albedo is increased to 0.95, the surface temperature cools and the percentage of incoming solar energy absorbed by the surface is reduced to $\sim 1\%$ (cf. 2.5% in Tomasko *et al.* 1980). This configuration of the atmosphere is also associated with less active convection near the surface, an aspect which will be explored later by the OPUS-Vr with the aim of studying its effect on the global circulation.

The option to change the number of spectral bands used in the integration of the long-wave scheme affects the accuracy of the results and the speed of integration (it is faster for smaller numbers of bands). The gas absorption in the lower atmosphere is very sensitive to changes in the spectral resolution. Upon decreasing the number of spectral bands, the deep atmosphere becomes more opaque and reduces the upward thermal radiation flux from this region that reaches the clouds. The OPUS-Vr simulations presented in the next chapters use a four component spectral binning of the reference resolution defined in the k-tables.

This parameterisation, based on a radiative transfer formulation, gives a much more realistic picture of the radiative energy exchange in the atmosphere than the Newtonian cooling approach used in the OPUS-Vs. This improvement in OPUS-V is essential to get simulations of the atmospheric circulation closer to the real Venus atmospheric conditions.

The radiative transfer formulation developed here is more flexible to adapt to different atmospheric conditions than the one developed for the LMD Venus GCM (Eymet *et al.* 2009 and Lebonnois *et al.* 2010a). The main advantages of the new scheme are the explicit calculation of the solar fluxes and the easy adaptability to different optical structures. This

flexibility is appropriate for GCM studies, and allows for the exploration of, e.g., active cloud transport feedback in the atmospheric circulation. The thermal radiation code of the LMD model also has problems in producing realistic surface temperatures when implemented in the GCM. The LMD code needs to multiply the magnitude of the collision-induced absorption coefficients of CO_2 by an empirical factor (a factor of six represents the best adjustment) to produce surface temperatures larger than 700 K, which was not the case in the new code presented in this chapter.

The convection scheme developed in this chapter will be also implemented in the OPUS-Vr. It is a dry convection adjustment formulation and takes into account the dependence of the c_p with temperature, which is significant in the region of the Venus atmosphere studied here.

4

OPUS-Vr

4.1 Summary

This chapter presents the technical details of the new version of the Oxford Planetary Unified (Model) System for Venus (OPUS-Vr) that includes a radiative transfer formulation. This model is an expansion and improvement of the earlier simplified version (OPUS-Vs, Lee 2006; Lee *et al.* 2007). New parameterisations more suitable to simulate the extreme Venus climate were developed and implemented, such as: a new radiation scheme for the solar and thermal spectral regions, a new convection scheme, a physically-based boundary layer scheme and a modified dynamical core, which takes into account the dependence of the atmospheric heat capacity with temperature at constant pressure.

In the following sections the new parameterisations and the main changes from the original Earth GCM are described.

4.2 Introduction

The model developed for this work is based on version 4.5.1 of the UK Meteorological Office Portable Unified Model (UM). This Earth GCM is not the most recent version of the UK Met Office GCM at the time of writing but it was used in the past with success in numerical Earth weather prediction and for Earth climate research (e.g., Reichler & Kim 2008; Stott *et al.* 2000). The structure of the model is divided into two main sections: a dynamical core and a library of physical parameterisations. Physical processes such as radiation transfer, convection and boundary layer processes are modelled in parameterisations included in the

physics section. In the dynamical section the atmospheric fluid motion is treated explicitly by solving the primitive equations.

To adapt a complex model to the Venus conditions, the first step was to change the main planetary parameters such as: the rotation rate, planetary radius, acceleration due to gravity, planetary obliquity and surface pressure. These parameters are displayed in Table 1.1 and were first tested during the development of the simplified version, see Lee (2006) and Lee *et al.* (2007).

The next two sections describe the main changes in the dynamical core from the OPUS-Vs and present the details of the new physical parameterisations.

4.3 Dynamical Core

The dynamical core contains a numerical formulation that solves the nonlinear differential equations (primitive equations), which describe the global atmospheric flow. Based on a finite-difference formulation, the dynamical equations used in this work were derived from White & Bromley (1995), who solved the Navier-Stokes equations in a rotating spherical configuration using some less drastic approximations than is common for the meteorological primitive equations such as neglecting the metric and the cosine Coriolis terms ("traditional approximation"). The method suggested does not assume a shallow atmosphere approximation but replaces the planet radius by a "pseudo-radius" which varies with the geopotential height.

The primitive equations from White & Bromley (1995) are integrated using a split-explicit scheme on an Arakwa B grid (Arakawa 1977). This type of horizontal discretisation is formed using two grids with the same horizontal resolution and equally spaced in longitude and latitude, but arranged in such a way that they are offset by half a cell. The two grids are called the pressure and velocity grids. The pressure grid stores prognostic variables such as the temperature and geopotential height; while the velocity grid stores the zonal and meridional components of the horizontal wind. The model has the option of rotating the GCM grid, but in our simulations the poles of the GCM grid are set to be coincident with the geographical poles and arranged so that the poles are pressure points, avoiding the need for representation of wind directional components stored at the polar singularity. At the nearest row to the poles, the prognostic variables are updated using the neighbouring rates computed by the different parameterisations in the physical and dynamical cores. The

horizontal resolution is maintained from the OPUS-Vs as $5^\circ \times 5^\circ$, which was thought to be enough to resolve the important large eddies that transport momentum towards the equator (chapter 1).

The vertical coordinate η is hybrid, defined as a combination of sigma and pure pressure coordinates. The user may set the specific values for η at intermediate levels and also defines the nature of the coordinates in the model's interface, which are then used to calculate the respective $A_{k-\frac{1}{2}}$ and $B_{k-\frac{1}{2}}$ needed to compute the pressure at half-levels:

$$P_{k-\frac{1}{2}} = A_{k-\frac{1}{2}} + B_{k-\frac{1}{2}} \times p_s, \tag{4.1}$$

where the index k indicates a specific layer of a vertical column and p_s is the surface pressure. The lowest half-level pressure corresponds to the surface pressure where $A_{\frac{1}{2}} = 0$ and $B_{\frac{1}{2}} = 1$. To compute at full levels, the A_k and B_k are interpolated in the GCM. The vertical coordinates used here are based on the ones from the OPUS-Vs. The 37 layers cover the atmosphere from the surface up to an altitude of roughly 100 km with a maximum vertical spacing of 3.5 km. Table 4.1 lists the pressures at the centre of each layer and their approximate altitudes in kilometres. The pressure values at full levels are defined for each horizontal point as a function of surface pressure ($p_\star$) and of the constants A and B, and is similar to the equation for intermediate levels:

$$P_k = A_k + B_k \times p_s. \tag{4.2}$$

For the OPUS-Vr the vertical coordinates are terrain-following below layer nineteen and pure pressure levels above this layer ($B = 0$, see the smooth transition in Table 4.1). At the top and bottom (surface) of the model's domain, a vertical boundary condition is used which imposes a zero vertical velocity ($\dot{\eta} = 0$).

The time-step for dynamics in OPUS-Vr was typically five minutes. Next I describe the main changes in the original dynamical core, which was adapted to include the significant dependence of the specific heat capacity (c_p) of the Venusian air with temperature. More details on the Unified Model dynamical core used here can be found in Cullen *et al.* (1992).

4.3.1 The integration scheme

The integration of the equations in the dynamical core consists of two main steps: 1) adjustment; 2) advection. Below I describe briefly the two schemes and the main adaptations to the original formulation.

Level	A (hPa)	B	Pressure (hPa)	Altitude (km)	K ($\times 10^9$)
1	0.050	0.9995	9.19×10^4	0.07	2.0
2	0.13×10	0.9970	9.17×10^4	0.1	2.0
3	0.11×10^2	0.9904	9.11×10^4	0.2	2.0
4	0.87×10^2	0.9720	8.95×10^4	0.5	2.0
5	0.85×10^3	0.9041	8.40×10^4	1.5	2.0
6	0.30×10^4	0.7787	7.47×10^4	3.3	2.0
7	0.64×10^4	0.6284	6.43×10^4	5.6	2.0
8	1.0×10^4	0.4744	5.38×10^4	8.2	2.0
9	1.3×10^4	0.3354	4.39×10^4	11.1	2.0
10	1.5×10^4	0.2224	3.50×10^4	14.2	2.0
11	1.5×10^4	0.1384	2.74×10^4	17.5	2.0
12	1.4×10^4	0.0806	2.10×10^4	20.9	2.0
13	1.2×10^4	0.0437	1.58×10^4	24.4	2.0
14	0.96×10^4	0.0218	1.16×10^4	27.9	2.0
15	0.75×10^4	0.0097	0.84×10^4	31.5	2.0
16	0.56×10^4	0.0038	0.59×10^4	35.0	2.0
17	0.40×10^4	0.0010	0.41×10^4	38.6	2.0
18	0.28×10^4	0.0002	0.28×10^4	42.2	2.0
19	0.18×10^4	0.0	0.18×10^4	45.9	2.0
20	0.12×10^4	0.0	0.12×10^4	49.6	2.0
21	0.71×10^3	0.0	0.71×10^3	53.2	2.1
22	0.42×10^3	0.0	0.42×10^3	56.8	2.2
23	0.24×10^3	0.0	0.24×10^3	60.2	2.3
24	0.13×10^3	0.0	0.13×10^3	63.6	2.5
25	0.71×10^2	0.0	0.71×10^2	67.0	2.7
26	0.36×10^2	0.0	0.36×10^2	70.5	2.9
27	0.18×10^2	0.0	0.18×10^2	74.1	3.1
28	0.87×10	0.0	0.87×10	77.6	3.3
29	0.42×10	0.0	0.41×10	81.0	3.5
30	0.20×10	0.0	0.20×10	84.1	3.8
31	0.10×10	0.0	0.10×10	86.9	4.1

Level	A [hPa]	B	Pressure [hPa]	Altitude [km]	K ($\times 10^9$)
32	0.56	0.0	0.56	89.2	4.4
33	0.34	0.0	0.33	91.2	4.7
34	0.23	0.0	0.23	92.5	5.0
35	0.15	0.0	0.14	94.2	5.3
36	0.067	0.0	0.068	97.1	5.9
37	0.032	0.0	0.032	99.0	6.5

Table 4.1: Vertical discretisation of the OPUS-Vr. The full level pressure values were obtained using the surface pressure equal to 92 bar (1 bar = 10^5 Pa).

4.3.1.1 Adjustment step

This routine uses a forward-backward explicit formulation. In the forward step the horizontal wind fields are computed. The equations used in this scheme to update zonal wind velocity and the geopotential height were changed from the original structure to take into account the variation of c_p with temperature (these two equations depended explicitly on a constant c_p).

The iterative step n for the wind in the zonal direction, u, is obtained using the following equation:

$$\begin{aligned} u_k^{n+1} &= u_k^n + \delta t\Big[\frac{1}{2}F^n(v_k^n + v_k^{n+1} - \\ &\quad \frac{1}{r_s\cos\phi}\overline{\{\delta_\lambda\Phi_k + R\overline{(T+\mu T_s)_k}^{\lambda}\delta_\lambda[\ln p_k]^n\}}^{\phi}\Big]. \end{aligned} \tag{4.3}$$

The notation used here is the same as from Cullen *et al.* (1992): k is the index of the respective pressure layer, δt is the time step, F is a source term that includes the diffusion, v is the wind speed in the meridional direction, λ is latitude, ϕ is longitude, R is the dry gas constant, T_s is the basic state temperature, r_s is the pseudo-radius and Φ the geopotential height. μ is defined as,

$$\mu = \frac{f_2 u - f_1 u + \frac{u^2+v^2}{r_{s0}}}{g} \tag{4.4}$$

where g is the planetary gravitational acceleration and f_1 and f_2 are Coriolis terms defined by

$$f_1 = -2\Omega\sin\lambda\cos\phi_0, \tag{4.5}$$

$$f_2 = 2\Omega \cos\phi \sin\phi_0 - \sin\phi \cos\lambda \cos\phi_0. \tag{4.6}$$

In Eqs. 4.5 and 4.6, λ and ϕ are the longitude and latitude in spherical coordinates, λ_0 and ϕ_0 are the longitude and latitude of the coordinate pole set by the user (related with the rotating GCM grid option), and Ω is the rotation rate of the planet. The geopotential height is computed from the dry hydrostatic equation which was also changed from its original form. The new formulation solves the approximated hydrostatic equation from

$$\Phi_k = \Phi_\star - \sum_{m=1}^{k-1} R(T_m + \mu T_s)(\ln p_{m+\frac{1}{2}} - \ln p_{m-\frac{1}{2}}) + R(T_m + \mu T_s)(\ln p_{k-\frac{1}{2}} - \ln p_k) \tag{4.7}$$

where $\Phi_\star$ is the value of the geopotential height at the surface.

In the backward part the equations were not changed, and the variables such as the potential temperature and surface pressure are updated using the new values obtained in the forward method.

4.3.1.2 Advection step

In this part the wind fields are updated from the nonlinear advection terms following a fourth-order Heun conservative advection scheme (Mesinger 1981). The winds obtained in the adjustment step part are used in this routine to calculate the horizontal advection. The computation of the vertical advection is based on the continuity equation. In this routine there was no need to change the formulation of the equations due to the dependence of c_p with temperature.

The Exner function which converts absolute temperature into potential temperature in several parts of the GCM code was replaced by Eq. 3.42. More details concerning the integration scheme can be found in part 3 of Cullen *et al.* (1992).

4.3.2 Numerical Stability

The formulation of the numerical equations was done assuming appropriate approximations which may allow unphysical solutions. These difficulties potentially compromise the numerical stability of the simulations.

To ensure numerical stability from the explicit integration scheme presented (adjustment and advection steps) the Courant-Friedrichs-Lewy (CFL) stability criterion must be satisfied. This is a necessary condition for convergence of the numerical solution that requires the time-step to be shorter than the time for a wave or air parcel to travel between adjacent

grid points (determined by the gravity wave speed in the adjustment step and the wind values in the advection step). Upon refining the horizontal resolution, the upper limit for the time-step also decreases. The GCM has a Fourier filter implemented to avoid the use of very short time steps constrained by the CFL condition at high latitudes, where the longitudinal horizontal resolution in spatial units becomes much finer. This scheme filters (by Fourier damping) any zonal winds that violate the CFL condition for a particular latitude. The filter routine requires two values to be set by the user: the external gravity wave speed and a filtering safety multiplying factor. These values are used to define the minimum threshold for the filtering. In OPUS-Vr these values are the same as those used in the simplified version (Lee 2006): 1500 m s^{-1} and 0.33 respectively.

Another numerical routine present in the GCM to ensure the stability of the model is the horizontal numerical diffusion. This routine is needed to control numerical noise and to qualitatively represent the physical phenomena of turbulence and eddy viscosity on the sub-grid scale. This scheme is applied to the entire model domain, and filters the variables u, v and θ. This procedure is carried out for each vertical level and the amount of diffusion is dependent on two values set by the user: the order of diffusion (j) and the coefficient that determines strength of diffusion (K). As in the Fourier filtering the values chosen for this parameterisation are the same as the ones used for the OPUS-Vs, which were extensively explored in Lee (2006). The value of j chosen is equal to three, which means sixth order diffusion,

$$D^3(X) = D(D(D(X))), \tag{4.8}$$

where D is the conservative second order filter and X is the variable filtered. The option chosen, $j = 3$, diffuses more at short spatial scales than the other two options present in the model (see Cullen *et al.* 1992 for more details about the operator). The K coefficients, which are related to the strength of the diffusion used for each vertical level are shown in Table 4.1. K is constrained by a numerical stability criterion for the diffusion scheme which follows equation

$$\Delta t(\frac{4K}{{r_T}^2 \Delta\phi^2})^j \leq 1. \tag{4.9}$$

From this equation, K needs to be tuned for changes in horizontal resolution ($\Delta\phi$), planet radius (r_T), time-step (Δt) and order of diffusion (j). An inappropriately strong diffusion can make fine atmospheric structures disappear, so the optimal values should be just large enough to ensure a stable model integration (preventing the growing of instabilities).

4.4 Physical Core

The physical routines force the flow motion of a particular atmosphere to follow its planetary conditions. In comparison with the HadCM3, all the original physical parameterisations were removed except the boundary layer scheme which was adapted to the Venus conditions. These schemes, coupled with the dynamical core described in the previous section, simulate the atmospheric circulation of a dry atmosphere. The surface pressures are set to the Venus values to represent the huge, massive atmosphere in comparison with the Earth's case. In this model, the values displayed in Table 1.1 were implemented. Weak seasonal variations were neglected upon setting the declination angle to zero.

The new version is more complex and complete than the OPUS-Vs version (see chapter 1). Only the sponge layer parameterisation that acts at the top of the model's domain was maintained from the old version (Lee 2006). The physical time-step used in the simulations that will be presented next is ten minutes, which is the same as the one used for the OPUS-Vs simulations presented in Lee (2006) and in chapter 1. In the next sub-sections I describe the new physical parameterisations developed for OPUS-Vr.

4.4.1 Soil model

The OPUS-Vr includes a simplified parameterisation to simulate the evolution of the temperatures in the subsurface. The surface temperature is also affected by this formulation due to the interchanges of thermal conduction in the soil. The conduction equation that is used to update the temperatures is

$$\frac{\partial T}{\partial t} = \frac{1}{C}\frac{\partial}{\partial z}(-\lambda\frac{\partial T}{\partial z}), \tag{4.10}$$

where C is the specific heat per unit volume and λ is the soil conductivity. The soil thermal inertia ($\mathrm{I} = \sqrt{\lambda C}$) used is equal to 2200 $Jm^{-2}K^{-1}s^{-\frac{1}{2}}$ which corresponds to a basalt soil (Rees 1999).

The parameterisation uses also a multilayer soil formulation (ten layers) that was developed by Warrilow *et al.* (1986), and produces accurate results for responses to variations of the temperature forcing at the surface. The code for this routine was adapted from the Oxford Mars GCM code but it was first developed and tested for the LMD Mars GCM (Hourdin *et al.* 1993).

4.4.2 Boundary Layer

The Rayleigh friction parameterisation used in OPUS-Vs to represent the mechanical interaction between the surface and the atmosphere is replaced in this new version by a more physically-based scheme. The code used in OPUS-Vr is an adaptation of one of the schemes available in the HadCM3 for the Earth (Smith 1993a and Smith 1993b). This boundary layer scheme is based on a bulk transport turbulent mixing parameterisation (Jacobson 2005). This code was already explored under Venus conditions by Lee (2006), but here the parameterisation was revised and adapted to take into account the variations of the atmospheric c_p with temperature (e.g., in the computation of the layer depths). Further improvements are related to the direct interaction of this code with the radiative transfer model and the use of the surface thermodynamic properties from the simplified soil model described above. Below, I describe very briefly this parameterisation. More details concerning the boundary layer model and scientific description can be found in Smith (1993a) and Smith (1993b).

The newly adapted boundary layer parameterisation computes in three steps the turbulent fluxes of heat and momentum between surface and atmosphere and/or between the atmospheric levels within the boundary layer active region. The first step in this scheme is to calculate the heights of the boundary layer. These values are limited by the maximum number of model layers set for this routine, which is ten for the simulations presented in this work, or by the height where the bulk Richardson number is equal to one. The dimensionless bulk Richardson number represents the ratio of buoyancy to vertical shear, and is calculated using

$$R_i = \frac{g\Delta z(\Gamma_d(\bar{T}) - \Gamma)}{\bar{T}[(\Delta U)^2 + (\Delta V)^2]}, \tag{4.11}$$

where g is the acceleration of gravity, $\Gamma_d(\bar{T})$ and Γ are the dry adiabatic and the current lapse rates, $\bar{T}$ is the mean temperature of the layer, Δz is the difference in height, and ΔU and ΔV are the variations in height of the zonal and meridional wind speed in the layer. Γ_d depends on temperature due to the variation of c_p with temperature (see chapter 3).

In the second step the surface fluxes are computed, based on the idea that between the lowest model level and the surface, the wind speed and temperature must relax to zero and to the temperature surface values, respectively. The mixing of momentum under neutral (R_i values close to zero) or non-neutral atmospheric conditions in the boundary layer is done using different methods. In neutral conditions, the surface flux is determined by solving

$$\frac{\delta u}{\delta z} = \frac{U_s}{kz}, \tag{4.12}$$

where k is the von Kármán constant ($k = 0.4$) and U_s is the friction velocity. This method is known as Prandt's mixing length hypothesis. The wind has a logarithmic profile and decreases with height (z). In non-neutral conditions the solution is more complex. In this case the wind shear is related to a non-dimensional formulation

$$\frac{kz}{U_s}\frac{\delta u}{\delta z} = \phi(\frac{z}{L}) \tag{4.13}$$

where ϕ is the Monin-Obhukov stability function and L is the Monin-Obukhov length (Monin & Obukhov 1954). The parameter L is defined in the model by

$$L = -\frac{\rho(U_s^2 + \gamma^2 U_{sf}^2)^{3/2}}{kF}, \tag{4.14}$$

where ρ is the atmospheric density, γ is a dimensionless empirical parameter and F is the surface boundary flux. The variable U_{sf} is called the free convective velocity scale and is defined by

$$U_{sf} = (z_h \frac{F}{\rho})^{1/3} \tag{4.15}$$

where z_h is the boundary layer depth. The surface boundary flux under non-neutral conditions is estimated from an iterative process that determines L. The mixing of heat in the boundary layer is done using the same approach.

The friction velocity is related to the orography and the roughness length. The latter is a parameter that describes the type of surface. It represents the height above the surface at which the logarithmic profile of the wind speed as a function of altitude extrapolates to zero. A smooth surface is represented by a low roughness length, which is associated with low level of turbulence arising from the horizontal flow that passes over the surface. High values of z_0 are associated with stronger turbulence produced by a rougher surface, such as over rocky terrains. In this work the roughness length was set to 0.03 m, following the previous experiments carried out by Lee (2006) for Venus. This number represents a Venus surface composed of small boulders/rocks.

The third and last step is the computation of the physical rates that update the surface temperature and the wind and temperature values in the boundary layer active region, using an implicit scheme. More details about these three steps can be found in Smith (1993a) and Smith (1993b).

At the three top layers of the model's domain an identical sponge parameterisation to the one used in the OPUS-Vs is used to damp the *eddy* component of the wind field *only* to zero (chapter 1 and Lee 2006).

4.4.3 Radiative transfer model

The radiative transfer code implemented in the OPUS-Vr is the same as the one presented in chapter 3. This formulation computes the radiative heating and cooling rates in the atmosphere and is very flexible to adapt to different atmospheric conditions. This code, suitable for climate studies, is divided into two parts that work in two distinct spectral ranges: solar radiation (0.1-5.5μm) and thermal radiation (1.7-260μm).

The solar radiation code is based on an adding layer method and a δ-Eddington approximation (two-stream-type). These two methods simulate qualitatively the multiple scattering phenomena. The δ-Eddington approximation scheme calculates the transmissivity and reflectivity of each layer in a vertical column, that are later combined using the adding layer method. See more details about these two methods in section 3.3 or in Briegleb (1992). The spectral range analysed is divided into fifty five bands with 0.1 μm resolution each. The physical properties in each layer are assumed to be horizontally homogenous. Several components of the atmosphere that interact with the solar radiation were taken into account: three gases (CO_2, H_2O and SO_2), three size distribution modes of cloud droplets assumed to be 75% sulphuric acid and 25% water, an UV absorber component and the Rayleigh scattering effect due to the presence of CO_2 and N_2 molecules. To minimize the errors of the computed fluxes in the lower atmosphere over the spectral range 0.4 - 1.0 μm in comparison with the Pioneer Venus data, an extra absorption was included within this specific spectral range (see the section 3.3.1.4).

The amount of incoming solar radiation at the top of the vertical column for a specific band and the length of the optical paths are controlled by the solar zenith angle. This angle was corrected to include the effect of the atmospheric spherical curvature. The equation from Rodgers (1967), gives a good estimate of the real zenith angle, taking into account the effective solar path length. This formulation has been used with some success in Earth and Mars GCMs (e.g., Rodgers 1967 and Hourdin *et al.* 1993), and it is also a good approximation for the Venus case because of the similar planet dimensions,

$$\frac{1}{\mu} = \frac{35}{\sqrt{1224 \times \mu_0 + 1}} \tag{4.16}$$

where μ is the effective zenith angle cosine corrected and μ_0 is the original value (not corrected).

The final total solar upward and downward spectral fluxes at each interface boundary are combined in each layer to compute the solar heating rates, which depends on the c_p varying with temperature as well. The solar heating rates are evaluated typically every 1.5 Earth days during the OPUS-Vr simulations.

The thermal radiation code is based on an absorptivity/emissivity formulation (neglecting scattering). This method combines all the thermal emission from isolated layers of a vertical column to compute total upward and downward thermal fluxes at each spectral band. The angular integration is done in this parameterisation using a diffusivity factor that depends on the layer optical depth. The spectral range analysed is divided into two hundred and seventy three bands with variable resolution. In section 3.4 more details about the formulation implemented can be found. The physical properties in each layer are assumed to be horizontally homogenous as in the solar radiation scheme. The optical properties of three gases (CO_2, H_2O and SO_2), three size distribution modes of cloud droplets assumed to be 75% sulphuric acid and 25% water and the continuum absorption due to CO_2-CO_2 and H_2O-H_2O collisions, were taken into account in this scheme.

As in the solar radiation scheme the thermal cooling rates are calculated in this parameterisation from the total flux differences across each layer. These rates are updated every 1.5 Earth hour during the OPUS-Vr simulations. This code has a routine implemented which reduces the number of spectral bands from a binning average process. In the simulations studied in this work, a factor of four in the binning average process was chosen. This procedure saved a significant fraction of GCM's integration time and did not compromise the accuracy of the calculated radiative cooling rates. Section 3.4, discusses the effects of the binning processes.

4.4.4 Convection

The convection parameterisation implemented in the OPUS-Vr is the same as the convective adjustment routine described in section 3.5.1. This new formulation for a dry atmosphere was developed taking into account that during the mixing of the potential temperature in unstable columns ($\delta\theta/\delta p > 0$), the total specific entropy of the system is conserved. In this parameterisation the dependence of c_p with temperature is also included. For more details see section 3.5.1.

4.5 Conclusion

In this chapter the dynamical and the physical representations of the Venus atmosphere included in the OPUS-Vr were described. The dynamical section was made consistent with the physical section in relation to the c_p varying with temperature. This model includes a complete radiative transfer formulation, which makes it very flexible to adapt to different atmospheric conditions and to calculate more realistically the radiative cooling and heating rates in the atmosphere and surface. This model flexibility differentiates it positively from recent Venus GCMs such as the one presented in Lebonnois *et al.* (2010a)(restricted to the study of one reference atmosphere). This advantage of the OPUS-Vr is mainly related to the inclusion of the short-wave radiation scheme, which avoids the use of pre-computed tables of solar fluxes.

5

OPUS-Vr - Baseline simulation

5.1 Summary

This chapter presents the first tests of the OPUS-Vr, and defines the model setup for the baseline simulation. The results of the baseline simulation are analysed by studying the mean fields of the main prognostic variables and the transport of angular momentum in the atmosphere, and by exploring the properties of the atmospheric waves simulated. Using a particular atmosphere and model configuration, we aimed to have a better understanding of what are the main mechanisms driving the Venus atmospheric circulation between 0 and 100 km altitude. We identify the main possible mechanisms for the formation and maintenance of the observed atmospheric super-rotation. A comparison of the model results with observational data is made to study the consistency of the results obtained and to identify some possible poor representations of physical phenomena in the GCM structure.

5.2 Introduction

As was presented in chapter 1 the Venus atmospheric circulation has some characteristics which remain poorly understood, such as the mechanism of formation and maintenance of the atmospheric super-rotation. The super-rotation is characterized by a much faster rotation of the atmosphere compared to the rotation rate of the solid planet. The Venus atmosphere has been explored by several space missions in the past: Venera, Pioneer Venus and Magellan, and more recently the European Venus Express mission. These missions made atmospheric data available which increased the interest in the development of global circulation models capable of interpreting the data and guiding their analysis. The numerical

study of the global Venus atmospheric circulation started more than thirty years ago, with the complexity and accuracy improving along the years (see chapter 1). Recently typical Venus numerical models that use very simplified representations of radiation and boundary layer processes (e.g., Yamamoto & Takahashi 2003 and Lee *et al.* 2007), have suggested that the global atmospheric super rotation is sustained by the poleward momentum transport via synoptic eddies from high latitude baratropicaly unstable jets. This mechanism is known as the GRW mechanism (Gierasch 1975; Rossow & Williams 1979). Evolving towards more complex physically-based models we find the work by Lebonnois *et al.* (2010a) and Ikeda *et al.* (2007), who included for instance a self-consistent computation of temperature using a radiative transfer formulation. In these cases the diurnal cycle is not neglected, which revealed to be an important factor in the atmospheric dynamics produced. The diurnal cycle excites migrating thermal tides especially in the Venus cloud region due to the large extinction of solar energy there. The thermal tides play an important role maintaining the super rotation, since they transport prograde momentum vertically and predominantly at low latitudes, from above the cloud region to the upper cloud deck (e.g., Newman & Leovy 1992 and Lebonnois *et al.* 2010a). These two momentum transport mechanisms by barotropic eddies and thermal tides, are responsible for the eddy terms indicated in chapter 1 as indispensable for the formation and maintenance of strong zonal winds at low latitudes: $\overline{u'v'}$ and $\overline{u'w'}$ terms respectively. The OPUS-Vr is aimed at studying these mechanisms, exploring which are the right atmospheric conditions for the formation of an atmospheric circulation similar to the one observed.

5.3 Defining the baseline simulation

5.3.1 Reference atmosphere and surface

We start the exploration of the OPUS-Vr results from the reference atmosphere described in chapter3, which uses the reference albedo calculated from a fit to the observational data from Pieters *et al.* (1986). The planet surface is flat and the atmosphere started from a rest state with every vertical temperature profile close to the VIRA profile (Seiff *et al.* 1980), and surface pressure at 92 bars (1 mb = 1 hPa). The distribution of the clouds is assumed to be constant in the longitude and latitude directions. Hereafter this atmospheric state is referred to as IRVA (**I**nitial **R**eference **V**enus **A**tmosphere).

The available potential energy stored in the atmosphere is converted to kinetic energy during the initial model integration, which is forced by radiation processes and convection. This conversion starts the flow moving in the stably stratified atmosphere at rest. The term "spin-up phase" is applied to GCMs to describe the time period required by these complex models to reach a statistical equilibrium state (in the Venus case the global kinetic energy of the atmosphere stays roughly at the same level as a function of time). The period of integration chosen, 215.5 Venus days (25000 Earth days), has been shown by other works to be enough for representing the spin-up phase typically required by the Venus GCMs (e.g., Lee 2006 and Lebonnois *et al.* 2010a). This long period is associated with the large time-scale for thermal adjustment of the deep atmosphere.

Fig. 5.1 shows a time-series of the global super-rotation index (S, Eq. 1.3) for the last 42 Venus days of the long integration using the reference albedo. The black solid line does not describe a monotonic evolution of S, but instead a long term variation. To understand these variations in S, we study three meridional cross-section maps of zonally and time averaged (over one Venus day) zonal winds for days 181, 201 and 211, shown in Fig. 5.2. The large oscillations in S are related to long term oscillations in the magnitudes and sizes of two weak jets located near the surface at $\sim 4.3 \times 10^4$ hPa ($\sim$10 km) at latitudes of $\pm 50°$. A very large percentage of the atmospheric mass is concentrated in the lower atmosphere ($\sim$ 90% below the 9.5 bars pressure level) which has therefore a large influence on the total angular momentum of the atmosphere. Comparing days 181 and 201, we can clearly see a larger region in the deep atmosphere with prograde winds, which influenced the increase of S. Another factor related to the variability of S, but less important, is the presence of an unstable retrograde equatorial jet at a pressure level of 100 hPa (70 km, in the cloud top region, and with a clear presence in Fig. 5.2c). Despite S not being uniform, it oscillates over only a limited range (with a maximum value that was never exceeded during the long simulation), and this variable evolution is considered in this work to be related to an intrinsically stable regime of the system.

Fig. 5.3 shows the zonal and time averaged zonal winds between the surface and a pressure level of 1 hPa ($\sim$90 km), similar to the maps shown in Fig. 5.2, but now averaged over the last 5 Venus days of the simulation. This map also does not show any sign of strong prograde zonal winds comparable with the ones retrieved from observational data throughout the entire atmosphere (see Fig. 1.6). The black lines in Fig. 5.3 represent the zonally and time averaged mass stream function. In the deep atmosphere these lines

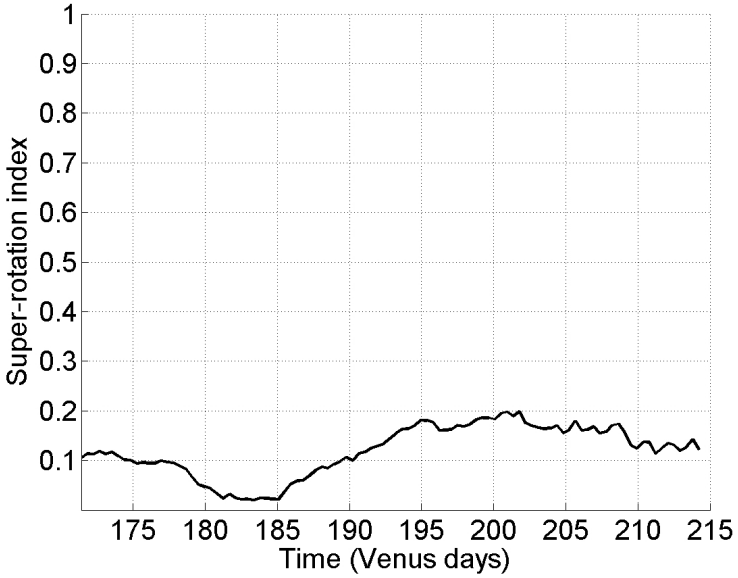

Figure 5.1: Global super-rotation index about the simulation testing the reference albedo.

show the clear presence of a large deep convection circulation pattern. In this region of the atmosphere the momentum is transported upward in the equatorial region and transported poleward at the top of the deep convection cell, creating two peaks in the zonal wind field at 4.0×10^4 hPa ($\sim$10 km) in each hemisphere. Above this region the mass stream function contours show the clear presence of two significant regions of convection. At the pressure level of 3×10^3 hPa two planet-wide thermally direct atmospheric cells lie within the clouds with the bottom of the cells coincident with the cloud base. In this region most of the upwelling infrared radiation that comes from the deep atmosphere is absorbed, creating a region of active convection. The other region of convection is located within the upper cloud region at 100 hPa mainly due to the presence of the UV absorber. Despite the efficient latitudinal transport of momentum by the mean circulation at these pressures (within the upper clouds), the model did not produce any high latitude jets. The atmospheric circulation developed shows four retrograde equatorial maxima, despite the one at 100 hPa being very variable as was shown in Fig. 5.2.

Fig. 5.4(a) compares the global averaged temperature profile obtained by the GCM against the one obtained by the 1D R-CM explored in chapter 3. The two simulations were produced for the same atmospheric conditions and are in good agreement despite the slightly hotter profile below 31 km altiude obtained by OPUS-Vr. Fig. 5.4(b) and 5.4(c) show two

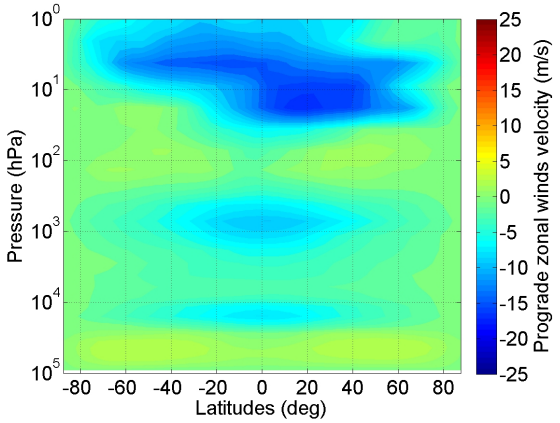

(a) Day 181.

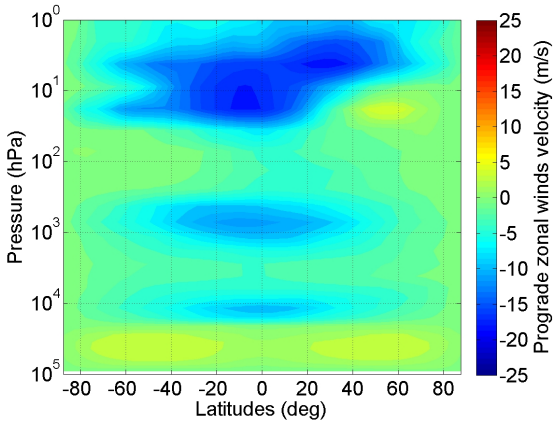

(b) Day 201.

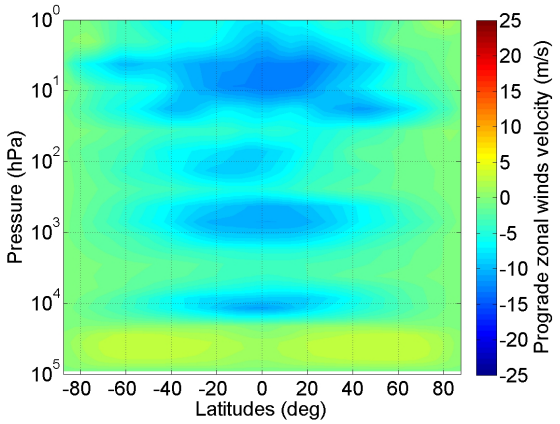

(c) Day 211.

Figure 5.2: Mean zonal winds at three different Venus days (days 181, 201 and 211) from the OPUS-Vr simulation testing the reference albedo ($\alpha < 0.15$). The values were zonally averaged and time averaged for 1 Venus day.

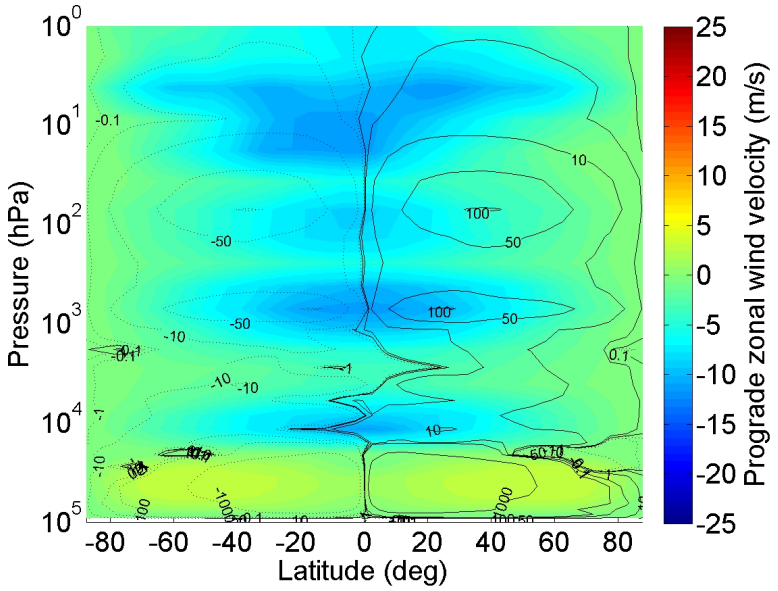

Figure 5.3: Averaged zonal winds and mass stream function (in units of 10^9kg/s) from the OPUS-Vr simulation testing the reference albedo. The dashed lines represent the anti-clockwise circulation and the solid lines the clockwise. The values were zonal and time averaged for 5 Venus day.

longitudinal-pressure temperature anomaly maps for two different instants separated by 50 Earth days at the equator. It is possible from these two maps to identify the disturbances from the deep convection patterns as the source of pulses of gravity waves that travel upward. This very active convection region exerts a drag on the atmospheric circulation and disables the production of super-rotation.

From the cloud top region observations (e.g. Sánchez-Lavega *et al.* 2008; Moissl *et al.* 2009) it is suggested that the atmosphere is in a cyclostrophic regime, with strong prograde winds at low latitudes ($\sim$ 100 m/s) decreasing linearly poleward of 50°. In this experiment we obtained a subsolar-to-antisolar circulation at these altitudes. Fig. 5.5 shows clearly this regime where the colours represent the vertical velocity and the arrows the horizontal component of the wind velocity at 40 hPa (70 km). The redder region corresponds to upwelling flow which diverges to the other side of the planet.

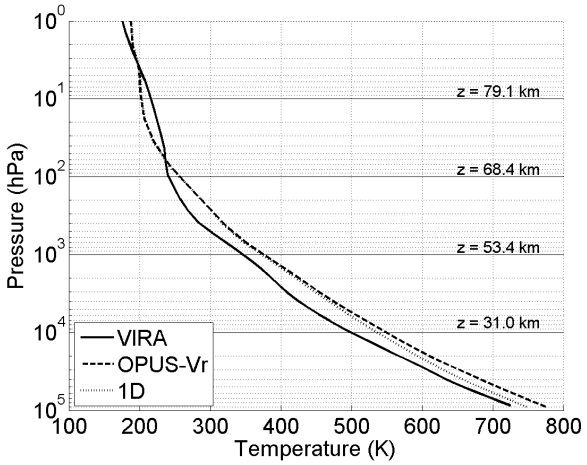

(a) Vertical temperature profile.

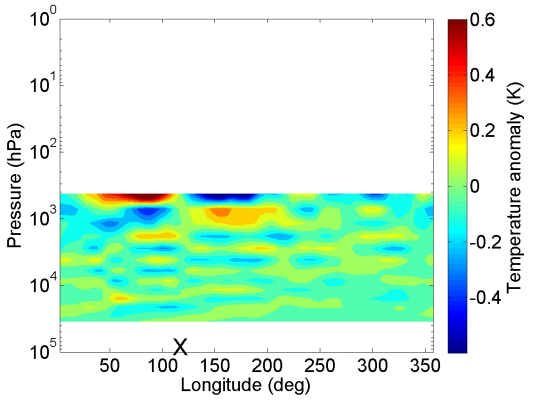

(b) Temperature anomaly map.

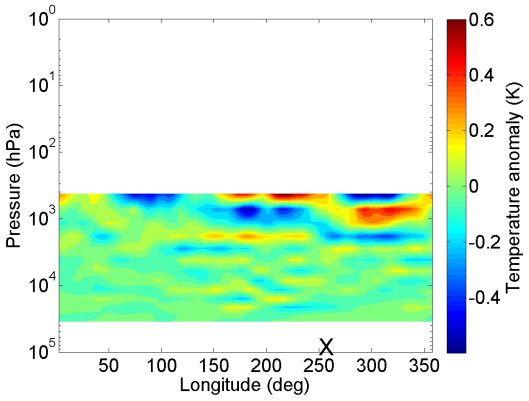

(c) Temperature anomaly map after 50 Earth days of (b).

Figure 5.4: (a) Comparison of three globally averaged vertical temperature profiles. The solid line is the VIRA profile and the dotted line represents the results obtained by the 1D R-CM for the 4 bin averaging in the long-wave scheme. The dashed lined is obtained from OPUS-Vr and it was averaged over latitude, longitude and time (5 Venus days). (b) and (c) are two longitude-height temperature anomaly maps at the equator after the longitude averages were removed. The two are separated by 50 Earth days in the OPUS-Vr integration and the cross in each the map indicates the position of the hottest location at the surface (close to local midday).

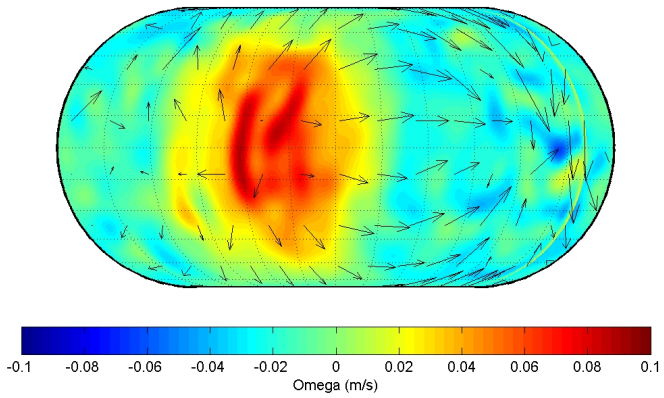

Figure 5.5: Horizontal projection of the atmospheric flow at 100 hPa (70 km) for the OPUS-Vr simulation using the reference surface short-wave albedo. The colors represent the vertical velocity in units of m/s and the vector field represents the relative magnitude and direction of the atmospheric flow.

5.3.2 Albedos larger than the reference one

We study now the effect of applying different values for the surface short-wave albedo on the circulation produced: $\alpha = 0.2$, 0.5, 0.75 and 0.95 (assumed constant with wavelength for simplicity). This parameter controls the amount of solar energy absorbed by the surface. By varying this parameter we explore the influence of different strengths of deep convection near the surface on the atmospheric circulation. The larger values are not likely to be realistic but are intrepreted here as representing the existence of some possible extra components in the thermal budget of the lower atmosphere that are missing.

For each simulation that tested the effect of different surface short-wave albedos, the initial atmospheric state used was IRVA (described in chapter 5). Each of the five experiments were integrated for roughly 215.5 Venus days ($\sim$ 25000 Earth days).

The values of S in Fig. 5.6 for the experiments using albedos of 0.2 or 0.5 converge roughly to the same value, which is governed mainly by the deep atmospheric circulation near the planetary surface as discussed above. The profiles obtained using the albedos 0.75 and 0.95 produce an S that is less variable and converges to larger values. The main reason

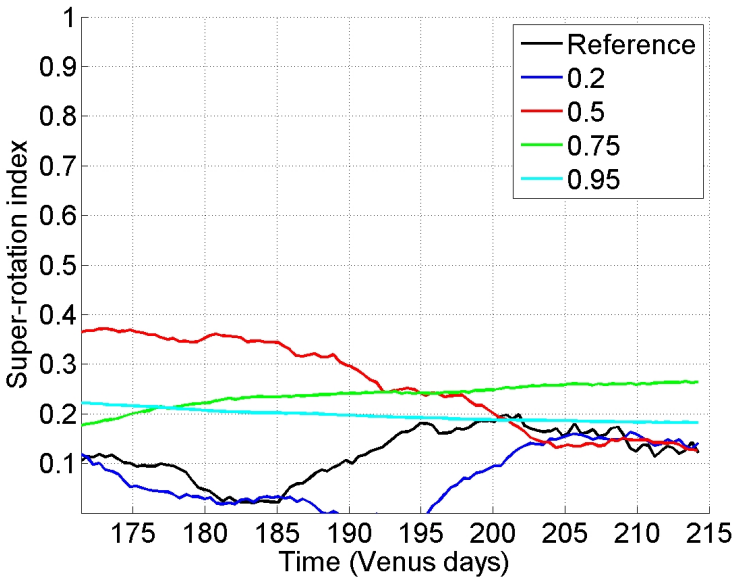

Figure 5.6: Global super-rotation index for simulations testing different surface albedo: the black line is the reference albedo, blue 0.2, red 0.5, green 0.75 and finally 0.95 is the cyan line.

for these differences are analysed below when discussing the zonal wind maps.

Fig. 5.7 shows the zonal winds and mass-stream function obtained at the end of each simulation, averaged for five Venus days and over longitude. In general, larger short-wave albedos result in a weaker convection cell in the deep atmosphere, as is evident from the mass stream function values obtained. The zonal winds in the upper cloud region are also significantly affected by the increasing of the albedo, and when the albedo is equal to 0.5 they change their average direction. There is a relation between the intensity of the deep convection phenomena near the surface and the intensity of the winds in the prograde direction at 100 hPa, as it is possible to verify from the results of the simulations using higher albedos or comparing the winds from Figs. 5.2(a) and 5.2(c) (the last one with larger convection cells). As was mentioned before, the upward propagation of instabilities produced by the vigorous convection near the surface exerts a drag on the atmosphere. Note that the colour scale for the zonal wind map in Fig. 5.7(e) is different, because in this simulation the winds obtained are much stronger than 25 m/s (the maximum of the other scales).

For the case where the albedo is equal to 0.75, a prograde jet in the upper clouds is produced. Two strong convection cells are still obtained near the surface, but weaker than

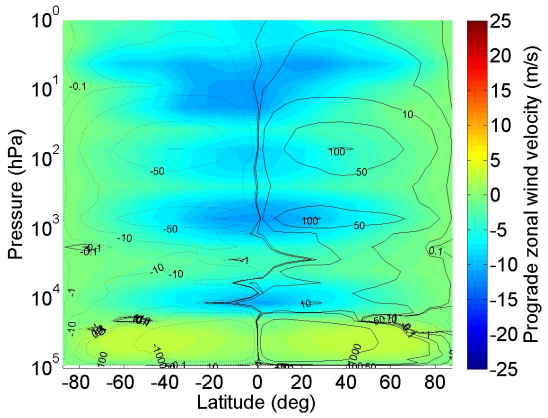

(a) Reference.

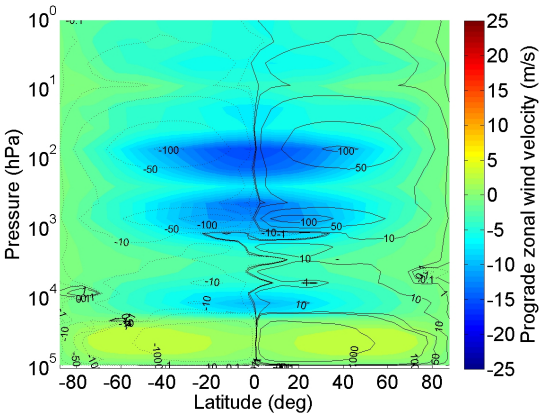

(b) Albedo = 0.2

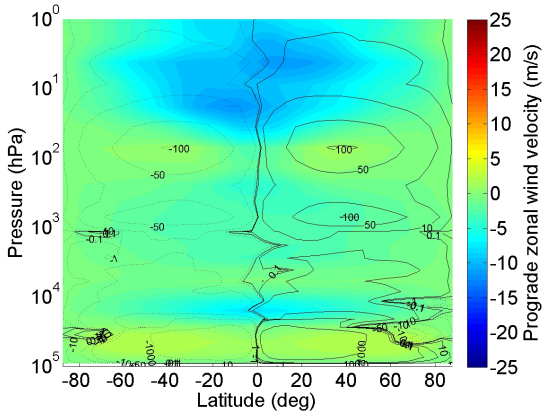

(c) Albedo = 0.5

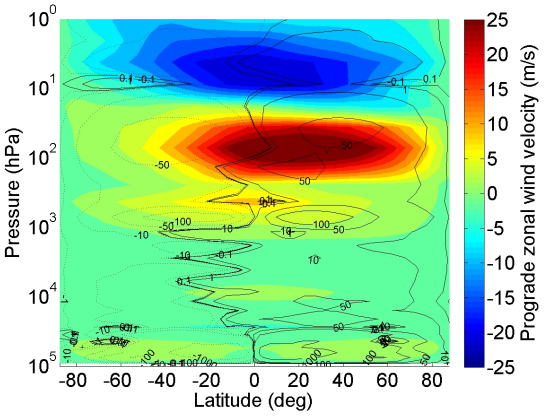

(d) Albedo = 0.75

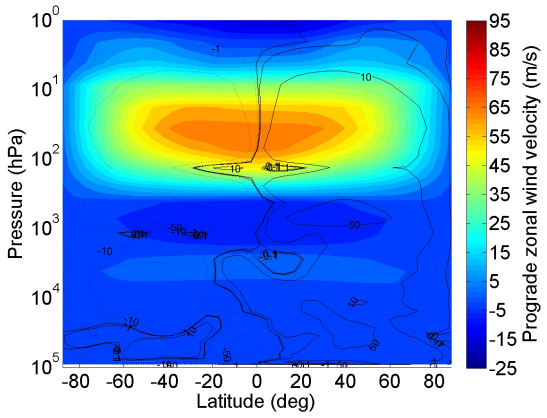

(e) Albedo = 0.95

Figure 5.7: Zonally and time averaged (5 Venus days) zonal wind (m/s) and mass stream-function (10^9kg/s) for five simulations using five different surface albedos in the solar radiation scheme: **(a)** reference, **(b)** 0.2, **(c)** 0.5, **(d)** 0.75 and finally **(e)** 0.95. Note that the colour scale in the map **(e)** is different from the others.

in the other cases with smaller short-wave albedos. The super-rotation index (S) is larger here than for lower surface short-wave albedo cases, because in this simulation the two jets are still produced near the surface, in addition to the relatively strong prograde winds in the cloud region. The atmospheric circulation is not totally symmetric in this case mainly due to long-term variations in the size and strength of the atmospheric cells in the region around 10^4 hPa, which consequently affects the atmosphere above. A longer time averaging would remove many of the asymmetries shown.

When the surface short-wave albedo is set to 0.95 just $\sim 1\%$ of the total solar incoming energy is absorbed by the surface, and as was shown using the 1D R-CM, it produces a statically stable atmosphere near the surface. In this case, the occurrence of vigorous convection near the surface are more unlikely, being more consistent with observational data from Pioneer Venus which actually showed a statically stable atmosphere near the surface (Schubert *et al.* 1980).

From the four maps shown in Fig. 5.8, we clearly see a cyclic behaviour in the strength of the zonal winds in the cloud region. The wind profile shown at day 214 is very similar to that shown in Lebonnois *et al.* (2010a). The weakening/strengthening of the prograde winds in the upper cloud region is followed by a strengthening/weakening of the convection cells in the same region. This long term variability of the zonal winds in the cloud region is related to a large-scale variation in the atmospheric circulation pattern in the lower atmosphere. Clear signs in these maps of the variation in the lower atmosphere are evident in the anti-symmetric patterns of the mass stream function below 10^3 hPa between the days 173 and 244, and in the formation of a weak prograde equatorial jet at 5×10^3 hPa in the intermediate days.

Fig. 5.9 shows that in the days 173 and 244, the zonal wind magnitudes above the pressure level 100 hPa are in good agreement with the observations. These two days are in the phase of the long term oscillation where stronger zonal winds are obtained.

Oscillations with periods similar to the one found here (tens of Venus days) or longer in the Venus atmospheric state are not new in numerical or observational studies. Parish *et al.* (2011) used a GCM with physical routines similar to the ones from the OPUS-Vs and high horizontal spatial resolution ($1^\circ \times 1^\circ$), and found large scale oscillations in the zonal wind distribution with a period of ten Earth years. In those results, the largest variations were located below the cloud base, where the zonal winds varied with a period of ten Earth years between super-rotation and sub-rotation. From the observational side, we find indications

of long term oscillations (on periods of tens of Venus days) in the zonal flow, temperature and composition, in the cloud region and above it: e.g.del Genio & Rossow (1990), Belyaev *et al.* (2008) and Clancy *et al.* (2012).

Fig. 5.10 shows the solar radiation flux absorbed at the surface for the different experiments, and also data obtained from various descent probes (Moroz *et al.* 1985). It is clear that, in the cases with short-wave surface albedos smaller than 0.75, the model is overestimating the amount of solar radiation absorbed by the surface. The case when the short-wave albedo is set to 0.75 shows similar results when compared to the observations for different zenith angles. In the experiment with albedo = 0.95, the model actually underestimates the amount of solar energy absorbed by the surface compared to the observations. However, this was the value chosen for the baseline simulation because it produced a super-rotation more consistent with observations in the cloud region.

These values of short-wave albedo larger than the reference ones ($\alpha < 0.15$) do not represent well the optical properties of the surface, which is thought to be mainly composed of basalt. However, this heuristic method of increasing the albedo appears to alleviate the problem of overestimating the amount of solar energy absorbed by the surface, and yet does not compromise the calculation of the radiative heating rates in the atmosphere above, as we saw in chapter 3. This need to use large albedos can be interpreted as indicating an incomplete representation either of the radiative extinction in the extreme deep atmosphere, or of the possible existence of extra missing constituents of the atmosphere that interact with solar radiation, thereby modifying the static stability in this part of the atmosphere.

The atmospheric state shown in Fig. 5.8(a) will be referred to hereafter to as **S095VA**, which will be used as initial condition in some experiments. In this case, a super-rotation in the cloud region similar to the one observed is well represented.

5.3.3 Surface temperature constant

In order to explore the apparent link between the surface temperature gradient and the atmospheric circulation produced, we carried out one further experiment forcing the temperature of the surface to be uniform during an OPUS-Vr simulation. The model was integrated for 42 Venus days (∼5000 Earth days), starting from the atmospheric state shown in Fig. 5.8(a) and the surface temperature kept at roughly 740 K, which is the surface-averaged temperature of the results on day 173 of the simulation using a surface short-wave albedo

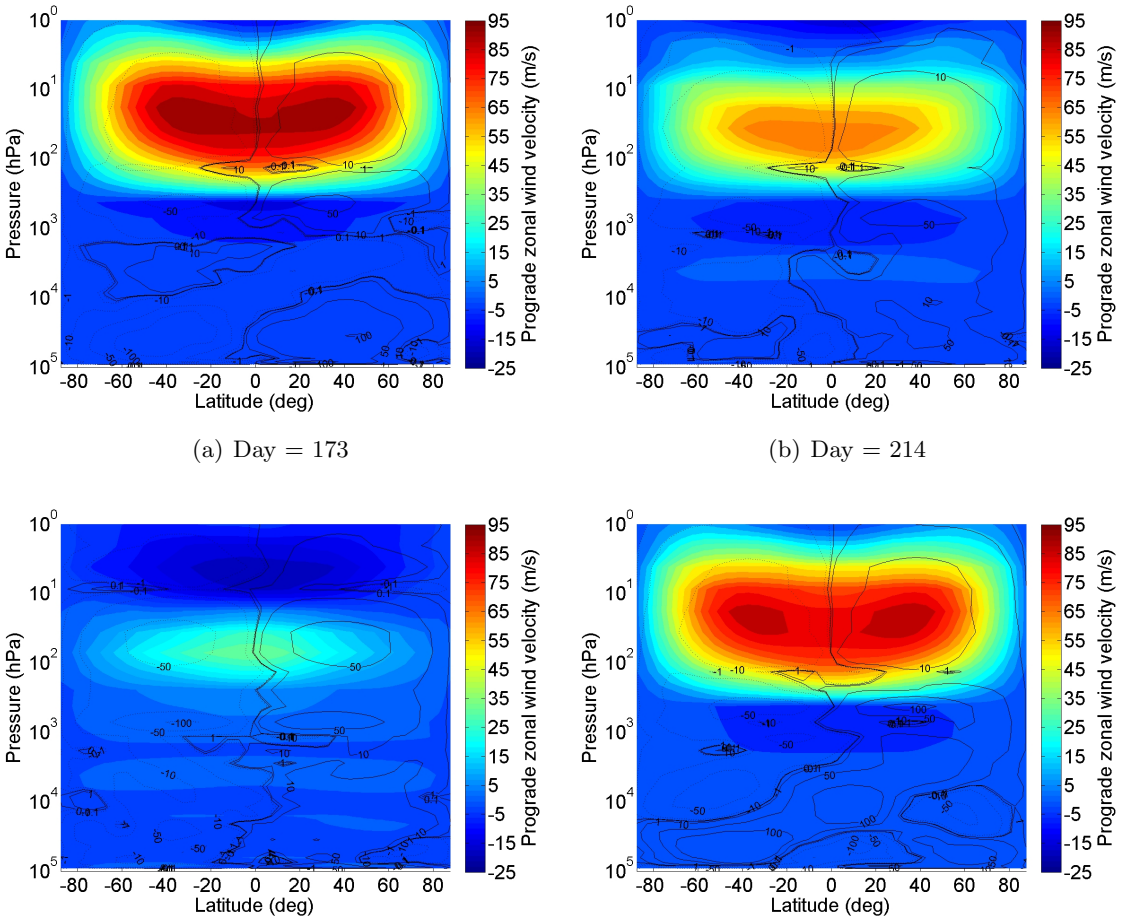

(a) Day = 173

(b) Day = 214

(c) Day = 223

(d) Day = 244

Figure 5.8: Zonally and time averaged (5 Venus days) zonal wind (m/s) and mass stream function (10^9kg/s) of the simulation using an albedo of 0.95 at four different days: (**a**) 173, (**b**) 214, (**c**) 223 and (**d**) 244.

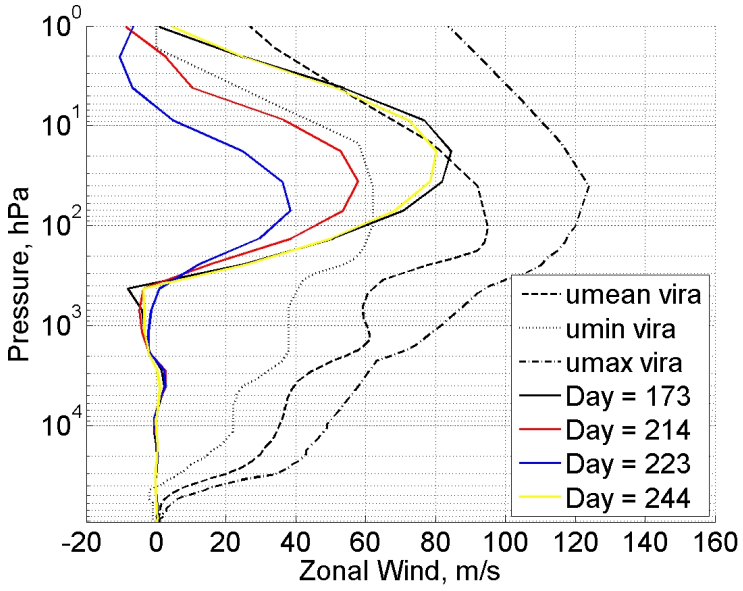

(a) Vertical profile.

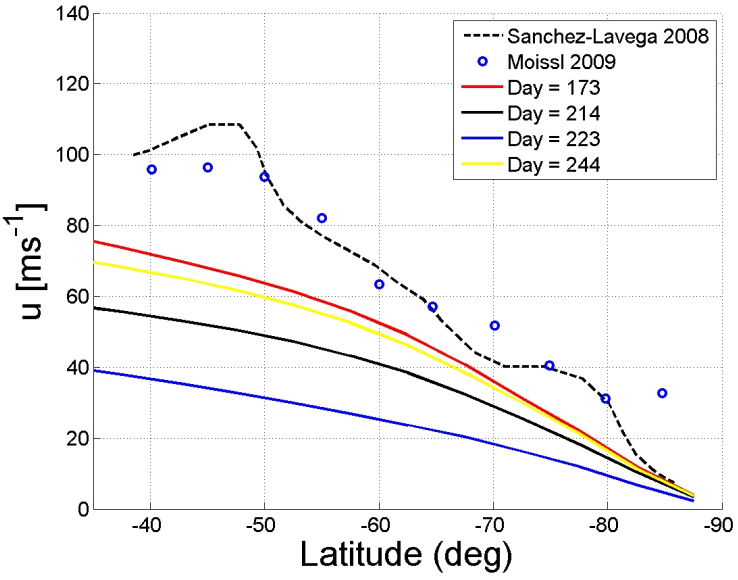

(b) Horizontal profile.

Figure 5.9: Vertical and horizontal profiles of zonal winds, comparing the different days results obtained in the experiment using an albedo of 0.95 with the observations. The observational data from the plot **(a)** was available in Kerzhanovich & Limaye (1985) and the mean winds from cloud tracking results at roughly 70 km shown in **(b)** were from Sánchez-Lavega *et al.* (2008) and Moissl *et al.* (2009). In both figures the model's mean zonal winds were zonally and time averaged for five Venus days. In the vertical profile the simulated winds were just averaged between 40°S and 40°N to be consistent with the observational data.

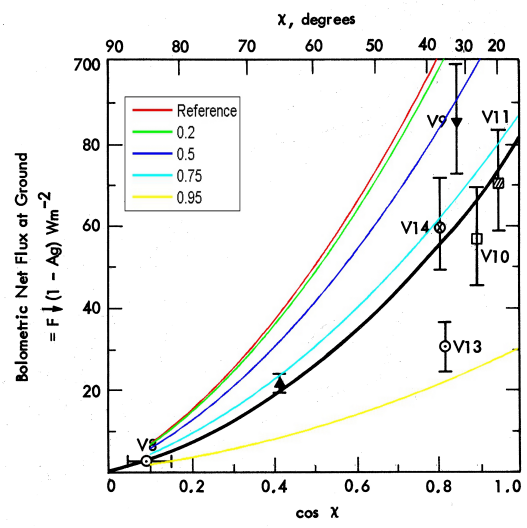

Figure 5.10: Bolometric net flux at the ground for simulations testing different surface albedos compared with observations. The different colours correspond to different short-wave albedos used in the simulation: red is the reference one (Pieters *et al.* 1986), green is the $\alpha = 0.2$, blue is the $\alpha = 0.5$, cyan is the $\alpha = 0.75$ and yellow is the $\alpha = 0.95$. The black line is a fit to the values retrieved by various descent probes (Moroz *et al.* 1985).

of 0.95. In this experiment the values for S decrease with time (Fig. 5.11a) because of the weaker dynamic activity in the deepest regions of the atmosphere. However, the strong zonal wind distribution and magnitude remained approximately constant in the cloud region (Fig. 5.11b).

In this simulation the instabilities that were exerting a drag in the atmospheric circulation in experiments with small surface short-wave albedo, are largely reduced. As a consequence, the strong zonal winds in the cloud region are roughly maintained. Another important result from the model is the possible coupling between the instabilities near the surface and the lower atmosphere circulation. This mechanism may be driving the long term oscillations in the atmospheric circulation seen above, which in this experiment have weaker amplitude.

5.3.4 Summary

The case that uses a short-wave surface albedo equal to 0.95 is the experiment that seems to represent the overall Venus atmospheric circulation. The surface short-wave albedo can induce the atmospheric circulation to evolve towards a particular state governed by a deep

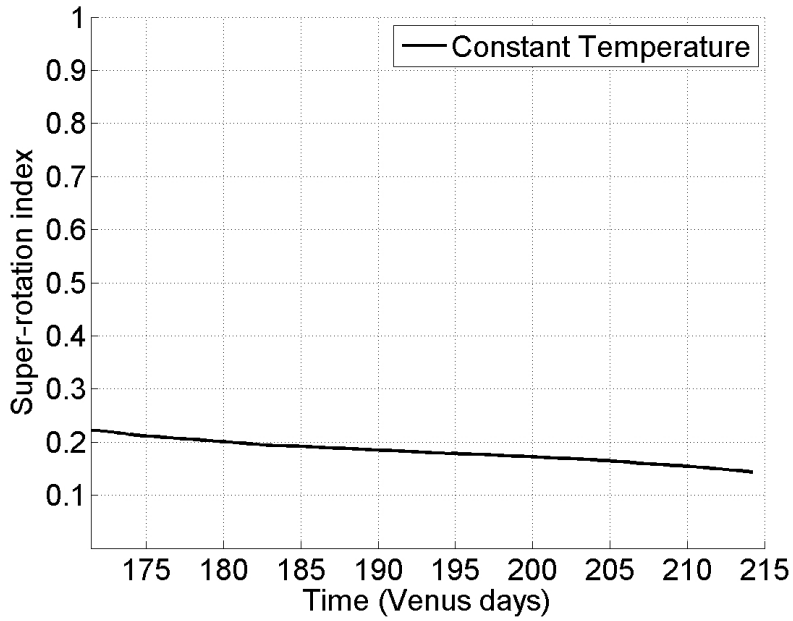

(a) Super-rotation index.

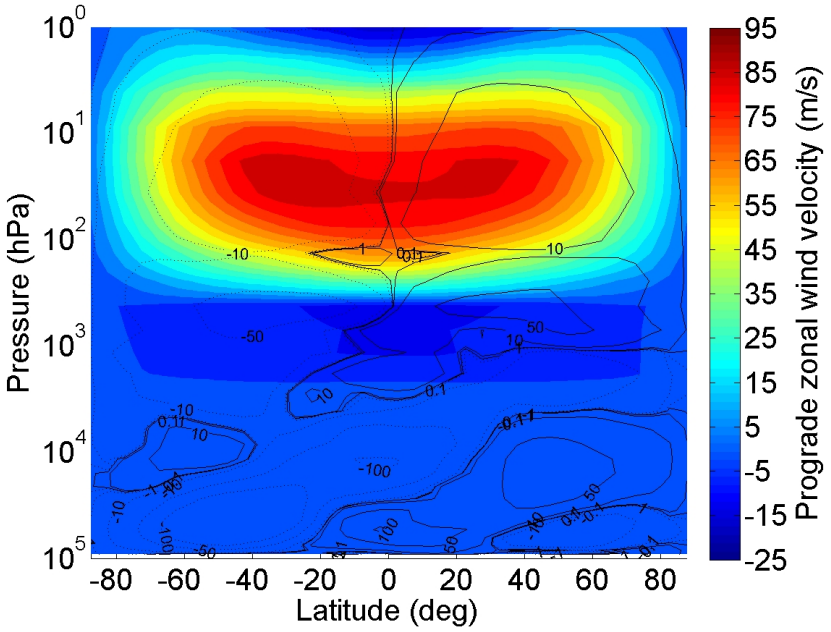

(b) Mean zonal wind.

Figure 5.11: Super-rotation index **(a)** and mean zonal winds **(b)** for the OPUS-Vr simulation with constant surface temperature of 740 K and initialised from S095VA. The black lines in **(b)** represent the mean stream-function (10^9kg/s).

convection cell near the surface. The value chosen assumes less active deep convection near the surface and yet does not compromise the match between the global static stability values and temperatures and the observations. The atmospheric circulation in this configuration also exhibits an apparent cyclic behaviour. In general, below 10^3 hPa the circulation is very weak with zonal wind magnitudes no larger than 3 m/s (with an unstable weakly prograde equatorial jet at 5×10^3hPa) and a retrograde jet located just above it. In the upper cloud region we find strong zonal winds with magnitudes consistent with the ones found in observational studies. This experiment was chosen to be the baseline simulation because it produces an atmospheric circulation in the cloud region closer to the one observed, allowing us to explore possible atmospheric mechanisms currently at work in Venus. Despite using an unrealistic surface albedo, two experiments in the next chapter explore two possibilities that could explain the need to increase the surface albedo, by including additional sources of opacity in the lower atmosphere.

Based on atmospheric circulation results from the simulations and comparing them with the expected atmospheric circulation from the observations, we can constrain the maximum amount of solar energy absorbed by the surface. This exercise could be used as a tool to explore the uncertainties in the radiative properties in the lower atmosphere.

5.4 Baseline simulation results

As we explained in the section above, where the time of integration and initial conditions are specified, the value of the surface short-wave albedo is assumed to be heuristically high for the baseline simulation, 0.95. The baseline simulation results of the OPUS-Vr are in this section studied in more detailed and, in particular, in the intermediate phase of the long cycle in the atmospheric circulation seen in the previous section (around day 214).

Fig. 5.12 shows the global super-rotation index (S, defined in chapter 1) of the atmosphere between the days 171 and 214 of the baseline simulation. The variable plotted tends to stabilise at 0.18 magnitude, which may indicate that a statistical steady state is reached. The variable S depends on the total angular momentum of the atmosphere, which is dynamically redistributed in the atmosphere by atmospheric advection, modified by the action of waves, and is destroyed by the mechanical interaction of the atmosphere with the surface.

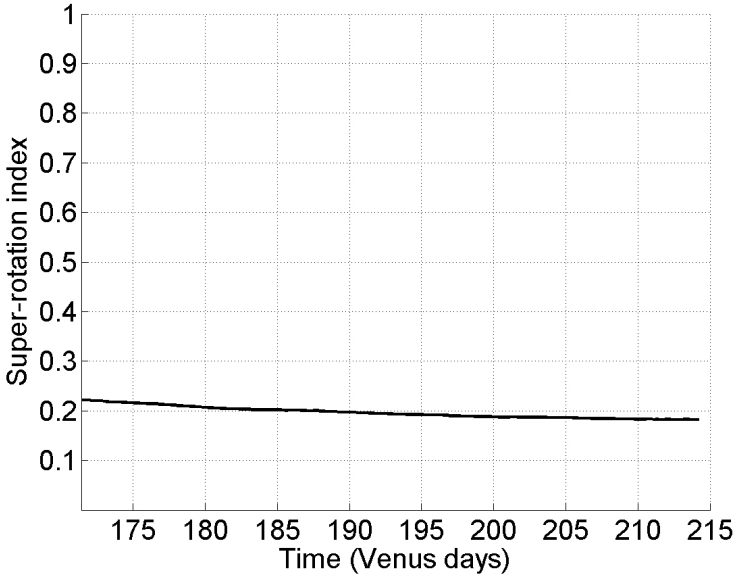

Figure 5.12: Global super-rotation index about the baseline simulation.

The results obtained by the baseline simulation are very different from the ones obtained by the simplified Venus GCMs presented in chapter 1. In these previous simplified models, a complete radiative transfer formulation is replaced by a simple linear temperature forcing routine, which results in inaccurate representations of the radiative heating and cooling rates in the atmosphere and surface. The different distribution of the radiative energy deposition in the atmosphere drives significantly different atmospheric circulations. In the simplified Venus GCMs the radiative forcing is also zonally symmetric, which neglects any atmospheric thermal tides induced by the diurnal cycle. The high latitudinal positions ($\pm 60°$) of the wind jets in these simplified models are typically a characteristic of the zonally symmetric forcing as will be seen from a later experiment with OPUS-Vr without a diurnal cycle. In simplified models the jet's structure reaches altitudes much deeper than the ones obtained by complete ones, which extend from the cloud top ($\sim$50 hPa) to pressures around 10^4 hPa (much deeper than the cloud base), see Fig. 1.8. The maxima in the winds are obtained at roughly 100 hPa and are weaker than the ones shown in Fig. 5.13(a) from the OPUS-Vr. The mean meridional circulation is governed typically by two large Hadley cells in each hemisphere which influence the transport of momentum from near the surface up to the cloud region (e.g., Lee 2006 and Lebonnois *et al.* 2011) and is in contrast to the more complex structures obtained by more sophisticated models (e.g., our new model

and Lebonnois *et al.* 2010a). This first brief comparison between simplified models and the OPUS-Vr, reveals the importance of the inclusion of a realistic radiative formulation in the Venus GCMs, such as the one that we have developed here.

The mean vertical temperature profile shown in Fig. 5.14(a) is very similar to the one obtained by the 1D R-CM (see the discussion in chapter 3). Fig. 5.13(b) shows the mean temperature anomaly map. The temperature values (T_a) in this map are deviations from the horizontal mean on pressure levels, and were calculated using

$$T_a = T - \frac{\int_{\lambda=0}^{\lambda=2\pi} \int_{\phi=-pi/2}^{\phi=pi/2} T a^2 \cos\phi d\lambda d\phi}{\int_{\lambda=0}^{\lambda=2\pi} \int_{\phi=-pi/2}^{\phi=pi/2} a^2 \cos\phi d\lambda d\phi} \tag{5.1}$$

where T is the absolute temperature, a is the radius of the planet, ϕ is the latitude and λ is the longitude. The latitudinal variations in temperature shown in this map are largely influenced by the atmospheric circulation produced. The very small 1-2 K variations in the atmosphere at deeper levels than the 10^3 hPa pressure level are consistent with the results obtained by the LMD Venus GCM (Lebonnois *et al.* 2010a) but much smaller in comparison with the observations, which can evidently reach equator-to-pole differences of 30K (Tellmann *et al.* 2009; Lebonnois *et al.* 2010a). The zonal winds produced in this region and shown in Fig. 5.13(a) are also small, with the zonal winds reaching maxima with the same magnitude as the maxima of the latitudinal variation found in the temperature anomaly map. The winds in this region are much smaller than the ones observed (see later Fig. 5.16a). The atmosphere in this region is characterized by a weak static stability (Fig. 5.14d) with two relative maxima of stability, one near the surface and another at roughly 2×10^3 hPa ($\sim$ 45 km). The atmospheric circulation near the surface is not symmetric about the equator in Fig. 5.13(a), but is dominated by the turbulent influence of the interchanges between the surface and atmosphere, which might mean that a thermally equilibrated state solution has still not been reached in the deepest regions.

A zonal equatorial maximum ($\sim$3 m s^{-1}) is obtained at 5×10^3 hPa, which is close to a relative maximum in the atmospheric stability profile. The formation of this dynamic structure may be related to the absorption of downward propagating thermal gravity waves produced in the lower cloud region, coupled with the mean circulation in the deep atmosphere. We will come back to this subject later, when we discuss the transport of momentum. Despite the existence of this jet, the magnitude of the winds are much weaker than the values ob-

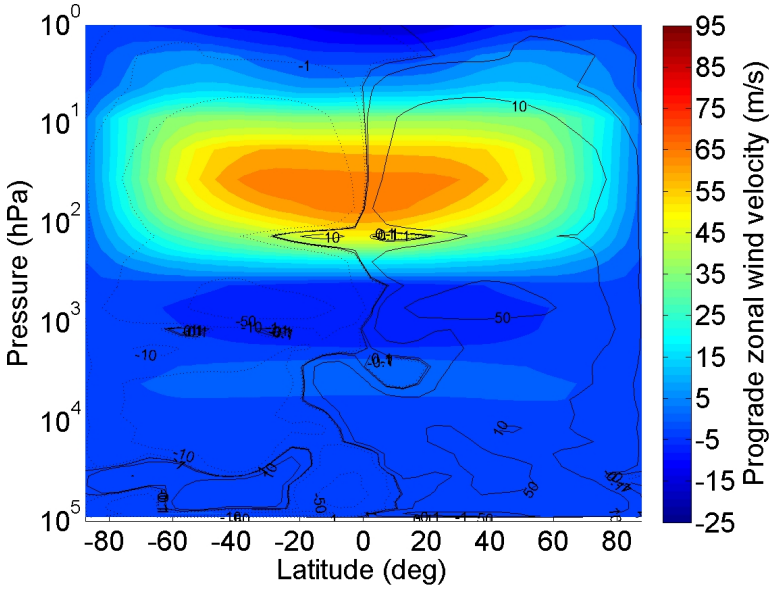

(a) Mean zonal winds.

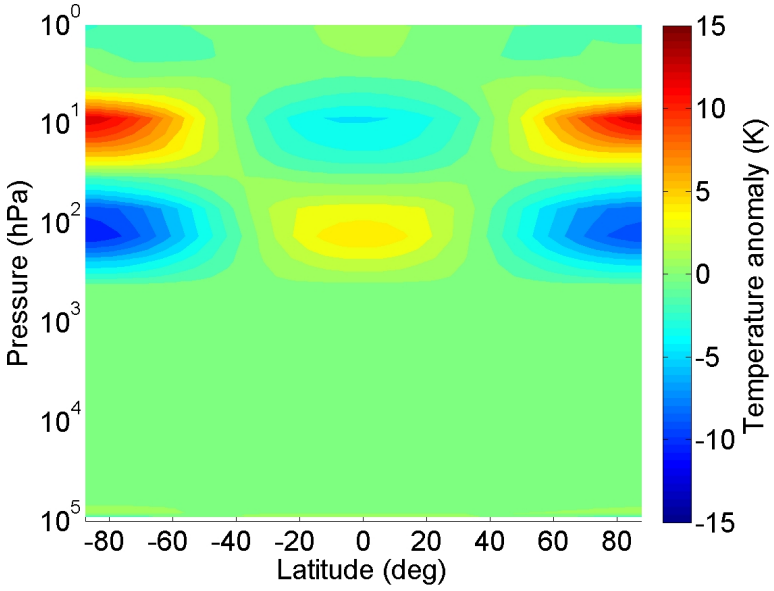

(b) Temperature anomaly.

Figure 5.13: Baseline results - Mean zonal winds and temperature anomaly maps. **(a)** and **(b)** are the zonal and time averaged (five Venus days) zonal winds and temperature anomaly maps obtained around the day 214.

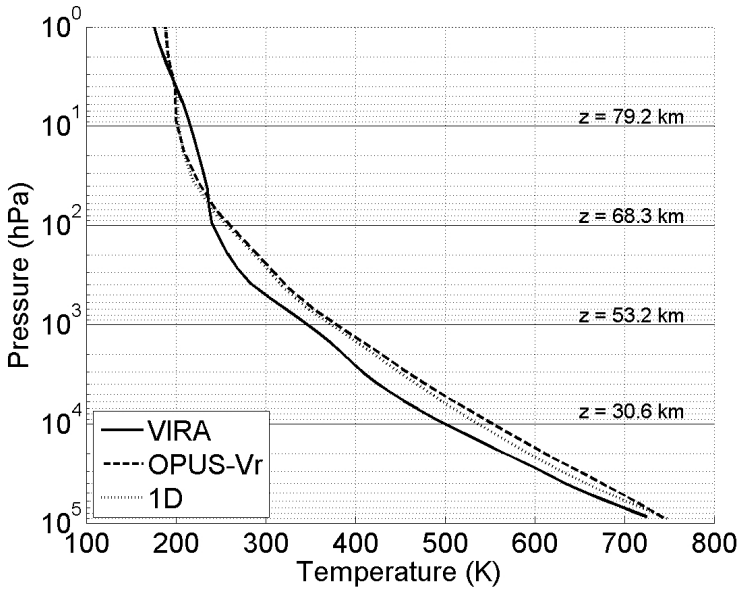

(a) Global mean temperature.

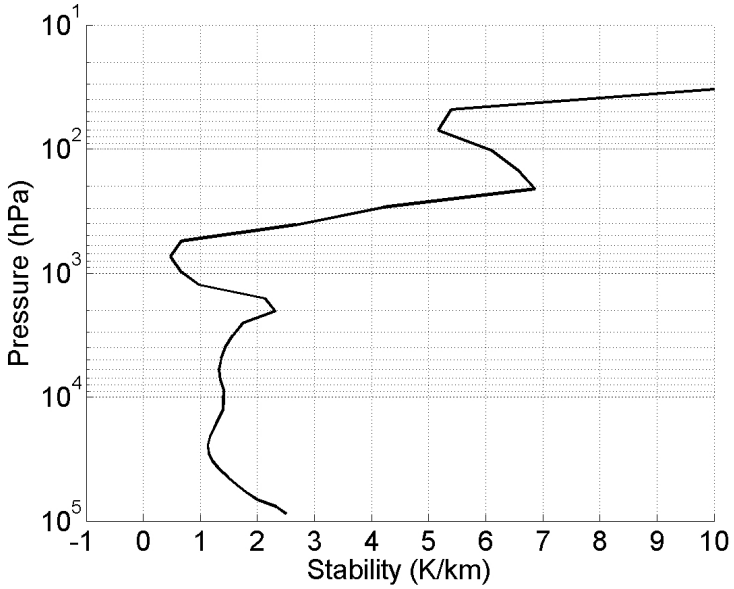

(b) Stability.

Figure 5.14: Baseline results - Global mean profiles of stability and temperature. **(a)** and **(b)** are horizontal and time averages (five Venus days) of absolute temperature and atmospheric static stability ($d\theta/dz$, where θ is the potential temperature).

served. Possible explanations for the poor representation of the atmospheric circulation in the lower atmosphere are discussed in chapter 8.

At 10^3 hPa there is a region of weak stability, which is associated with the base of the cloud deck. In this region, as it was pointed out before, most of the upwelling infrared radiative energy from the deepest regions of the atmosphere is blocked by the clouds. The location of the weakly stable atmospheric region is in agreement with recent observational results of the VeRa experiment (Tellmann *et al.* 2009) and also with the LMD Venus GCM (Lebonnois *et al.* 2010a). This region of weak stability, is a region where upward convection motions are likely to occur. That is clearly seen in the stream-function map from Fig. 5.13(a), and is related to the base of a relatively strong Hadley circulation at 10^3 hPa.

Going up in altitude, we find just above 10^3 hPa, a weak retrograde jet. The mechanisms for the formation of this jet are associated with the downward propagating component of gravity waves, that are thermally excited at the cloud top and absorbed by the atmosphere far from that region. These gravity waves transport momentum vertically and have the tendency to accelerate zonal flow in the prograde direction in the region where they are excited (cloud region), balancing the deceleration in the region where they are absorbed (see chapter 1). In this region the zonal winds are weakened by the significant mean meridional circulation, and by the absorption of the above mentioned downward propagation of gravity waves.

Above a pressure level of 500 hPa, the zonal winds start to increase their magnitude with altitude, reaching a maximum of roughly 60 m/s in the equatorial region at 70 hPa. This zonal wind pattern is consistent with a cyclostrophic regime. From the thermal wind equation we expect that in the region where there is a negative poleward gradient in temperature, the zonal winds increase with height (70-500 hPa). The gradient of temperature is reversed above 70 hPa and the zonal wind then decreases its magnitude. The hotter polar region above 70 hPa is consistent with the results of Lebonnois *et al.* (2010a), and is likely a product of adiabatic heating from air compression into the poleward branch of the equator-to-pole Hadley cell (associated with a maximum temperature difference of 20 K between high and low latitudes). From the static stability profile it is also possible to infer the formation of a convection cell (weaker than the one formed at the cloud base) from the relative minimum in the plot at these altitudes, which is largely induced by the presence of the unidentified UV absorber in the upper cloud region.

In Fig. 5.15(a) I show three time series of the winds in the zonal direction in three different geographical locations. These points are at the same pressure level of 36 hPa and longitude of 0°, but different latitudes: two mid-latitude points (47.5°S and 47.5°N) and one near the equator (2.5°S). We can see a roughly sinusoidal varying wind, superimposed on a nearly constant background wind field. In this sample, which corresponds to the last fourteen Venus days of the simulation, the phase difference between the maxima of the two mid latitude points seems to be roughly π most of the time. Upon studying this variability in more detail we compute a Fourier-transform analysis of those winds and the results are shown in Fig. 5.15(b). For the three locations the influence of the thermal tides is large, with the amplitude of the diurnal tide (with a period of one Venus day) being roughly 5.5 m s^{-1} and the semidiurnal tide roughly 3.5 m s^{-1}. Two broad peaks show up at mid latitude locations (mid latitude jets) with periods of 1.86 and 2.14 Venus days. The causes of these long term oscillations are explored in a wave analysis section later. In a recent work from Khatuntsev *et al.* (2013), long-term wind variations and periodicities were analysed using a cloud-tracking method covering a period of ten Venus years of data from the Venus Monitoring Camera (VMC) instrument aboard the Venus Express probe. The data revealed that, from a Fourier analysis of the wind field, there are periodicities related to the thermal tides (diurnal and semidiurnal tides), faster oscillations of the jets with periods of roughly 4.8 Earth says, and three long-term periodicities of 22.1, 2.05 and 1.90 Venus days. The period of 22.1 Venus days detected was not discussed in Khatuntsev *et al.* (2013) and its existence is arguable since the period is longer than the space mission. The two other maxima in the spectrum (2.05 amd 1.90 Venus days), despite appearing to be reproduced in the results of the OPUS-Vr, were claimed in Khatuntsev *et al.* (2013) to be a result of the sampling periodicities in the VMC observations, which makes it difficult to compare the observations and simulation results on this topic.

5.5 Comparing with observational wind data

In Fig. 5.16(a) we used available observational data from a Venus reference model of the atmospheric circulation (Kerzhanovich & Limaye 1985) to do a direct comparison with the baseline results obtained with OPUS-Vr. The OPUS-Vr values compared refer to vertical profiles of zonally and time averaged (five Venus days) zonal winds between the surface and 1 hPa. The observational data correspond to the latitudinal region between 40°S and 40°N,

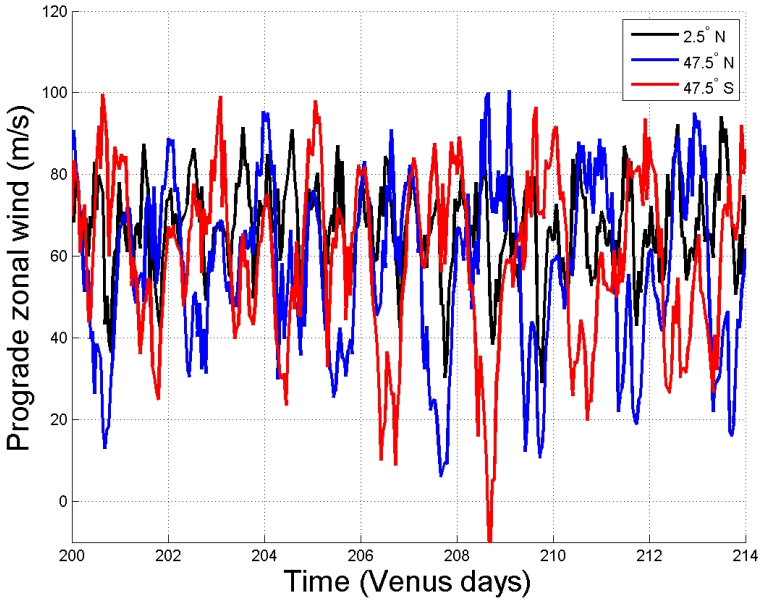

(a) Zonal wind Vs Time.

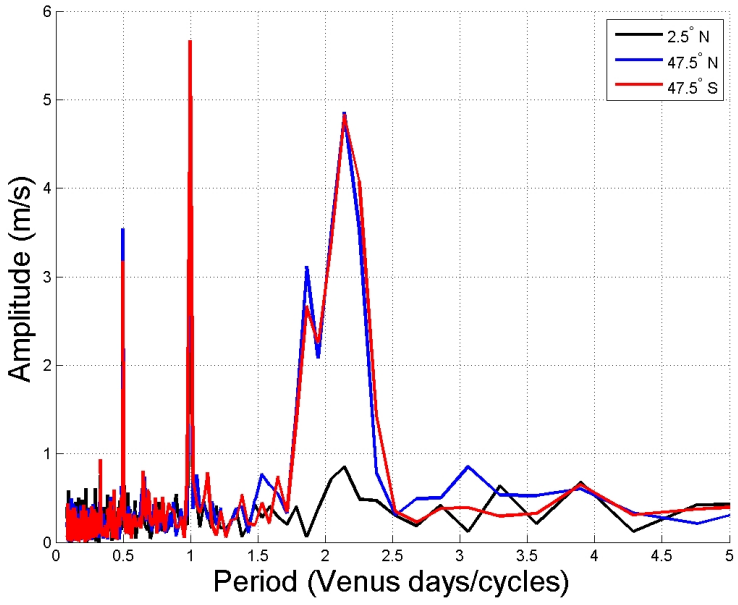

(b) Spectrum.

Figure 5.15: Zonal wind time series and spectrum from the baseline simulation. The time series were retrieved from three locations at 36 hPa: two mid-latitude points (47.5°S and 47.5°N) and one near the equator (2.5°S). These results correspond to data obtained in the last fourteen Venus days of the simulation.

and our model values were also averaged in that region. The zonal winds simulated by OPUS-Vr are weaker throughout all altitudes in the atmosphere; however, there is a good correspondence between the relative maxima in the observations and the values modelled. The peaks in the zonal winds are mostly produced by thermally induced gravity waves influencing the angular momentum transport (discussed below).

Using more recent observational data from Venus Express, we compared recent results from cloud tracking methods (Sánchez-Lavega *et al.* 2008 and Moissl *et al.* 2009) that retrieved zonal winds at the cloud top ($\sim$ 70 km), with the OPUS-Vr latitudinal profile of the zonal winds at roughly the same altitude. As would be expected from Fig. 5.16(a), Fig. 5.16(b) shows also weak winds in comparison to values retrieved from cloud motions at $\sim$ 70 km. The values modelled have a latitudinal gradient very similar to a solid body rotation, which suggests that atmospheric waves must have an important role in redistributing momentum at high latitudes, as was discussed in chapter 2.

5.6 Momentum transport

To gain a better understanding of the main momentum transport mechanisms responsible for the simulated atmospheric circulation, we calculated the zonally averaged transport of angular momentum separated into three different contributions: mean circulation [A], stationary waves [B] and transient waves [C]. Note that in this analysis we are not taking into account the mechanical transport due to the interaction of the surface with the atmosphere and the contribution from the momentum mixing during atmospheric convection. A representation of momentum mixing during convection is not included in this baseline simulation but it is tested in a sensitivity experiment later. To analyse the total meridional transport of angular momentum (M) in the baseline results we used the following equation (Peixoto & Oort 1992):

$$[\overline{vM}] = \underbrace{[\overline{v}][\overline{M}]}_{[\mathrm{A}]} + \underbrace{[\overline{v^\star M^\star}]}_{[\mathrm{B}]} + \underbrace{[\overline{v'M'}]}_{[\mathrm{C}]} \tag{5.2}$$

where v is the meridional component of the wind velocity. The bars over the variables indicate temporal averages and the square brackets a zonal mean. The disturbances in relation to these two averages are represented by: $M' = M - \overline{M}$ and $M^\star = M - [M]$. To analyse the vertical transport, the variable v is replaced by w in m s^{-1}. The vertical velocity

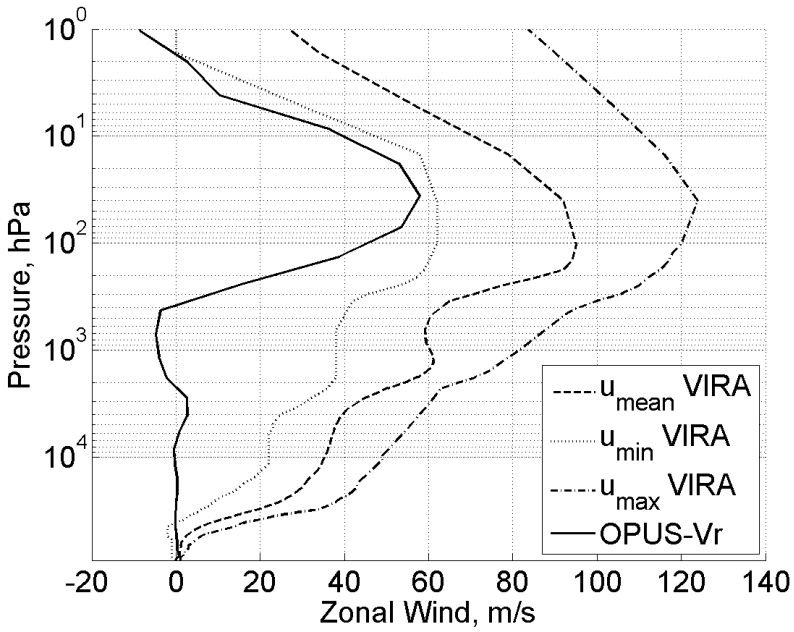

(a) Vertical profile.

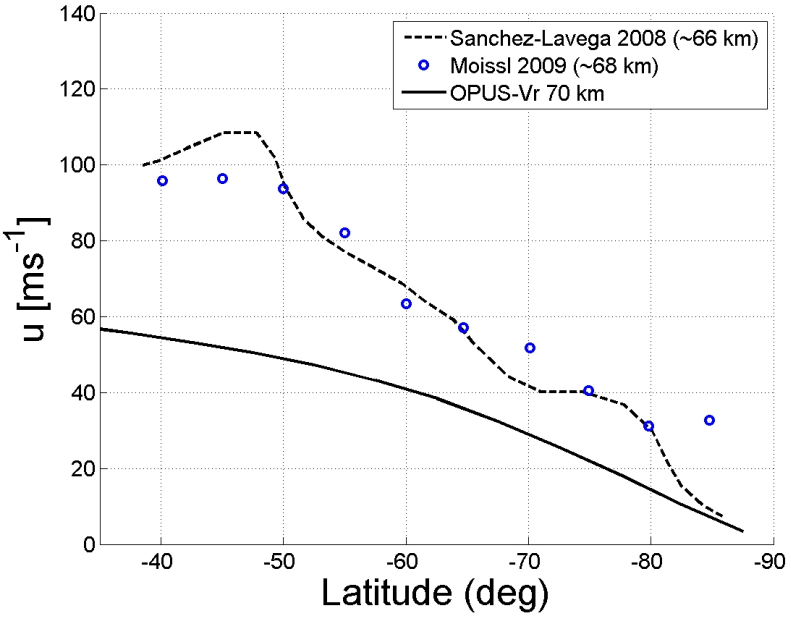

(b) Horizontal profile.

Figure 5.16: Vertical and horizontal profiles of zonal winds, comparing the baseline results with the observations. The observational data from the plot **(a)** was available in Kerzhanovich & Limaye (1985) and the mean winds from cloud tracking results shown in **(b)** were from Sánchez-Lavega *et al.* (2008) and Moissl *et al.* (2009). In both figures the model's mean zonal winds are represented by a solid line and were zonally and time averaged for five Venus days. In the vertical profile the simulated winds were just averaged between 40°S and 40°N to be consistent with the observational data.

w is calculated by the GCM in Pa s^{-1}, and later converted to m s^{-1} using:

$$\omega = \frac{dz}{dt} = -\frac{RT}{pg}\frac{dp}{dt} \tag{5.3}$$

For each GCM cell, the respective relative angular momentum M is calculated using

$$M = m \times u \times a\cos\phi \tag{5.4}$$

where m is the atmospheric mass of a GCM cell, u the zonal wind, ϕ the latitude and a the planetary radius.

In Fig. 5.17 two components of the meridional transport of angular momentum, and also the net contribution are shown. The map of the stationary wave contribution is not included, because in this case its magnitude is much weaker than the other two means of transport. Fig. 5.17(b) shows the calculated meridional transport by the mean circulation, and, as expected, it is in good agreement with the mass stream function plot in Fig. 5.13(a). The transport by the mean circulation is the dominant mechanism to transport angular momentum in the atmosphere in the meridional direction, as can be seen from the similarities between Fig. 5.17(b) (mean circulation) and Fig 5.17(a) (net transport). In general, prograde angular momentum is transported from low latitudes to high latitudes by the large thermally direct cells above the cloud base region. At roughly 100 hPa, mainly due to the presence of the unknown UV absorber, significant thermal tides are formed which produce two thermally indirect cells at low latitudes (one in each hemisphere). This phenomenon reinforces the transport of momentum towards the equatorial region, aligned with the lower branch of the large clockwise convection cell in the northern hemisphere. The main feature in the horizontal transient wave representation is the equatorward transport of angular momentum above the 100 hPa pressure level. In Fig. 5.18 the data were analysed using a solar fixed longitude, which allows us to separate the transport due to the thermal tides, now stationary waves in this reference frame, from other transient processes. In this figure it is clear that the thermal tides have an important contribution in transporting prograde momentum equatorward above and poleward below 100 hPa. The transient waves mainly produced by the barotropic unstable jets have a secondary impact (the GRW mechanism explained in chapter 1). This phenomenon weakens the strength of the jets. Despite the presence of mid-latitude jets in Fig. 5.13(a) not being clear, it is possible to see in Fig. 5.15(a) the presence of two jets varying in magnitude in the upper cloud region. The existence of these transient waves is clarified in the next section, where we use a wave analysis

to explore the baseline results. Low frequency modes such as mixed Rossby-gravity waves are also found in the atmosphere with relevant amplitude, but their impact on the transport of momentum is much weaker than the other mechanisms mentioned above.

The vertical transport of angular momentum is also largely influenced by the mean circulation, but in this case the vertical transient waves in Fig. 5.19 have a more relevant role in transporting momentum than the horizontal transient waves. The two regions of active convection in the cloud transport momentum upward at low latitudes and downward at high latitudes. These large convection cells are confined between the cloud base at 10^3 hPa and upper cloud top at 100 hPa. The mean circulation transports momentum upwards in both upper cloud and cloud base regions, despite the negative values of M in the latter. These negative values at the cloud base are due to the presence of a retrograde equatorial jet. In the upper clouds, the positive values of vertical transport mean that the atmospheric mean circulation is transporting prograde momentum to higher altitudes. The prograde jet just above 10^4 hPa is located in a region of a long-term disturbance that is breaking the symmetry between the two hemispheres. The downward transport of prograde wind by thermal tides excited in the lower cloud and absorbed in this region, may be contributing to strengthen this weak jet. Below this region, the analysis of vertical momentum transport becomes more complex due to the turbulent flow in the deepest regions of the atmosphere.

The stationary waves for the case with non-sun-synchronised data have again a much weaker impact than that due to transient waves (includes thermal tides) or the mean meridional circulation. Upon separating the thermal tides from other wave effects in the transient wave map (Fig. 5.19c), we see clearly in Fig. 5.20 that thermal tides dominate the vertical wave transport of momentum. Fig. 5.20(a) shows the effect of the induced thermal gravity waves transporting angular momentum in the downward direction from roughly 10 hPa (above the cloud region) into the cloud region. These waves in our simulation correspond mainly to the thermally-excited diurnal and semi-diurnal tides (studied in the wave analysis section), which are more intense in the equatorial region and are consistent with the theoretical work of Newman & Leovy (1992). The efficiency of the vertical transport of momentum by the mean circulation is weakened by the thermal tides, which are an important source of momentum at low latitudes. The results shown in Fig. 5.20(a) are consistent with the action of thermally-induced gravity waves which accelerate the atmosphere in the region where they are excited and decelerate it where the waves are absorbed by radiative damping (see a more detailed explanation in chapter 1). The acceleration of the equatorial flow by

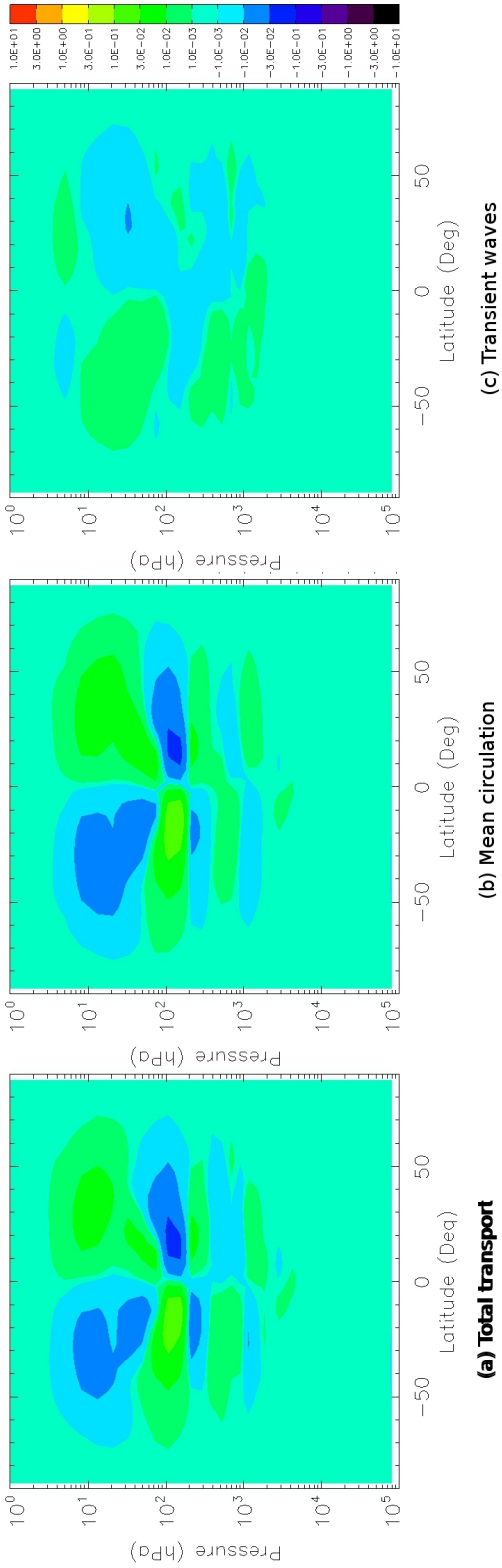

Figure 5.17: Meridional transport of angular momentum of the baseline results. The data used to produce these results correspond to the last five days of the ∼214 Venus day-long simulation. $[\overline{vM}]$ is the net transport, $[\overline{v}][\overline{M}]$ is the mean circulation and $[\overline{v'M'}]$ is the transient waves. The units of the colour bars are in (kg m^3 s^{-2})×10^{24}.

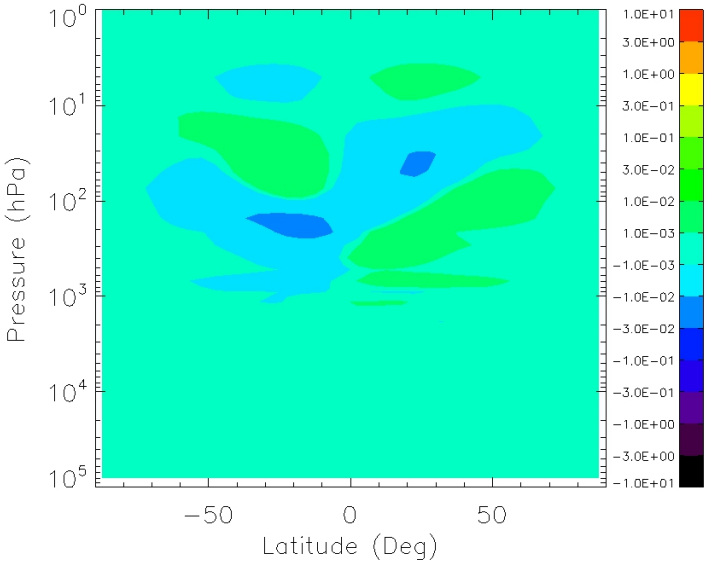

(a) Stationary waves.

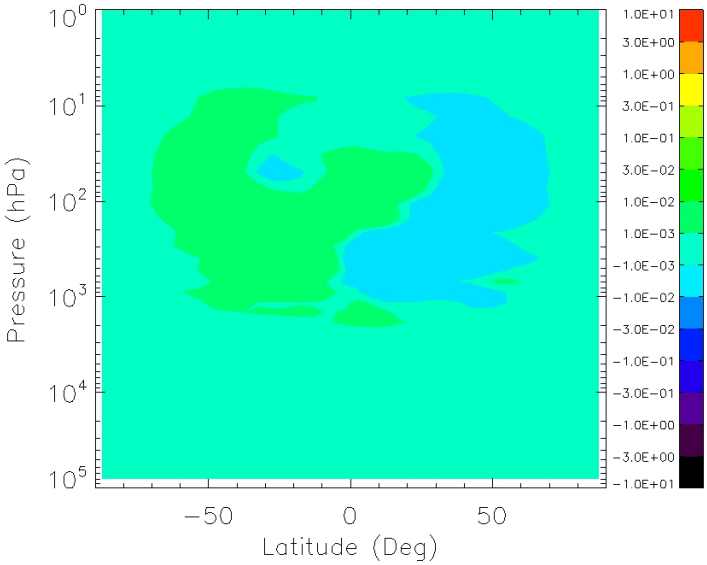

(b) Transient waves.

Figure 5.18: Meridional transport of angular momentum by waves in the baseline results, calculated using a solar-fixed longitude. The data used to produce these results correspond to the last five days of the ∼214 Venus day-long simulation. **(a)** and **(b)** are the horizontal transport by stationary ($[\bar{v}^\star \bar{M}^\star]$) and transient waves ($[\overline{v'M'}]$) respectively. The units of the colour bars are in (kg m^3 s^{-2})×10^{24}.

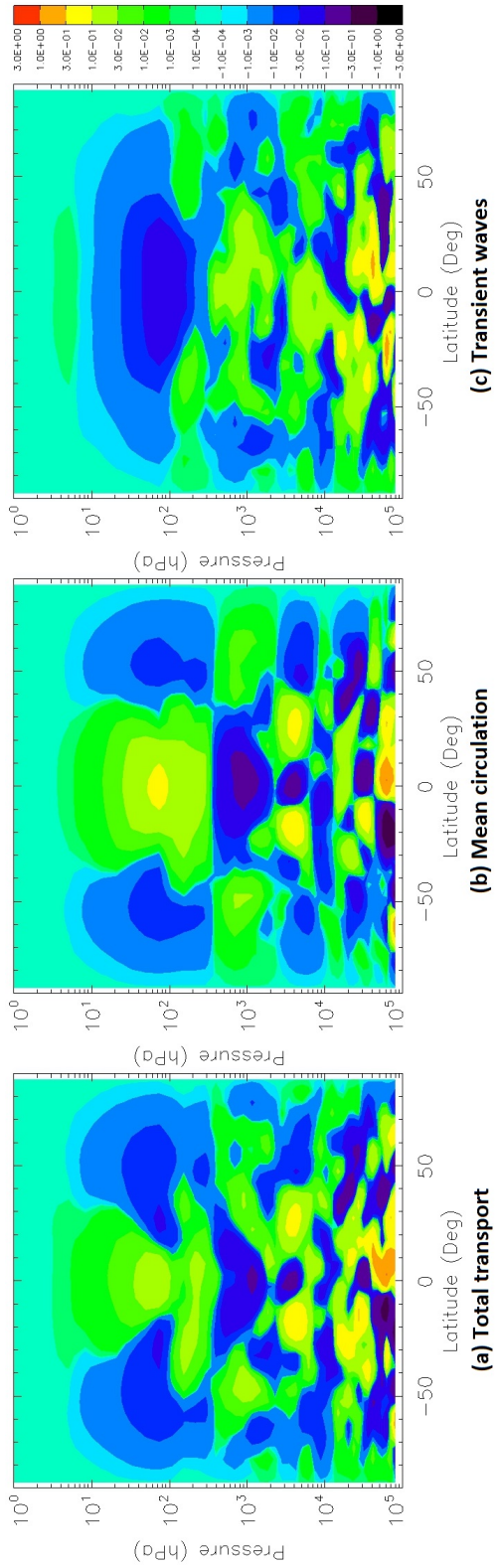

Figure 5.19: Vertical transport of angular momentum of the baseline results. The data used to produce these results correspond to the last five days of the ~214 Venus day-long simulation. $\bar{w}\bar{M}$ is the net transport, $[\bar{w}][\bar{M}]$ is the mean circulation and $[\bar{w}^{\star}[\bar{M}^{\star}]$ is the transient waves. The units of the colour bars are in (kg m^3 s^{-2})$\times 10^{24}$.

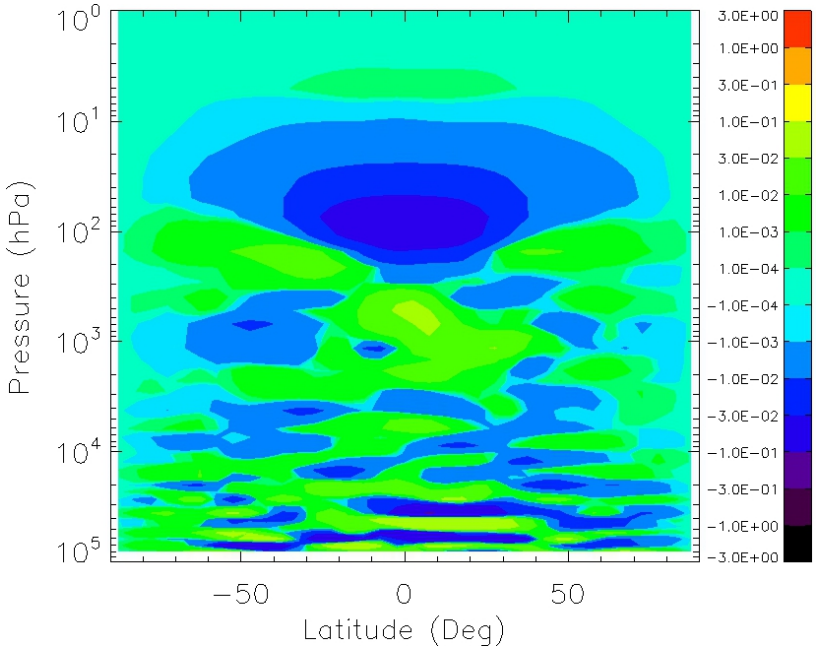

(a) Stationary waves.

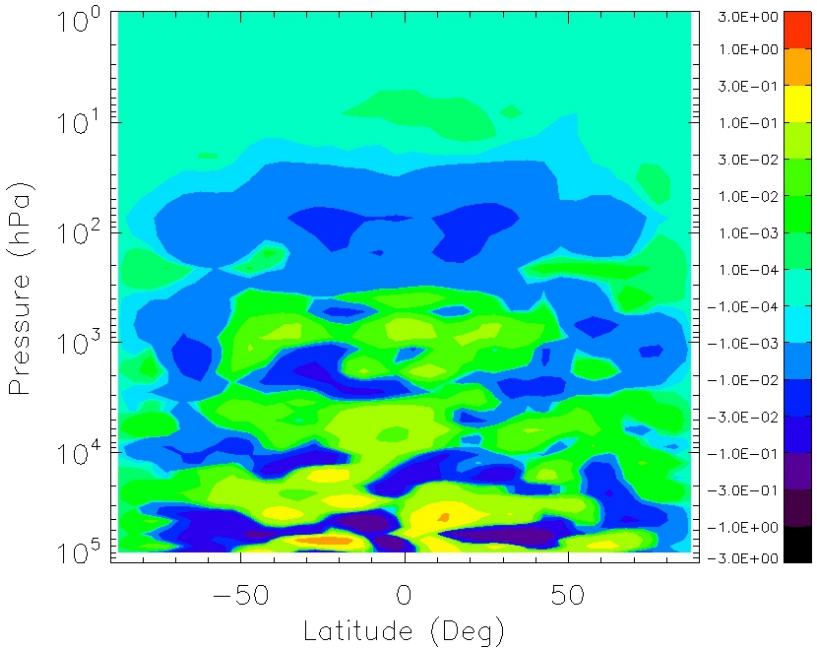

(b) Transient waves.

Figure 5.20: Vertical transport of angular momentum by waves in the baseline results, calculated using a solar-fixed longitude. The data used to produce these results correspond to the last five days of the ∼214 Venus day-long simulation. **(a)** and **(b)** are the vertical transport by stationary ($[\bar{\omega}^{\star}\bar{M}^{\star}]$) and transient waves ($[\overline{\omega' M'}]$) respectively. The units of the colour bars are in (kg m^3 s^{-2})$\times 10^{24}$.

the thermal tides decreases the latitudinal wind variation between the two mid-latitude jets typically found at roughly 50° latitude.

5.7 Wave analysis

The temperature data analysed here from the baseline simulation have a temporal resolution of one Earth day (with more than 100 points for each Venus day) and correspond to the last five Venus days of the ∼214 Venus day-long simulation. In Fig. 5.21, transient travelling waves (relative to the underlying planet) are identified and characterized in terms of their period. These atmospheric waves are responsible for the momentum transport in the atmosphere, seen before in Figs. 5.17(c) and 5.19(c), and are an essential part of the mechanism to produce the atmospheric circulation obtained. In Fig. 5.21 it is shown three amplitude spectra of the temperature field: two as a function of pressure for two latitudinal locations (equator and mid-latitude) and one as a function of latitude at a pressure level of 100 hPa (upper cloud region). In all spectra the thermal tides due to the diurnal cycle are very clear. The more dominant harmonics are the diurnal and semidiurnal tides (with periods of 1 and 0.5 Venus days), and their amplitudes are larger in the upper cloud region and then above the 30 hPa pressure level at all latitudes. The largest amplitudes found for these waves at the regions mentioned are ∼3 K for the diurnal tide and ∼1.5 K for the semi-diurnal tide. For altitudes above 1hPa (not shown in the maps) the diurnal tides become more intense with amplitudes reaching 10 K. In the maps that show the wave amplitude as a function of altitude, there is clear evidence of the two convection cells located respectively at the upper cloud level and at the cloud base (100 hPa and 1000 hPa) preventing and/or weakening the wave propagation.

In Fig. 5.22 is shown the comparison between the temperature variability, T', of values from the OPUS-Vr and based on a temperature field from Venus Express data (presented in chapter 2) at 45°S. The variable T' is defined by the difference between the temperature field and its average over the time period of data analysed. The figure shows clearly the dominant semi-diurnal tide. The values from the OPUS-Vr simulation were averaged over five Venus days, and are similar to what has been obtained from the observations (Grassi *et al.* 2010) in terms of wave amplitude and location.

The spectrum as a function of latitude from Fig. 5.21(c), shows that the mid-latitudes are regions of stronger wave activity. These waves have small amplitude and are located

predominantly in regions of strong wind, which indicate that they are being produced in association with the unstable mid-latitude jets. These waves contribute to the meridional momentum transport by transient waves from mid-latitudes to low latitudes, which weakens the mid-latitude jets and strengthens the zonal winds in the equatorial region. However, this mechanism has a weaker impact than the meridional transport by the thermal tides (discussed in the momentum transport section 5.6).

Weak transient wave amplitudes of roughly 0.1 K are found in the equatorial region at ∼100 hPa, which seems to be compatible with the so-called 'wave IV' found by Lebonnois *et al.* (2010a). These waves have a period of 4-5 Earth days and, despite their small amplitude, may be related to the planetary scale wave modes at the Venus cloud tops found by del Genio & Rossow (1990) using Pioneer Venus UV images. These weak waves found in the GCM results have some characteristics consistent with equatorial Kelvin waves: they peak in amplitude in equatorial regions and do not have a significant meridional velocity component (see Fig. 5.25(b) below).

Figs. 5.23(a) and 5.23(b) show Hovmöller plots of T', to demonstrate the propagation of waves identified. The Hovmöller plot is a useful tool to detect wave-like features in the atmosphere, and the axes are space versus time. In Fig. 5.23(a) and 5.23(b), altitude-time and longitude-time Hovmöller plots are shown for an equatorial latitude. As we would expect from the spectra, the dominant waves are the first two harmonic components of the solar tides, propagating in the eastward (retrograde) direction. The semidiurnal tide is present in both maps, despite the presence of the two convection cells mentioned before (at 100 and 10^3 hPa) which weaken the upward and downward propagation of this wave. A weak downward component of the solar tides seems to propagate deeper than the 10^3 hPa pressure level. The temperature increases very slightly with time in the deep atmosphere which may indicate that the thermal structure in this region is still adjusting to a steady state.

At mid-latitudes, waves with a shorter period than the dominant diurnal and semidiurnal tides are displayed in Fig. 5.24, using a Fourier bandpass filter method. The waves in the altitude-time and longitude-time Hovmöller plots correspond to waves with periods between 0.1 and 0.2 Venus days (11.6 to 23.2 Earth days). These disturbances in the atmosphere are a product of the unstable jets, and they propagate generally westward with the zonal atmospheric motion.

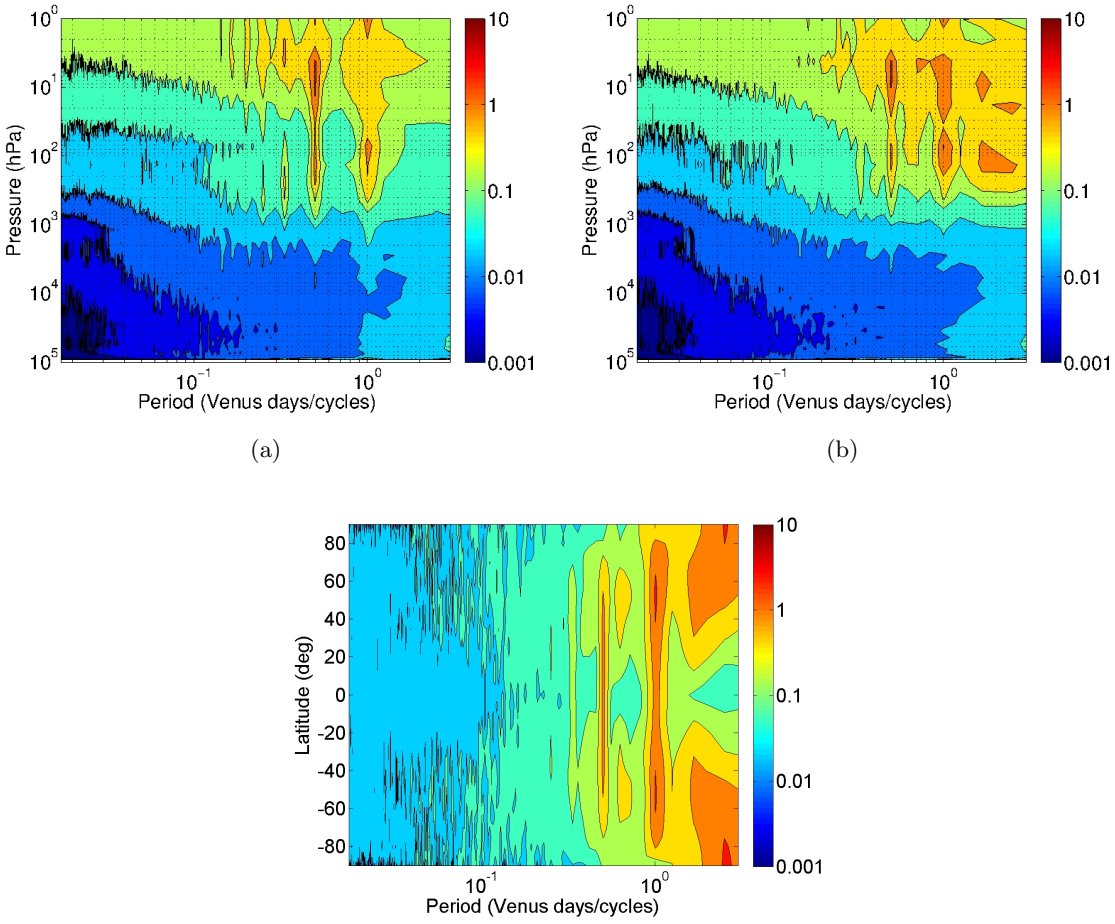

(a) (b)

(c)

Figure 5.21: Amplitude spectra for the temperatures (K) of the baseline results. The values of the spectra were zonally averaged and correspond to the last five Venus days of the long simulation. **(a)** and **(b)** show spectra contoured as a function of pressure and wave period (in Venus days) for the equator and 45°N respectively; **(c)** shows spectra contoured as a function of latitude and wave period at a pressure level of 100 hPa.

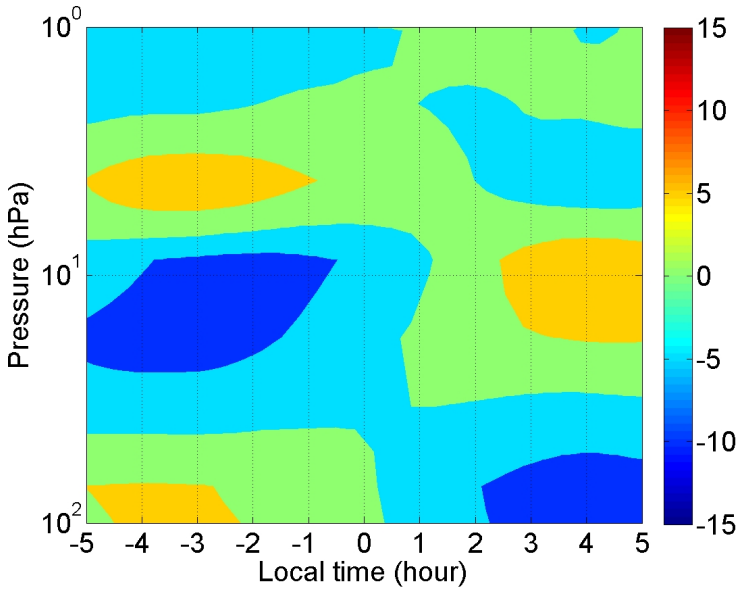

(a) OPUS-Vr

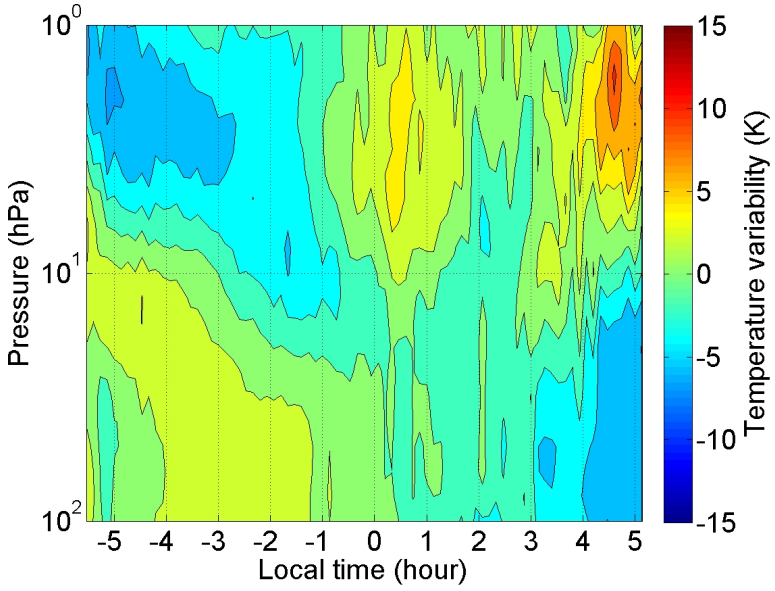

(b) Venus Express

Figure 5.22: Temperature variability (K) comparison between OPUS-Vr **(a)** and Venus Express results **(b)**. The results shown from the GCM results were averaged over five Venus days at 45°S. The observational result used was based on data from Grassi *et al.* (2010) at 45°S.

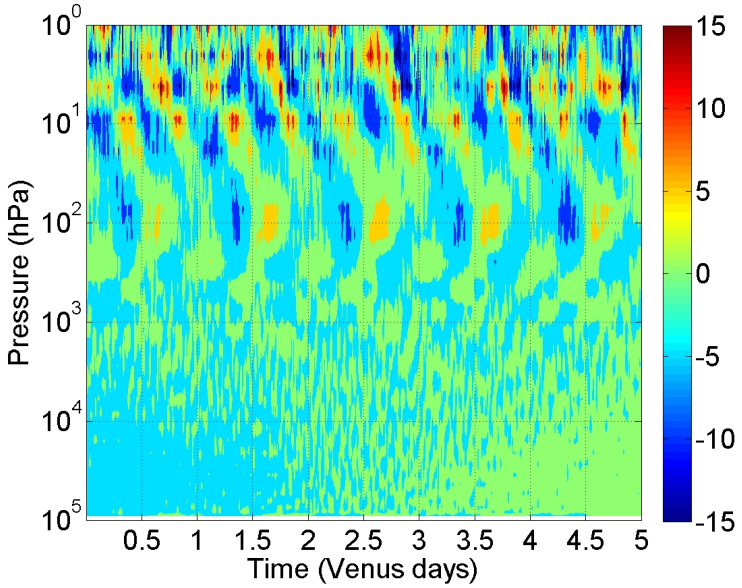

(a)

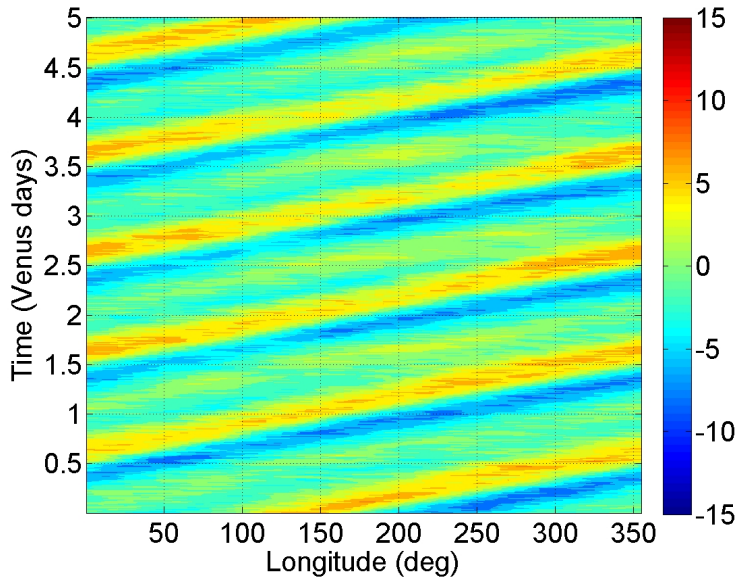

(b)

Figure 5.23: Hovmöller plots of temperature variability (K) for baseline results at the equator. The temperature variability in **(a)** is measured at a fixed longitude of 0° and in **(b)** is measured at a pressure level of 100 hPa. These results correspond to the last five Venus days of the ∼214 Venus day-long simulation.

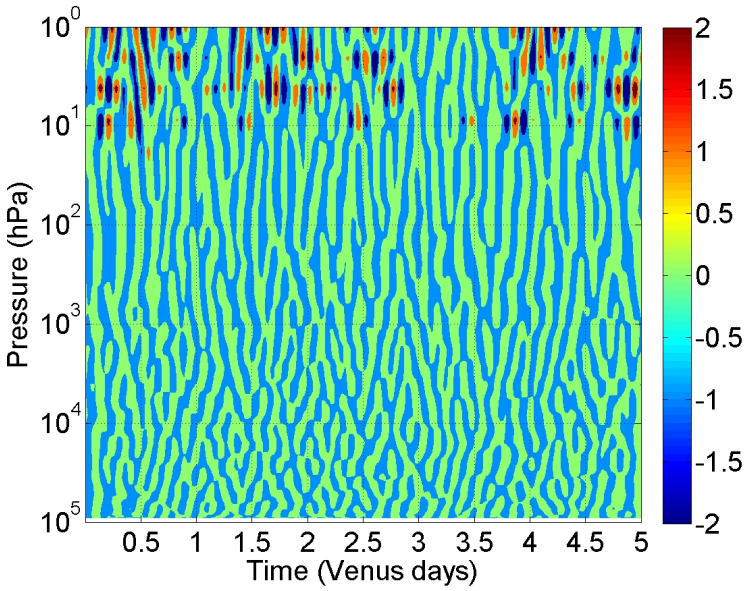

(a)

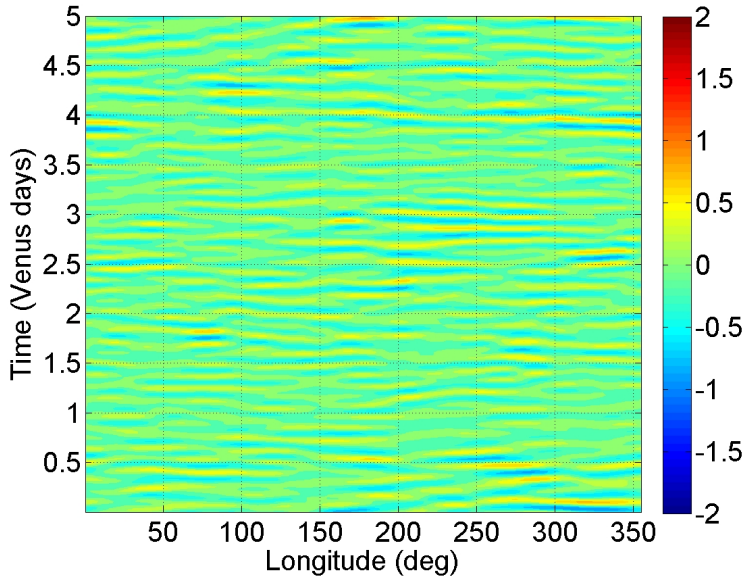

(b)

Figure 5.24: Hovmöller plots of temperature variability (K) for baseline results at mid-latitudes (45°N). The temperature variability in **(a)** is measured at a fixed longitude of 0° and in **(b)** is measured at a pressure level of 100 hPa. These results correspond to the last five Venus days of the ∼214 Venus day-long simulation and the data filter for periods between 0.1 and 0.2 Venus days.

Two high latitude waves with quasi-bidiurnal periods are also found in the temperature field and are shown in Figs. 5.25 and 5.26. The amplitude of these waves is roughly 1.5 K, and is related to the two low-frequency waves found before in the zonal wind field (Fig. 5.15). A wave with a quasi-bidiurnal period, was also found by Lebonnois *et al.* (2010a) but not explored. These simulated waves have a meridional component, as it is possible to see in Figs. 5.25 and 5.26. These characteristics, together with having opposite phases in the waves' zonal winds shown in Fig. 5.15 for different hemispheres, suggests that these low-frequency waves are an anti-symmetric equatorial wave mode, such as the mixed Rossby-gravity (or Yanai) wave (e.g., Andrews *et al.* 1987).

These waves have a retrograde propagation in relation to the mean flow, just as mixed Rossby-gravity waves do (Andrews *et al.* 1987). In Fig. 5.27 the maximum amplitudes of the mixed Rossby-gravity waves analysed in the temperature field are shown. As expected, the larger magnitudes are localized at higher latitudes and a minimum is obtained at the equator. For these results, a Fourier bandpass filter was applied, retaining just the waves with periods shorter than 2.5 and longer than 1.5 Venus days.

Other characteristics of these mixed Rossby-gravity waves can be found in the Hovmöller maps shown in Fig. 5.28. In these results the model data were again filtered for periods shorter than 2.5 and longer than 1.5 Venus days to focus on the long-wave properties. The results show that the temperature and zonal velocity are anti-symmetric about the equator while the meridional component is symmetric. A more detailed analysis of the mixed Rossby-gravity wave properties would require an exploration of its dispersion relation. The mixed Rossby-gravity waves are excited in the upper cloud region, and propagate upwards. It is in a region above the 1 hPa pressure level that they are mostly absorbed by the atmosphere via radiative damping (together with the thermally excited gravity waves mentioned before). Other forms of dissipation are taken into account numerically in the model such as diffusion, but this is much less relevant. These low frequency waves act in a region which corresponds to where transient waves transport angular momentum horizontally towards low latitudes. However, their contributions to angular momentum transport are small in comparison with the thernal tides or the barotropic waves associated with the mid-latitude jets. These features of the mixed Rossby-gravity waves are reflected in the zonal wind field presented before on Fig. 5.15, where eddy zonal winds are in anti-phase between each hemisphere and have significant variations with a bi-diurnal period (1.86 and 2.14 Venus days). As it was pointed out before, these variations in the wind field were found in Venus Express data in

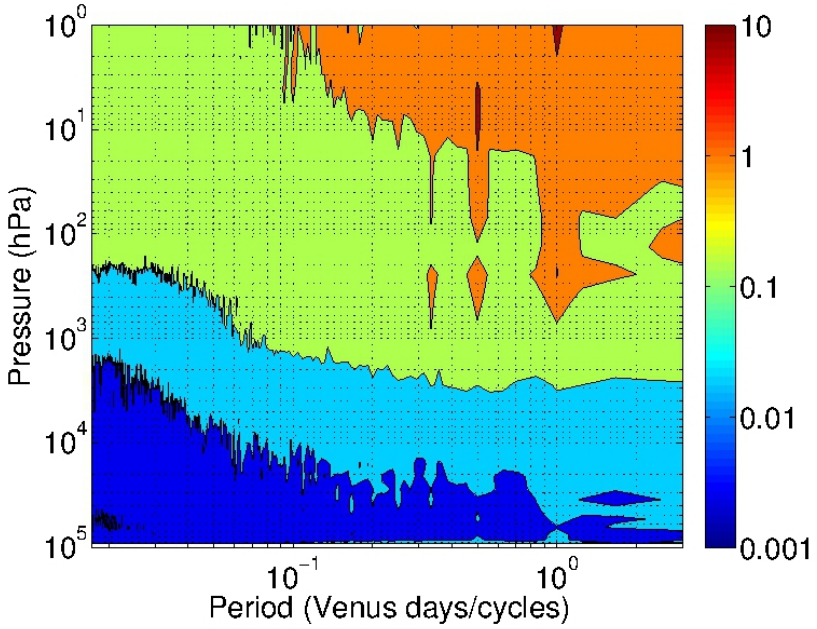

(a)

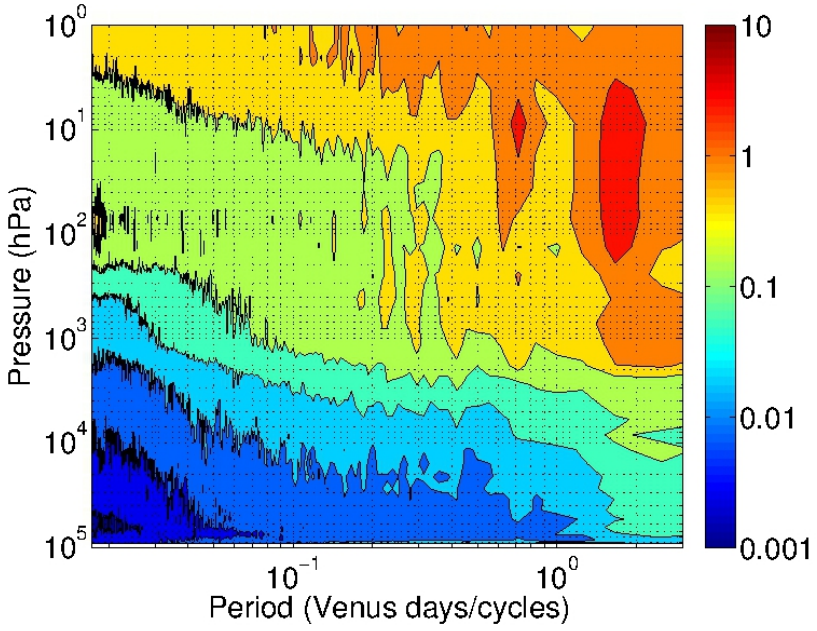

(b)

Figure 5.25: Zonally averaged amplitude spectra for the horizontal wind components (m/s) of the baseline results in the equatorial region. **(a)** is a result retrieved from the zonal wind field and **(b)** from the meridional wind component.

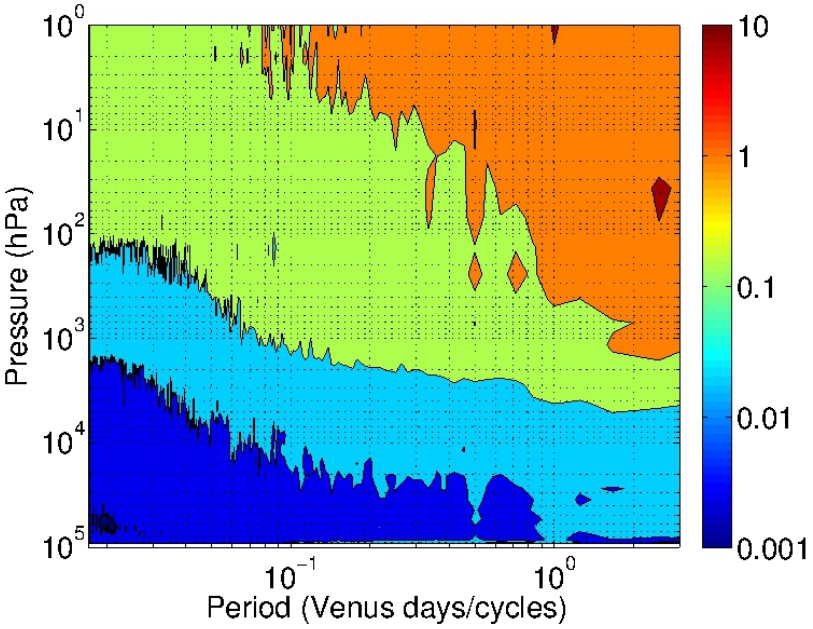

(a)

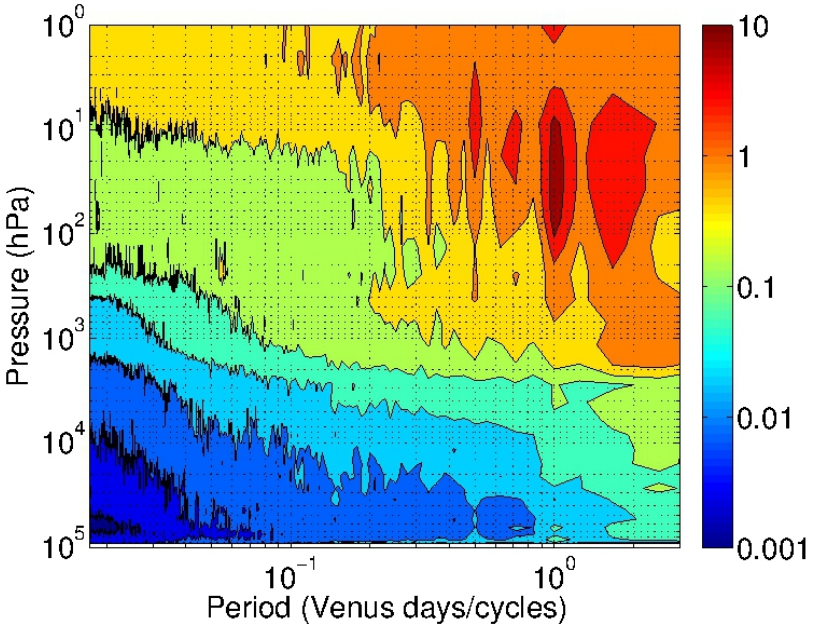

(b)

Figure 5.26: Amplitude spectra for the horizontal wind components of the baseline results at mid-latitudes. **(a)** is a result retrieved from the zonal wind field and **(b)** from the meridional wind component.

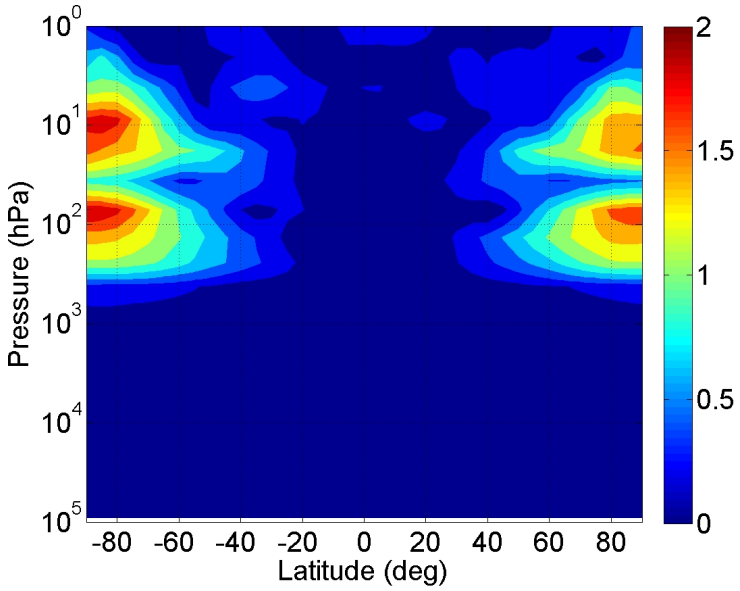

Figure 5.27: Low-frequency waves maximum amplitudes in the temperature field. A Fourier bandpass filtering was applied for periods shorter than 2.5 and longer than 1.5 Venus days.

Khatuntsev *et al.* (2013), but claimed to be a product of the natural peridiocities of the instrument.

5.8 Conclusion

The amount of solar radiation deposited at the surface can modify the global configuration of the atmospheric circulation. For certain conditions explored in this work, the model formed deep convection cells and instabilities near the surface that exerted a drag on the circulation above, inhibiting the development of a strong super-rotation. However, this problem was empirically alleviated by increasing the surface albedo for short-wave radiation. The need for larger short-wave albedos may be an indication of problems in the representation of radiative properties under the extreme atmospheric conditions of the deepest regions of the atmosphere, and/or uncertainties in the distribution of clouds and aerosols at those depths. The ability to change one parameter in the model, e.g., in the radiation code, and then to study its effects on the atmospheric circulation had an important role in this work. By exploring different amounts of solar energy absorbed by the surface we could investigate which cases would be more likely to accurately represent the physics of Venus's atmospheric

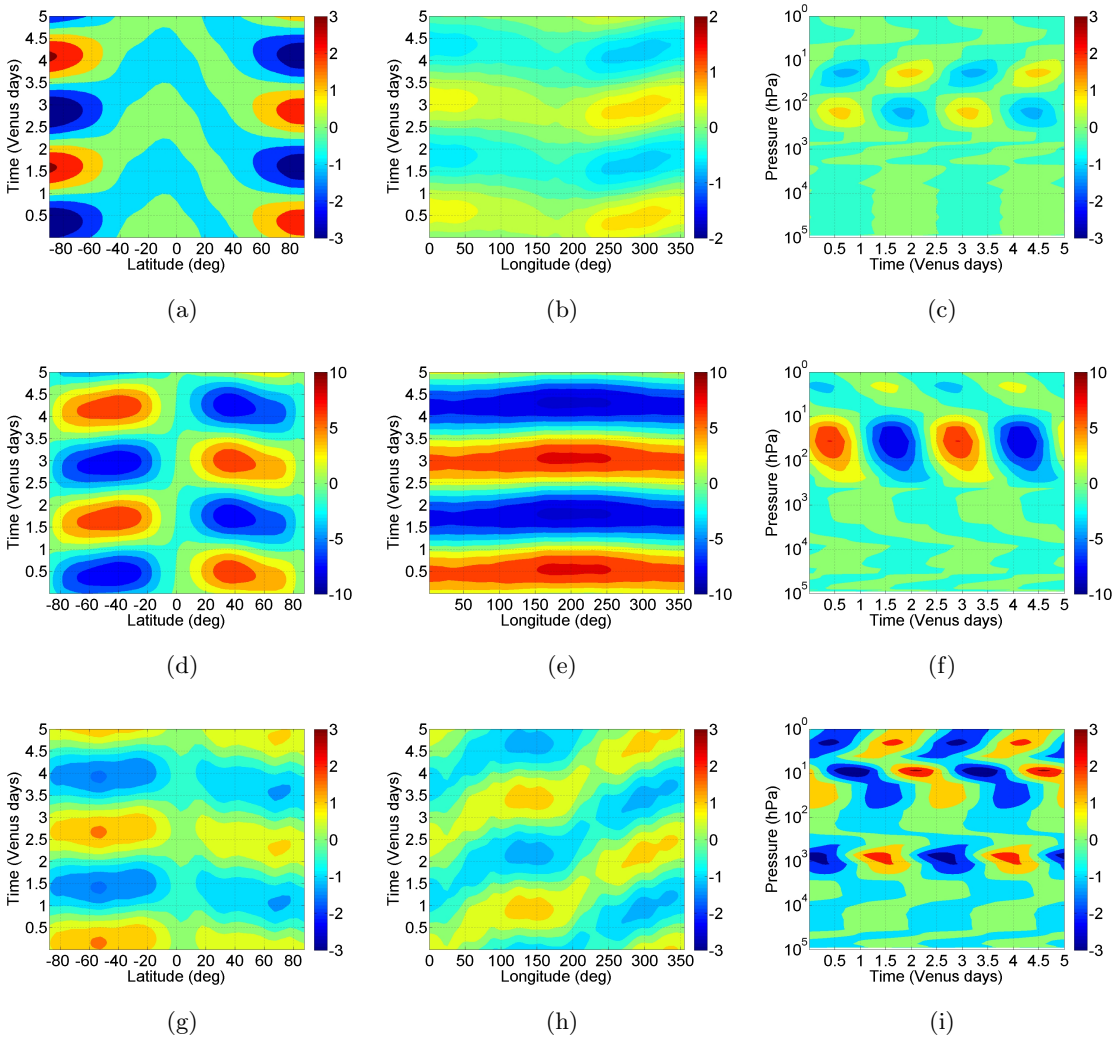

Figure 5.28: Hovmöller plots of the low frequency waves. The data shown were filtered for periods shorter than 2.5 and longer than 1.5 Venus days. The three rows correspond to the analysis of three different variables: **(a)**, **(b)** and **(c)** temperature (K); **(d)**, **(e)** and **(f)** zonal wind (m s^{-1}); **(g)**, **(h)** and **(i)** meridional wind (m s^{-1}). The three columns are times series as a function of latitude (fixed in longitude - 0° and pressure - 70 hPa), longitude (fixed in latitude - 45N and pressure - 70 hPa) and pressure (fixed in longitude - 0° and latitude - 45N).

circulation.

The OPUS-Vr has improved the agreement between the observational data and the atmospheric circulation simulated above the cloud base when compared to simplified models. The Venus atmospheric super-rotation is not a temporary state for its current atmospheric conditions, and supporting this idea are the results of long numerical simulations and the consistency between the observations over the last decades. However, the Venus atmospheric circulation is not steady. As an example, the variability of the zonal wind distribution at jet altitudes is significantly affected by long term oscillations (tens of Venus days) and the ∼bidiurnal planetary mixed Rossby-gravity waves. These low frequency waves (also found in the LMD Venus GCM, Lebonnois *et al.* 2010a) may be the same ones as found in observations by Khatuntsev *et al.* (2013).

The OPUS-Vr baseline simulation showed that the nature of the mechanisms involved in the formation of atmospheric super-rotation above and below the cloud base are different. In the upper atmosphere (above the cloud base) the strong zonal winds are the result of the contribution of momentum transport from both the zonal mean circulation and transient (non-tidal) waves. The simulations indicated two regions of significant convection: one near the cloud base and another in the upper clouds. The existence of these two dynamical regions is mainly related to the significant absorption of solar radiation in the upper cloud region and the blocking at the cloud base of upwelling infrared radiation from the hot lower atmosphere. The mean circulation is characterised in the cloud region by two planetary-scale Hadley cells in each hemisphere induced by the convection regions. The atmospheric cells on Venus are in general larger (equator-to-pole cells) than the ones found on the Earth's atmosphere, due to the weak coriolis acceleration (slow rotating planet). These circulations transport momentum poleward in the upper branches that drives the formation of mid-latitude jets but weakens the zonal winds at low latitudes. The eddy-zonal flow interactions have a crucial role in replenishing the equatorial region with angular momentum.

The Venus atmospheric dynamics includes eddy activity on all spatial scales. These dynamical fluid motions are essential in the transport of momentum and energy in the atmosphere, and to simulate the Venus atmosphere accurately they need to be well represented. Our meridional transport analysis confirmed that transient waves in the upper cloud region transport momentum towards low latitudes.

For this mechanism to work, we identified the contribution of two types of waves: thermal tides and eddy motions produced by the barotropically unstable jets. An important property

of the latter is its barotropic behaviour that avoids diffusing heat and consequently reducing the strength of the meridional circulation. However, these eddy motions have an impact on the meridional transport that is smaller than the effect produced by the thermal tides, which also have an important role in the vertical transport. In the upper cloud region, the radiative time-scale is smaller than a Venus day, and several harmonics of the thermal tides are produced. The components with largest magnitudes are the zonal wave numbers one (diurnal tide) and two (semi-diurnal tide). However in the upper cloud region it is the wave number two component that has more impact on the atmospheric circulation. It is the thermal excitation of this retrograde wave (the Sun moves slowly in the retrograde direction in relation to the mean flow) in the upper cloud region that accelerates the atmosphere in the prograde direction. In the region where the waves are absorbed (via radiative damping) by the atmosphere, predominantly above the cloud region, the forcing in the atmosphere acts in the reverse direction. The different regions of more predominant absorption or excitation drive the clear relative maxima and minima in the vertical profiles of the zonal winds seen in the simulations which are in agreement with the observations. The thermal tides are very clear in the observational data, but the same cannot be said of the other other transient waves. The main difficulty in retrieving barotropic eddy motions from observational data is the low resolution of the images available from any space mission to date.

Below the cloud base the radiative time-scale becomes much larger than a solar day, and the influence of the thermal tides in the atmosphere becomes negligible. In general, the mean atmospheric circulation in this region is apparent from the simulations as large, deep, equator-to-pole convection cells, which extend from the surface to the cloud region. Nevertheless, in common with the LMD Venus GCM (Lebonnois *et al.* 2010a), OPUS-Vr was not capable of reproducing strong zonal winds comparable with the observations in this region. Some important physical representation is evidently missing in the lower atmosphere. In chapter 8, the super-rotation of the lower atmosphere is discussed in more detail.

6

OPUS-Vr - Sensitivity simulations

6.1 Summary

The sensitivity of the simulations to some sets of parameters in the model can help us learn more about the main mechanism driving the atmosphere and the limitations of the numerical model. It is based on that sensitivity that we explore the atmospheric circulations for different sets of model configurations. We are interested to learn the impact of certain parameters in the Venus meteorology such as the ones from the radiative formulation, which in some cases are poorly constrained by the observations (e.g., optical properties in the deep atmosphere) but influence the circulation simulated.

In this chapter we explore the effect of adding extra sources of opacity in the lower atmosphere, the absence of a diurnal cycle, the convection momentum mixing representation and the impact of a realistic Venus topography.

6.2 Introduction

The evaluation procedure of the OPUS-Vr described in this chapter is an important step toward identifying the main deficiencies of the numerical model, and to have a better understanding of the main factors that are driving the atmosphere toward its currently observed dynamical state. For this reason, several parameters in the OPUS-Vr were varied. The following experiments explore the results of the OPUS-Vr when:

- additional sources of opacity in the lower atmosphere are included;
- the diurnal cycle is suppressed;

- we include a convection momentum mixing representation;
- topography is taken into account;

Some of these parameters were already explored in previous Venus GCM studies by other authors. These include the effect of no diurnal cycle or adding topography (e.g., Lee 2006 and Lebonnois *et al.* 2010a). In Lee (2006) a simplified formulation of the diurnal cycle was used in OPUS-Vs, while in Lebonnois *et al.* (2010a) a self-consistent radiative formulation allowed them to study the thermal tide influence in more detail. The latter showed that when the diurnal cycle is suppressed the main momentum transport mechanisms are via the mean circulation in large-scale Hadley cells and via the large-scale barotropic eddies associated with the high-latitude jets that transport momentum towards low latitudes (GRW mechanism). However, without the diurnal tides they concluded that strong zonal winds in the cloud region that are comparable in strength to the observed ones cannot be produced. The effect of including realistic topography in the simplified GCM shown in Lebonnois *et al.* (2011) was not conclusive due to the variety of different results. In the most recent LMD Venus GCM (Lebonnois *et al.* 2010a), the topography had an impact on the results, enabling a faster spin-up and increasing the amplitude of the jets and total angular momentum of the atmosphere.

In this chapter we also explore the influence of different optical properties in the Venus atmosphere. The structure of the radiative formulation used in Lebonnois *et al.* (2010a) does not allow the exploration of several parameters in the radiative code, because of the absence of explicit computations of the solar radiation. For that reason their sensitivity tests were restricted to the study of a reference atmosphere, to keep consistency between the atmospheric composition in the thermal and solar radiation routines. This difficulty is overcome in our work, which uses a more versatile radiative transfer formulation as described in chapter 3. In the following sections, the radiative properties of the lower atmosphere were an important motivation for these sensitivity experiments, since it is in this region where we find large uncertainties.

6.3 Additional opacities in lower atmosphere

In the previous chapter we showed how it is necessary to increase the surface albedo in the short-wave scheme in order to obtain a realistically super-rotating atmosphere. This

reduced the amount of solar radiation absorbed by the surface and consequently reduced the intensity of the deep convection near the surface. The need to adjust this albedo suggests that there are significant errors in the assumed radiative properties of the atmosphere and surface under the extreme conditions prevailing in the deep atmosphere and/or inadequacies associated with uncertainties in the distribution of clouds and aerosols in this part of the atmosphere. Two experiments are discussed next in which the radiative absorption in the lower atmosphere was increased while retaining the reference albedo mentioned in chapter 3 ($\alpha < 0.15$): (**a**) by including an extra amount of aerosols prescribed near the surface (between 1 - 2 km) or (**b**) by correcting the total gas opacity to be more efficient at absorbing solar radiation below the cloud base.

In these cases the parameters of the extra opacity were calibrated to change the amount of solar radiation that is absorbed by the surface to match the case where the surface albedo of 0.95 was used in the solar radiation scheme. Fig. 6.1 shows the globally averaged net solar flux. The black solid line corresponds to VIRA data derived from observations (Moroz *et al.* 1985). The blue line represents the net flux for the simulation using a reference surface albedo for the short-waves, and as we saw in the previous section the amount of solar energy absorbed by the surface is overestimated by roughly 65%. If the surface albedo is increased to 0.95 (baseline simulation), the cyan line is obtained, which represents results in general much closer to the VIRA profile. An almost identical result is obtained when a thin aerosol deck is included near the surface. In this case the optical properties at long-waves were also changed but the impact on the thermal fluxes is negligible. The case with extra gas opacity in the short-wave range in the lower atmosphere also has a profile closer to the observed ones, but in this one the variation with altitude is different than in the other experiments. At 10^3 hPa the net solar fluxes are similar to the ones calculated with the reference albedos, but converge to profiles closer to the observations at lower altitudes.

6.3.1 An aerosol layer near the surface?

In the first case, a layer of scattering/absorbing aerosols near the surface was included in OPUS-Vr, which started integrating from an atmosphere at rest (IRVA). The possibility of the existence of a cloud deck near the surface was previously suggested by Grieger *et al.* (2004) from reanalysis of Venera 13/14 spectrophotometry data. In Fig. 6.2, the pronounced peak in the extinction profiles near the atmosphere (1-2 km) is clearly seen in both Venera probes data (Grieger *et al.* 2004). Despite the debate on the quality of these data near

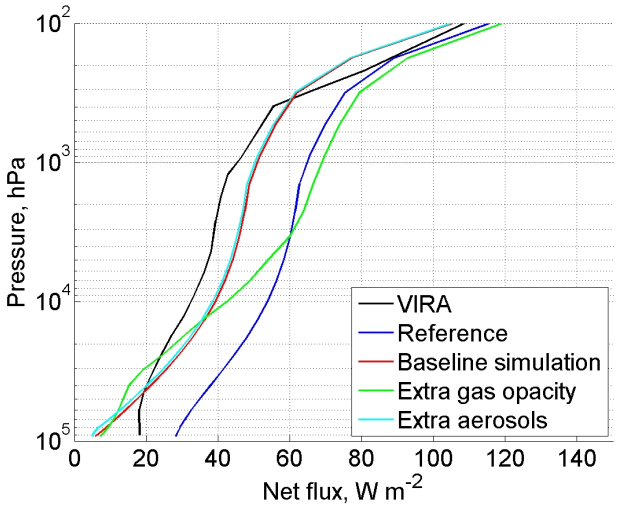

Figure 6.1: Global averaged total downwards solar flux in simulations with extra opacities in the lower atmosphere. The black line represents the VIRA profile (Moroz *et al.* 1985). The other color lines are: blue is the simulation that uses the reference albedo, red is from the baseline simulation, green is from the experiment where the gas opacity was increased in the lower atmosphere and cyan is from the experiment that takes into account an extra aerosol deck near the surface.

the surface, it is intriguing that the results of both Venera probes consistently indicate a possible peak in the extinction profiles near the surface and up to altitudes of 20-30 km (Grieger *et al.* 2004).

The possibility that an additional source of short-wave opacity in the deep atmosphere raises the obvious question as to how this might originate. The hot and massive atmospheric conditions near the Venus surface rules out many materials as possible condensible species. Schaefer & Fegley (2003) suggested that compounds of Pb and/or Bi such as Bismuthite (Bi_2S_3) and/or Galena (PbS), would be likely to condense at 2-5 km altitude. Other processes which do not involve condensation are also possible, however, including volcanic ash from volcanic eruptions and aeolian processes lifting mineral dust from the surface.

Direct observations of volcanic eruptions have never been seen, however, although the observed episodic sulphur dioxide injections in the upper clouds could be an indirect indication of volcanic plumes present in the lower atmosphere (Marcq *et al.* 2013). Aeolian dust lifting at the surface is also very likely to occur in Venus due to the atmospheric conditions found near the very dry surface, yet reservoirs of fine particles and also surface winds capa-

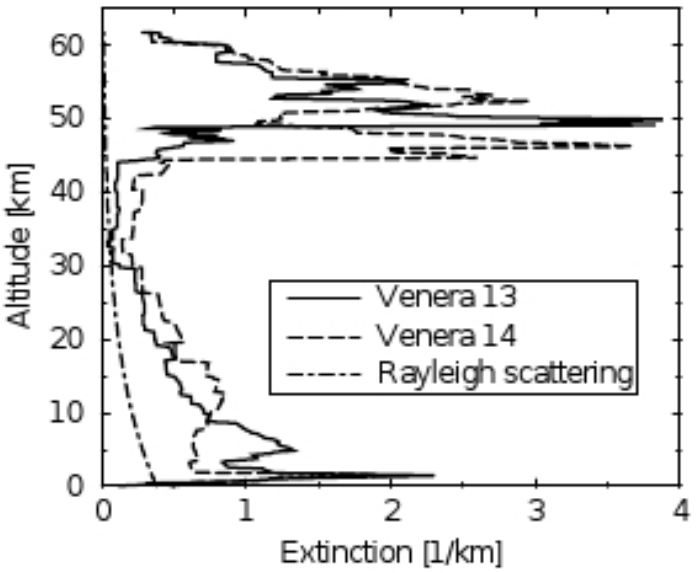

Figure 6.2: Extinction profiles retrieved from Verera 13 and 14 spectrophotometer data at 700-710 nm (Grieger *et al.* 2004).

ble of raising those particles are needed. In images from the Venus orbiter Magellan, dunes with lengths ranging from 500 m to 10 km and 200 m wide were identified (Greeley *et al.* 1992). The wind streaks associated with the dunes suggest that these reservoirs of small particles are in transverse forms, where the dune crests are perpendicular to the prevailing wind direction (Greeley *et al.* 1992). In Weitz *et al.* (1994) they claim that, due to an inadequate angle of the radar beam from Magellan observations, it was not possible to detect small dunes (microdunes). In order to estimate the sizes of the most easily lifted particles and also the threshold friction velocity, we used the following equation,

$$v_{\star t} = A_N \sqrt{\frac{\rho_p - \rho_a}{\rho_a} g D_p + \frac{\gamma}{\rho_a D_p}}, \tag{6.1}$$

where A_N is a dimensionless parameter, ρ_p and ρ_a are the particle and atmospheric densities, D_p is the particle diameter, g is the constant of gravitational acceleration and γ is a parameter that scales the strength of the interparticles cohesive forces. This simple expression was suggested in Shao & Lu (2000), and balances the aerodynamic drag and lift forces against the gravity and interparticle cohesive forces. The atmospheric density needed to solve the

above equation was computed from the ideal gas law assuming a temperature surface of 750 K and pressure of 92×10^3 hPa. The other parameters used were set to $A_N = 1.1$ (Shao & Lu 2000) and $\gamma = 2.9 \times 10^{-4}$ which was estimated in Kok & Renno (2006). As we pointed out in previous chapters, the Venus surface is mainly composed of basalt, so the expected sand density at the surface is $\rho_p = 3000$ kg/m^3 (Kok *et al.* 2012). Fig. 6.3 shows a plot of the saltation fluid threshold as a function of equivalent particle diameter for the Venus case. The minimum obtained indicates the most easily lifted particle size, which from our calculation has a diameter of 106 μm and a saltation threshold of 3.2 cm/s. From its size this particle is considered a sand particle (between 62.5 and 2000 μm of diameter, Kok *et al.* 2012). The small threshold is mainly due to the large air density in the deep Venus atmosphere.

The lowest layer in OPUS-Vr is located at roughly 50 m altitude. To estimate what would be the minimum wind speed at 50 m altitude that could lift particles with a diameter of 106 μm, we used the following equation assuming a logarithmic wind law,

$$u = \frac{v_{\star t}}{k} \ln \frac{z}{z_0} \tag{6.2}$$

where k is the von Kármán constant (k approximately equal to 0.4), z is the altitude ($z = 50$ m) and z_0 is the roughness length (assumed to be $z_0 = 0.03$ m in the OPUS-Vr). The value obtained is approximately 0.6 m/s. In the baseline simulation of OPUV-Vr, the order of magnitude of the wind speed at the lowest level is cm/s. However, if the short-wave albedo of the surface is reduced to the reference values shown in chapter 3 ($\alpha < 0.15$), so that the surface absorbs more incoming solar radiation, the magnitude of the winds near the surface will actually increase. In those experiments, the wind speed was found to reach a few dm/s, which can therefore occasionally exceed the threshold limit. The amount of particles lifted can work as negative feedback on the lifting process, since they will reduce the solar energy that reaches the surface.

Upon estimating the possibility of a persistent dust/sand haze in the atmosphere we can examine the ratio of diffusive time constant τ_d (turbulent upward diffusion) to the settling time constant τ_s (gravitational settling) as suggested in Hess (1975). When $\tau_d/\tau_s \gg 1$, settling dominates and the presence of hazes are not expected. In the case of a small ratio the vertical diffusion process has a larger weight and allows particles to stay suspended in the atmosphere. However, this depends on the atmospheric circulation which varies with

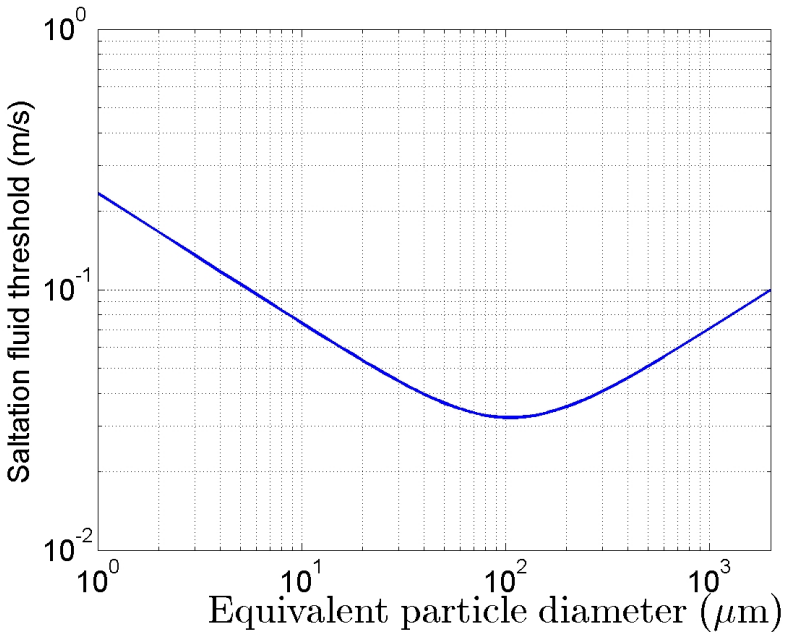

Figure 6.3: Saltation fluid threshold against particle diameter for Venus conditions. The analytic expression used to compute the profile was derived in Shao & Lu (2000).

location. Doing some scaling analyses of the variables involved, Hess (1975) proposed for the lowest 50-100 m,

$$\frac{\tau_d}{\tau_s} \approx \frac{v_t}{k v_{\star t}}, \tag{6.3}$$

where v_t is the Stokes velocity and the other variables are the same as in Equation 6.2. Using the results obtained above on the properties of the most easily raised particle, and computing its related stokes velocity (0.5 m/s using a dynamic viscosity for Venus conditions from Kok *et al.* 2012), we obtained a ratio around 39. From this result we would not expect to have suspended particles (sand hazes) at altitudes of 50-100 m. However, Hess (1975) estimates that the eddy viscosity coefficient at roughly 2 km starts to became large enough so that the upward diffusion processes became dominant.

The physics involved in aeolian processes is complex, and other contributions such as the lifting of smaller particles by impacts of larger particles at the surface can be important. In the future Venus GCM simulations including aeolian processes will allow us to study this hypothesis of dust/sand hazes formation near the surface in more detail. To study the impact of a peak in the radiative extinction profiles near the surface on the OPUS-Vr results, between 1 and 2 km altitude, a thin cloud layer of aerosols of mode 1 was included

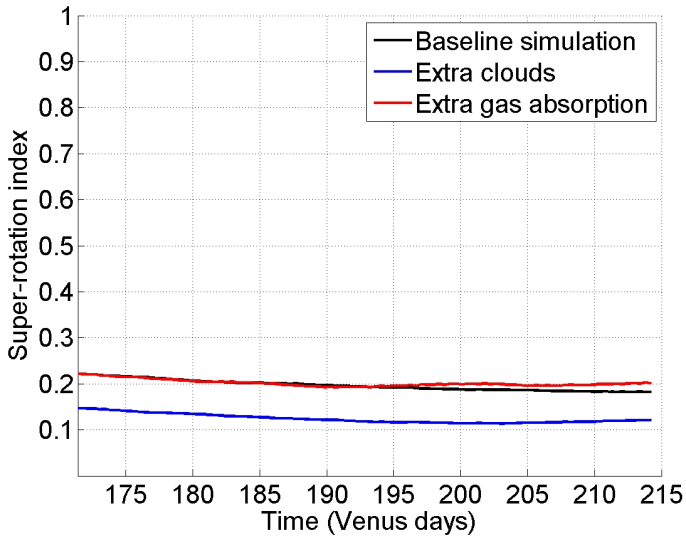

Figure 6.4: Time variation of the global super-rotation index of the simulations with extra opacities in the lower atmosphere. The black line represents the simulation using a surface short-wave albedo of 0.95, the blue one with extra aerosols near the surface and the red line includes extra gas opacity below the cloud base.

(as described in chapter 3). The density of the extra cloud deck was tuned, following a Gaussian profile in altitude, until the solar radiation absorbed by the planetary surface was the same as when increasing the surface solar albedo to 0.95. Fig. 6.4 shows a super-rotation index (S) smaller than the values obtained in the simulation that used a surface short-wave albedo equal to 0.95 (baseline simulation). As may be seen in Fig. 6.5, the main causes for the differences in S between the two simulations are associated with the prograde winds produced in the mesosphere (above the cloud base), which are weaker at the same integration time. However, as we have seen before, the winds amplitude and distribution in the baseline simulation have a cyclic behaviour, and continue to decrease after 243 days of integration. The result shown in Fig. 5.8 is very similar to Fig. 6.5(c).

6.3.2 Increasing the total gas opacity

This second simulation started from the S095VA (defined in the previous chapter), and was integrated for 43 Venus days. In this simulation the optical depth of the atmospheric gases was increased in the short-wavelength range. The extra optical depth was assumed to depend exponentially on the atmospheric pressure and temperature, and was calibrated once

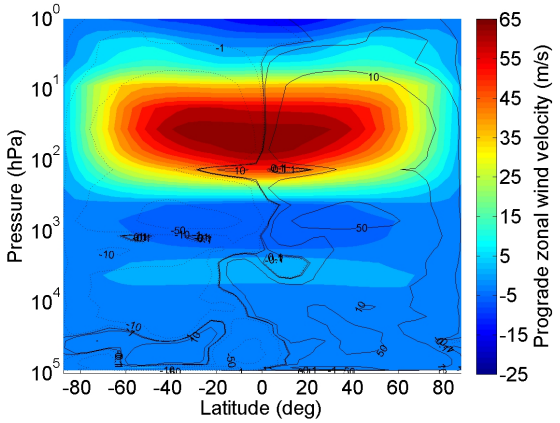

(a) Albedo = 0.95.

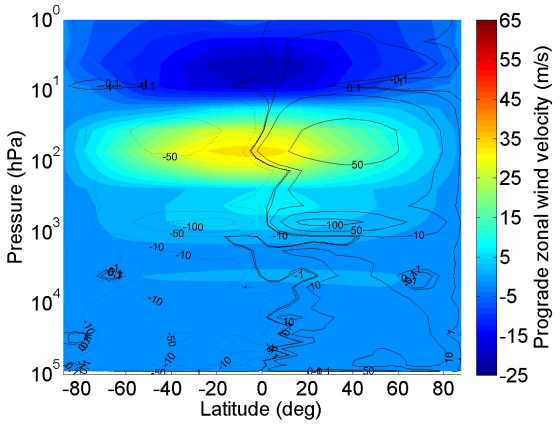

(b) Extra clouds.

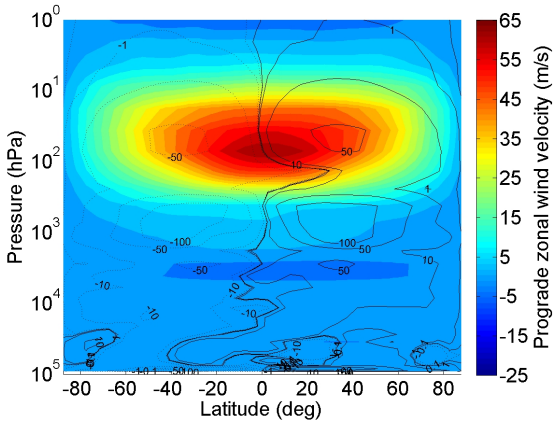

(c) Extra gas absorption.

Figure 6.5: Zonally and time averaged (5 Venus days) zonal wind and mass stream function for three simulations using three different absorption properties in the deep atmosphere in relation to the reference atmosphere: **(a)** short-wave albedo equal to 0.95, **(b)** extra clouds near the surface and **(c)** extra gas opacity below the cloud base.

again to match the value of the total absorbed solar energy in the surface in the baseline simulation using an empirical equation (the same for all wavelengths),

$$\tau_{gas} = \tau_{gas} \times c \tag{6.4}$$

$$c = \beta \times \left(\frac{T}{T_0}\right)^{\alpha_T} \left(\frac{P}{P_0}\right)^{\alpha_P}, \tag{6.5}$$

where c is the correction factor, and $\beta = 1.1$, $\alpha_T = 2.9$ and $\alpha_P = 2.9$ are empirical parameters. The correction was just applied when the atmospheric temperature (T) and pressure (P) were larger than T_0 and P_0 respectively ($T_0 = 350$ K and $P_0 = 10^3$ hPa). These values were tuned to have a larger correction in the deepest regions of the atmosphere as it is possible to see in Fig. 6.1 .

The values of S are very similar to the ones obtained in the baseline simulation. The main difference shows up in the last 17 Venus days with a slight increase in the simulated S with more gas absorption. At the day 243, S is slightly larger than 0.2. Comparing Fig. 6.5(a) and 6.5(c), we verified that when increasing the gas absorption below the cloud base, the strength of the convection cells increases, especially the ones located at the cloud base, the super-rotation winds in the upper clouds decrease, the direction of the retrograde winds in the lower cloud region (450-1000 hPa) is reversed and the winds are slightly increased throughout the lower atmosphere (below the cloud base).

6.3.3 Summary

The main objective of these two experiments was to explore the influence of changing some radiative properties in the lower atmosphere on the mean atmospheric circulation. The two atmospheric conditions explored here came out as physically plausible alternatives to the increase of the surface albedo in the short-wave range, that correct for the apparent excess of solar energy absorbed by the surface. The real cause could be a mixture of these two atmospheric conditions or even related to other factors such as inaccurate properties and distribution of clouds and the unknown UV absorber.

The results obtained in the simulation that assumes a thin cloud deck near the surface are very similar to the ones obtained in the baseline simulation. In the case where the total gas absorption in the lower atmosphere is increased the zonal winds in the prograde direction also increase, and change the wind direction in the lower cloud region. However, the winds produced in the simulation are still weak in comparison with the winds retrieved

from the observations (Schubert *et al.* 1980). The mechanisms of momentum transport in both cases are very similar to the ones obtained and analysed for the baseline simulation results.

Note that the mode 1 aerosols are very unlikely to condense in the deepest regions pointed out above. However, the aim of that experiment was to study the impact of a thin cloud layer covering the surface in the circulation produced, which could have a different composition and particle distribution from the ones proposed above.

6.4 No diurnal cycle

The diurnal cycle has been shown to play an important role in producing and maintaining strong zonal winds in the Venus mesosphere (e.g., our baseline simulation, Newman & Leovy 1992 and Lebonnois *et al.* 2010a). In this section the solar forcing in the atmosphere and surface is zonally averaged, removing the diurnal cycle effect from the simulation. From this experiment it is possible to evaluate if mechanisms such as the GRW mechanism (explained in chapter 1) alone can produce some global or local super-rotation phenomenon in the atmosphere in the absence of the daily radiative forcing.

The simulation was initialised with IRVA (defined in the previous chapter) and was integrated for ~ 214 Venus days (25000 Earth days). The surface albedo in the short-wave scheme was set to be 0.95, so we can compare directly with the baseline simulation that used the same albedo but with a diurnal cycle. Fig. 6.6 shows the evolution of the super-rotation index (S) for these two simulations, which seems to be converging to the same magnitude $S \approx 0.18$. The period represented corresponds to the last 45 Venus days of the long model integration. Fig. 6.7 shows a meridional cross-section of two zonally averaged quantities (averaged over five Venus days): the zonal winds (colour map) and the mass stream function (black contours). The convection cells obtained in this simulation are very similar to the ones from the baseline simulation (Fig. 5.13(a)), but in this case slightly stronger in the cloud region. These similarities are consistent with the identical structure of the atmosphere with respect to its optical properties (e.g., same cloud deck position). The atmospheric circulation in the lower atmosphere (below the cloud base) produces a weak jet at roughly 4×10^3 hPa. This weak peak in the zonal winds (maximum of 3 m/s) extends in latitude from 60°S to 60°N. Larger magnitudes of the winds are obtained for higher altitudes. Two high latitude jets are formed at each hemisphere and stretched from

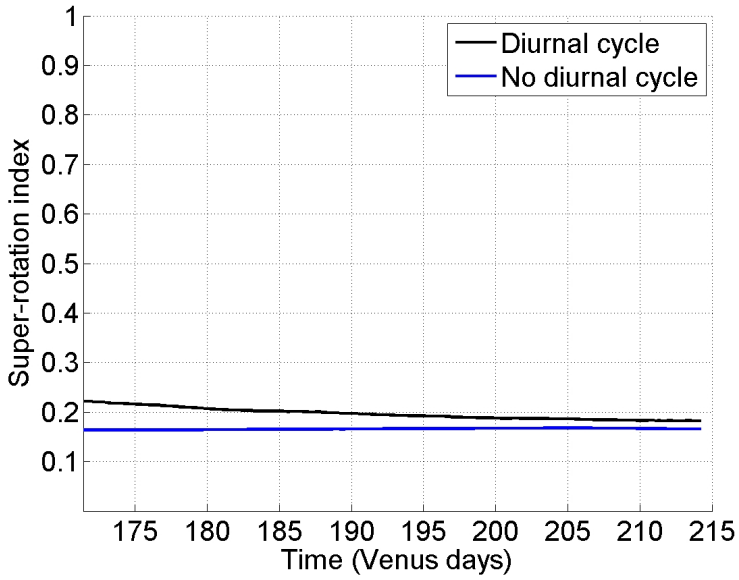

Figure 6.6: Global super-rotation index of the simulation without diurnal cycle (blue line). The black line represents the baseline simulation.

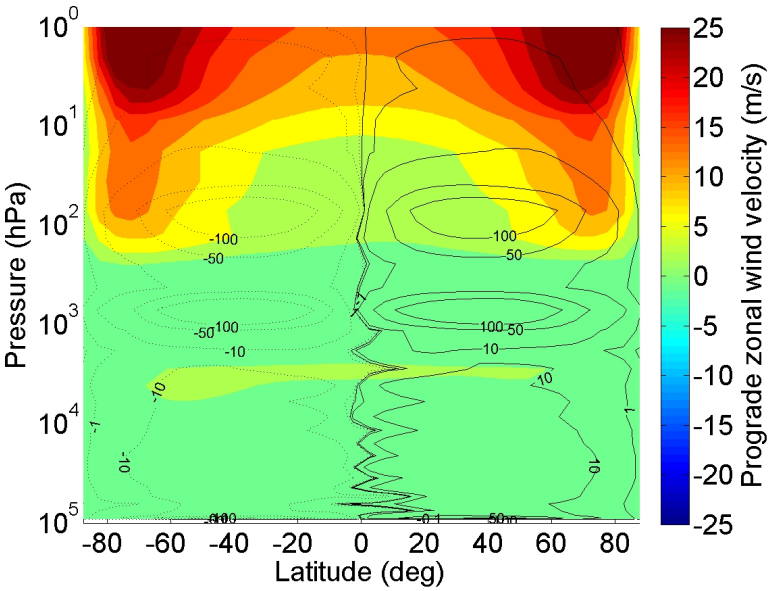

Figure 6.7: Zonally and time averaged (5 Venus days) zonal winds (m/s) and mass stream function(10^9kg/s). The colours represent the magnitude of the winds and the contour lines the mass stream function: solid lines clockwise circulation and dashed lines anti-clockwise.

pressure levels around 100 hPa to pressures smaller than 1 hPa. The jets reach a maximum of 35 ms^{-1} at around 1 hPa, and are the product of the poleward transport of momentum from a convective cell induced mainly by the solar radiation that is absorbed in the upper cloud. The winds in the equatorial region are maintained by the equatorward transport of momentum by large scale barotropic eddies such as in the OPUS-Vs simulations (GRW mechanism, chapter 1).

The influence of the thermal tides produced by the diurnal cycle is clear from this simulation. The angular momentum transport by the thermal tides is essential to produce a zonal wind field more consistent with the observations. The high latitudinal position of the jets is expected from the zonal average of the radiative forcing as it was obtained in other models (e.g. Newman & Leovy 1992 and the simplified Venus GCMs mentioned in the chapter 1). The thermal tides evidently weaken the meridional circulation in the upper clouds, bringing the jets to lower latitudes.

Studying the momentum transport in more detail, Figs. 6.8 and 6.9 show the three different contributions in the meridional and vertical directions, similarly to what was done for the baseline results. The results associated with the momentum transport due to stationary waves are again much weaker in comparison with the contribution of transient waves or mean circulation to the momentum transport. The meridional and vertical transport of momentum by the mean circulation is mainly governed by planetary convection cells at 100 hPa and 10^3 hPa (upper clouds and cloud base). Figs. 6.8(a) and 6.9(a) show that the angular momentum is in general being transported upward at low latitudes and downward at high latitudes ($> 50°$). The efficient poleward transport of momentum by the planetary Hadley cells results in the formation of high latitude jets. The negative values at low latitudes and positive at high latitudes, clear in the vertical transport plot, are associated with the retrograde zonal winds in that region. Just below the 100 hPa pressure level, within the cloud region, the mean meridional circulation transports momentum equatorward, due mainly to the lower branch of the convection region at 100 hPa.

Fig. 6.8(c) shows the meridional transport by transient waves, clearly demonstrating the correlation between regions of stronger equatorward transport and stronger zonal winds. However, in the baseline simulation the meridional transport of momentum by transient waves has a large contribution from the thermal tides. The transient waves here, are produced by instabilities of the strong winds at high latitude and have the same role as those proposed by the GRW mechanism (see chapter 1), which produce a surplus of momentum

at low latitudes and consequently accelerates the zonal winds. The vertical transport in Fig. 6.9(c) is associated with thermally excited waves traveling away from the cloudy region, but much weaker than in the baseline results.

6.4.1 Summary

The total transport illustrated in Figs. 6.8 and 6.9, shows the mean circulation as the dominant process transporting momentum in the atmosphere, forming high latitude jets above the cloud tops. The strong winds at high latitudes produce instabilities which return angular momentum to low latitudes.

The results produced in this simulation emphasize the importance of the diurnal cycle in the Venus atmospheric circulation. Without the redistribution of momentum by the thermal tides, the model is unable to produce results consistent with the observations.

6.5 Mixing momentum in convection

The new simplified convection scheme developed as the default scheme for OPUS-Vr does not take into account the exchange of momentum between the model layers during atmospheric convection. The intensity of this physical phenomenon is difficult to estimate even with more complex parameterisations, and is usually constrained using empirical parameters. However, a simple approximation was explored, which was first suggested by Hourdin *et al.* (1993). The intensity of the momentum mixing in a statically unstable column depends on the amplitude of the thermal adjustment:

$$\alpha = \frac{\int_{z_{bot}}^{z_{top}} |\theta - \bar{\theta}| \rho dz}{\int_{z_{bot}}^{z_{top}} \bar{\theta} \rho dz},\ \bar{u} = \frac{\int_{z_{bot}}^{z_{top}} u \rho dz}{\int_{z_{bot}}^{z_{top}} \rho dz},\ \bar{v} = \frac{\int_{z_{bot}}^{z_{top}} v \rho dz}{\int_{z_{bot}}^{z_{top}} \rho dz},$$

$$u_{new} = u + \alpha(\bar{u} - u), \tag{6.6}$$

$$v_{new} = v + \alpha(\bar{v} - v),$$

where z_{top} and z_{bot} are the altitudes at the top and bottom of the unstable column. This equation gives a qualitative estimate of the momentum mixing during a natural convection event and has a larger impact for larger instabilities. In this equation, $\bar{\theta}$ is the mean potential temperature computed in the reference convective adjustment scheme from chapter 4.

In order to study the impact of this simplified form of representation of angular momentum mixing during upward convection, OPUS-Vr was integrated for $\sim$ 214 Venus days from

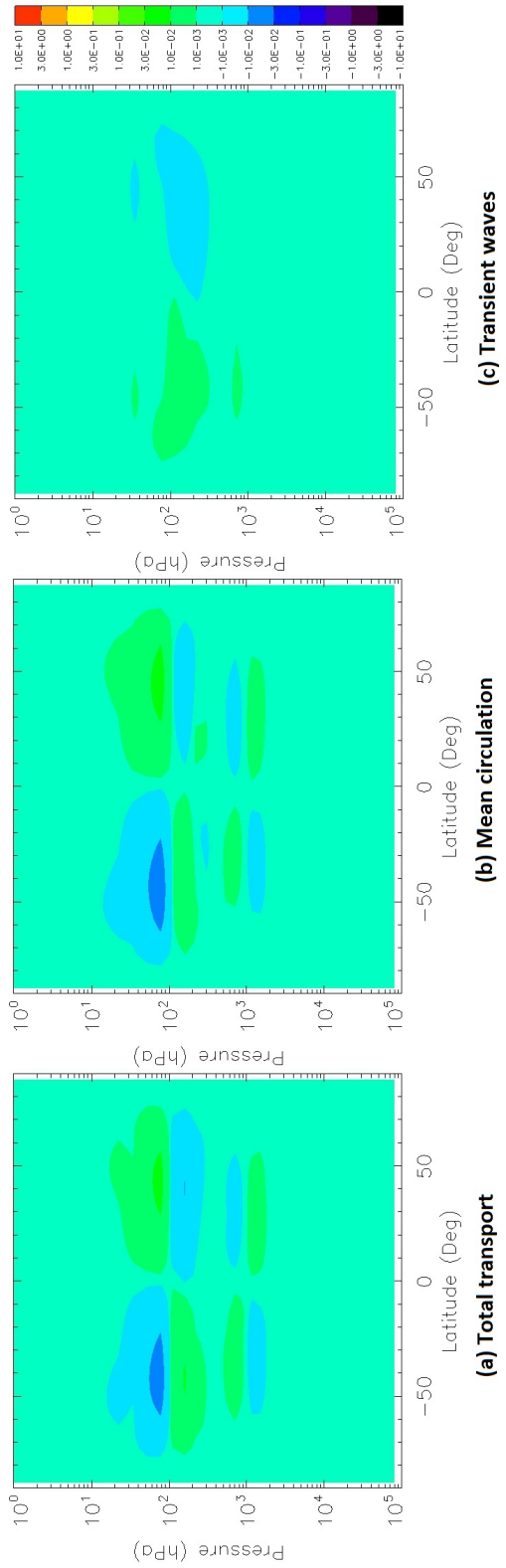

Figure 6.8: Meridional transport of angular momentum in the simulation without diurnal cycle. The data used to produce these results correspond to the last five venus days of the simulation. $v\bar{M}$ is the net transport, $[\bar{v}][\bar{M}]$ is the mean circulation and $[v^{\star}[M^{\star}]$ is the transient waves. The units of the colour bars are in (kg m^3 s^{-2})$\times 10^{24}$.

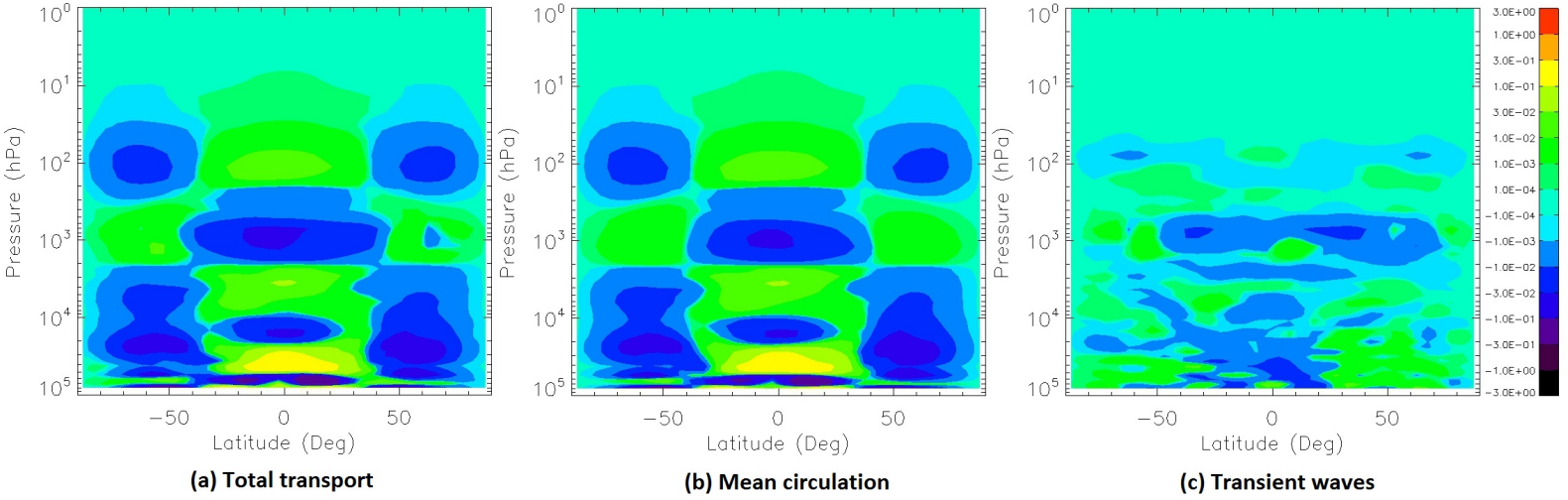

Figure 6.9: Vertical transport of angular momentum in the simulation without diurnal cycle. The data used to produce these results correspond to the last five Venus days of the simulation. $w\bar{M}$ is the net transport, $[\bar{w}][\bar{M}]$ mean circulation and $[\bar{w}^{\star}[\bar{M}^{\star}]$ is the transient waves. The units of the colour bars are in (kg m^3 s^{-2})$\times 10^{24}$.

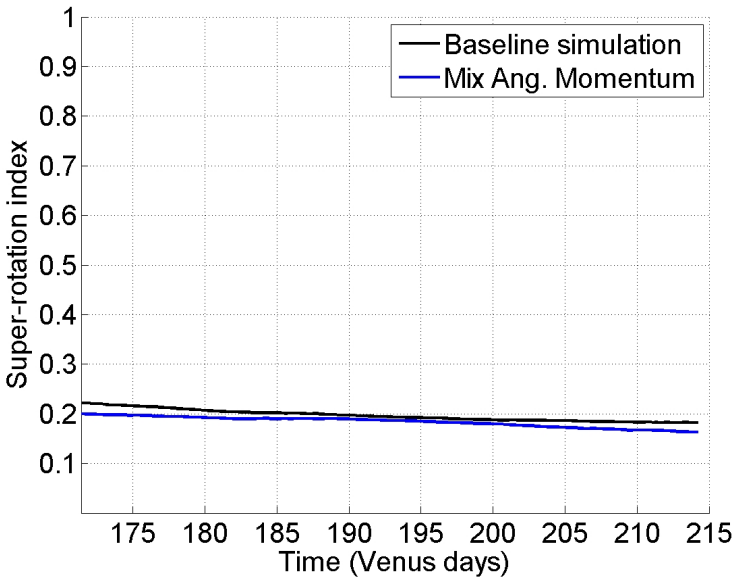

Figure 6.10: Global super-rotation index for simulations testing the effect of including mixing of momentum in convective adjustment. The black line represents the baseline simulation and the blue line the simulation that includes the simple representation to mix angular momentum during convective adjustment.

IRVA and the surface albedo in the short-wave scheme was set to 0.95 (the same as the baseline simulation). Fig. 6.10 shows the global super-rotation index (S) for two simulations: the baseline simulation and the same but with a simple representation of momentum mixing during convective adjustment. The two lines are very similar and have the same trend for the integration period shown. Fig. 6.11 shows also similar maps of mean mass stream function and zonal winds. The main differences are the slightly stronger zonal winds in the prograde direction in the region 100-10 hPa (upper cloud region), and a larger region of retrograde winds in the 400-2000 hPa layer in the simulation that mixes momentum in the dry convection adjustment routine. This version also produces a less noisy mass stream function in the deep atmosphere, which is also closer to what was obtained by Lebonnois *et al.* (2010a), who used the same parameterisation.

6.5.1 Summary

In general, the inclusion of a simplified representation of the vertical transport of momentum from natural convection did not have a significant impact in the final statistically steady

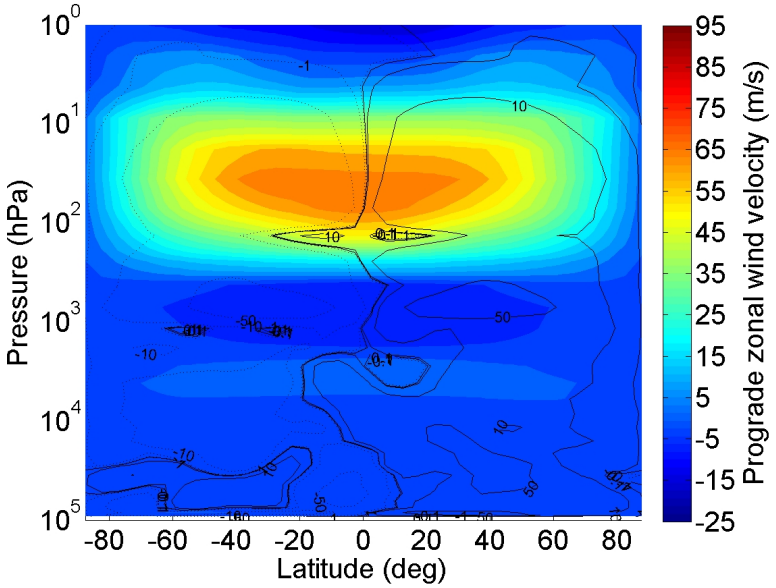

(a) Baseline simulation.

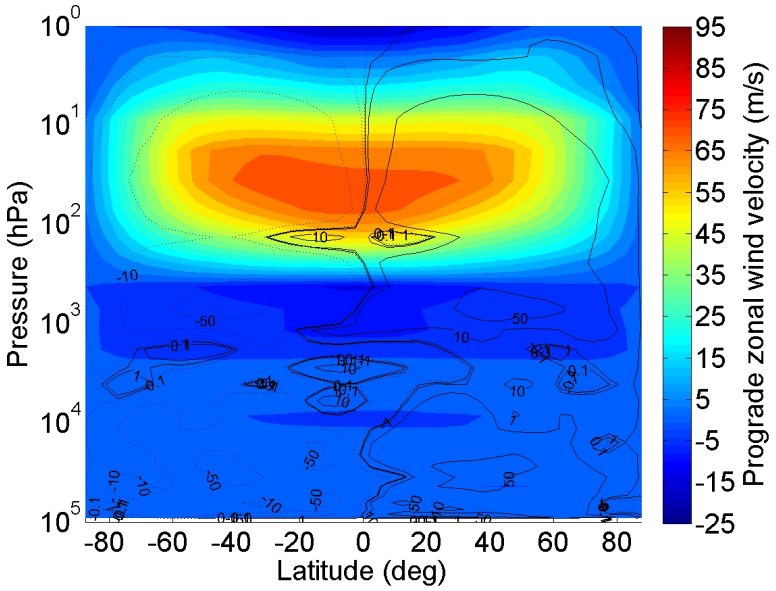

(b) Mix momen.

Figure 6.11: Zonally and time averaged (5 Venus days) zonal wind and mass stream function for 2 simulations: (**a**) is the baseline simulation and (**b**) is the simulation including representation of momentum mixing in a buoyantly unstable column. The black lines represent the mean stream-function (10^9kg/s).

state obtained. This result is in agreement with the work from Lebonnois *et al.* (2010a), who claimed that the momentum mixing during convection is most of the time much weaker (by roughly one order of magnitude) than the vertical transport by the mean circulation and transient waves. The direction of the transport by this mechanism depends on the vertical shear. In the two main convection regions (upper clouds and cloud basis) the transport of prograde momentum in this form is, in general, in the downward direction.

This parameterisation was not included in any further experiments reported here, although these results suggest for future reference that it could help to keep the natural convection effects more physical realistic in the GCM simulations. The main reasons for this are its weak impact on the final atmospheric circulation (secondary role) and to help keep the GCM as simple as possible.

6.6 Topography

The baseline simulation and previous experiments assumed a flat planet surface. However, a realistic topography has already been tested in the OPUS-Vs by Lee (2006). Using a more realistic model than OPUS-Vs, Lebonnois *et al.* (2010a) took into account the topography and showed that it influences significantly the circulation of the deep atmosphere and consequently the global super-rotation index (S). The zonal winds in the cloud region were also affected, increasing their intensity when the topography was included.

In this section we explore the impact of adding the topography on the global atmospheric circulation. The data used to define the topographic values at each surface grid point are the same as those used by Lee (2006) and Lebonnois *et al.* (2010a). This data set was obtained from the Magellan mission (Ford & Pettengill 1992). The original map is a high-resolution data set at 1° resolution in latitude and longitude, which was smoothed to the 5° resolution used by OPUS-Vr (Fig. 6.12).

The orographic field is used two times explicitly in OPUS-Vr. In the physical core these values contribute to the computation of the roughness length of the surface, and the effective values are calculated in the boundary layer parameterisation (Smith 1993a and Smith 1993b). In the dynamical core the orographic field is used to calculate the geopotential height at each GCM grid point, from the hydrostatic equation (Eq. 4.7).

Several simulation experiments carried out with the new OPUS-Vr showed some numerical instabilities when the new formulation of the dynamical core (which takes into account

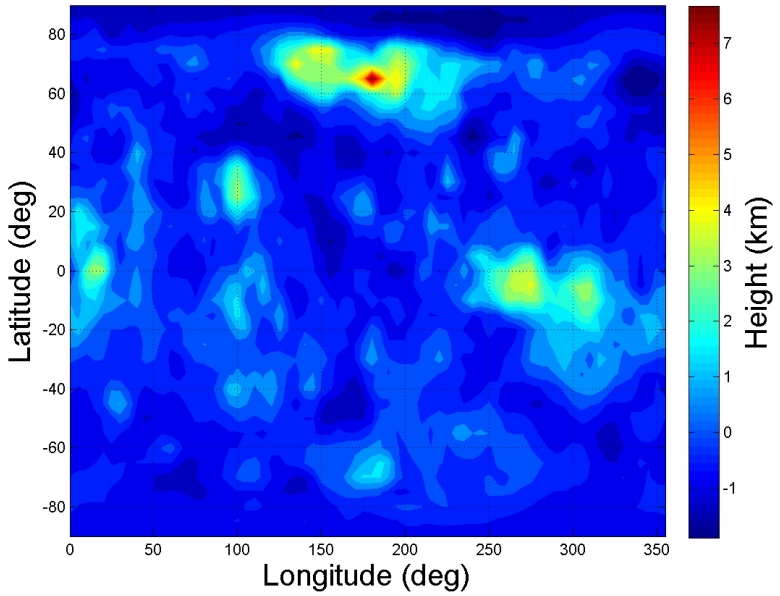

Figure 6.12: Venus topography with 5° resolution. The topography data shown here was obtained from the Magellan mission (Ford & Pettengill 1992).

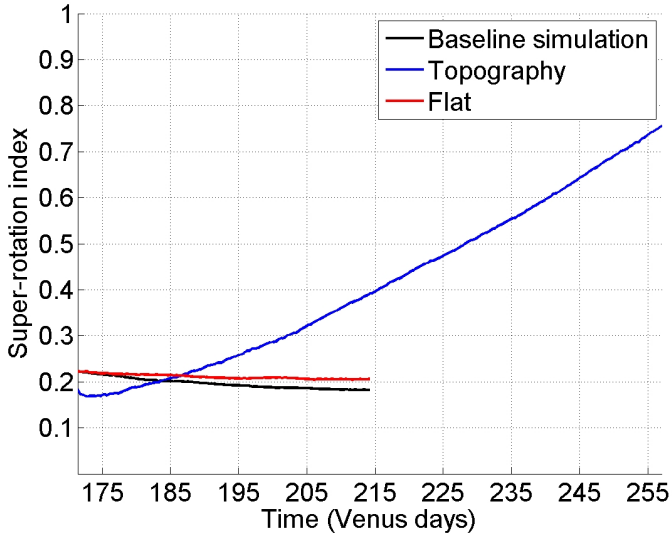

Figure 6.13: Global super-rotation index of the simulations testing the effect of adding a representation of surface topography. The black line is the baseline simulation, the blue line from using the modified OPUS-Vr with topography and the red line was obtained without topography. In the simulations represented by the red and blue lines the c_p was kept constant in the adjustment step.

the dependence of c_p with temperature) was coupled with realistic topography. The problem was identified in the adjustment routine for the calculation of the horizontal pressure gradient at each grid point, which produced unrealistic instabilities near the surface that propagate upwards. The prognostic fields show a noisy map with gravity waves breaking in the upper layers of the model's domain. The location of the largest wave amplitude is associated with the location of the highest mountains. The most satisfatory solution to this problem would be to reformulate the explicit method to a more stable formulation, but that option was not explored in this work because of insufficient time to finish the project. In the experiments with topography explored next, we instead assumed a c_p constant with temperature in the adjustment step of the dynamical core. The value of c_p assumed here is 900 $J^{-1}K^{-1}Kg$, the same as used in OPUS-Vs (see results in chapter 1).

The two simulations explored in this section started with S095VA, and were integrated for 85 Venus days with topography and 42 Venus days for a flat surface. The simulation without topography tested here was done to study if the assumption of keeping c_p constant in the adjustment step routine would allow the model to produce results consistent with the baseline simulation. In Fig. 6.13 the global super-rotation of three simulations are represented by three different colours. The black line corresponds to the baseline simulation and the red line is from the new flat planet simulation. Despite the red line having values slightly larger over the 43 Venus days it shows the same behaviour as the baseline simulation. The larger (red) values are associated with the underestimated c_p in the deep atmosphere, which makes that region more dynamically active. When the topography is included the super-rotation index evidently increases steadily with time. The 85 Venus days of model integration obtained so far are evidently not enough for the model to reach a steady state. However, the impact of the topography on the circulation of the lower atmosphere is clear.

Fig. 6.14(b) shows a zonal wind distribution and mass stream function similar to what was obtained in the baseline results. When the topography is included, Fig. 6.14(a) shows the zonal winds to be slightly larger everywhere, and especially in the atmosphere near the surface. These results are in agreement with the LMD Venus GCM results (Lebonnois *et al.* 2010a). This clearly suggests that the more turbulent flow in the deepest levels of the atmosphere in this case is linked with the presence of topography.

Figs. 6.15 and 6.16 show the meridional and vertical momentum transport by stationary and transient waves, and the mean circulation in the simulation with topography included. The results above 10^4 hPa are very similar to the ones obtained in the baseline simulation,

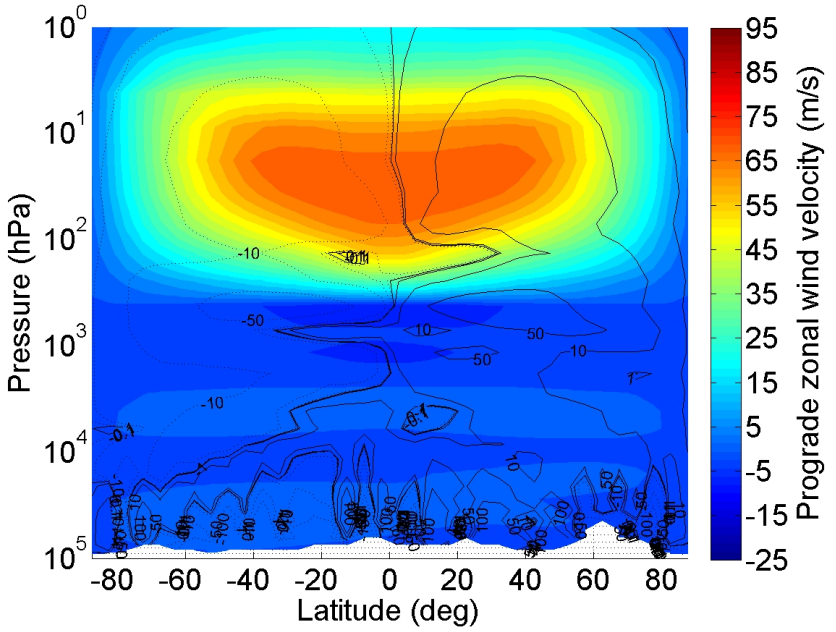

(a) Topography.

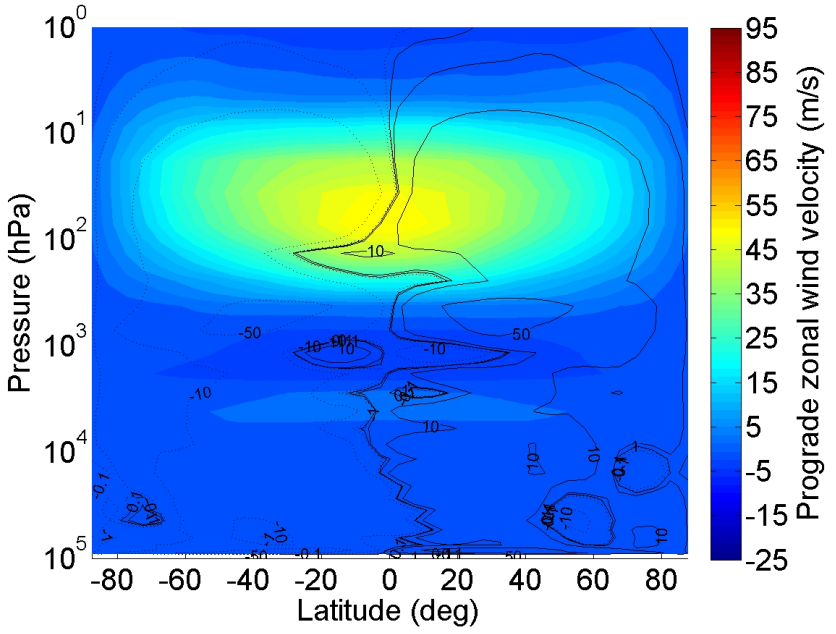

(b) Flat.

Figure 6.14: Zonally and time averaged (5 Venus days) zonal wind and mass stream function for two simulations testing the effect of topography (c_p is constant in the adjustment step): **(a)** topography is included and **(b)** without topography. The black contour lines represent the mean stream-function (10^9kg/s).

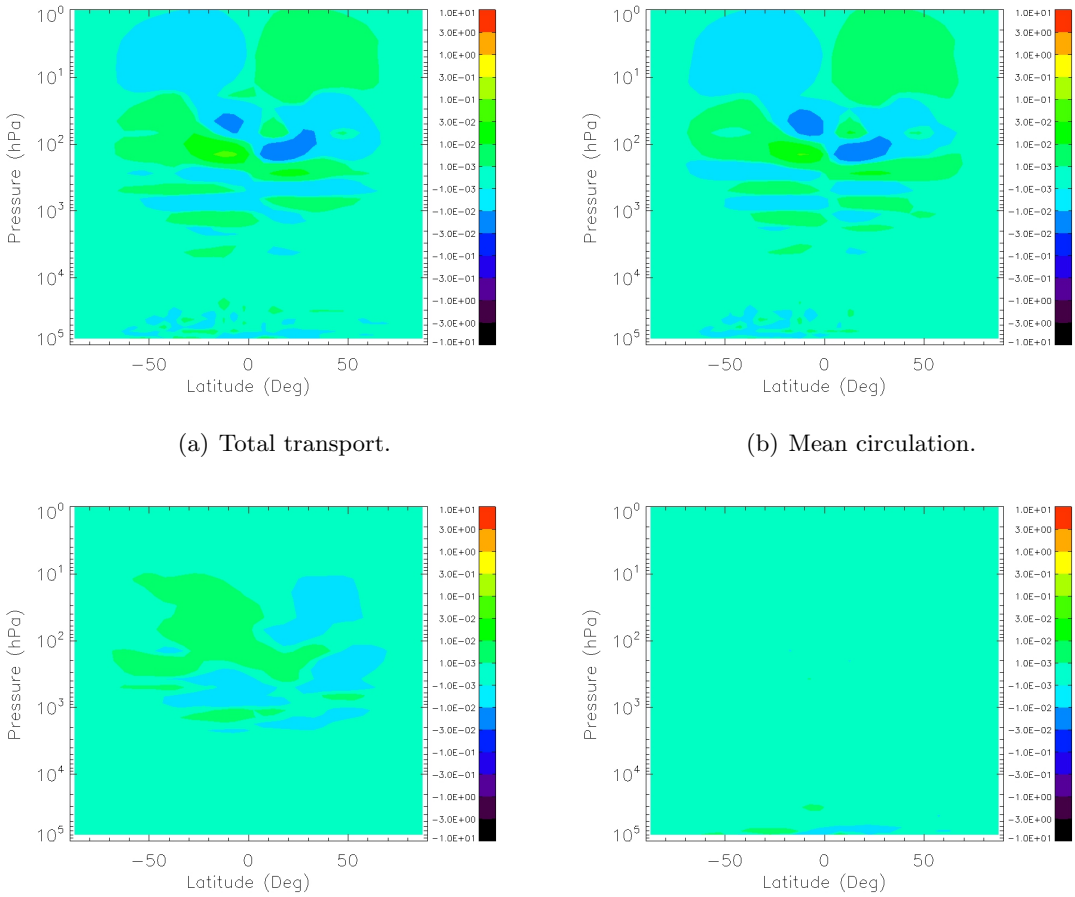

(a) Total transport.

(b) Mean circulation.

(c) Transient waves.

(d) Stationary waves.

Figure 6.15: Meridional transport of angular momentum in the simulation with topography. The data used to produce these results correspond to the last five Venus days of the simulation. $v\bar{M}$ is the net transport contribution due to: mean circulation ($[\bar{v}][\bar{M}]$), stationary waves ($[\bar{v}^{\star}\bar{M}^{\star}]$) and transient waves ($[v\bar{M}]$). The units of the colour bars are in (kg m^{3}s^{-2})$\times 10^{24}$.

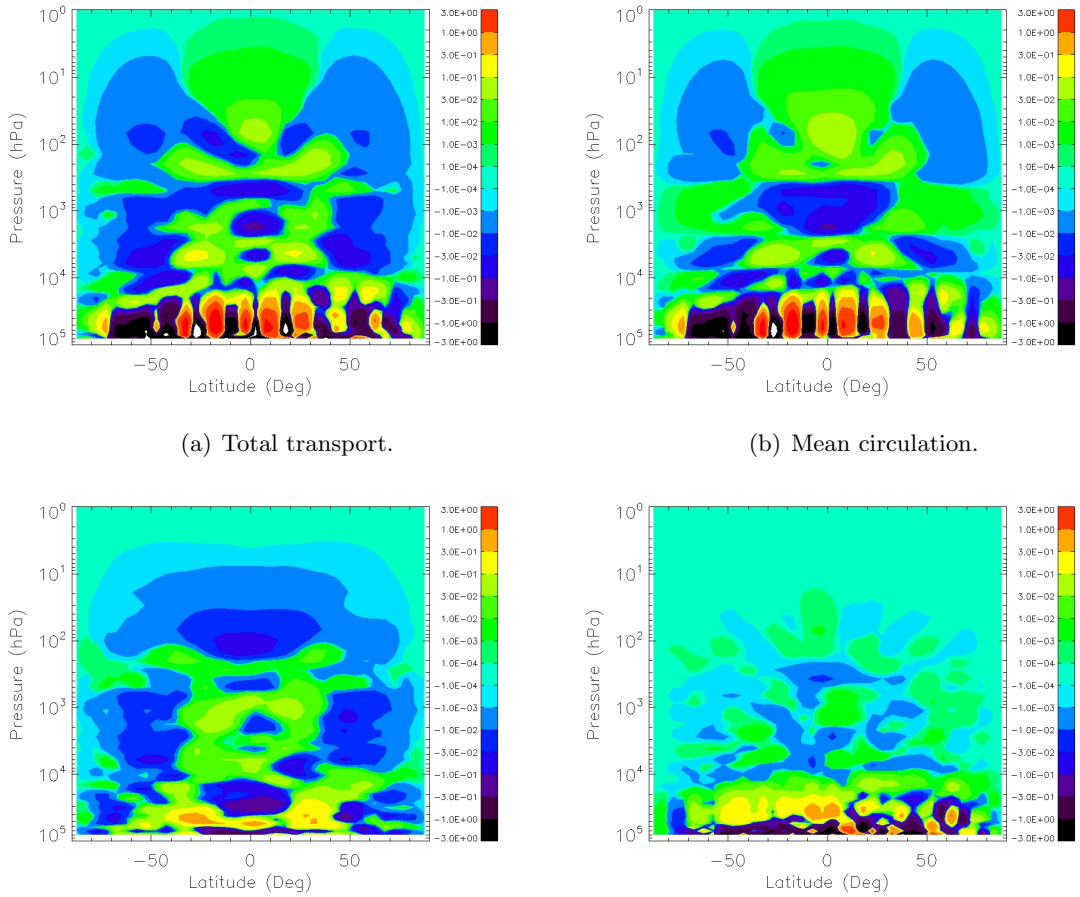

(a) Total transport.

(b) Mean circulation.

(c) Transient waves.

(d) Stationary waves.

Figure 6.16: Vertical transport of angular momentum in the simulation with topography. The data used to produce these results correspond to the last five Venus days of the simulation. $w\bar{M}$ is the net transport contribution due to: mean circulation ($[\bar{w}][\bar{M}]$), stationary waves ($[\bar{\omega}^{\star}\bar{M}^{\star}]$) and transient waves ($[w\bar{M}]$). The units of the colour bars are in (kg m^{3}s^{-2})$\times 10^{24}$

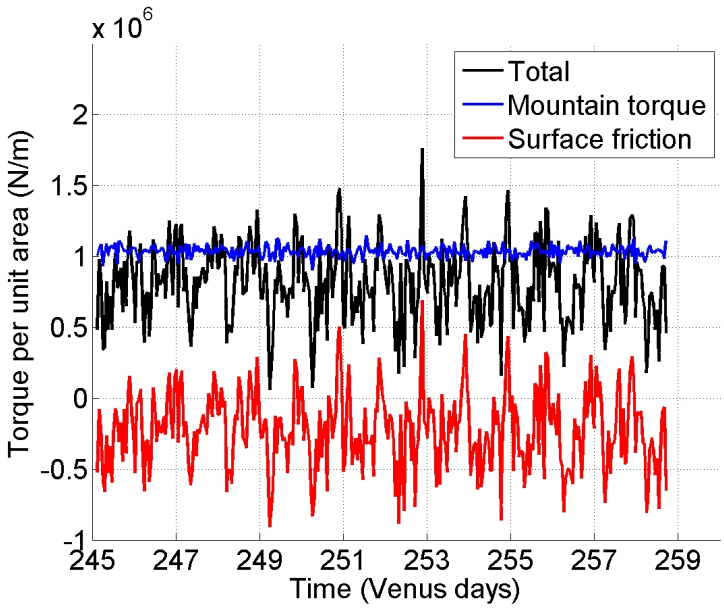

Figure 6.17: Time variations of the zonal component of the total mountain torque (blue line) and surface friction torque (red line). The total contribution of these two terms is represented by the black line.

except there is a much weaker meridional transport by transient waves. Below this altitude the topography has a significant impact on the circulation simulated. The maps of mean circulation and transient waves show complex structures near the surface. This active region is presumably due to a more turbulent state of the flow. As expected, the upward momentum transport by stationary waves is clear in Fig. 6.16(d). Fig. 6.17 shows the zonal component of the total mountain torque (MT) and surface friction torque (FT) per unit area over the last seven Venus days of the long integration. The friction term was calculated based on the accelerations induced by the boundary layer scheme at each grid box of the model. More details about the method used to compute these terms can be found in, e.g., Lebonnois *et al.* (2010a). The results in Fig. 6.17 show the form drag enabling more angular momentum to be pumped into the lower atmosphere, which is compatible with the momentum transport results shown above. The roughly steady profile is associated with the on going spin up phase of the model. This phenomenon is responsible for the increase of the prograde zonal wind amplitude in the lower atmosphere, because the total contribution of both terms (MT and FT) is consistently positive.

6.7 Conclusion

The inclusion of a flexible radiative transfer formulation has allowed us to explore the different radiative properties of the Venusian atmosphere in the model simulations. This new characteristic of OPUS-Vr is one of the main differences in relation to other existing new generation Venus models (e.g., Lebonnois *et al.* 2010a; Ikeda *et al.* 2007).

The parameters and parameterisations in the model were explored in this chapter to try to understand their importance in the atmospheric circulation modelled. Experiments testing the mixing of momentum during convective adjustments or including additional sources of opacity in the lower atmosphere did not lead to results that departed significantly from the results obtained in the baseline simulation. In the case where realistic topography was included, the model seemed capable of sustaining stronger global super-rotation and slightly greater zonal winds in the lower atmosphere. The main reason for this is that when the topography is included there is a more efficient exchange of angular momentum between the surface and the atmosphere. The effect of the diurnal cycle was also tested. In this case, the experiment showed that the meridional transport by transient waves (not including the thermal tides) alone is insufficient to produce zonal winds in the upper clouds close to the observed ones.

7

Cloud distribution experiments in OPUS-Vr

7.1 Summary

In this chapter we study the influence of different cloud structures in the Venus atmospheric circulation. We test two distinct variations in the conditions when compared with the baseline simulation: a different global amount of clouds and a different amount of the unidentified UV absorber in the upper cloud region.

The last experiment explores the effect on the circulation if the UV absorber is being actively transported with the main clouds. This test is done under some simple approximations due to the associated uncertainties. However, we aimed to explore in a first approximation the influence of a mobile, dynamically advected cloud distribution in the atmospheric circulation.

7.2 Introduction

Understanding and taking into account the role of the Venus clouds in the atmospheric circulation is crucial to better understand the global circulation and phenomena such as the global super-rotation. The active cloud feedback in the circulation remains poorly explored in general circulation models, largely because of the limited parameterisations used to represent the radiative properties of the atmosphere. In this chapter we use the flexible OPUS-Vr to study different scenarios of cloud structure. The OPUS-Vr results presented here repre-

sent a first step towards a better understanding of the impact of radiative-dynamical cloud feedbacks on the Venus global circulation.

Venus is completely covered by a cloud deck which extends from 45 to 65 km with hazes above and below. Chapters 1 and 3 described the cloud distribution and its associated optical properties. The cloud model used was based on the parameters suggested in Crisp (1986). In general, the clouds are described as a trimodal size distribution, where mode one refers to the smallest particles (hazes) and mode three to the largest particles. The particles are estimated to have a radius from less than 0.5μm up to 15μm and the cloud composition is thought to comprise 75% H_2SO_4 and 25% H_2O. However, large uncertainties are associated mainly with the composition of the smallest particles (Taylor 2006). These clouds conservatively scatter radiation mostly at visible and near infrared wavelengths, which cannot be related to the clear contrast features seen in ultraviolet (UV) images. These structures are present in the upper cloud region, and tracking their motions has been important for studying the cloud morphology and circulation in the topmost cloud level (Titov *et al.* 2012). However, its composition has not been identified yet.

A significant part of the incoming solar radiation is absorbed by the atmosphere within the cloud region, which has an important impact on the atmospheric circulation. As we saw from chapters 5 and 6, the thermal tides, excited mainly in the cloud region, have an important role in producing and maintaining the atmospheric super-rotation in this region. The mean circulation is largely influenced, therefore, by the presence of the cloud deck. The positions of two regions of upward convection are associated with the presence of the cloud deck (in the upper cloud and in the cloud base regions). The circulation in the lower atmosphere, below the cloud base, is also influenced by the cloud deck, since the clouds have a large influence in controlling the amount of solar energy that reaches this region.

In Lee & Richardson (2011) the spatial distribution of a passive tracer with characteristics of a mono-modal H_2SO_4 particles were studied, using a condensing cloud parameterisation (Lee 2006) implemented in the OPUS-Vs. The results of Lee & Richardson (2011) show that OPUS-Vs is able to produce results which are qualitatively and morphologically consistent with the observations such as: the "Y" shaped cloud structure and the decrease of the cloud top from the equator to the pole. The formation of the "Y" shape was associated with dynamical processes alone, due to advection of cloudy material by the equatorial Kelvin and mixed Rossby-gravity waves and also by the mean prograde flow. Note that

in Lee & Richardson (2011) the clouds transported do not interact with the routine that represents the radiative forcing in the atmosphere.

In the first two sections of this chapter we explore the impact on the global circulation of a reduction of the cloud amount (representing the three particle modes and the unidentified UV absorber) in order to evaluate the sensitivity of the modeled circulation to cloud radiative forcing. In the last section the influence of changing the amount of UV radiation absorbed in the upper cloud region in the global circulation is studied. This section also includes experiments where a simplified representation of the transport of the unidentified radiatively active absorber is explored. The latter experiments also allow for a qualitative analysis of the global cloud distribution.

Note: all the simulations presented in this chapter were started from the S095VA atmospheric state and also kept the short-wave albedo of the surface at 0.95 as in the baseline simulation.

7.3 Reducing cloud radiative effects

In this section we test the impact of cloud radiative forcing in Venus's atmosphere. This was most readily achieved by artificially reducing the density of cloudy material at the levels where clouds actually condense on Venus, while keeping the specific optical properties of the cloud particles fixed. Two different cloud densities in each layer were tested: density 0 to remove the effect of the clouds altogether or multiplied by 0.5 to represent half the realistic cloud density. The clouds in these two simulations refer to the three cloud modes and the unidentified UV absorber discussed before (chapter 3). The two simulations were integrated for a total of 43 Venus days.

In Fig. 7.1 the effect of cloud density on the super-rotation index (S) is shown. The results show that changes in the cloud density can dramatically affect the atmospheric circulation globally. By reducing the cloud amount, more radiation reaches the deeper atmosphere, inducing the atmosphere to adopt a more dynamically active state in that region, which then evidently contributes to an increase of S. The largest impact happens in S when clouds are removed altogether. This is clear in Fig. 7.1, where the magnitude of S is much bigger than twice the effect of reducing the clouds to 50%, so the effect must be nonlinear. The atmospheric circulations obtained are very distinct as we can see in Fig. 7.2

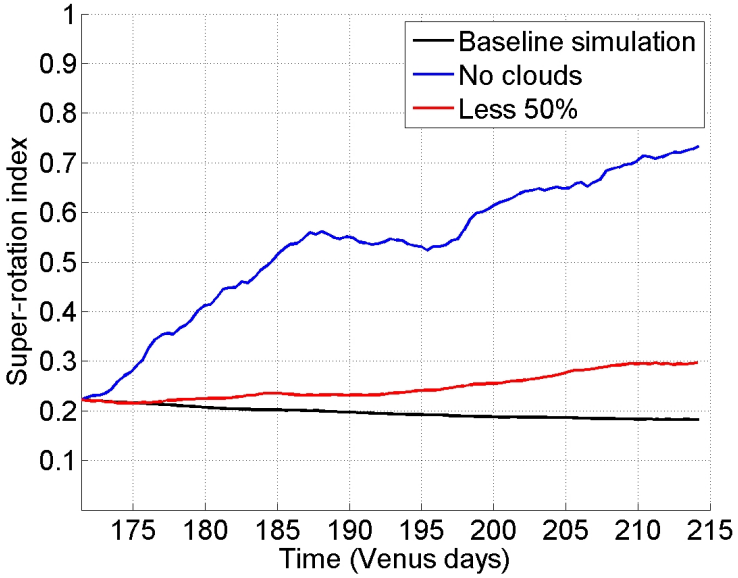

Figure 7.1: Global super-rotation index of simulations with different global cloud amounts. The black line represents the baseline simulation, the blue one represents a simulation of an atmosphere without clouds and the red line has 50% less of clouds than the baseline simulation.

and described below. In general, the region with stronger prograde winds moves deeper in the atmosphere with the reducing of the clouds amount, which consequently increases S.

Fig. 7.2(b) shows the effect of reducing the clouds to 50% of the original amount on the meridional structure of the zonal mean circulation. In this case, as was seen from the results of the 1D R-CM, the deep atmosphere evidently gets warmer due to more solar energy being able to pass through the cloud layers. This change in the thermal structure of the atmosphere also induces stronger convection cells in the cloud base region, which changes significantly the distribution of the winds. Qualitatively the most important changes are the stronger equatorial prograde jet at 3×10^3 hPa and a retrograde jet within the upper cloud region.

The effect of removing all the clouds in the atmospheric circulation is clear from the contours of the mass stream function (cf. Figs. 7.2(a) and 7.2(c)). A large part of the incoming solar radiation is now absorbed by the deepest regions of the atmosphere and surface. The mass stream function contours show the formation of large and strong convection cells, from pressure levels near the surface up to roughly 100 hPa. Two prograde jets are formed at 10^4 hPa, which causes an increase in S. An equatorial jet, this time retrograde, is also produced

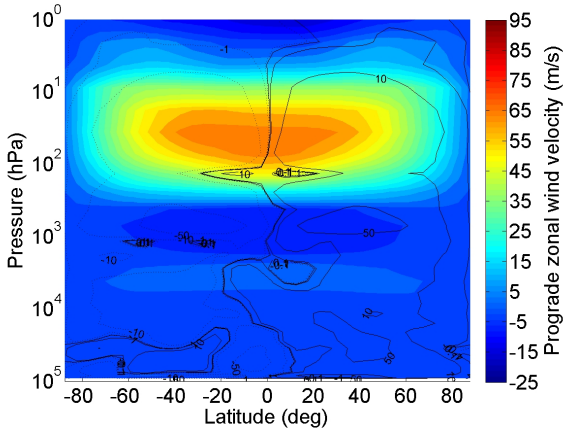

(a) Baseline simulation.

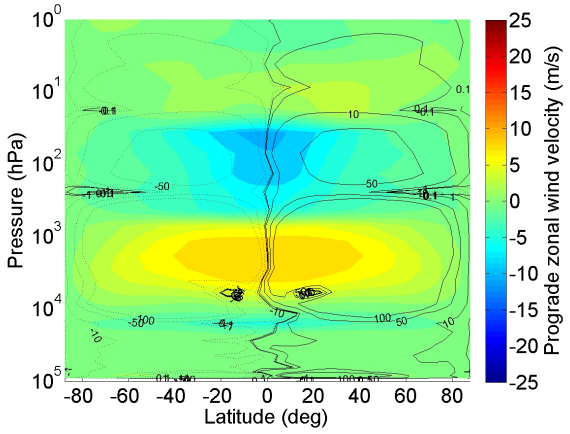

(b) Less 50% of clouds.

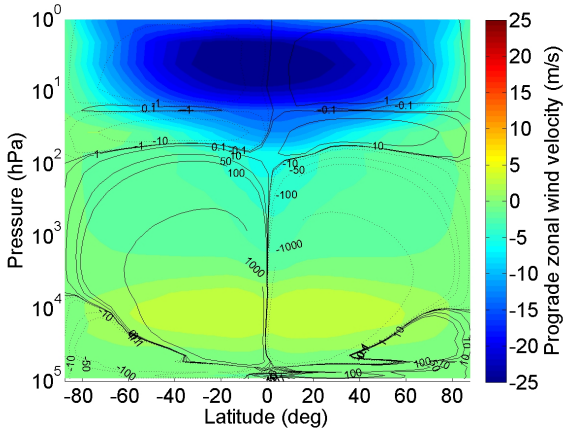

(c) No clouds.

Figure 7.2: Zonally and time averaged (5 Venus days) zonal wind and mass stream function for three simulations using different global cloud amounts: **(a)** reference cloud structure, **(b)** less 50% of clouds (3 aerosols and the unidentified UV absorber) and **(c)** no clouds.

in the atmosphere at very low pressures (5 hPa) and with a magnitude of around 25 m/s. The distribution of the mass stream function here is similar to what is obtained with the simplified Venus GCMS (chapter 1), which may suggest that the simplified thermal forcing contains a poor representation of the Venus clouds.

7.4 Different amounts of UV absorber

The presence of the unidentified UV absorber in the atmosphere has a significant impact on the atmospheric circulation and thermal structure. As was explained in chapter 3 a large part of the incoming solar energy is deposited in the upper clouds due to the presence of this UV absorber. This particular distribution of energy deposition significantly contributes to the formation of the thermally excited gravity waves in the upper clouds, which are important for the development of strong prograde winds in that region (chapter 5). However, the composition and vertical distribution of this substance in the atmosphere is still largely unknown (Esposito 1980; Pollack *et al.* 1980; Titov *et al.* 2012). Here we carry out two experiments in which we multiply the absorption coefficients of the unidentified UV absorber by a constant factor. The spatial distribution, however, is kept the same from the baseline results.

The bolometric albedo obtained in the baseline simulation is roughly 0.778, a value that is within the range estimated by observational studies: which suggest values between 0.72 and 0.79 (Taylor *et al.* 1980; Moroz 1983 and Moroz *et al.* 1985). These observational values constrain the possible range of absorption efficiency values in the UV band. The absorption coefficients of the UV absorber included in our model can be multiplied by a factor within the range [0.5-3.5], and still reproduce bolometric albedo results consistent with the observations. Other method to parameterise the amount of the UV absorber was described in chapter 3 (suggested in Crisp 1986). This method entailed tuning the spherical albedo for the UV band (between 0.3 and 0.7 μm) to match the observations changing the absorption efficiency of the unidentified UV absorber, so that it has also the same vertical distribution as the mode one cloud particles in the upper cloud region. The spherical albedo is the fraction of incident light reflected by a sphere at all angles as a function of wavelength.

In the next experiments we investigate different atmospheric circulations obtained under different conditions of absorption in the upper cloud region: absorptions of the UV absorber weaker by 50% or stronger by 50%. Each experiment was integrated for 43 Venus days. The

bolometric albedo for the two additional experiments studied here are 0.779 and 0.762, and hence are also within the observational uncertainty. Changing the UV absorption coefficient by plus or minus 50% has a negligible effect on the global super-rotation index. Fig. 7.3 shows the averaged zonal winds and mass stream-function for the modified UV absorber cases. The simulation that represents a weaker UV absorption efficiency at the upper clouds reproduces two reasonably clear mid-latitude jets. The mid-latitude jets represented in the figure have a maximum magnitude around 85 m/s, which is larger than the values obtained in the baseline simulation. The position of each jet varies with time and the wind velocity maxima can sometimes reach values larger than $\sim$ 110 m/s. The presence of the two mid-latitude jets is mainly caused by a weakening of the thermally excited gravity waves in the upper cloud region that, in turn, strengthen the Hadley circulation. The decrease in the UV absorption in the upper cloud region weakens the indirect cells at 100 hPa, and allows for more solar energy to be deposited at deeper levels. This change in the thermal structure induces stronger convection cells within the cloud region and near the surface. As a consequence of the more efficient momentum transport by mean circulation in the deep atmosphere, two weak mid-latitude jets are also formed below 10^4 hPa.

The increase by 50% of the UV absorption strengthens the transport due to the thermal tides in the upper cloud region. The results obtained in this case are very similar to those obtained in the baseline results, but now with stronger zonal winds of 80 m/s in the equatorial region.

The efficiency of the unidentified substance in absorbing UV radiation seems to have an important impact on the atmospheric circulation produced in the upper cloud region, and also in controling the solar energy deposited in the deepest regions. This amount of solar energy can have an important role in the formation of gravity waves excited by small scale convection. These waves, when absorbed in a critical-level below the cloud base, can have an influence on the development of super-rotation in the lower atmosphere. These phenomena are represented typically in GCMs by including a non-orographic gravity wave drag parameterisation (e.g., McLandress & Scinocca 2005), but this has not been explored in the present study.

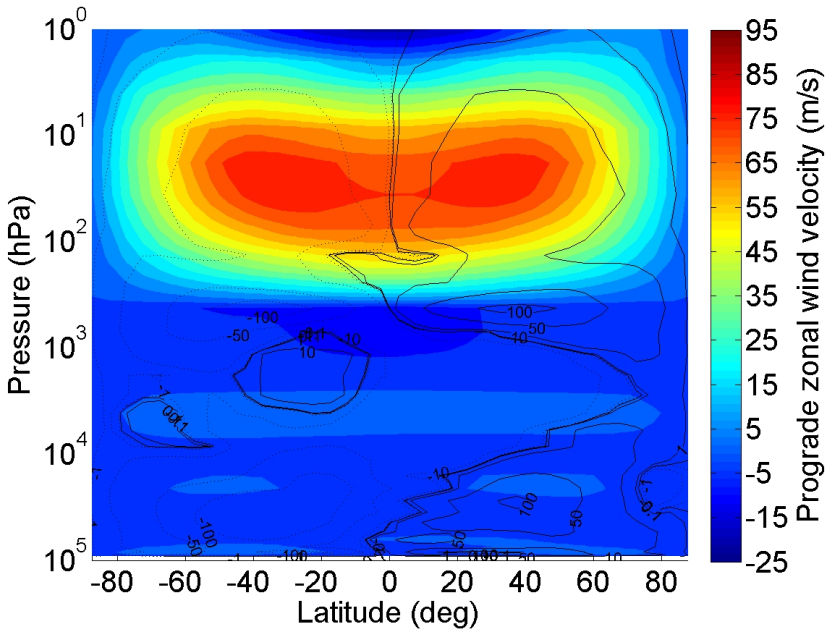

(a) Less 50% UV absorption.

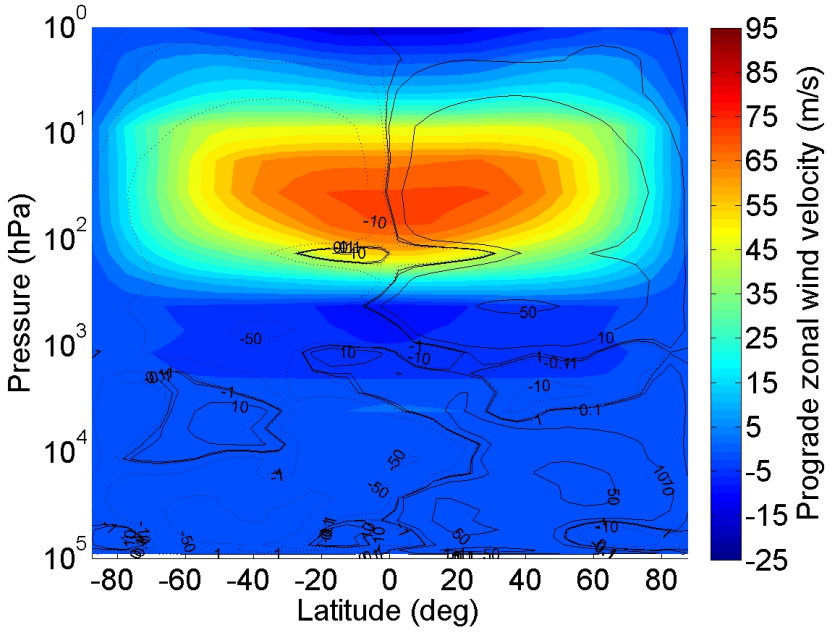

(b) More 50% UV absorption.

Figure 7.3: Zonally and time averaged (5 Venus days) zonal wind and mass stream function for two simulations using different magnitudes of absorption coefficients assumed for the unidentified UV absorber in the upper cloud region: **(a)** corresponds to 50% less and **(b)** to 50% more than in the baseline simulation.

7.5 Mobile UV absorber

In the following experiments we set a percentage of the unidentified UV absorber to be transported in the atmosphere. The physical properties of this substance are still unknown, so the conversion between optical properties was kept very simple and based on

$$d\tau_{ext} = \Pi \frac{dp}{g} \tag{7.1}$$

where τ_{ext} is the extinction optical depth and Π is a constant of proportionality which has mass units. Π is usually described as $\Pi = k_{abs} \times \chi$, where k_{abs} is the absorption coefficient and χ the mass mixing ratio, however, as we do not know what is the composition of the UV absorber in the cloud region, we cannot compute each term separately. In the following experiments this constant of proportionality Π, despite not being exactly the mass, it is that measure of concentration which is advected during the simulations. The advection of the unidentified substance is carried out using the positive-definite advection scheme available in the HadCM3 (Met Office UM,Cullen *et al.* 1992 and Cullen & Barnes 1997). This formulation is basically solving the following equation

$$\frac{\delta C}{\delta t} + u\frac{\delta C}{\delta x} + v\frac{\delta C}{\delta y} + \dot{\eta}\frac{\delta C}{\delta \eta} = 0, \tag{7.2}$$

where x and y are the cartesian coordinates, η the vertical coordinate (see chapter 4) and C is the tracer concentration (Cullen & Barnes 1997). From this equation it is easy to verify that the results of advecting C are equivalent to advecting Π divided by a constant, since k_{abs} is assumed to not change with the atmospheric conditions. The aim of these experiments was not to reproduce very accurately the influence of the atmospheric constituent transported, but to study qualitatively its effect, so the parameterisations are kept as simple as possible (e.g., microphysics is neglected).

The absence of any parameterisation that controls the production and destruction of this substance was corrected by assuming three approximations:

1. We do not take into account any quantities outside the vertical limit (between 56.5 km and 71 km altitude) as suggested in chapter 3. The vertical distribution of the unidentified UV absorber has not been accurately determined yet by observational studies. In this work, as explained in chapter 3, we follow Crisp (1986), who constrained his parameters with results from Pioneer Venus measurements (Tomasko *et al.* 1980 and Pollack *et al.* 1980). The vertical distribution assumed was the same as for the mode

one particles in the upper cloud region, and the radiative UV absorption properties were tuned for a match between the computed spherical albedo and the observed values, as mentioned before.

2. Just a fixed percentage of the total mass is advected, and the rest is maintained. Several experiments which advect the total mass of the unidentified UV absorber showed that the atmospheric super-rotation regime was not stable in the mesosphere. In that case the atmosphere transited in a few Venus days to an antisolar-to-subsolar circulation in the upper cloud region. The main reason for this transition is due to the fact that this substance has the tendency to be transported to the night side of the planet. As a consequence, the solar UV radiation could then reach deeper regions in the atmosphere on the day side causing the formation of strong convection usually at the cloud base, which exerts a drag in the circulation. These results may indicate that the UV absorber is approximately well mixed horizontally in the upper cloud region, produced below the upper clouds (upward transport in the dayside) and destroyed photochemically at the cloud tops. The experiments explored below have a fraction of the unidentified UV absorber's total mass (total optical depth) being transported which is never larger than 50%.

3. To ensure that the total mass (total optical depth) is conserved, we apply a correction factor to the opacities in each layer that contain the mobile UV absorber. This update in the total mass is done at every thirty minutes of the integrated time.

Next, we show the results of three experiments where 50% of the total mass (total optical depth) assumed in the baseline simulation is transported and added to three different constant profiles: the original profile (experiment 1x), twice the original (experiment 2x) and three times (experiment 3x).

Fig. 7.4 shows a time series of S over $\sim$8.5 Venus days (1000 Earth days). The three cases have more UV absorbers in the upper clouds than in the baseline simulation. A more detailed analysis would require a longer integration. The three simulations seem stable despite a slight decrease of S. Fig. 7.5 shows a clear correlation between an increase in the quantity of UV absorber in the upper clouds and the increase of the strength of the zonal winds. The main reason is due to an increase in the impact of the thermal tides, which have their magnitudes amplified. These results are in agreement with two recent observations: a

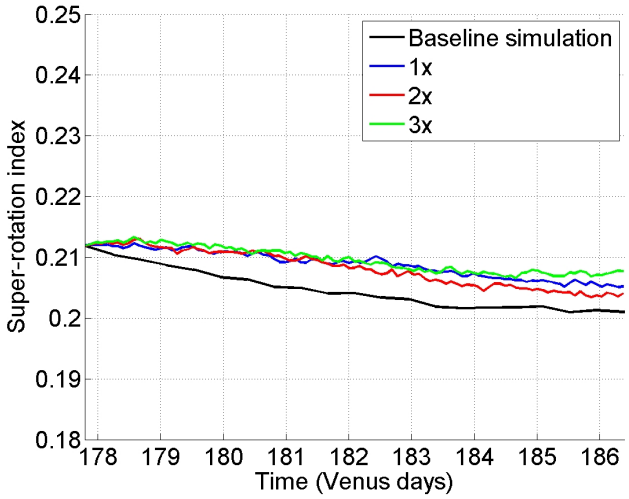

Figure 7.4: Global super-rotation index for simulations testing different constant distributions of unidentified UV absorber plus an advecting amount. In these experiments a quantity of 50% of the UV absorber of the baseline profile is actively transported in the atmosphere. The three different amounts of non-advected UV absorber are: **(a)** the same used in the baseline results, **(b)** twice as **(a)** and **(c)** three times as **(a)**.

long term increase in the zonal winds at the cloud top from Khatuntsev *et al.* (2013) and a decrease in the relative UV brightness (Marcq *et al.* 2013).

Figs. 7.5(a) and 7.3(b) have the same amount of UV absorber, but in Fig.7.3(b) there is no active transport. Comparing the two we see that the zonal wind distribution and magnitude are not significantly affected. The main difference is the larger grid length perturbations below the jet on the equator (inertial instabilities) in the case where part of the unknown substance is been transported, and also stronger convection cells in the upper clouds. The inertial instabilities at low latitudes are easily seen for the cases with more UV absorber looking at the multiple stacked cells below the 10^3 hPa pressure level.

In Fig. 7.6(a) we compared the averaged zonal winds for different cases with the ones from observational studies, obtained from recent cloud tracking measurements (Sánchez-Lavega *et al.* 2008 and Moissl *et al.* 2009). These model cases show the magnitude of the winds increasing with the UV absorber amount in the upper cloud region. Fig. 7.6(b) shows a vertical profile, and in this case it is also possible to see the increase of the winds in the cloud region with increasing UV absorber. The magnitude in the lower atmosphere did not change significantly, however, which is not surprising, given that the downward component

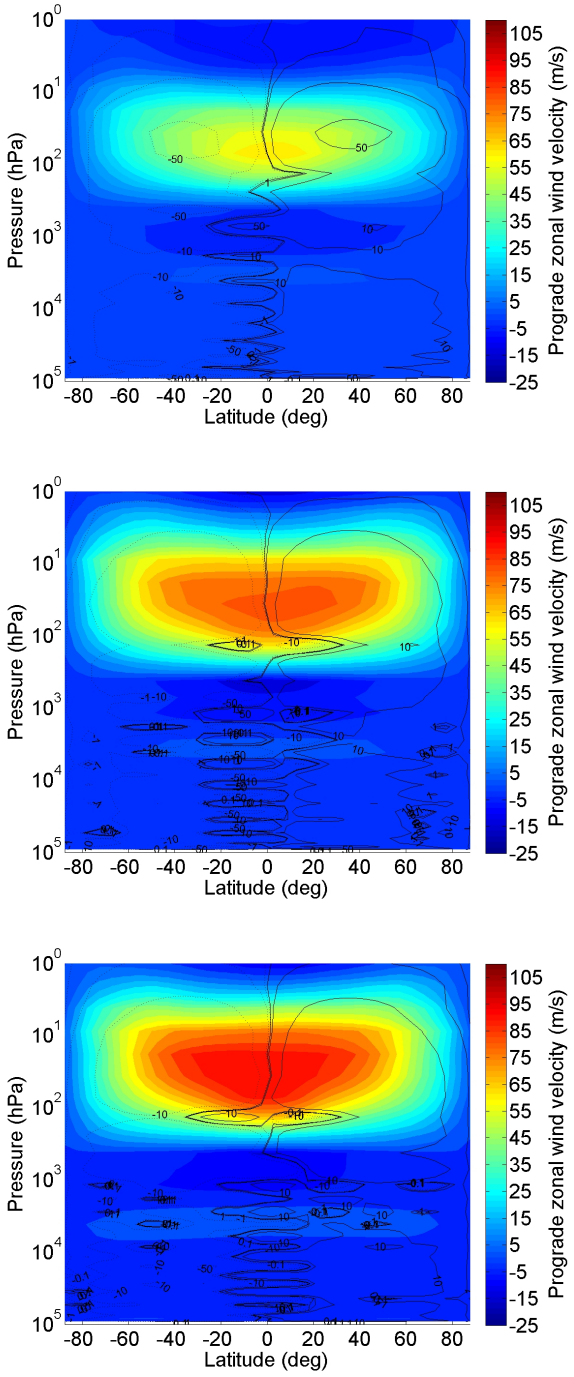

Figure 7.5: Zonally and time averaged (2 Venus days) zonal wind (m/s) and mass stream-function (10^9kg/s) for three simulations using different constant distributions of unidentified UV absorber plus an advecting amount. In these experiments a quantity of 50% of the UV absorber of the baseline profile is actively transported in the atmosphere simulated. The three different amounts of non-advected UV absorber are: **(a)** the same as used in the baseline results, **(b)** twice as **(a)** and **(c)** three times as much as **(a)**.

of the thermal tides is weak due to the large thermal inertia of the deeper atmosphere.

Fig. 7.6 also includes an extra test where the experiment 1x is repeated but with the clouds made transparent to infrared radiation (the global averaged winds for this case are shown in Fig. 7.7). The goal of this simulation was to study the effect of reducing the strength of the convection cell at the cloud base. As we saw before, the low static stability in this region is due to the upwelling infrared radiation from the deepest regions of the atmosphere that is blocked at the cloud base. In this test the model was also integrated for 8.5 Venus days. The figures indicate that, with a less strong convection cell at the cloud base, the winds produced in the upper cloud region are stronger, and fit the observations well. These results may indicate that, without an efficient transport of heat (strong prograde winds) at the cloud base, it is difficult to reproduce the results observed. In this case, more work needs to be done to gain a better understanding of what mechanism is missing in the lower atmosphere to reproduce the strong observed global super-rotation (see chapter 8 for more discussion on this topic). It is also worth noticing that the static stability of the lower atmosphere was changed when the clouds were assumed to be transparent to infrared radiation. This result drove the atmosphere to produce a relatively strong convection cell below the cloud region, which showed once again how the atmospheric conditions of the cloud region or above can affect the atmospheric circulation of the lower atmosphere.

The new atmospheric circulations obtained here drove the production of a wave one phenomenon in the temperature field, which has similar characteristics to the observed "cold collar" phenomenon (Taylor *et al.* 1979). Fig. 7.8 represents a temperature map at 36 hPa from 2x experiment. These results show a depression in temperature locked to the sun's position and localised in the morning part of the atmosphere. This region of the atmosphere is weakly forced by the solar radiation or not forced at all. The magnitude of the temperature disturbance (maximum of $\sim$12K) and its latitudinal position (temperature decreasing from 45° to 65° latitude) are in good agreement with results obtained from Venera-15 Infrared Fourier Spectrometer measurements (Lellouch *et al.* 1997). This phenomenon is also seen in the baseline experiment during the phase of the long term oscillation when the strongest zonal winds in the upper cloud region are reproduced.

7.5.1 UV absorber distribution

The atmosphere inside the temperature depression seen above, is associated with an area surrounded by a steep gradient in Ertel Potential Vorticity (PV) (Hoskins *et al.* 1985).

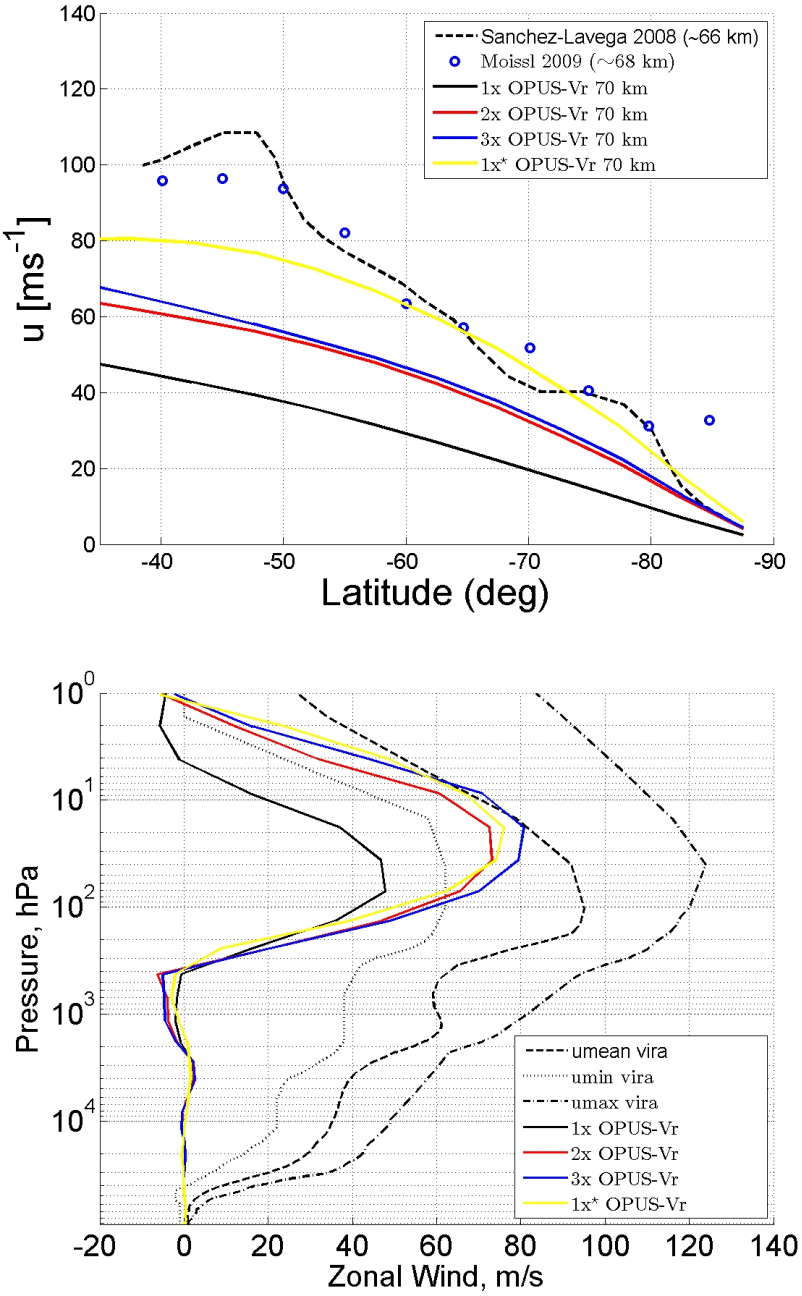

Figure 7.6: Vertical and horizontal profiles of zonal winds, comparing simulations using different amounts of UV absorber and the observations. The cases 1x, 2x, 3x have once, twice and three times amount of UV absorber in comparison with the reference profile. The yellow line represents the case where the clouds and transparent to the infrared. In all the cases a quantity of half the one indicated in the UV reference profile is transported in the atmosphere. The observational data is from Sánchez-Lavega *et al.* (2008), Moissl *et al.* (2009) and Kerzhanovich & Limaye (1985).

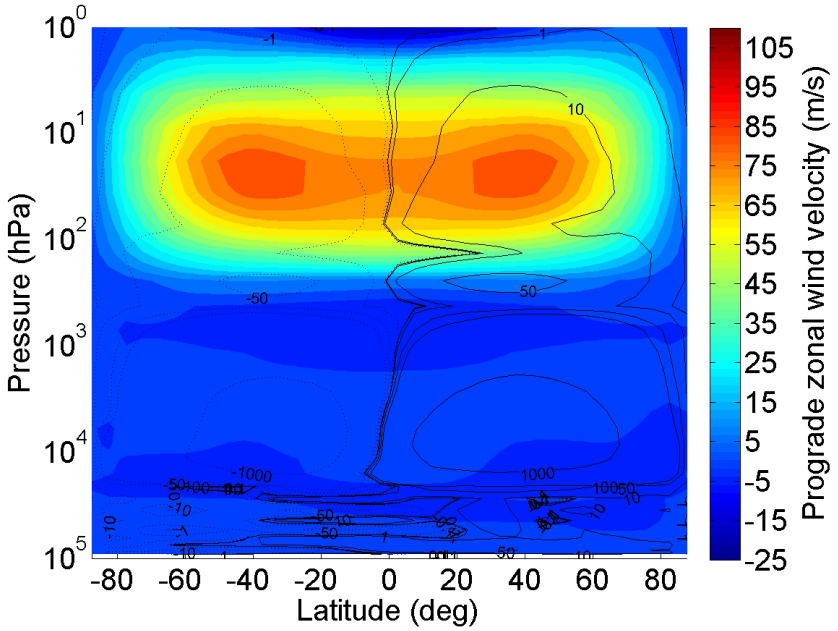

Figure 7.7: Zonally and time averaged (2 Venus days) zonal wind (m/s) and mass stream function (in units of 10^9kg/s) of the simulation 1x but with the clouds transparent to infrared radiation.

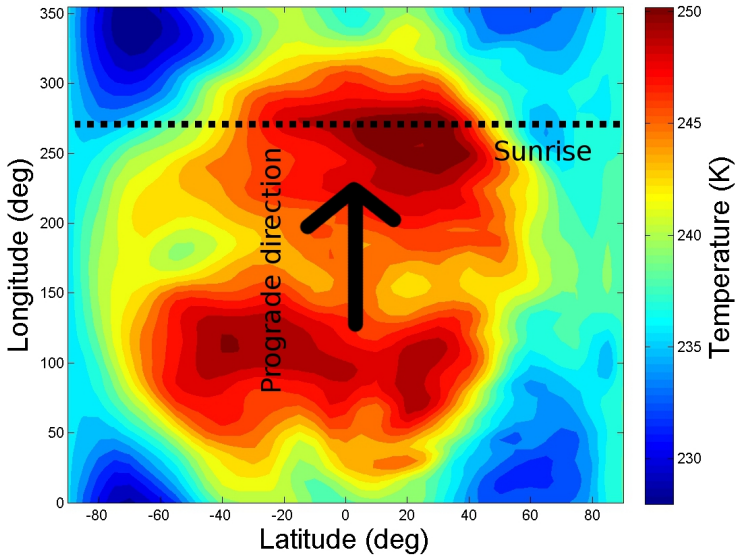

Figure 7.8: Horizontal temperature map at 36 hPa from 2x experiment at a particular instant.

Large PV gradients are often associated with a phenomenon called a "transport barrier" on an isentropic level. Such 'transport barriers' are well-known phenomena in the Earth's atmosphere, and its mechanism is used to explain the isolation of the Antarctic ozone hole (e.g., Chen 1994; Bowman 1993). In the results shown here there are several characteristics similar to the ones observed in the Earth's stratospheric vortex, such as the temperature depression and sharp gradient in the amounts of UV absorber and PV at the vortex-edge (see Figs. 7.10, 7.11, 7.12 and 7.13). In the areas where this phenomenon occurs, the Rossby-wave restoring mechanism suppresses Rossby-wave breaking. As a consequence, the parcel displacements take the form of reversible wavelike motions, and irreversible transport is inhibited. However, this process does not act as a perfect "barrier", because the permeability of the barrier is reduced by the erosion of waves at all scales and due to vertical transport. In reality, chemical processes may also be important, but they are not taken into account in this model. Vigorous wave breaking in the vortex-edge region can also steepen the gradients of PV and increase the difference in atmospheric composition or drive the formation of thin filaments on an isentropic level (e.g., Mariotti *et al.* 1994). The Venus Express observations indicate rapid changes with latitude in temperature, cloud morphology and structure, composition and zonal wind fields at the upper cloud region (50°-60° S), all of which suggest the possible existence of a transport barrier (Titov *et al.* 2008 and Markiewicz *et al.* 2007). A more quantitative exploration of the atmospheric permeability to this phenomenon can be carried out in the future by computing the effective diffusivity on an isentropic level of an atmospheric tracer map (e.g. Haynes & Shuckburgh 2000a and Haynes & Shuckburgh 2000b). Results showing evidence of a large effective diffusivity would correspond to strong mixing (high permeability) and small values to weak mixing ("barriers"), which can vary with time and height. However, Figs. 7.10, 7.11, 7.12 and 7.13 suggest a possible transport "barrier" at high latitudes in the upper cloud region. Note that the isentropic levels mapped are not the same for the two experiments because the upper cloud region in the experiment 1x* is colder. Comparing these figures, it is possible to observe clear differences in the amounts of UV absorber inside and outside the region delimited by the maximum gradient of PV, which suggests the existence of a partial "transport barrier". This unknown substance is not radiatively active when trapped inside this region, because it is phase locked with the sun's position on the night side (and is more prominent in the morning sector as mentioned before).

The polar vortex seems to exhibit a large variety of morphologies, one of which is a transient inverted S-shape observed over the southern pole by Venus Express (Piccioni *et al.* 2007b). A similar shape was also observed years before in Pioneer Venus images in the infrared, but over the northern pole (Taylor *et al.* 1979). In the Venus polar vortex, at cloud altitudes, the dominant instability mechanism is likely to be barotropic instability. Barotropic instability in Venus arises from the horizontal shear instability of the strong mid-latitude jets in the cloud region. In Limaye *et al.* (2009), data from Pioneer Venus were used to estimate the latitudinal profile of relative vorticity in the north hemisphere. The results show that the meridional gradient of vorticity has an inflection-point at the vortex-edge, which satisfies a necessary (though not sufficient) condition for the occurrence of barotropic instability according to the *Rayleigh-Kuo stability criterion* (e.g., Andrews *et al.* 1987). This condition is also satisfied in the OPUS-Vr simulations, as it is possible to see in Fig. 7.9. The barotropic instabilities in the polar flow seem to be the mechanism that is driving the different morphologies of the polar vortex (Limaye *et al.* 2009). The larger meridional gradient of vorticity near the vortex-edge may also be associated with the formation of a region with low atmospheric permeability on an isentropic level (a region described above as a transport "barrier"). An OPUS-Vr experiment with high horizontal resolution could in the future show in more detail the formation of some of the shapes that have been observed. However, a wavenumber two zonally traveling disturbance is sometimes seen in the simulation data, such as in Fig. 7.13. Note that, observational studies do not indicate large quantities of UV absorber in the polar region (e.g., Titov *et al.* 2012), in contrast with the results obtained here. The main reason for this difference is related to the downward transport of this material from above the cloud region in the simulation, which remains trapped in the polar region delimited by the proposed transport "barrier". This result can be an indication that this UV absorber should be extinct above the cloud top.

In the global distribution maps of the UV absorber (Fig. 7.14 and 7.15), the presence of a bright band (implying less UV absorber) surrounding a dark polar oval region is evident. This phenomenon is clearer in the 1x* experiment and also resembles UV images acquired from the Venus Monitoring Camera instrument aboard Venus Express (Titov *et al.* 2012). Note that brighter regions are associated with areas with low UV absorber density and the opposite applies to darker regions. Dark spiral arms were also obtained in the simulation as a result of erosion by planetary waves in the dark polar cap. These results are also visible in Figs. 7.14 and 7.15, which show a global view of the UV absorber distribution at a

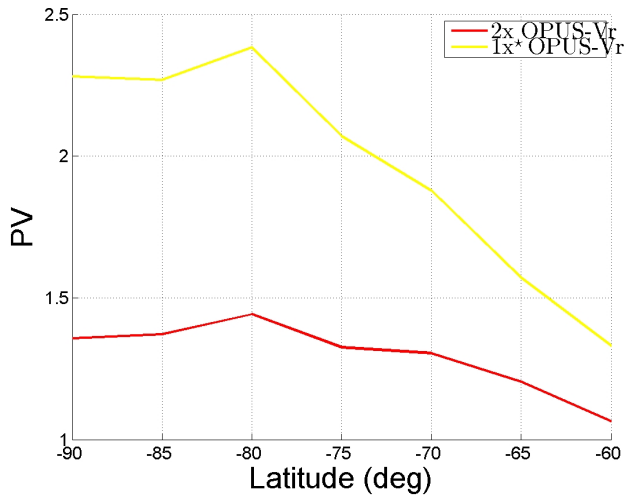

Figure 7.9: Latitudinal profiles of Ertel potential vorticity on an isentropic surface from two experiments with the OPUS-Vr in the southern hemisphere. The red line is related to the 2x experiment at 980 K and the yellow line to the 1* experiment at 950 K. The results are zonally and time averaged for two solar Venus days. The PV units are in (K m^2 s^{-1} kg^{-1})$\times 10^5$.

pressure level of 36 hPa. In general, the particles advected in the model are transported away from the equator in the morning sector and pulled back in the evening. Rossow *et al.* (1980) explored data from Pioneer Venus and found apparently similar cloud motions. The morning sector has a tendency to be brighter but in the late morning dark regions transported from deeper regions emerge and are pushed away from the equator forming bow-wave-like features. The area near the sub-solar point is marked in these maps by the brightest region. However, an atmospheric circulation with stronger zonal winds seems to reduce the brightness in that location, due to a more efficient transport of the clouds. The particular dynamical transport modelled can drive the clouds to form the well-known "Y" shape feature (Rossow *et al.* 1980), which is seen several times at the cloud top region during the simulation. Darker mid-latitude bands are also seen in the results, and their position is influenced by low frequency mixed Rossby-gravity waves which were analysed in the baseline results. The maps shown here represent just four days of each simulation, and do not represent all the cloud features obtained during the simulation. They showed large variability on a timescale of a few Earth days. These simulations did not take into account the transport of the trimodal cloud droplets, however, which are also an important feature in the observed properties of the Venus atmosphere in the UV band. It is due

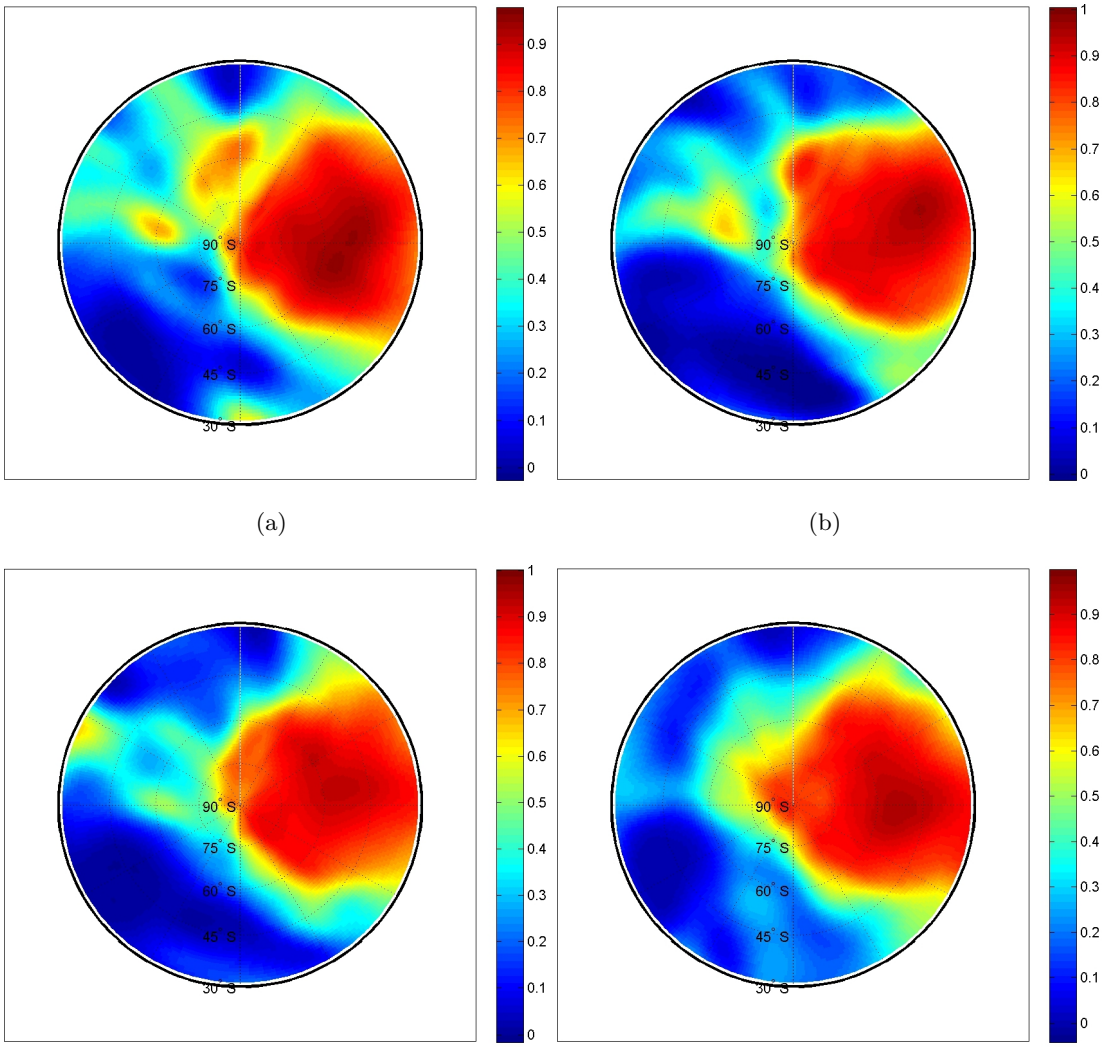

Figure 7.10: UV absorber distribution maps in the polar region for the 2x experiment. The values are normalised relative to the maximum of all four images. The different maps are snapshots separated by one Earth day at roughly the top of the UV distribution region (980 K).

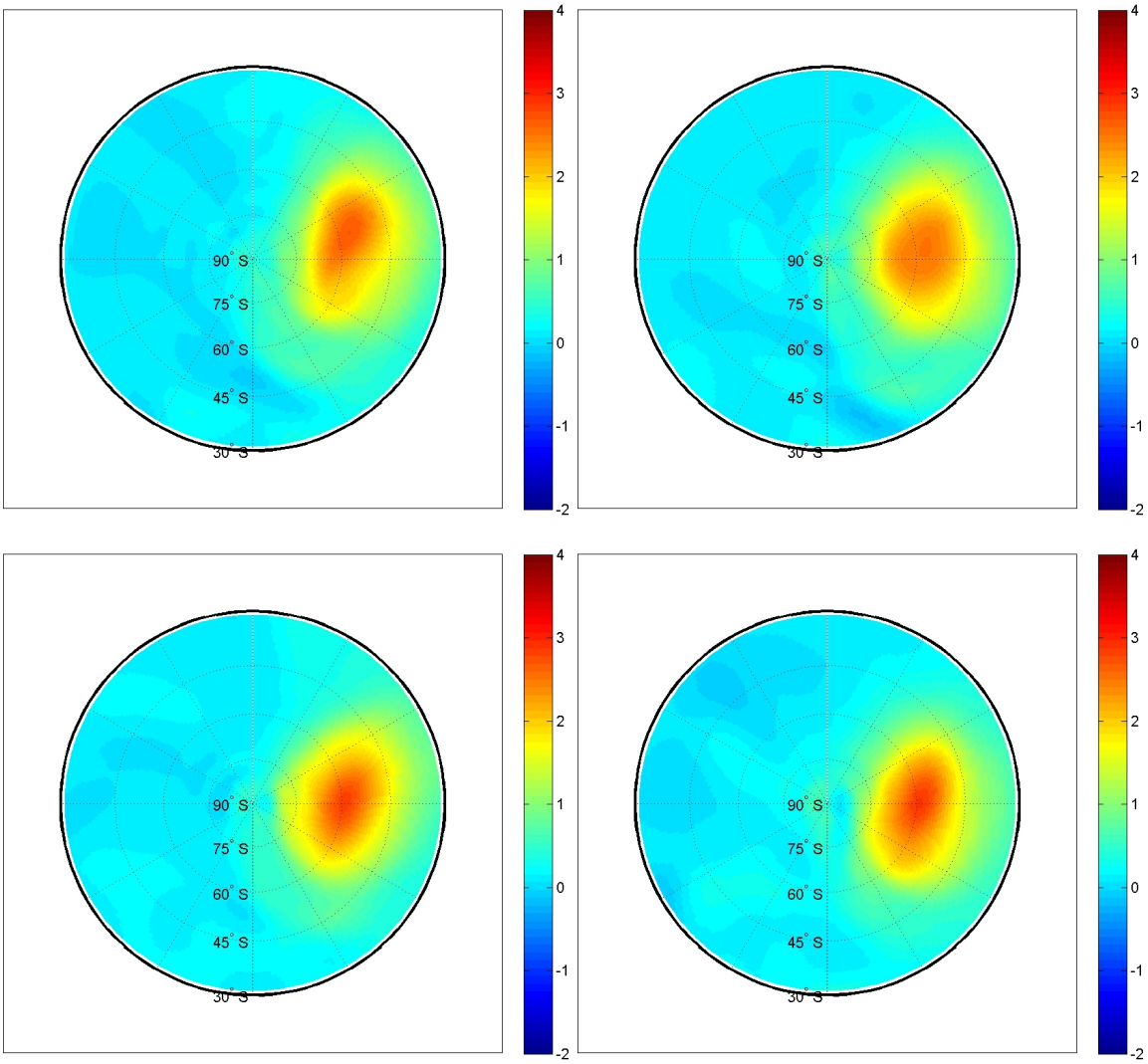

Figure 7.11: Ertel potential vorticity on an isentropic surface (980 K) in the polar region for the 2x experiment. The different maps are snapshots separated by one Earth day at roughly the top of the UV distribution region, and correspond to the different maps in Fig. 7.10. The units are in (K m^2 s^{-1} kg^{-1})×10^5.

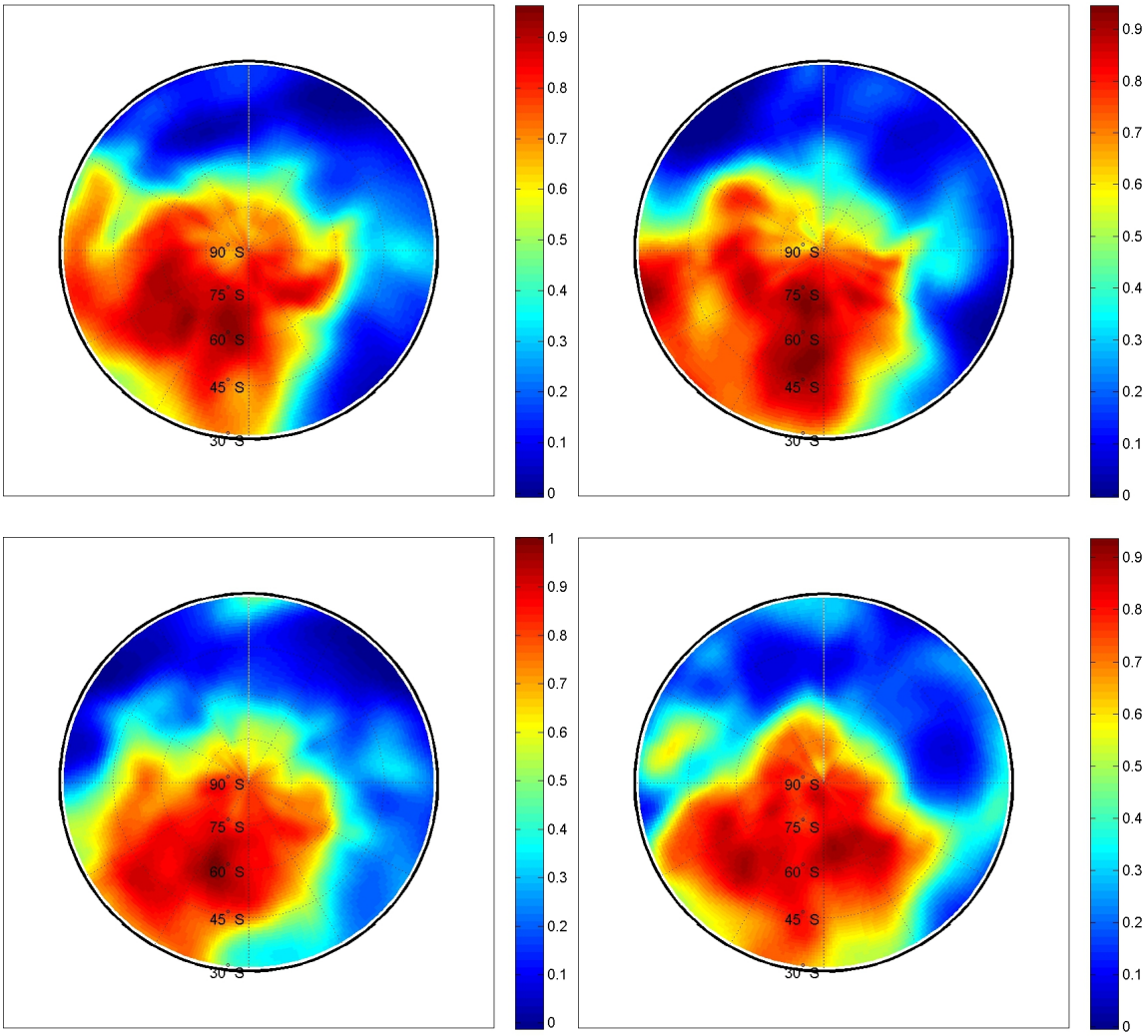

Figure 7.12: UV absorber distribution maps in the polar region for the 1x* experiment. The values are normalised relative to the maxima of each map. The different maps are snapshots separated by one Earth day at roughly the top of the UV distribution region (950 K).

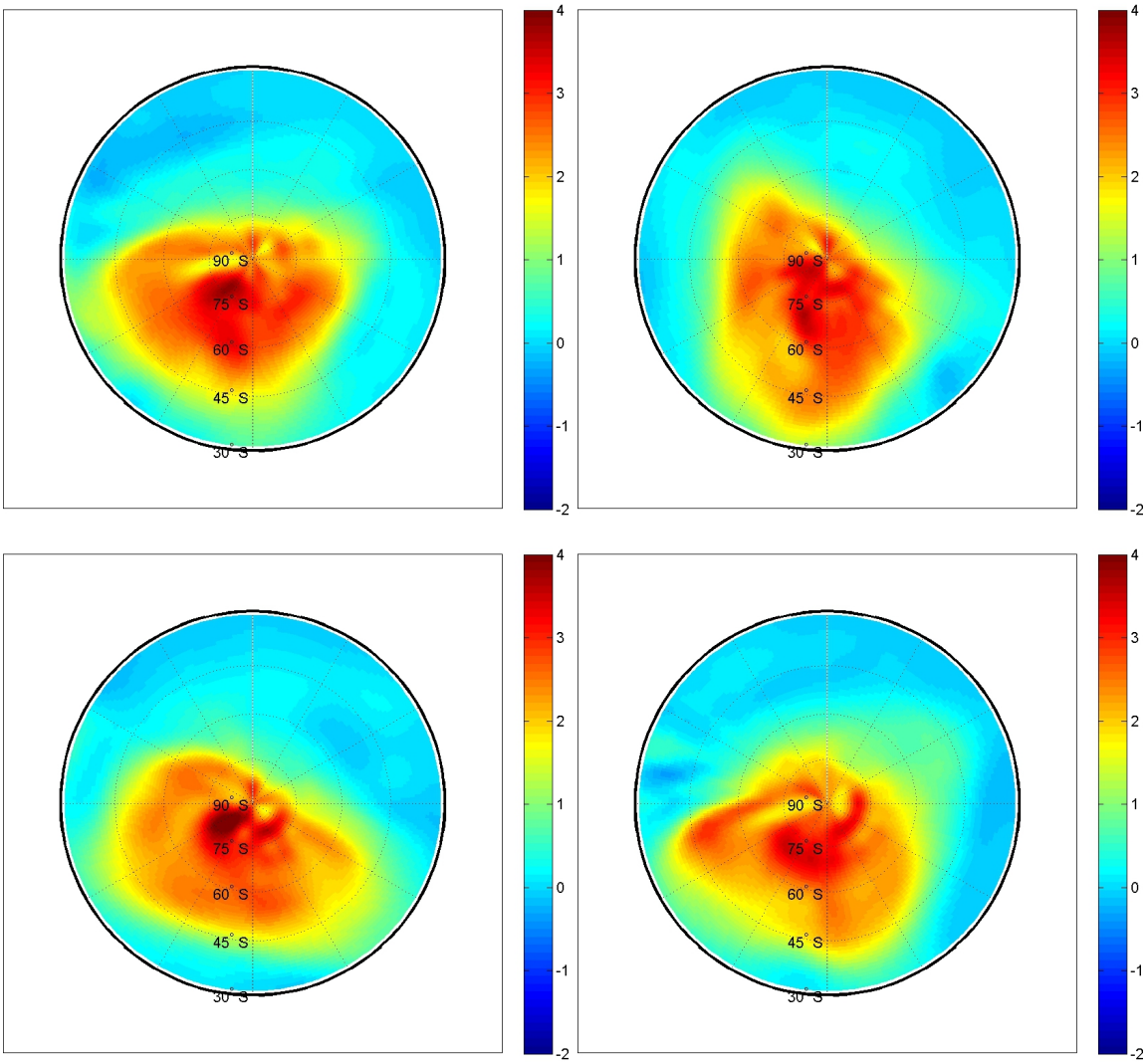

Figure 7.13: Ertel potential vorticity on an isentropic surface in the polar region for the 1x* experiment. The different maps are snapshots separated by one Earth day at roughly the top of the UV distribution region, and correspond to the different maps in Fig. 7.12. The units are in (K m^2 s^{-1} kg^{-1})$\times 10^5$.

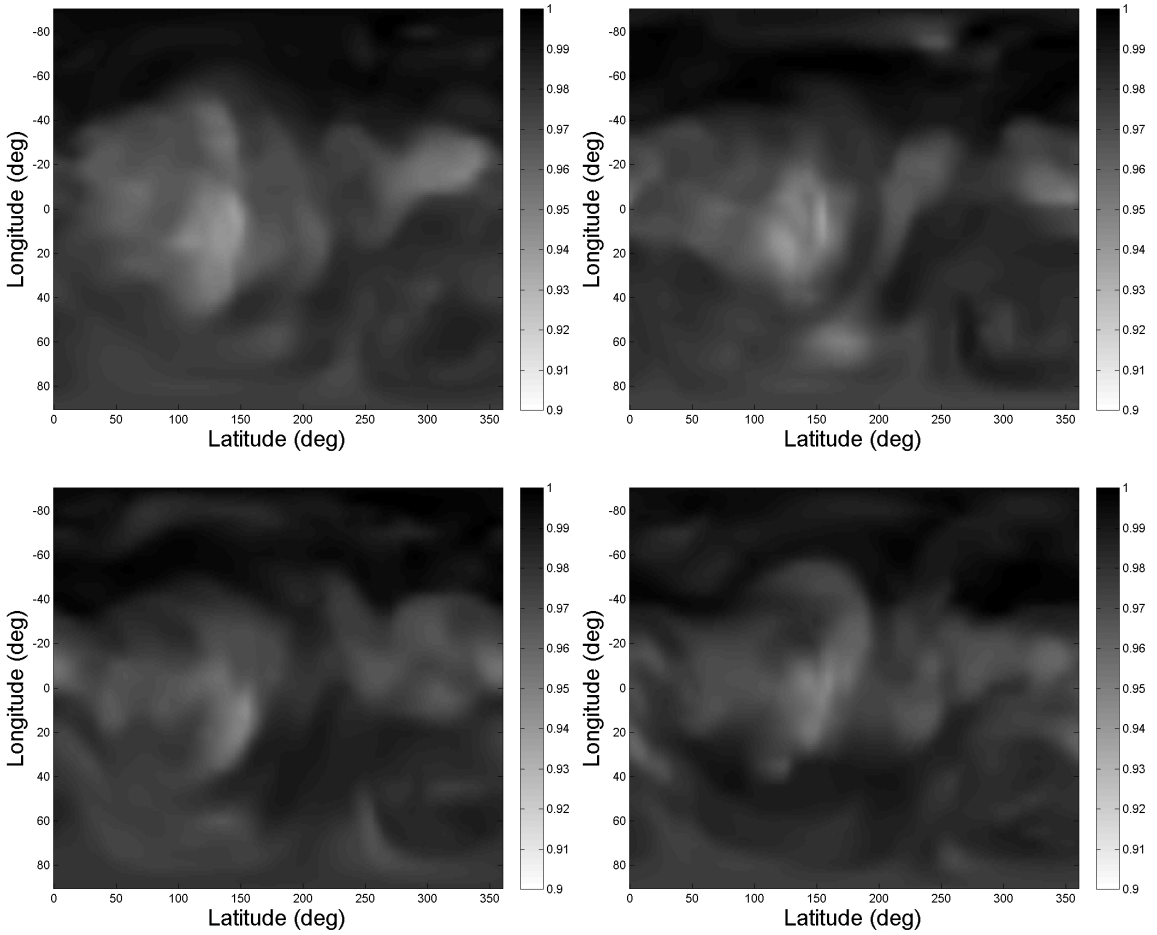

Figure 7.14: Global distribution maps of the unidentified UV absorber for the 2x experiment. The values are normalised relative to the maximum of each map. The different maps are snapshots separated by one Earth day at a pressure level of 36 hPa.

to variations in the ratio between these two components (unidentified UV absorber and trimodal cloud droplets) that produce the bright and dark regions in the UV. However, the simplified approach used here is already capable of reproducing some of the cloud features observed (e.g. Rossow *et al.* 1980 and Titov *et al.* (2008)).

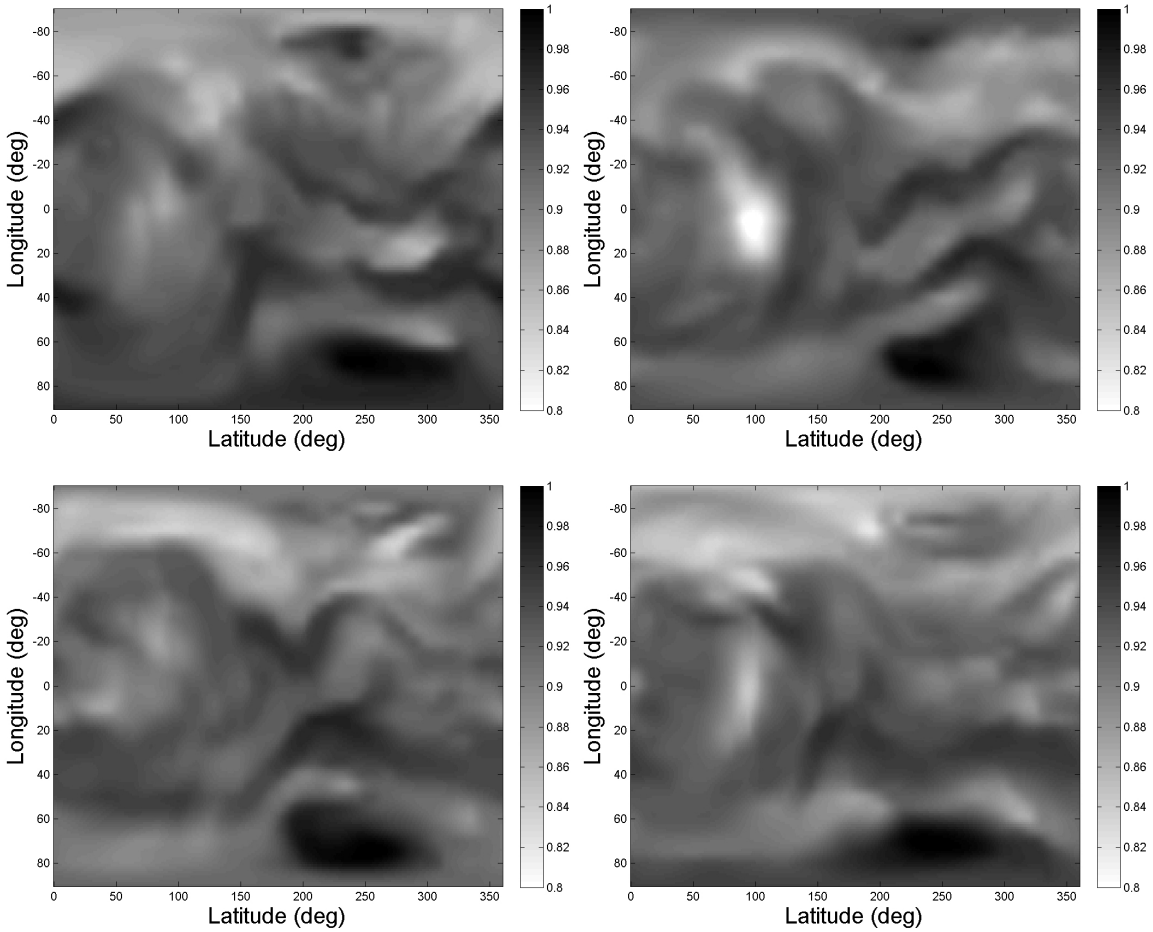

Figure 7.15: Global distribution maps of the unidentified UV absorber for the 1x* experiment. The values are normalised relative to the maxima of each map. The different maps are snapshots separated by one Earth day at a pressure level of 36 hPa.

7.6 Conclusion

It is clear from the results presented above that the changes in the cloud distribution can have a great impact on the atmospheric circulation. A reduction in cloud opacity enables more solar radiation energy to be deposited in deeper regions of the atmosphere, driving the atmosphere towards a different global circulation state. The different thermal structures produced for different cloud amounts had an important influence on the location and size of planetary cells. On reducing the cloud amount, we found that stronger cells are located deeper in the atmosphere, which changes the mean transport of prograde angular momentum and consequently the zonal wind distribution. The cases that allow more solar energy to be deposited in the deep atmosphere (i.e., with less clouds) bring the strong prograde jet to lower altitudes, now lower than the upper cloud region, and also induces the formation of two mid-latitude jets just below the 10^4 hPa pressure level. This latter result is similar to what was obtained in the cases explored in chapter 6 when the short-wave albedo of the surface was set low.

The amount of ultraviolet (UV) absorber in the upper cloud region has an important impact on its dynamics. The experiments here showed that an increase of the UV absorber amount increases the strength of the zonal winds in the same region. This acceleration results from the increased strength of the thermal tides. These experiments provided an opportunity to study the phenomena produced by stronger super-rotation regimes, which revealed the formation of a "cold-collar" phenomenon very similar to the one observed, and based mainly on dynamical processes in the atmosphere (the interaction/superposition of a planetary-scale wave of wave-number one). The experiments transporting the UV absorber allowed us to make direct comparisons of atmosphere properties with UV images. The distribution of the UV absorber in the atmosphere obtained in the simulations showed several similarities with UV images retrieved by Venus Express and Pioneer Venus instruments. Some of those features obtained are, among others: bright high latitude bands encircling a dark oval shape, dark bow shapes in the equatorial region, and a single dark horizontal "Y" shape encircling the planet. These experiments allowed the study of the cloud top polar vortex as well. In this region the particular dynamics induces the formation of a region encircled by a boundary with low permeability. This boundary is clearly seen due to the fast transition in the tracer amount in and out of the region and by the sharp gradient of PV. This indicates

the presence of a transport "barrier", and there are several indicators in the observational data which suggest the existence of this dynamical feature in the Venus atmosphere.

A very simple example of how the lower atmosphere circulation might influence the atmospheric circulation above can be seen in the results of the simulation, where the cloud deck was assumed to be transparent to the infrared radiation. These results indicate that an inaccurate representation of the heat transport at the cloud base can make it difficult to obtain atmospheric winds in the upper regions similar to the observations.

8

Conclusions and Future work

8.1 Conclusions

The Venus global atmospheric circulation is studied in this work by exploring several numerical tools with increasing levels of complexity. Some of the tools newly added or developed for this study included a radiative transfer model, a 1D radiative-convective model (R-CM) and two versions of the general circulation model (OPUS-Vs and OPUS-Vr). Our research aimed to better understand the mechanisms that form and maintain the global atmospheric super-rotation and to contribute to the interpretation of observational data.

The existing OPUS-Vs developed in Oxford can reproduce some features of the Venus meteorology (Lee 2006 and Lee *et al.* 2007), despite the very simplified representations of boundary layer processes and radiative transfer formulation (as a linear form of Newtonian cooling). In chapter 2, the data from OPUS-Vs is used to assess the cyclostrophic balance approximation in the 1-100 hPa region (within the mesosphere) and the main sources of errors when retrieving the zonal thermal winds at high latitudes. Previous work on retrieving cyclostrophically balanced zonal winds from temperature fields in the Venus mesosphere, were shown to be inaccurate at high latitudes when compared with other more direct methods (e.g., cloud tracking). Based on our analysis of the model's results we suggested a method to better estimate the lower boundary condition at high latitudes, thereby improving the accuracy and consistency of the zonal thermal winds retrieved in the mesosphere. This method was later applied to temperature fields derived from the Visible and Infrared Thermal Imaging Spectrometer (VIRTIS) data on board the Venus Express spacecraft. The results of the thermal wind equation using this new method are in better agreement with

cloud tracking results than previous attempts to retrieve cyclostrophic zonal winds on Venus. The approach followed in this chapter is a good example of how the current global climate models can help to interpret the available observational data and improve the data analysis method.

A complete radiative transfer formulation was developed and implemented in OPUS-Vr. This scheme has some advantages in relation to other existing routines for Venus GCMs (e.g., Lebonnois *et al.* 2010a), as explained in chapter 3. One of the main advantages is the explicit computation of solar heating rates and the consequently straightforward and flexible ability of the code to take account of atmospheric conditions with varying cloudiness. The scheme was explored for different atmospheric cases in the 1D version of the model, and shown to be fast and accurate in computing the radiative fluxes in the atmosphere. Results of this new scheme were validated by comparisons with more sophisticated and complete existing radiative transfer codes (although these are not suitable for climate simulations in GCMs because of the high computational resources required), showing good agreement.

This parameterisation was then tested in a 1D R-CM to simulate the globally averaged vertical temperature profile. The convection in this simple model was simulated by a new convective adjustment scheme that takes into account the dependence of c_p with temperature. The results obtained are similar to the ones from the Venus International Reference Atmosphere (VIRA, Kliore *et al.* 1985) and also to the results of recent work by Lee & Richardson (2011). The 1D R-CM was also used to carry out the important code optimisations of the new radiative transfer formulation before its implementation in the complex GCM. Various opacity structures of the atmosphere associated with different cloud amounts, were explored to learn how the diverse distributions of radiative energy deposition in the atmosphere affected the vertical temperature structure. The reduction of cloud amount allowed more solar energy to be deposited in the deeper regions of the atmosphere producing a hotter lower atmosphere and surface.

OPUS-Vs was extended to include more physically-based parameterisations and other modifications, including:

- New complete radiative transfer formulation;
- New convection scheme;
- Adaptation of one of the HaCM3 boundary layer schemes;

- Adaptation of the parameterisations in the dynamical and physical cores to take into account the variations of the atmospheric heat capacity with temperature, at constant pressure.

These changes are the main differences between the simplified version and the new OPUS-Vr. The model is now capable of producing an atmospheric circulation above the cloud base that appears to be very similar to the one observed. The OPUS-Vr flexibility allowed me to explore several parameters in the radiation code which were important for the atmospheric circulation developed, such as the cloud distribution and the amount of solar energy absorbed by the surface. The latter, if overestimated, can influence the atmosphere to form vigorous convection near the surface which tends to favour the development of inertial instabilities that may exert a drag on the atmospheric circulation.

A sensitivity study of the cloud distribution was made focusing on different amounts of the different cloud constituents. Fewer clouds allowed for more solar energy to be deposited in deeper regions of the atmosphere, and the cloud base to be less efficient at blocking upwelling thermal radiation. As a consequence, the atmospheric circulation of the lower atmosphere became more active, although it did not produce the strong zonal winds observed at low latitudes in any of the tests.

Another factor which has an important impact on the circulation of the lower atmosphere is the topography. The inclusion of a realistic topography in the model was found to increase the exchange of momentum between the surface and atmosphere, which in turn increased the magnitude of the winds in the lower atmosphere and seemed to contribute to maintain the super-rotation in the cloud region.

The mechanism for the formation of super-rotation in the cloud region is associated with a coupling between the mean circulation and transient waves. At the upper cloud region the meridional transport by approximately axisymmetric equator-to-pole Hadley cells favours the formation of barotropically unstable mid-latitude jets. The eddies produced by these jets transport angular momentum back towards low latitudes. However, the main role in redistributing angular momentum in the vertical and meridional direction is taken by thermal tides. In every experiment, except when the diurnal cycle was turned off, the momentum transport by the semi-diurnal tide was essential to accelerate the zonal winds at low latitudes. These waves mainly transported momentum from the upper atmosphere to the cloud region, and their impact on the atmospheric circulation was found to be larger

if the amplitude of the thermal tides was increased (e.g., by increasing the amount of UV absorber). A simple sketch summarising the main phenomena influencing the Venus atmospheric circulation is presented in Fig. 8.1.

Experiments where a particle tracer (UV absorber) is advected in the simulated atmosphere allowed us to study, with some simplifications, the cloud distribution in the upper cloud region. The region delimited in the polar region by a large gradient in the potential vorticity and in the UV absorber concentration measured along an isentropic level, suggests the possible presence of a phenomenon called "transport barrier". However, this phenomenon needs to be explored in a more quantitative approach, using for example methods such as the one from Haynes & Shuckburgh (2000a) and Haynes & Shuckburgh (2000b) where the effective diffusivity on an isentropic level of an atmospheric tracer is computed. If present in the real Venus atmosphere, this phenomenon can have an important role influencing the cloud and chemical distribution at high latitudes in the cloud region.

The magnitude of the zonal winds in the upper cloud region in some of the simulations is similar to the ones observed, and it depends on the amount of UV absorber and on the strength of the convection cell at the cloud base. The atmospheric circulation in the lower atmosphere needs to be better represented, however, since the zonal wind profile below 30-40 km altitude seems to be poorly reproduced in both our model and that of Lebonnois *et al.* (2010a). In the following section, the atmospheric circulation in the lower atmosphere is described in more detail, and possible mechanisms for the formation of the super-rotation in this region are suggested.

8.2 Future work

8.2.1 Super-rotation in the lower atmosphere

The baseline simulation obtained a global super-rotation index (S) of roughly 0.2, which is one order of magnitude lower than the value estimated from observational data in chapter 1: $S = 7.66^{+4.15}_{-3.56}$. The variable S is a mass weighted quantity, which means that the largest contributions come from the deeper atmosphere. As it is possible to see from Fig. 5.16, the vertical distribution of the zonal winds produced by the OPUS-Vr fails to reproduce the observed values below the upper cloud region (100 hPa). This incapability of our model to reproduce simulations with a realistic atmospheric circulation in the lower atmosphere starting from rest, is also shared by the LMD Venus GCM (Lebonnois *et al.* 2010a). The

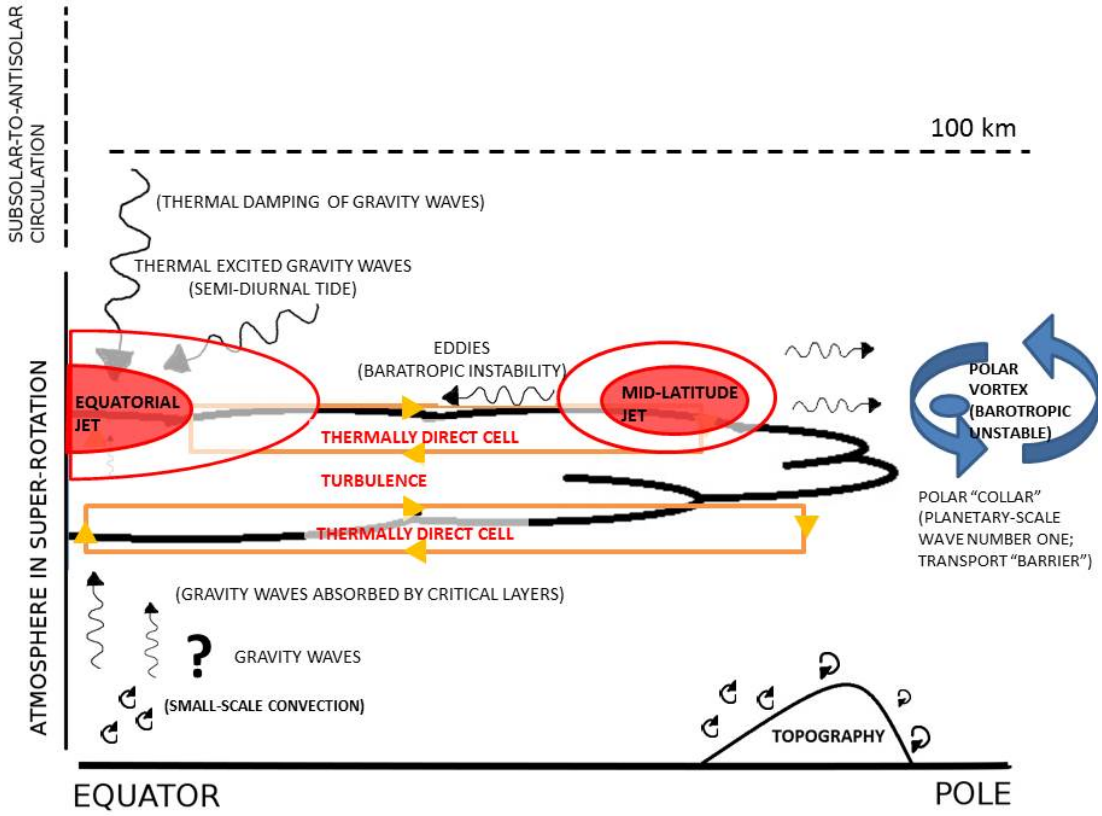

Figure 8.1: Sketch summarising the key ideas about the main mechanisms that drive the atmospheric circulation from the new OPUS-Vr results. The wavy arrows are related to the direction of momentum transport by transient waves and the relevant physical phenomena responsible are within brackets. The horizontal axis is related with latitude from the equator to the pole, and the vertical axis is altitude from the surface up to altitudes higher than 100 km. The vertical axis is divided in two to distinguish between two regions with different dynamical regimes.

main cause for the poor representation of the atmospheric circulation in this region is still unknown. This problem in the models is the next main challenge for all Venus circulation models. This work needs to be done in association with future observational studies of the deeper atmosphere. The characterization of the dynamical regime of the lower atmosphere from observational data is still relatively crude, since it is based on roughly a dozen entry probes from Pioneer Venus and Venera space missions (Schubert *et al.* 1980). These observations each correspond to one specific instant in time and location on the planet. Despite covering different parts of the planet and local times, they are insufficient to describe the global mean state of the atmosphere.

The problems encountered by the current Venus GCMs (e.g., our OPUS-Vr and LMD Venus GCM presented in Lebonnois *et al.* 2010a) in reproducing strong prograde winds in the lower atmosphere may be related to the poor representation of certain physical mechanisms in the atmosphere. In the lower atmosphere the radiative time-scale becomes much longer than the solar day, which implies that the mechanisms driving the strong winds in this region are different from the ones with greatest impact in the upper cloud region: i.e., the thermal tides. In the lower atmosphere the vertical profiles of static stability are correlated with profiles of zonal wind shear at low latitudes, where large shears are found in very stable layers (Schubert *et al.* 1980). In the OPUS-Vr results this correlation was also found, but it is less clear than the ones obtained from observational data (Fig. 5.14(b) and 5.16(a)). In the regions of high static stability, upward convection is less likely to occur and, as a consequence, vertical mixing is inhibited. The presence of vertical convective mixing can reduce the magnitude of the atmospheric super-rotation phenomenon, since the vertical mixing is likely to transport angular momentum down-gradient near the equator (in general, the zonal wind magnitudes increase from less than 10 m/s at 10 km to roughly 100 m/s at cloud heights). Following Hide's theorem (Read 1986) mentioned in chapter 1, the formation of an equatorial super-rotation (at any altitude) requires an up-gradient transport of angular momentum, which could be achieved by phenomena associated with mean circulation and/or upward-propagating waves. In Schubert *et al.* (1980) a relatively large horizontal temperature contrast in the lower atmosphere (below the cloud base) is found in observational probe measurements. This thermal structure is an indication of significant eddy activity and a weak Hadley circulation (its existence is uncertain). The mechanism (or a combination of different mechanisms) involved in the formation of the strong zonal winds must be working under these constrained atmospheric conditions.

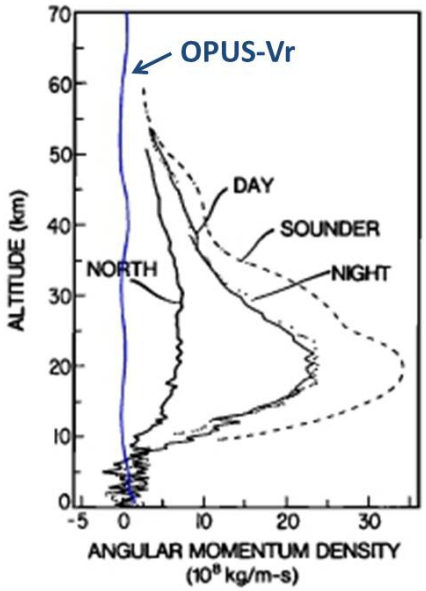

Figure 8.2: Prograde angular momentum density of the atmosphere as a function of height. The OPUS-Vr values are from the baseline simulation, and obtained from a horizontal and time average over five solar Venus days. The observational measurements are from Pioneer Venus probes (Schubert *et al.* 1980).

Fig. 8.2 shows the prograde angular momentum density of the atmosphere as a function of height computed using the following equation,

$$L = \rho a u \cos\phi \tag{8.1}$$

where ρ is the atmospheric density, a the planetary radius, u the zonal wind speed and ϕ the longitude. At 20 km altitude there is a maximum in the angular momentum density. The magnitude of this peak is not reproduced in the results of the OPUS-Vr baseline simulation (blue line). It is the region near 20 km altitude which gives the largest contribution to the global super-rotation index (S). Latitudinal prograde wind profiles shown in Schubert *et al.* (1980), and measured by interferometric tracking of Pioneer Venus probes, have approximately a solid body rotation shape at altitudes of 20 km.

There are two main possibilities for the source of the angular momentum excess in the lower atmosphere: an excess driven by the solar energy deposition or exchanges of momentum between the atmosphere and the planetary surface. After the excess of momentum is deposited, it is likely to be redistributed through the atmosphere by the mean circulation

and by eddies as we showed in previous chapters. Another source of energy capable of influencing the atmospheric dynamics is the release of latent heat from condensation of H_2SO_4 cloud droplets. However, this is not very relevant for atmospheric circulation due to the small mass loading of the clouds (Rossow 1978).

Despite just a small fraction of the incoming solar radiation reaching the deepest regions of the atmosphere, Hou & Farrell (1987) and Ikeda *et al.* (2007) suggested that this radiation can drive/initiate a mechanism to explain the strong prograde winds in the lower atmosphere. These authors proposed that such strong winds in Venus' lower atmosphere (below the cloud deck), could be produced by critical level absorption of gravity waves from small-scale convection excited near the surface or in a deep atmospheric region with low static stability (e.g., between 11×10^3 hPa and 33×10^3 hPa). However, the fully self-consistent physical representation of this phenomenon needs simulations with high spatial resolution or the use of a non-orographic wave drag parameterisation. For the latter case there are already schemes suitable for GCM studies such as the one developed by McLandress & Scinocca (2005). In Ikeda *et al.* (2007) the representation of wave drag due to breaking of non-orographic gravity waves in the atmosphere below the cloud region increased, in general, the zonal winds in the lower atmosphere. In this case, the wind profiles in the lower atmosphere were shown to be very close to the ones observed (e.g. Schubert *et al.* 1980). However, there are several uncertainties associated with this type of parameterisation that need to be explored in more detail. Some of those uncertainties are associated with the adequate knowledge of the source spectra in the atmosphere and the estimation of the free parameters needed in the numerical scheme due to the typical simplifications used.

By using the LMD Venus GCM, which includes a radiative transfer formulation, Lebonnois *et al.* (2010b) showed that simulations started with different atmospheric initial states (different magnitudes of global super-rotation) reach equilibrium towards different distributions of zonal winds in terms of amplitude and location. The mechanisms that maintain the strong winds remain largely the same and are similar to the ones shown in our baseline simulation, although the magnitude of angular momentum transported in the atmosphere is different (e.g., by mean circulation and transient waves). This possibility of multiple atmospheric equilibrium states was also explored with OPUS-Vr. Some test simulations were made by starting the model with a very strong initial global super-rotation, which implied a more efficient heat transport in longitude at all altitudes. However, despite the model having reproduced realistic winds in comparison with the observed ones for a short

period, the atmosphere ended up relaxing towards the states shown in the baseline simulation, which did not confirm Lebonnois et al's conclusion concerning the existence of multiple super-rotation equilibria.

Other factors that may have an important impact in the lower atmospheric circulation and that need to be better explored are the impact of a radiatively active dust cycle in the deep atmosphere, as suggested in chapter 6. The impact of realistic surface topography on the exchange of angular momentum between atmosphere and surface and the resulting balanced flows also needs to be explored more thoroughly, especially if it affects the range of multiple equilibrium states supported by the atmosphere.

8.2.2 Surface interaction with the atmosphere and dynamical core

The impact of the Venus topography on the atmospheric circulation produced in model simulations remains inadequately explored within the Venus climate community. From the observational side, the characterization of the circulation in the lowest scale height of the atmosphere, which is thought to be largely influenced by the surface, is not clear (namely whether it is super-rotating or not). The few data available from Pioneer entry probes show winds that are relatively weak in relation to the underlying planet (Schubert *et al.* 1980).

The physical interaction between the surface topography and the atmosphere above allows them to exchange momentum and heat. Form drag forces (due to pressure differences across topography) and turbulent frictional stresses arise from this interaction, and in spite of the presence of weak winds, they can have a significant influence due to the high density of the atmosphere at these levels. It is important for better understanding the main mechanisms driving the global circulation to have a good estimate of the impact of the topography on the overall momentum budget, and it is in line with the idea that the boundary layer formulation presented in chapter 4 needs to be extended. To complement the bulk transport turbulent mixing parameterisation, it is necessary to implement a gravity wave drag code (e.g., Alexander & Dunkerton 1999) which would provide a better representation of mountain drag and boundary layer interaction.

In general, mountain-induced internal gravity waves are usually considered to exert a stress on the atmosphere, dragging its motion towards a state of rest through the breaking of vertically propagating waves, the phase speed of which is stationary in the horizontal. Fels (1977), however, has also suggested that topographic scattering of downward propagating gravity waves may also be a possible atmospheric feature with an important impact on the

tidal momentum flux in the Venus atmosphere. This phenomenon can actually accelerate the atmosphere, in contrast to mountain drag, and is suggested by Fels (1977) to be an important possible mechanism for the angular momentum transport with a positive contribution to the equatorial super-rotation. However, this effect is still poorly explored in Venus GCMs.

The new OPUS-Vr presented some technical problems with an unknown origin in the integration of the new dynamical core (especially the part that takes into account the dependence of c_p with temperature) when the topography was included. In this case unphysical instabilities were produced which compromised the simulation of the global atmospheric circulation. It would be important to test new dynamical cores, however, these problems were overcome in this work by assuming a c_p constant with temperature, which was shown to be a good approximation (see chapter 6). The robustness study of the results of different dynamical cores is important. In Lebonnois *et al.* (2011) the results of different simplified Venus GCMs have been compared. Using similar physical schemes and parameters, the models produced different circulations. This highlights the importance of the dynamical core in the atmospheric motion modelled, and the problems in the momentum conservation at the Venus massive atmosphere conditions. An interesting work would be a similar exercise to the one done in Lee & Richardson (2010) and Lebonnois *et al.* (2011), but now using a c_p varying with temperature, physically based parameterisations for radiative heating and cooling and boundary layer processes. These tests could help us to build a dynamical core more suitable for the Venus atmospheric conditions, and could also be used to test the angular momentum conservation by doing comparison studies between two or more versions of dynamical cores. Other types of GCM grids may also be interesting to investigate, such as the ones that avoid the well-known "pole problem" (e.g. using an icosahedral grid), which would allow us to do a more detailed study of the polar vortex dynamics.

8.2.3 High spatial resolution

The Venus simulations take a very long time to stabilise into a steady state regime, also implying very long integrations in real time. Each one of the long simulations of the OPUS-Vr from chapter 5 and 6, took roughly two months to complete using a single CPU of a standalone desktop PC (Ubuntu Linux v8.04.2 with four Intel®Core™2 Q9300 2.50GHz processors and 2GB RAM). In the future, adapting the OPUS-Vr code to run on a CPU cluster would reduce the time of integration significantly and make feasible the exploration of possible very long trends in the simulated atmospheric circulation. Other advantages of

running the model on parallel CPU architecture would include the possibility of resolving some physical phenomena that are hidden at small-scales with very high resolution simulations. However, two experiments with finer spatial resolution have already been tested.

The model's configuration in the baseline simulation uses a horizontal spatial resolution of five degrees and a vertical resolution of thirty seven vertical layers (Table 4.1). In the following experiments we explored first the impact of increasing the horizontal resolution to $\sim 2.5^\circ \times 2^\circ$, and also a vertical spatial resolution of 0.8 km below the cloud base (total of 74 vertical layers). A finer horizontal resolution may be expected to improve the representation of horizontal momentum transport by eddies. The change in the vertical resolution was also intended to improve the accuracy of the convective adjustment, and see if it could have significant impact on the lower atmospheric circulation.

To avoid unphysical solutions during the model integration with different horizontal resolutions, its configuration must satisfy the stability criterion mentioned previously in Eq. 4.9. This stability depends on the strength and order of diffusion, spatial resolution, planetary radius and time-step. In the experiment where the horizontal resolution is being increased by a factor of approximately two, Eq. 4.9 indicates that the horizontal diffusion strength needs to be reduced to keep the model numerically stable (keeping the same order of diffusion, planet radius and time-step). A reduction of the diffusion strength by a factor of four for each model layer was applied in the horizontal resolution experiment in comparison with the baseline simulation.

The two simulations were started from the S095VA atmospheric state and were integrated for 8.5 Venus days (1000 Earth days). Fig. 8.3 shows the two trends of the super-rotation index that are very similar to the one from the baseline simulation, despite the short period of integration. In the future a longer integration of this version of OPUS-Vr will be required for a more detailed comparison.

Fig. 8.4 shows strong prograde winds in the mesosphere, but if they are following the same trend as the baseline simulation, they do not correspond to a steady state atmosphere yet. The causes for the differences in the distribution of zonal winds between the two simulations are not clear. The different horizontal diffusion strength used may also have an impact in the values simulated. The larger differences are below the cloud base. In this region the experiment with better vertical resolution has the capability of resolving the intense eddy activity near the surface and the possible formation of small scale convection. The magnitudes of the zonal winds are slightly different and the size of the region with

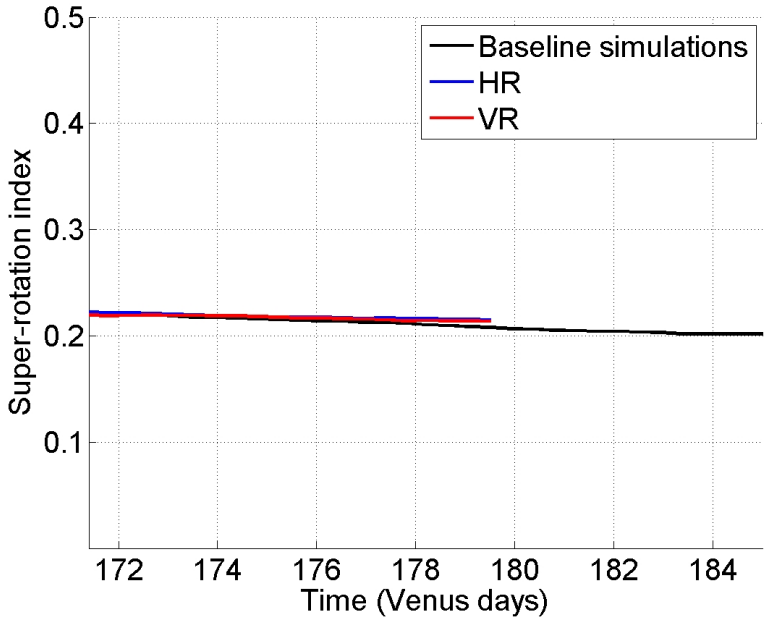

Figure 8.3: Global super-rotation index for simulations testing the spatial resolution. The black line represents the baseline simulation and the blue line the simulation that tests the higher horizontal resolution grid and the red line the vertical resolution.

retrograde winds is different as well (smaller in the experiment with finer vertical resolution). However, it is not clear if the atmosphere simulated has reached a steady state, and a longer period of integration is required to stabilise the atmosphere. The sensitivity of the OPUS-Vr results to the spatial resolution needs to be explored in more detail. In general the different spatial resolutions used do not seem to have a significant impact on the mean atmospheric circulation simulated, though these are preliminary results.

8.2.4 Complex cloud chemistry and microphysics

The flexibility of the radiation formulation in the OPUS-Vr allows us to implement other physical processes such as those associated with atmospheric chemistry and cloud microphysics. However, it is important to have first a good representation in the GCM results of the Venus global atmospheric circulation and thermal structure, to constrain these physical processes, cloud physics and atmospheric chemistry, and make them evolve as closely as possible to those in the observed Venus environment.

These complex schemes are fundamental to an understanding of the chemical-radiative

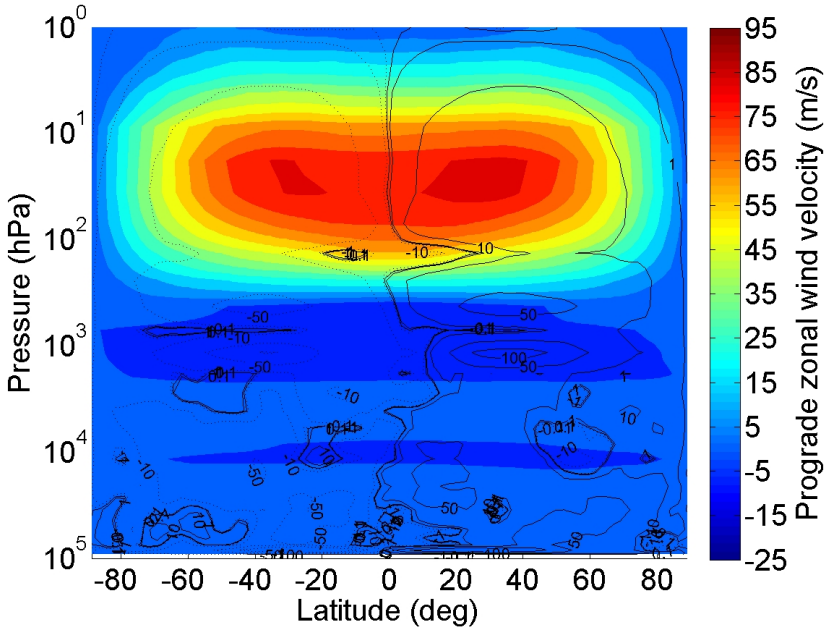

(a) Finer horizontal resolution.

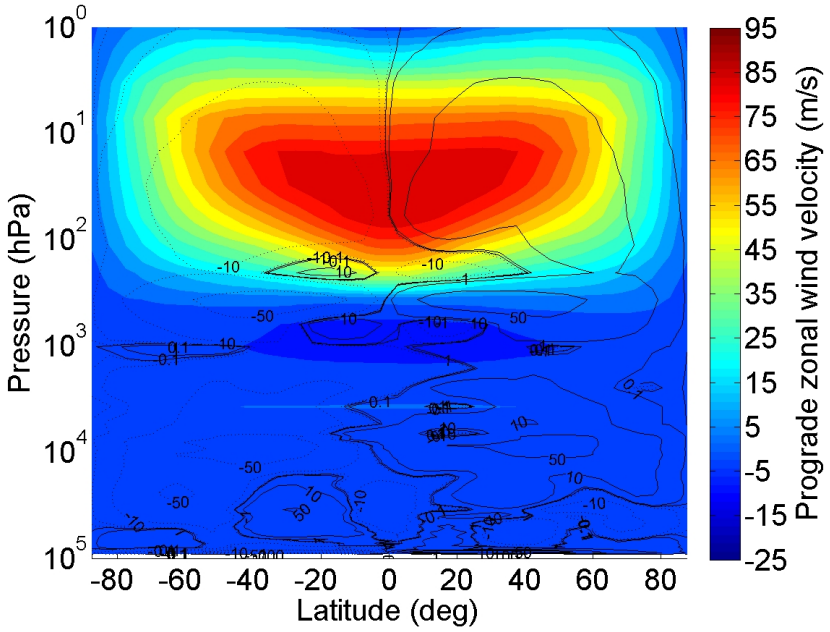

(b) Finer vertical resolution.

Figure 8.4: Zonally and time averaged (2 Venus days) zonal wind and mass stream function for the simulations that test different vertical and horizontal resolutions. The black lines represent the mean meridional stream-funtion (in units of 10^9kg/s).

feedback on the atmospheric circulation, and to support atmospheric studies of the cloud region. Their inclusion would improve the representation of physical properties in the cloud region such as the thermal structure. Some of the main difficulties in their implementation are related to the increase of the integration time of the GCM, and also to the selection of the main chemical reactions and species necessary to be considered in a realistic cloud scheme. However, some suitable microphysical parameterisations, such as those developed by McGouldrick (2011), are already available. These parameterisations have had some success in simulating the maintenance of the lower, middle and upper clouds and hazes in 1D models of the Venus atmosphere and could be considered to be included in a future OPUS-Vr study.

Bibliography

Alexander, M.J. & Dunkerton, T.J. (1999). A Spectral Parameterization of Mean-Flow Forcing due to Breaking Gravity Waves. *Journal of Atmospheric Sciences*, **56**, 4167–4182.

Allen, D.A. & Crawford, J.W. (1984). Cloud structure on the dark side of Venus. *Nature* , **307**, 222–224.

Allison, M. & Travis, L.D. (1985). The Jovian Atmospheres. *NASA Conference Publication 2441, New York*.

Andrews, D.G., Holton, J.R. & Leovy, C.B. (1987). Middle atmosphere dynamics. *Academic Press, New York, NY, USA*.

Arakawa, A. & Lamb, V.R. (1981). A potential enstrophy and energy conserving scheme for the shallow water equations. *Monthly Weather Review*, **109**, 18–36.

Arakawa, V.R., A.and Lamb (1977). Computational design of the basic dynamical processes of the UCLA general circulation model. *Methods in Computational Physics*, **17**.

Atkins, P.W. (1982). Physical Chemistry. *Oxford University Press, second edition*.

Basilevsky, A.T. & McGill, G.E. (2007). Surface evolution of Venus. *Washington DC American Geophysical Union Geophysical Monograph Series*, **176**, 23–43.

Bell, J.F., III, Lucey, P.G., Ozoroski, T.A., Sinton, W.M. & Crisp, D. (1991). Spectroscopic observations of bright and dark emission features on the night side of Venus. *Science*, **252**, 1293–1296.

BIBLIOGRAPHY

Belyaev, D., Korablev, O., Fedorova, A., Bertaux, J.L., Vandaele, A.C., Montmessin, F., Mahieux, A., Wilquet, V. & Drummond, R. (2008). First observations of SO_2 above Venus' clouds by means of Solar Occultation in the Infrared. *Journal of Geophysical Research (Planets)*, **113**, E00B25.

Bougher, S.W., Alexander, M.J. & Mayr, H.G. (1997). Upper Atmosphere Dynamics: Global Circulation and Gravity Waves. *Venus II: Geology, Geophysics, Atmosphere, and Solar Wind Environment. Tucson, AZ: University of Arizona Press*, p. 259.

Bowman, K.P. (1993). Large-scale isentropic mixing properties of the Antarctic polar vortex from analyzed winds. *Journal of Geophysical Research* , **98**, 23013–23027.

Briegleb, B.P. (1992). Delta-Eddington approximation for solar radiation in the NCAR community climate model. *Journal of Geophysical Research* , **97**, 7603–7612.

Bullock, M.A. (1997). *The Stability of Climate on Venus*. Ph.D. thesis, University of Colorado at Boulder.

Bullock, M.A. & Grinspoon, D.H. (1996). The stability of climate on Venus. *Journal of Geophysical Research* , **101**, 7521–7530.

Carlson, R.W., Baines, K.H., Kamp, L.W., Weissman, P.R., Smythe, W.D., Ocampo, A.C., Johnson, T.V., Matson, D.L., Pollack, J.B. & Grinspoon, D. (1991). Galileo infrared imaging spectroscopy measurements at Venus. *Science*, **253**, 1541–1548.

Carpenter, R.L. (1964). Symposium on Radar and Radiometric Observations of Venus during the 1962 Conjunction: Study of Venus by CW radar. *The Astronomical Journal*, **69**, p. 2.

Chen, P. (1994). The permeability of the Antarctic vortex edge. *Journal of Geophysical Research* , **99**, 20563–20572.

Chub, E.V. & Iakovlev, O.I. (1980). Temperature and zonal circulation of the atmosphere of Venus based on the data of radio probe experiments. *Cosmic Research*, **18**, 331–336.

Clancy, R.T., Sandor, B.J. & Moriarty-Schieven, G. (2012). Thermal structure and CO distribution for the Venus mesosphere/lower thermosphere: 2001-2009 inferior conjunction sub-millimeter CO absorption line observations. *Icarus*, **217**, 779–793.

Coakley, J.A., Jr., Cess, R.D. & Yurevich, F.B. (1983). The Effect of Tropospheric Aerosols on the Earth's Radiation Budget: A Parameterization for Climate Models. *Journal of Atmospheric Sciences*, **40**, 116–138.

Colin, L. (1983). Basic facts about Venus. *Venus II. Tucson, The University of Arizona Press*, 10–26.

Correia, A.C.M. & Laskar, J. (2001). The four final rotation states of Venus. *Nature* , **411**, 767–770.

Counselman, C.C., Gourevitch, S.A., King, R.W., Loriot, G.B. & Ginsberg, E.S. (1980). Zonal and meridional circulation of the lower atmosphere of Venus determined by radio interferometry. *Journal of Geophysical Research*, **85**, 8026–8030.

Coustenis, A. & Taylor, F. (1999). Titan : the earth-like moon. *Singapore: World Scientific, ISBN 9810239211*.

Covey, C. & Schubert, G. (1983). Venus atmospheric waves: A challenge for nonlinear dynamics. *Physica D Nonlinear Phenomena*, **6**, 241–248.

Covey, C., Pitcher, E.J. & Brown, J.P. (1986). General circulation model simulations of superrotation in slowly rotating atmospheres - Implications for Venus. *Icarus*, **66**, 380–396.

Crisp, D. (1986). Radiative forcing of the Venus mesosphere. I - Solar fluxes and heating rates. *Icarus*, **67**, 484–514.

Crisp, D. (1989). Radiative forcing of the Venus mesosphere. II - Thermal fluxes, cooling rates, and radiative equilibrium temperatures. *Icarus*, **77**, 391–413.

Crisp, D. & Titov, D. (1997). *The thermal balance of Venus atmosphere. In: Bougher, S.W., Hunten, D.M., Phillips, R.J. (Eds.), Venus II. Tucson, The University of Arizona Press, pp. 353-384*.

BIBLIOGRAPHY

Cullen, M.J.P. & Barnes, R.T.H. (1997). Positive definite advection scheme. *Unified Model Documentation Paper No. 11. Meteorological Office, UK.*.

Cullen, M.J.P., Davies, T. & Mawson, M.H. (1992). Conservative finite diferences schemes for a unified forecast/climate model. *Unified Model Documentation Paper No. 10. Meteorological Office, UK.*.

de Bergh, C., Bezard, B., Crisp, D., Maillard, J.P., Owen, T., Pollack, J. & Grinspoon, D. (1995). Water in the deep atmosphere of Venus from high-resolution spectra of the night side. *Advances in Space Research*, **15**, 79–88.

del Genio, A.D. & Rossow, W.B. (1990). Planetary-scale waves and the cyclic nature of cloud top dynamics on Venus. *Journal of Atmospheric Sciences*, **47**, 293–318.

del Genio, A.D. & Suozzo, R.J. (1987). A comparative study of rapidly and slowly rotating dynamical regimes in a terrestrial general circulation model. *Journal of Atmospheric Sciences*, **44**, 973–986.

del Genio, A.D. & Zhou, W. (1996). Simulations of Superrotation on Slowly Rotating Planets: Sensitivity to Rotation and Initial Condition. *Icarus*, **120**, 332–343.

del Genio, A.D., Zhou, W. & Eichler, T.P. (1993). Equatorial superrotation in a slowly rotating GCM - Implications for Titan and Venus. *Icarus*, **101**, 1–17.

Drossart, P., Piccioni, G., Adriani, A., Angrilli, F., Arnold, G., Baines, K.H., Bellucci, G., Benkhoff, J., Bézard, B., Bibring, J.P., Blanco, A., Blecka, M.I., Carlson, R.W., Coradini, A., di Lellis, A., Encrenaz, T., Erard, S., Fonti, S., Formisano, V., Fouchet, T., Garcia, R., Haus, R., Helbert, J., Ignatiev, N.I., Irwin, P.G.J., Langevin, Y., Lebonnois, S., Lopez-Valverde, M.A., Luz, D., Marinangeli, L., Orofino, V., Rodin, A.V., Roos-Serote, M.C., Saggin, B., Sanchez-Lavega, A., Stam, D.M., Taylor, F.W., Titov, D., Visconti, G., Zambelli, M., Hueso, R., Tsang, C.C.C., Wilson, C.F. & Afanasenko, T.Z. (2007). Scientific goals for the observation of Venus by VIRTIS on ESA/Venus express mission. *Planetary and Space Science*, **55**, 1653–1672.

Elsasser, W.M. (1942). Heat Transfer by Infrared Radiation in the Atmosphere. *Harvard Meteorological Studies, Harvard University Press*, **6**.

Esposito, L.W. (1980). Ultraviolet contrasts and the absorbers near the Venus cloud tops. *Journal of Geophysical Research* , **85**, 8151–8157.

Eymet, V., Fournier, R., Dufresne, J., Lebonnois, S., Hourdin, F. & Bullock, M.A. (2009). Net exchange parameterization of thermal infrared radiative transfer in Venus' atmosphere. *Journal of Geophysical Research (Planets)*, **114**, E11008.

Fels, S.B. (1977). Momentum and energy exchanges due to orographically scattered gravity waves. *Journal of Atmospheric Sciences*, **34**, 499–514.

Fels, S.B. & Lindzen, R.S. (1974). The Interaction of Thermally Excited Gravity Waves with Mean Flows. *Geophysical and Astrophysical Fluid Dynamics*, **6**, 149–191.

Ford, P.G. & Pettengill, G.H. (1992). Venus topography and kilometer-scale slopes. *Journal of Geophysical Research* , **97**, 13103–13114.

Fu, Q. (1991). *Parameterization of radiative processes in vertically nonhomogeneous multiple scattering atmospheres*. Ph.D. thesis, Utah Univ., Salt Lake City.

Fu, Q. & Liou, K.N. (1993). Parameterization of the Radiative Properties of Cirrus Clouds. *Journal of Atmospheric Sciences*, **50**, 2008–2025.

Gierasch, P.J. (1975). Meridional circulation and the maintenance of the Venus atmospheric rotation. *Journal of Atmospheric Sciences*, **32**, 1038–1044.

Gierasch, P.J., Goody, R.M., Young, R.E., Crisp, D., Edwards, C., Kahn, R., Rider, D., del Genio, A., Greeley, R., Hou, A., Leovy, C.B., McCleese, D. & Newman, M. (1997). The General Circulation of the Venus Atmosphere: an Assessment. *Venus II: Geology, Geophysics, Atmosphere, and Solar Wind Environment. Tucson, AZ: University of Arizona Press*, p. 459.

Goldstein, R.M. (1964). Symposium on Radar and Radiometric Observations of Venus during the 1962 Conjunction: Venus characteristics by earth-based radar. *The Astronomical Journal*, **69**, p. 12.

Grassi, D., Migliorini, A., Montabone, L., Lebonnois, S., Cardesìn-Moinelo, A., Piccioni, G., Drossart, P. & Zasova, L.V. (2010). Thermal structure of Venusian nighttime mesosphere as observed by VIRTIS-Venus Express. *Journal of Geophysical Research (Planets)*, **115**, E09007.

Greeley, R., Arvidson, R.E., Elachi, C., Geringer, M.A., Plaut, J.J., Saunders, R.S., Schubert, G., Stofan, E.R., Thouvenot, E.J.P. & Wall, S.D. (1992). Aeolian features on Venus - Preliminary Magellan results. *Journal of Geophysical Research* , **97**, 13319.

Grieger, B., Ignatiev, N.I., Hoekzema, N.M. & Keller, H.U. (2004). Indication of a near surface cloud layer on Venus from reanalysis of Venera 13/14 spectrophotometer data. In A. Wilson, ed., *Planetary Probe Atmospheric Entry and Descent Trajectory Analysis and Science*, vol. 544 of *ESA Special Publication*, 63–70.

Haynes, P. & Shuckburgh, E. (2000a). Effective diffusivity as a diagnostic of atmospheric transport 1. Stratosphere. *Journal of Geophysical Research* , **105**, 22777–22794.

Haynes, P. & Shuckburgh, E. (2000b). Effective diffusivity as a diagnostic of atmospheric transport 2. Troposphere and lower stratosphere. *Journal of Geophysical Research* , **105**, 22795–22810.

Held, I.M. & Hou, A.Y. (1980). Nonlinear Axially Symmetric Circulations in a Nearly Inviscid Atmosphere. *Journal of Atmospheric Sciences*, **37**, 515–533.

Hess, S.L. (1975). Dust on Venus. *Journal of Atmospheric Sciences*, **32**, 1076–1078.

Hide, R. (1969). Dynamics of the Atmospheres of the Major Planets with an Appendix on the Viscous Boundary Layer at the Rigid Bounding Surface of an Electrically-Conducting Rotating Fluid in the Presence of a Magnetic Field. *Journal of Atmospheric Sciences*, **26**, 841–853.

Hollingsworth, J.L., Young, R.E., Schubert, G., Covey, C. & Grossman, A.S. (2007). A simple-physics global circulation model for Venus: Sensitivity assessments of atmospheric superrotation. *Geophysical Research Letters*, **34**, 5202–+.

Hoskins, B.J., McIntyre, M.E. & Robertson, A.W. (1985). On the use and significance of isentropic potential vorticity maps. *Quarterly Journal of the Royal Meteorological Society*, **111**, 877–946.

Hou, A.Y. & Farrell, B.F. (1987). Superrotation induced by critical-level absorption of gravity waves on Venus - an assessment. *Journal of Atmospheric Sciences*, **44**, 1049–1061.

Hourdin, F., Le van, P., Forget, F. & Talagrand, O. (1993). Meteorological Variability and the Annual Surface Pressure Cycle on Mars. *Journal of Atmospheric Sciences*, **50**, 3625–3640.

Ignatiev, N.I., Titov, D.V., Piccioni, G., Drossart, P., Markiewicz, W.J., Cottini, V., Roatsch, T., Almeida, M. & Manoel, N. (2009). Altimetry of the Venus cloud tops from the Venus Express observations. *Journal of Geophysical Research (Planets)*, **114**, E00B43.

Ikeda, K., Yamamoto, M. & Takahashi, M. (2007). Superrotation of the Venus atmosphere simulated by an Atmospheric General Circulation Model. In *IUGG/IAMAS Meeting*, vol. Perugia, Italy.

Ip, W.H. & Fernandez, J.A. (1988). Exchange of condensed matter among the outer and terrestrial protoplanets and the effect on surface impact and atmospheric accretion. *Icarus*, **74**, 47–61.

Jacobson, M.Z. (2005). Fundamentals of Atmospheric Modelling. *Cambridge University Press*.

Kalnay de Rivas, E. (1975). Further numerical calculations of the circulation of the atmosphere of Venus. *Journal of Atmospheric Sciences*, **32**, 1017–1024.

Kasting, J.F. (1988). Runaway and moist greenhouse atmospheres and the evolution of earth and Venus. *Icarus*, **74**, 472–494.

Kerzhanovich, V.V. & Limaye, S.S. (1985). Circulation of the atmosphere from the surface to 100 KM. *Advances in Space Research*, **5**, 59–83.

Khatuntsev, I., Patsaeva, M., Ignatiev, N., Titov, D. & Markiewicz, W.J. (2013). Variations of zonal wind speed at Venus cloud tops from Venus Monitoring Camera UV images. In *EGU General Assembly Conference Abstracts*, vol. 15 of *EGU General Assembly Conference Abstracts*, 11880.

Kliore, A.J., Moroz, V.I. & Keating, G.M. (1985). The Venus International Reference Atmosphere. *Advances in Space Research*, **5**.

Knollenberg, R.G. & Hunten, D.M. (1980). The microphysics of the clouds of Venus - Results of the Pioneer Venus particle size spectrometer experiment. *Journal of Geophysical Research*, **85**, 8039–8058.

Kok, J.F. & Renno, N.O. (2006). Enhancement of the emission of mineral dust aerosols by electric forces. *Geophysical Research Letters*, **33**, 19.

Kok, J.F., Parteli, E.J.R., Michaels, T.I. & Karam, D.B. (2012). The physics of wind-blown sand and dust. *Reports on Progress in Physics*, **75**, 106901.

Kylling, A., Stamnes, K. & Tsay, S. (1995). A reliable ans efficient two-stream algorithm for spherical radiative transfer: Documentation of accuracy in realistic layered media. *Journal of Atmospheric Chemistry*, **21**.

Lacis, A.A. & Oinas, V. (1991). A description of the correlated-k distribution method for modelling nongray gaseous absorption, thermal emission, and multiple scattering in vertically inhomogeneous atmospheres. *Journal of Geophysical Research* , **96**, 9027–9064.

Lebonnois, S., Hourdin, F., Eymet, V., Crespin, A., Fournier, R. & Forget, F. (2010a). Superrotation of Venus' atmosphere analyzed with a full general circulation model. *Journal of Geophysical Research (Planets)*, **115**.

Lebonnois, S., Hourdin, F., Forget, F., Eymet, V. & Fournier, R. (2010b). The super-rotation mechanism based on Global Circulation Model simulations. *VEXAG International Workshop*.

Lebonnois, S., Lee, C., Yamamoto, M., Dawson, J., Lewis, S.R., Mendonca, J., Read, P.L. & Parish, H. (2011). Weakly forced atmospheric GCMs : Lessons from model comparisons. In *EPSC-DPS Joint Meeting 2011*, 144.

Lebonnois, S., Lee, C., Yamamoto, M., Dawson, J., Lewis, S.R., Mendonca, J., Read, P., Parish, H.F., Schubert, G., Bengtsson, L., Grinspoon, D., Limaye, S.S., Schmidt, H., Svedhem, H. & Titov, D.V. (2013). Models of Venus Atmosphere. *Towards Understanding the Climate of Venus, ISSI Scientific Report Series, Volume 11. ISBN 978-1-4614-5063-4, Springer Science+Business Media New York*, p. 129.

Lee, C. (2006). *Modelling of the Atmosphere of Venus*. Ph.D. thesis, Oxford University.

Lee, C. & Richardson, M.I. (2010). A general circulation model ensemble study of the atmospheric circulation of Venus. *Journal of Geophysical Research (Planets)*, **115**, 4002.

Lee, C. & Richardson, M.I. (2011). A Discrete Ordinate, Multiple Scattering, Radiative Transfer Model of the Venus Atmosphere from 0.1 to 260μm. *Journal of Atmospheric Sciences*, **68**, 1323–1339.

Lee, C., Lewis, S.R. & Read, P.L. (2005). A numerical model of the atmosphere of Venus. *Advances in Space Research*, **36**, 2142–2145.

Lee, C., Lewis, S.R. & Read, P.L. (2007). Superrotation in a Venus general circulation model. *Journal of Geophysical Research* , **112 (E4), E04S11**.

Lellouch, E., Clancy, T., Crisp, D., Kliore, A.J., Titov, D. & Bougher, S.W. (1997). Monitoring of Mesospheric Structure and Dynamics. In S.W. Bougher, D.M. Hunten & R.J. Phillips, eds., *Venus II: Geology, Geophysics, Atmosphere, and Solar Wind Environment*, 295.

Leovy, C.B. (1973). Rotation of the upper atmosphere of Venus. *Journal of Atmospheric Sciences*, **30**, 1218–1220.

Limaye, S.S. (1985). Venus atmospheric circulation - Observations and implications of the thermal structure. *Advances in Space Research*, **5**, 51–62.

Limaye, S.S. (2007). Venus atmospheric circulation: Known and unknown. *Journal of Geophysical Research (Planets)*, **112**, 4.

Limaye, S.S., Kossin, J.P., Rozoff, C., Piccioni, G., Titov, D.V. & Markiewicz, W.J. (2009). Vortex circulation on Venus: Dynamical similarities with terrestrial hurricanes. *Geophysical Research Letters*, **36**, p. L04204.

Liou, K.N. (1992). Radiation and Cloud Processes in the Atmosphere. *New York: University Press*.

Liou, K.N. (2002). An Introduction to Atmospheric Radiation. *Academic Press, 2 Edition*.

Luz, D., Hourdin, F., Rannou, P. & Lebonnois, S. (2003). Latitudinal transport by barotropic waves in Titan's stratosphere. II. Results from a coupled dynamics-microphysics-photochemistry GCM. *Icarus*, **166**, 343–358.

Marcq, E., Bertaux, J.L., Montmessin, F. & Belyaev, D. (2013). Variations of sulphur dioxide at the cloud top of Venus's dynamic atmosphere. *Nature Geoscience*, **6**, 25–28.

Mariotti, A., Legras, B. & Dritschel, D.G. (1994). Vortex stripping and the erosion of coherent structures in two-dimensional flows. *Physics of Fluids*, **6**, 3954–3962.

Markiewicz, W.J., Titov, D.V., Limaye, S.S., Keller, H.U., Ignatiev, N., Jaumann, R., Thomas, N., Michalik, H., Moissl, R. & Russo, P. (2007). Morphology and dynamics of the upper cloud layer of Venus. *Nature* , **450**, 633–636.

Marov, M.Y., Avduevsky, V.S., Borodin, N.F., Ekonomov, A.P., Kerzhanovich, V.V., Lysov, V.P., Moshkin, B.Y., Rozhdestvensky, M.K. & Ryabov, O.L. (1973). Preliminary Results on the Venus Atmosphere from the Venera 8 Descent Module. *Icarus*, **20**, 407.

Mayr, H.G. & Harris, I. (1983). Quasi-axisymmetric circulation and superrotation in planetary atmospheres. *Astronomy and Astrophysics*, **121**, 124–136.

McGouldrick, K. (2011). Microphysical and radiative transfer model of the lower, middle, and upper clouds of Venus. In *EPSC-DPS Joint Meeting 2011*, 1604.

McGouldrick, K.B. (2007). *Microphysics and radiative-dynamical feedback in the near infrared brightness features in the Venus clouds*. Ph.D. thesis, University of Colorado at Boulder.

McLandress, C. & Scinocca, J.F. (2005). The GCM Response to Current Parameterizations of Nonorographic Gravity Wave Drag. *Journal of Atmospheric Sciences*, **62**, 2394–2413.

Meadows, V.S. & Crisp, D. (1996). Ground-based near-infrared observations of the Venus nightside: The thermal structure and water abundance near the surface. *Journal of Geophysical Research* , **101**, 4595–4622.

Mendonça, J.M., Read, P.L., Wilson, C.F. & Lewis, S.R. (2012). Zonal winds at high latitudes on Venus: An improved application of cyclostrophic balance to Venus Express observations. *Icarus*, **217**, 629–639.

Mesinger, F. (1981). Horizontal Advection Schemes of a Staggered Grid - An Enstrophy and Energy-Conserving Model. *Monthly Weather Review*, **109**, 467.

Moissl, R., Khatuntsev, I., Limaye, S.S., Titov, D.V., Markiewicz, W.J., Ignatiev, N.I., Roatsch, T., Matz, K.D., Jaumann, R., Almeida, M., Portyankina, G., Behnke, T. & Hviid, S.F. (2009). Venus cloud top winds from tracking UV features in Venus Monitoring Camera images. *Journal of Geophysical Research (Planets)*, **114**, 0–+.

Monin, A.S. & Obukhov, A.M. (1954). Basic laws of turbulent mixing in the ground layer of the atmosphere. *Trans. Geophys. Inst. Akad. Nuak.*, **151**, 1963–1987.

Moroz, V.I. (1983). *Stellar magnitude and albedo data of Venus*, 27–35.

Moroz, V.I., Ekonomov, A.P., Moshkin, B.E., Revercomb, H.E., Sromovsky, L.A. & Schofield, J.T. (1985). Solar and thermal radiation in the Venus atmosphere. *Advances in Space Research*, **5**, 197–232.

Moskalenko, N.I., Ilin, I.A., Parzhin, S.N. & Rodionov, L.V. (1979). Pressure-induced infrared radiation absorption in atmospheres. *Akademiia Nauk SSSR Fizika Atmosfery i Okeana*, **15**, 912–919.

Neron de Surgy, O. & Laskar, J. (1997). On the long term evolution of the spin of the Earth. *Astronomy and Astrophysics*, **318**, 975–989.

Newman, M. & Leovy, C. (1992). Maintenance of strong rotational winds in Venus' middle atmosphere by thermal tides. *Science*, **257**, 647–650.

Newman, M., Schubert, G., Kliore, A.J. & Patel, I.R. (1984). Zonal winds in the middle atmosphere of Venus from Pioneer Venus radio occultation data. *Journal of Atmospheric Sciences*, **41**, 1901–1913.

Parish, H.F., Schubert, G., Covey, C., Walterscheid, R.L., Grossman, A. & Lebonnois, S. (2011). Decadal variations in a Venus general circulation model. *Icarus*, **212**, 42–65.

Pechmann, J.B. & Ingersoll, A.P. (1984). Thermal tides in the atmosphere of Venus - Comparison of model results with observations. *Journal of Atmospheric Sciences*, **41**, 3290–3313.

Peixoto, J.P. & Oort, A.H. (1992). Physics of climate. *New York: American Institute of Physics*.

Piccialli, A., Titov, D.V., Grassi, D., Khatuntsev, I., Drossart, P., Piccioni, G. & Migliorini, A. (2008). Cyclostrophic winds from the Visible and Infrared Thermal Imaging Spectrometer temperature sounding: A preliminary analysis. *Journal of Geophysical Research (Planets)*, **113**.

Piccialli, A., Tellmann, S., Titov, D.V., Limaye, S.S., Khatuntsev, I.V., Pätzold, M. & Häusler, B. (2012). Dynamical properties of the Venus mesosphere from the radio-occultation experiment VeRa onboard Venus Express. *Icarus*, **217**, 669–681.

Piccioni, G., Drossart, P., Sanchez-Lavega, A., Hueso, R., Taylor, F.W., Wilson, C.F., Grassi, D., Zasova, L., Moriconi, M., Adriani, A., Lebonnois, S., Coradini, A., Bézard, B., Angrilli, F., Arnold, G., Baines, K.H., Bellucci, G., Benkhoff, J., Bibring, J.P., Blanco, A., Blecka, M.I., Carlson, R.W., di Lellis, A., Encrenaz, T., Erard, S., Fonti, S., Formisano, V., Fouchet, T., Garcia, R., Haus, R., Helbert, J., Ignatiev, N.I., Irwin, P.G.J., Langevin, Y., Lopez-Valverde, M.A., Luz, D., Marinangeli, L., Orofino, V., Rodin, A.V., Roos-Serote, M.C., Saggin, B., Stam, D.M., Titov, D., Visconti, G., Zambelli, M., Ammannito, E., Barbis, A., Berlin, R., Bettanini, C., Boccaccini, A., Bonnello, G., Bouye, M., Capaccioni, F., Cardesin Moinelo, A., Carraro, F., Cherubini, G., Cosi, M., Dami, M., de Nino, M., Del Vento, D., di Giampietro, M., Donati, A., Dupuis, O., Espinasse, S., Fabbri, A., Fave, A., Veltroni, I.F., Filacchione, G., Garceran, K., Ghomchi, Y., Giustini, M., Gondet, B., Hello, Y., Henry, F., Hofer, S., Huntzinger, G., Kachlicki, J., Knoll, R., Driss, K., Mazzoni, A., Melchiorri, R., Mondello, G., Monti, F., Neumann, C., Nuccilli, F., Parisot, J., Pasqui, C., Perferi, S., Peter, G., Piacentino, A., Pompei, C., Reess, J.M., Rivet, J.P., Romano, A., Russ, N., Santoni, M., Scarpelli, A., Semery, A., Soufflot, A., Stefanovitch, D., Suetta, E., Tarchi, F., Tonetti, N., Tosi, F. & Ulmer, B. (2007a). South-polar features on Venus similar to those near the north pole. *Nature* , **450**, 637–640.

Piccioni, G., Drossart, P., Suetta, E., Cosi, M., Ammannitto, E., Barbis, A., Berlin, R., A., B., Bonello, G., Bouye, M., Capaccioni, F., Cherubini, G., Dami, M., Dupuis, O., Fave, A., Filacchione, G., Hello, Y., Henry, F., Hofer, S., Huntzinger, G., Melchiorri, R., Parisot, J., Pasqui, C., Peter, G., Compei, C., Reess, J., Semery, A., Soufflot, A. & the VIRTIS Co-I team (2007b). VIRTIS: The Visible and Infrared Thermal Imaging Spectrometer. *ESA SP, 1295*.

Pieters, C.M., Head, J.W., Patterson, W., Pratt, S. & Garvin, J. (1986). The color of the surface of Venus. *Science*, **234**, 1379–1383.

Pollack, J.B., Toon, O.B., Whitten, R.C., Boese, R., Ragent, B., Tomasko, M., Eposito, L., Travis, L. & Wiedman, D. (1980). Distribution and source of the UV absorption in Venus' atmosphere. *Journal of Geophysical Research* , **85**, 8141–8150.

Preston, R.A., Hildebrand, C.E., Purcell, G.H., Ellis, J., Stelzried, C.T., Finley, S.G., Sagdeev, R.Z., Linkin, V.M., Kerzhanovich, V.V., Altunin, V.I., Kogan, L.R., Kostenko, V.I., Matveenko, L.I., Pogrebenko, S.V., Strukov, I.A., Akim, E.L., Alexandrov, Y.N., Armand, N.A., Bakitko, R.N., Vyshlov, A.S., Bogomolov, A.F., Gorchankov, Y.N., Selivanov, A.S., Ivanov, N.M., Tichonov, V.F., Blamont, J.E., Boloh, L., Laurans, G., Boischot, A., Biraud, F., Ortega-Molina, A., Rosolen, C. & Petit, G. (1986). Determination of Venus winds by ground-based radio tracking of the VEGA balloons. *Science*, **231**, 1414–1416.

Ramanathan, V., Cicerone, R.J., Kiehl, J.T. & Singh, H.B. (1985). Trace gas trends and their potential role in climate change. *Journal of Geophysical Research* , **90**, 5547–5566.

Read, P.L. (1986). Super-rotation and diffusion of axial angular momentum. II. A review of quasi-axisymmetric models of planetary atmospheres. *Quarterly Journal of the Royal Meteorological Society*, **112**, 253–272.

Rees, G. (1999). The Remote Sensing Data Book. *Cambridge University Press, ISBN 052148040X*.

Reichler, T. & Kim, J. (2008). How Well Do Coupled Models Simulate Today's Climate? *Bulletin of the American Meteorological Society*, **89**, 303.

Revercomb, H.E., Sromovsky, L.A., Suomi, V.E. & Boese, R.W. (1985). Net thermal radiation in the atmosphere of Venus. *Icarus*, **61**, 521–538.

Roberts, R.E., Biberman, L.M. & Selby, J.E.A. (1976). Infrared continuum absorption by atmospheric water vapor in the 8-12-micron window. *Applied Optics*, **15**, 2085–2090.

Rodgers, C.D. (1967). The radiative heat budget of the troposphere and lower stratosphere. *Planetary Circulation Project, Department of Meteorology Rep. A2, Massachusetts Institute of Technology*, 126.

Roos-Serote, M., Drossart, P., Encrenaz, T., Lellouch, E., Carlson, R.W., Baines, K.H., Taylor, F.W. & Calcutt, S.B. (1995). The thermal structure and dynamics of the atmosphere of Venus between 70 and 90 KM from the Galileo-NIMS spectra. *Icarus*, **114**, 300–309.

Rossow, W.B. (1978). Cloud microphysics - Analysis of the clouds of Earth, Venus, Mars, and Jupiter. *Icarus*, **36**, 1–50.

Rossow, W.B. (1983). A general circulation model of a Venus-like atmosphere. *Journal of Atmospheric Sciences*, **40**, 273–302.

Rossow, W.B. & Williams, G.P. (1979). Large-scale motion in the Venus stratosphere. *Journal of Atmospheric Sciences*, **36**, 377–389.

Rossow, W.B., del Genio, A.D., Limaye, S.S. & Travis, L.D. (1980). Cloud morphology and motions from Pioneer Venus images. *Journal of Geophysical Research* , **85**, 8107–8128.

Rothman, L.S., Wattson, R.B., Gamache, R., Schroeder, J.W. & McCann, A. (1995). HITRAN HAWKS and HITEMP: high-temperature molecular database. In J. C. Dainty, ed., *Society of Photo-Optical Instrumentation Engineers (SPIE) Conference Series*, vol. 2471 of *Society of Photo-Optical Instrumentation Engineers (SPIE) Conference Series*, 105–111.

Rothman, L.S., Jacquemart, D., Barbe, A., Chris Benner, D., Birk, M., Brown, L.R., Carleer, M.R., Chackerian, C., Chance, K., Coudert, L.H., Dana, V., Devi, V.M., Flaud, J.M., Gamache, R.R., Goldman, A., Hartmann, J.M.,

Jucks, K.W., Maki, A.G., Mandin, J.Y., Massie, S.T., Orphal, J., Perrin, A., Rinsland, C.P., Smith, M.A.H., Tennyson, J., Tolchenov, R.N., Toth, R.A., Vander Auwera, J., Varanasi, P. & Wagner, G. (2005). The HITRAN 2004 molecular spectroscopic database. *Journal of Quantitative Spectroscopy and Radiative Transfer*, **96**, 139–204.

Sagan, C. (1961). The Planet Venus. *Science*, **133**, 849–858.

Sánchez-Lavega, A., Hueso, R., Piccioni, G., Drossart, P., Peralta, J., Pérez-Hoyos, S., Wilson, C.F., Taylor, F.W., Baines, K.H., Luz, D., Erard, S. & Lebonnois, S. (2008). Variable winds on Venus mapped in three dimensions. *Geophysical Research Letters*, **35**, 13204.

Satoh, T., Imamura, T., Hashimoto, G.L., Iwagami, N., Mitsuyama, K., Sorahana, S., Drossart, P. & Piccioni, G. (2009). Cloud structure in Venus middle-to-lower atmosphere as inferred from VEX/VIRTIS 1.74 μm data. *Journal of Geophysical Research (Planets)*, **114**, E00B37.

Schaber, G.G., Strom, R.G., Moore, H.J., Soderblom, L.A., Kirk, R.L., Chadwick, D.J., Dawson, D.D., Gaddis, L.R., Boyce, J.M. & Russell, J. (1992). Geology and distribution of impact craters on Venus - What are they telling us? *Journal of Geophysical Research*, **97**, 13257.

Schaefer, L. & Fegley, B. (2003). Metallic Snow in the Venusian Highlands. In *AAS/Division for Planetary Sciences Meeting Abstracts #35*, vol. 35 of *Bulletin of the American Astronomical Society*, 984.

Schofield, J.T. & Diner, D.J. (1983). Rotation of Venus's polar dipole. *Nature* , **305**, 116–119.

Schubert, G. (1983). *General circulation and the dynamical state of the Venus atmosphere. In: Hunten, D., Colin, L., Donahue, T., Moroz, V. (Eds.), Venus. Tucson, University of Arizona Press*, 681–765.

Schubert, G., Covey, C., del Genio, A., Elson, L.S., Keating, G., Seiff, A., Young, R.E., Apt, J., Counselman, C.C., Kliore, A.J., Limaye, S.S., Revercomb, H.E., Sromovsky, L.A., Suomi, V.E., Taylor, F., Woo, R. & von Zahn,

U. (1980). Structure and circulation of the Venus atmosphere. *Journal of Geophysical Research* , **85**, 8007–8025.

Schubert, W.H., Montgomery, M.T., Taft, R.K., Guinn, T.A., Fulton, S.R., Kossin, J.P. & Edwards, J.P. (1999). Polygonal Eyewalls, Asymmetric Eye Contraction, and Potential Vorticity Mixing in Hurricanes. *Journal of Atmospheric Sciences*, **56**, 1197–1223.

Seiff, A. (1983). Thermal structure of the atmosphere of Venus. *Venus. Tucson, University of Arizona Press*, 215–279.

Seiff, A., Kirk, D.B., Young, R.E., Blanchard, R.C., Findlay, J.T., Kelly, G.M. & Sommer, S.C. (1980). Measurements of thermal structure and thermal contrasts in the atmosphere of Venus and related dynamical observations - Results from the four Pioneer Venus probes. *Journal of Geophysical Research* , **85**, 7903–7933.

Shao, Y. & Lu, H. (2000). A simple expression for wind erosion threshold friction velocity. *Journal of Geophysical Research* , **105**, 22437.

Smith, R.M.B. (1993a). Subsurface, surface and boundary layer processes. *Unified Model Documentation Paper No. 24 part 1. Meteorological Office, UK.*.

Smith, R.M.B. (1993b). Subsurface, surface and boundary layer processes. *Unified Model Documentation Paper No. 24 part 2. Meteorological Office, UK.*.

Smrekar, S.E., Elkins-Tanton, L., Leitner, J.J., Lenardic, A., Mackwell, S., Moresi, L., Sotin, C. & Stofan, E.R. (2007). Tectonic and thermal evolution of Venus and the role of volatiles: Implications for understanding the terrestrial planets. *Washington DC American Geophysical Union Geophysical Monograph Series*, **176**, 45–71.

Sonett, C.P. (1963). A Summary Review of the Scientific Findings of the Mariner Venus Mission. *Space Science Reviews*, **2**, 751–777.

Stamnes, K., Tsay, S., Wiscombe, W. & Laszlo, I. (2000). SISORT, a general-purpose Fortran program for discreteordinate-method radiative transfer in scattering and emitting layeres media: documentation of methodology. *Rep. available from ftp://climatel.gsfc.nasa.gov.wiscombe*.

Stott, P.A., Tett, S.F.B., Jones, G.S., Allen, M.R., Mitchell, J.F.B. & Jenkins, G.J. (2000). External Control of 20th Century Temperature by Natural and Anthropogenic Forcings. *Science*, **290**, 2133–2137.

Taylor, F.W. (2006). Venus before Venus Express. *Planetary and Space Science*, **54**, 1249–1262.

Taylor, F.W. (2011). Comparative planetology, climatology and biology of Venus, Earth and Mars. *Planetary and Space Science*, **59**, 889–899.

Taylor, F.W., McCleese, D.J. & Diner, D.J. (1979). Polar clearing in the Venus clouds observed from the Pioneer Orbiter. *Nature* , **279**, 613–614.

Taylor, F.W., Beer, R., Chahine, M.T., Diner, D.J., Elson, L.S., Haskins, R.D., McCleese, D.J., Martonchik, J.V., Reichley, P.E., Bradley, S.P., Delderfield, J., Schofield, J.T., Farmer, C.B., Froidevaux, L., Leung, J., Coffey, M.T. & Gille, J.C. (1980). Structure and meteorology of the middle atmosphere of Venus Infrared remote sensing from the Pioneer orbiter. *Journal of Geophysical Research* , **85**, 7963–8006.

Taylor, F.W., Crisp, D. & Bézard, B. (1997). Near-Infrared Sounding of the Lower Atmosphere of Venus. *Venus II: Geology, Geophysics, Atmosphere, and Solar Wind Environment, University of Arizona Press, Tucson*, 325–352.

Tellmann, S., Pätzold, M., Häusler, B., Bird, M.K. & Tyler, G.L. (2009). Structure of the Venus neutral atmosphere as observed by the Radio Science experiment VeRa on Venus Express. *Journal of Geophysical Research (Planets)*, **114**, p. E00B36.

Titov, D.V., Taylor, F.W., Svedhem, H., Ignatiev, N.I., Markiewicz, W.J., Piccioni, G. & Drossart, P. (2008). Atmospheric structure and dynamics as the cause of ultraviolet markings in the clouds of Venus. *Nature* , **456**, 620–623.

Titov, D.V., Markiewicz, W.J., Ignatiev, N.I., Song, L., Limaye, S.S., Sanchez-Lavega, A., Hesemann, J., Almeida, M., Roatsch, T., Matz, K.D., Scholten, F., Crisp, D., Esposito, L.W., Hviid, S.F., Jaumann, R., Keller, H.U. & Moissl, R. (2012). Morphology of the cloud tops as observed by the Venus Express Monitoring Camera. *Icarus*, **217**, 682–701.

Tomasko, M.G., Doose, L.R., Smith, P.H. & Odell, A.P. (1980). Measurements of the flux of sunlight in the atmosphere of Venus. *Journal of Geophysical Research* , **85**, 8167–8186.

Tomasko, M.G., Doose, L.R. & Smith, P.H. (1985). The absorption of solar energy and the heating rate in the atmosphere of Venus. *Advances in Space Research*, **5**, 71–79.

von Zahn, U. & Moroz, V.I. (1985). Composition of the Venus atmosphere below 100 KM altitude. *Advances in Space Research*, **5**, 173–195.

von Zahn, U., Kumar, S., Niemann, H. & Prinn, R. (1983). Composition of the Venus atmosphere. *Venus, University of Arizona Press, Tucson*, 299–430.

Warrilow, D.A., Sangster, A.B. & Slingo, A. (1986). Modeling of land surface processes and their influence on European climate. *Tech. Rep. DCTN 38, UKMO, Meteorological Office, London Road, Bracknell, Bershire, United Kingdom*.

Washburn, E.W. (1930). International Critical Tables of Numerical Data: Physics, Chemistry and Technology. *New York, NY: McGraw-Hill*.

Weitz, C.M., Plaut, J.J., Greeley, R. & Saunders, R.S. (1994). Dunes and microdunes on Venus: Why were so few found in the Magellan data? *Icarus*, **112**, 282–295.

White, A.A. & Bromley, R.A. (1995). Dynamically consistent, quasi-hydrostatic equations for global models with a complete representation of the Coriolis force. *Quarterly Journal of the Royal Meteorological Society*, **121**, 399–418.

Williams, D.R. (2003a). Earth fact sheet: National space science data center. *http://nssdc.gsfc.nasa.gov/planetary/factsheet/earthfact.html*.

Williams, D.R. (2003b). Venus fact sheet: National space science data center. *http://nssdc.gsfc.nasa.gov/planetary/factsheet/venusfact.html*.

Williams, G.P. (1988a). The dynamical range of global circulations - I. *Climate Dynamics*, **2**, 205–260.

Williams, G.P. (1988b). The dynamical range of global circulations - II. *Climate Dynamics*, **3**, 45–84.

Wiscombe, W.T. (1977). The delta-Eddington approximation for a vertically inhomogeneous atmosphere. *NCAR Tech. Note NCAR/TN-121+STR*, 66.

Yamamoto, M. & Takahashi, M. (2003). The Fully Developed Superrotation Simulated by a General Circulation Model of a Venus-like Atmosphere. *Journal of Atmospheric Sciences*, **60**, 561–574.

Yamamoto, M. & Takahashi, M. (2009). Influences of Venus' topography on fully developed superrotation and near-surface flow. *Earth, Planets, and Space*, **61**, 45–48.

Yoder, C.F. (1997). Venusian Spin Dynamics. *Venus II: Geology, Geophysics, Atmosphere, and Solar Wind Environment, University of Arizona Press, Tucson*, 1087.

Young, R.E. & Pollack, J.B. (1977). A three-dimensional model of dynamical processes in the Venus atmosphere. *Journal of Atmospheric Sciences*, **34**, 1315–1351.

Zasova, L.V., Linkin, V.M. & Khatuntsev, I.V. (2000). Zonal wind in the middle atmosphere of Venus. *Kosmicheskie Issledovaniia*, **38**, 54–70.

Zasova, L.V., Ignatiev, N., Khatuntsev, I. & Linkin, V. (2007). Structure of the Venus atmosphere. *Planetary and Space Science*, **55**, 1712–1728.